

MALDI TANDEM MASS SPECTROMETRIC TECHNIQUES FOR THE ANALYSIS AND
IMAGING OF LIGNOCELLULOSIC MATERIALS

By

KYLE ANN LUNSFORD

A DISSERTATION PRESENTED TO THE GRADUATE SCHOOL
OF THE UNIVERSITY OF FLORIDA IN PARTIAL FULFILLMENT
OF THE REQUIREMENTS FOR THE DEGREE OF
DOCTOR OF PHILOSOPHY

UNIVERSITY OF FLORIDA

2011

© 2011 Kyle Ann Lunsford

To Mom, Dad, Quin and Warren

ACKNOWLEDGMENTS

I would like to thank several people for their support, advice and guidance that ultimately led to obtaining a PhD. First, I would like to thank my research advisor, Dr. Yost. I cannot thank him enough, not only for accepting me into the group, but for also allowing me to become part of the 'Yost Group Family.' More importantly, Dr. Yost has managed to make me leave graduate school more passionate about science than when I began.

I would also like to thank Dr. Peter, for his insight into the 'plant world.' I would not have been able to accomplish as much as I did without his willingness to help me understand plants, as well as to provide wood samples. With his help, I became more confident in my research abilities, as well as being able explain mass spectrometry experiments to 'non mass spectrometrists.'

In addition, I would like to thank the Yost Group members, past and present. The Yost group has always been there to support me, to help me grow as a scientist, to help me understand the underlying science of my experiments and to guide me in the right direction. A special thanks to Dr. Dan and Rob for sharing an office with me for two years. Our in-depth conversations (both on- and off-topic) and the 'hard times' we gave each helped me to understand mass spectrometry and my research better.

I would also like to thank the Bio Imaging Mass Spectrometry laboratory at the FOM Institute AMOLF for allowing me to visit for 5 weeks. Specifically, Dr. Ron Heeren for allowing me to visit his lab and providing insight into ToF-SIMS imaging, Andras Kiss for helping me perform the ToF-SIMS analysis and Gert Eijkel for his help with statistics of ToF-SIMS imaging data (and for allowing me to use his ChemomeTricks program).

A true acknowledgements section would not be complete without thanking my family, Mom, Dad, and Quin. I would not be here without my parents paving a path for me to go to college, and ultimately graduate school. I cannot begin to express my gratitude for giving me every opportunity in the world—I realize that they did not have to give me anything, but instead they chose to give me everything. I hope I have shown my appreciation throughout the years and that this document helps make my case! And to my brother Quin, who I would like to thank for always supporting me in my decisions and helping me get through school and for being the best (and most protective) big brother out there.

Last and certainly not least, I would like to thank my husband, Warren, who has provided an irreplaceable support system. Our ‘science fights’ have helped me to grow from a shy, reserved scientist, into a scientist (and woman) more confident than I ever thought that I could be. I look forward to starting the next stage of our life, and scientific careers, together.

TABLE OF CONTENTS

	<u>page</u>
ACKNOWLEDGMENTS.....	4
LIST OF TABLES.....	10
LIST OF FIGURES.....	11
ABSTRACT.....	14
CHAPTER	
1 BACKGROUND.....	16
Biofuel Research.....	16
Bioethanol.....	16
Lignocellulosic Ethanol.....	17
Lignocellulosic Pretreatment.....	19
Analytical Approaches for LCM Analysis.....	20
Mass Spectrometry of Polysaccharides.....	21
Early MS of Polysaccharides.....	21
Tandem MS of Polysaccharides.....	23
Instrumentation.....	25
Matrix-Assisted Laser Desorption/Ionization.....	25
Ionization mechanism.....	25
MALDI matrix considerations.....	26
Secondary Ion Mass Spectrometry.....	27
Mass Analyzers.....	28
Figures of merit.....	29
Linear ion traps.....	29
Tandem MS with LIT.....	31
Time-of-flight.....	32
Tandem MS with ToF.....	34
Mass Spectrometric Imaging.....	35
Microprobe Mass Spectrometric Imaging of Tissue.....	36
Tissue Sectioning.....	36
MALDI Matrix Application.....	37
Mass Spectrometric Imaging Ionization Sources.....	39
SIMS.....	39
DESI.....	39
MALDI.....	40
Mass Spectrometric Imaging Mass Analyzers.....	41
Time-of-flight for imaging.....	41
Linear ion traps for MS imaging.....	42
Orbitraps for MS imaging.....	44

MS Image Generation	45
Overview of Dissertation	46
2 MALDI LINEAR ION TRAP TANDEM MS TECHNIQUES FOR THE ANALYSIS AND CHARACTERIZATION OF LIGNOCELLULOSE STANDARDS: POTENTIAL FOR MALDI-MS ANALYSIS OF INTACT TISSUE.....	58
Introduction	58
Experimental.....	59
Chemicals.....	59
Preparation of MALDI Matrices	59
MALDI Sample Plate Preparation.....	60
Untreated and Holocellulose Tissue	60
Instrumentation.....	61
Results and Discussion.....	62
β -Glucan.....	62
Choosing the optimal matrix.....	62
Optimization of MALDI matrix additives	64
Tandem MS characterization of β -glucan	64
Microcrystalline Cellulose (MCC)	66
MALDI-MS of MCC	67
Tandem MS of MCC	69
Xylan	71
MS of Birch xylan	71
Tandem MS of Birch xylan	72
Lignin.....	73
MALDI-MS of lignin	73
MALDI-MS analysis of lignin in untreated and holocellulose <i>Populus</i> tissue	75
Summary	75
β -glucan and MCC	76
Hemicellulose	77
Lignin.....	77
3 DIRECT MATRIX-ASSISTED LASER DESORPTION/IONIZATION MASS SPECTROMETRIC IMAGING OF CELLULOSE AND HEMICELLULOSE IN <i>POPULUS</i> TISSUE.....	98
Introduction	98
Experimental.....	100
Instrumentation and Data Analysis.....	100
MALDI Matrix.....	100
Wood Samples	100
MALDI Matrix Coating	102
Results and Discussion.....	102
Pine Wood Samples	102
Tandem MS of Young <i>Populus</i> Stem Tissue.....	103

	MS and Tandem MS Imaging of Young <i>Populus</i> Stem Tissue.....	104
	Conclusions	108
4	IMAGING OF <i>POPULUS</i> TISSUE BY FLUORESCENCE MICROSCOPY	117
	Overview.....	117
	Microscopy	117
	Fluorescence Microscopy.....	118
	Experimental.....	119
	TBO Stain.....	119
	Fluorescence Stains.....	119
	Sample Preparation and Instrumentation	120
	Results and Discussion.....	121
	TBO Stain.....	121
	CW Fluorescence Microscopy.....	121
	Acridine Orange Fluorescence Microscopy	124
	Conclusions	127
5	HIGH SPATIAL RESOLUTION IMAGING OF <i>POPULUS</i> TISSUE USING TOF-SIMS	137
	Overview.....	137
	ToF-SIMS Microscope Imaging.....	137
	Ionization.....	138
	Mass Analysis and Detection	139
	Experimental.....	140
	Instrumentation.....	140
	Sample Preparation.....	140
	Imaging Experiments.....	141
	Results and Discussion.....	142
	Standards	142
	<i>Populus</i> Tissue.....	143
	Positive ion mode.....	144
	Comparison of ToF-SIMS with MALDI-LIT-MS	148
	Negative Ion Mode.....	149
	Conclusions	150
6	MULTIVARIATE ANALYSIS OF MALDI-MS AND TOF-SIMS IMAGING DATA ...	162
	Overview.....	162
	Principle Component Analysis.....	163
	PCA of Lignocellulosic Material Standards	166
	Software	166
	Data Preprocessing.....	166
	PCA Results	168
	PCA and Hierarchical Cluster Analysis of ToF-SIMS Imaging Data	170
	Hierarchical Clustering	171

Software and Data Preprocessing.....	172
Imaging PCA Results	172
Conclusions	174
7 SUMMARY AND FUTURE DIRECTIONS	188
APPENDIX	
A DIFFICULTIES OF MALDI TIME-OF-FLIGHT ION MOBILITY SPECTROMETRY OF PLANT-RELATED STANDARDS AND <i>POPULUS</i> TISSUE.....	193
Overview.....	193
Experimental.....	193
Standard Analysis	193
Instrumentation and Traveling Wave Ion Mobility Parameters	193
Results and Discussion.....	194
LIST OF REFERENCES	202
BIOGRAPHICAL SKETCH.....	211

LIST OF TABLES

<u>Table</u>		<u>page</u>
1-1	Figures of merit for common mass analyzers	54
2-1	List of hypothesized cellulose ion m/z values to monitor in wood tissue.....	97

LIST OF FIGURES

<u>Figure</u>	<u>page</u>
1-1 Schematic of biomass conversion into ethanol.....	49
1-2 Cartoon illustration of cellulose and starch.....	50
1-3 Cartoon illustration of plant cell and zoomed-in portion of cell wall cross section.....	51
1-4 Domon and Costello nomenclature of polysaccharide fragmentation.....	52
1-5 Cartoon schematic of the MALDI process.....	53
1-6 Schematic of linear ion trap adapted from Schwartz et al.....	55
1-7 Mathieu stability diagram of the LIT adapted from Douglas et al.....	56
1-8 Workflow for MS imaging experiment.....	57
2-1 Cartoon representation of cellulose microfibril.....	79
2-2 MALDI-MS spectra of β -glucan standard using Different matrices.....	80
2-3 MS Spectra of β -glucan standard using DHB MALDI matrix with different salt additives.....	81
2-4 MS ² Spectrum of [Glc ₄ +Na] ⁺	82
2-5 MS ² spectra of different cationized β -glucan ions.....	83
2-6 Optical images of MALDI sample spots.....	84
2-7 Comparison of MCC MS by varying DHB concentrations.....	85
2-8 Plot of MALDI matrix and cellulose ion intensity versus laser energy.....	86
2-9 MS spectrum of MCC using optimized experimental parameters.....	87
2-10 MS ² spectrum of m/z 1157.....	88
2-11 MS ² -MS ⁴ analysis of MCC.....	89
2-12 Common hemicellulose structures.....	90
2-13 MS spectra of Birch Xylan extract.....	91
2-14 MS ² analyses of xylans.....	92

2-15	Common building blocks of lignin.	93
2-16	MALDI and LDI MS analysis of Spruce lignin extract.	94
2-17	MS ² analysis of <i>m/z</i> 181.	95
2-18	Optical and MALDI tandem MS image of untreated and holocellulose <i>Populus</i> tissue.	96
3-1	Optical image and average MS from Pine wood sample.	110
3-2	Comparison of spectra from different regions of tissue.	111
3-3	MS ² of <i>m/z</i> 1319→...from wood tissue	112
3-4	MS ² of <i>m/z</i> 1079...from wood tissue	113
3-5	Optical and MS images of cellulose ion in <i>Populus</i> stem..	114
3-6	Optical and MS images of hemicellulose ion in <i>Populus</i> stem.....	115
3-7	Optical and MS images of lignin ion in <i>Populus</i> stem.....	116
4-1	Jablonski Diagram representing energy level transitions involved in fluorescence emission.	129
4-2	Schematic of general fluorescence experimente.....	130
4-3	Schematic of fluorescence microscopy.	131
4-4	Chemical structures of fluorescence stains used.....	132
4-5	TBO Stained <i>Populus</i> stem.	133
4-6	CW stained and tandem MS images.	134
4-7	AO stained <i>Populus</i> stem.	135
4-8	Comparison of AO, CW stain and MS image of same <i>Populus</i> wood stem.....	136
5-1	Schematic of Physical Electronics TRIFT II ToF-SIMS instrument.....	152
5-2	Cartoon illustration representing secondary ionization.	153
5-3	Comparison of ToF-SIMS imaging modes.....	154
5-4	ToF-SIMS spectrum of Birch Xylan Extract coated with 2 nm gold.....	155
5-5	ToF-SIMS spectra from different regions of wood tissue.....	156

5-6	Optical, fluorescence and positive ion ToF-SIMS images of phloem and xylem of <i>Populus</i> wood stem. Images show localization of different ions in different regions of wood tissue.	157
5-7	Optical, fluorescence and positive ion ToF-SIMS images of pith and xylem of <i>Populus</i> wood stem.	158
5-8	Comparison of different imaging techniques.	159
5-9	Optical, fluorescence and negative ion ToF-SIMS images of phloem and xylem of <i>Populus</i> wood stem.	160
5-10	Optical, fluorescence and negative ion ToF-SIMS images of pith and xylem of <i>Populus</i> wood stem.	161
6-1	Graphical representation of PCA analysis.	176
6-2	Ideal PCA plot of three pure standards.	177
6-3	Data matrix set-up for PCA analysis.	178
6-4	PCA Scores plot of MCC, xylan and lignin analysis by MALDI-MS.	179
6-5	PC loadings plot compared with MALDI-MS spectrum of lignin.	180
6-6	PC loadings plot compared with MALDI-MS spectrum of MCC.	181
6-7	PC loadings plot compared with MALDI-MS spectrum of Birch xylan.	182
6-8	Illustration of hierarchical clustering adapted from Deininger et al.	183
6-9	Fluorescence images compared with PCA images generated by plotting the positive and negative loadings of PC1 and PC2 of ToF-SIMS imaging data.	184
6-10	PC2 loading plot and corresponding images.	185
6-11	PCA images of the pith and xylem.	186
6-12	PC1 loading plot and corresponding images.	187
A-1	Comparison of MADLI MS of wood tissue from two different instruments.	199
A-2	Ion mobility plot of LDI analysis of intact wood tissue sections.	200
A-3	Mass spectra from the different regions of the ion mobility plot from Figure A-2	201

Abstract of Dissertation Presented to the Graduate School
of the University of Florida in Partial Fulfillment of the
Requirements for the Degree of Doctor of Philosophy

MALDI TANDEM MASS SPECTROMETRIC TECHNIQUES FOR THE ANALYSIS AND
IMAGING OF LIGNOCELLULOSIC MATERIALS

By

Kyle Ann Lunsford

August 2011

Chair: Richard A. Yost
Major: Chemistry

The conversion of cellulosic material to ethanol begins with a dilute acid pretreatment to remove hemicellulose and alter the lignin distribution. Despite successful conversions, spatial changes of chemical composition throughout pretreatment are not well characterized. Developing nondestructive analytical methods to visualize changes that occur in biomass throughout the pretreatment processes could help increase efficient of biomass conversion into biofuels.

MALDI-mass spectrometric imaging (MS imaging) is a powerful analytical technique that displays a distribution of target molecules in intact tissue. MALDI-TOF (time-of-flight)-MS is commonly used to characterize polysaccharides, but tandem MS capabilities of a TOF are limited. The linear ion trap (LIT) mass analyzer offers tandem MS capabilities, which can provide structural information and monosaccharide composition of polysaccharides.

A MALDI-LIT tandem MS method was developed for to characterize three plant-related standards, microcrystalline cellulose (MCC), Birch xylan and Spruce lignin. The standard analysis determined the ions that are formed from MALDI and provide characteristic fragmentation pathways of these standard compound classes. MALDI-MS

imaging of intact *Populus* tissue sections illustrated a nearly even ion signal across the whole tissue. In contrast, tandem MS imaging was able to differentiate between isobaric ions to provide sensitive and selective than single-stage MS imaging of these compound classes. The tandem MS images showed localization of cellulose in the secondary xylem and phloem fiber cells, which are both known to have thickened secondary cell walls.

High correlation between MALDI tandem MS imaging, fluorescence imaging and ToF-SIMS imaging was observed. In addition, ToF-SIMS imaging provided a high spatial resolution, chemically selective images to characterize the material further. Principal component analysis (PCA) of MALDI-MS analysis of standards and ToF-SIMS imaging determined ions characteristic of lignified and non-lignified tissue.

In conclusion, this dissertation reports a comprehensive analysis of lignocellulosic material (LCM) using three different techniques, MALDI-LIT tandem MS imaging, fluorescence microscopy and ToF-SIMS imaging. Combining the information obtained from these techniques provided a more complete analysis of the tissue sections. Furthermore, the tools for analysis of LCM throughout a pretreatment analysis have been developed.

CHAPTER 1 BACKGROUND

Biofuel Research

Alternative energy research, specifically biofuel research, has gained attention in the recent years due to increasing energy consumption, global climate changes, air pollution and the limited availability of petroleum.¹⁻³ For approximately thirty years, the Department of Energy (DOE) has appointed research funds toward developing renewable, domestically produced energy sources.³ The DOE's Office of Fuels Development has headed the research developing renewable transportation fuels prepared from biomass material, otherwise termed 'biofuels.' Biofuel is loosely defined as 'fuel derived from living organisms containing at least eighty percent renewable materials' and encompasses a wide range of materials—the most common type of biofuel is bioethanol.⁴

Bioethanol

Traditionally, bioethanol is prepared by the fermentation of sugars from renewable sources, e.g., corn kernels and sugar cane; however, there are difficulties to overcome for bioethanol to become a viable alternative energy resource. For example, ethanol produces thirty percent less energy per gallon than gasoline used today, thus requiring larger volumes and larger storage containers for fuel than what is used currently.⁵ Another disadvantage is that the amount of ethanol generated from current corn and sugar sources accounts for merely 10% of the total energy demand in the US. Although farmers could devote more of their crops to bioethanol, this ultimately removes the produce from the food market, causing an increase in food prices.⁶ To overcome these limitations, scientists are developing methods to convert 'plant waste' or biomass (i.e.,

plant materials left over after food processing) into bioethanol. Bioethanol derived from biomass is no different from bioethanol derived from traditional methods. The advantage of 'lignocellulosic ethanol' over traditional bioethanol is that plant material remaining after processing, such as corn stalks, wheat straw, and forest trimmings that is otherwise discarded can now be converted into bioethanol.^{6,7}

Prior to using lignocellulosic materials (LCMs), bioethanol was commonly produced from readily available starch, an α -1,4-linked polymer of glucose, in corn kernels (or sucrose from other crops, such as sugar cane). As Figure 1-1 illustrates, conversion into ethanol starts with an enzymatic digestion of starch into individual glucose molecules. The glucose is then subjected to fermentation by bacteria (e.g., *Escherichia*) or fungi (e.g., *Saccharomyces cerevisiae*), which converts glucose into ethanol and carbon dioxide. Although the lignocellulosic ethanol is fermented by the same process, the structural and chemical properties of the material inherently make the conversion into ethanol more difficult.

Lignocellulosic Ethanol

The difference between corn-based and lignocellulosic ethanol is the composition of the starting material, as well as the polysaccharide that is fermented into ethanol. LCMs are primarily composed of cellulose (40–50% of entire mass), hemicellulose (20–25%), lignin (20–25%), and extractives (5%).⁸ Cellulose is a linear polymer of glucose, linked together by β -glycosidic bonds. Due to the orientation of $-\text{CH}_2\text{OH}$ group of the glucose monomer, strong hydrogen bonding occurs between the linear strands of cellulose, forming a secondary structure, i.e., 'microfibrils' (Figure 1-2). The interactions between each strand of cellulose forms a strong, microcrystalline structure, which increases resistance to enzymatic digestions.⁹

Hemicellulose is an amorphous, heterogeneous polysaccharide that can vary between species of woods. The most common hemicelluloses are a linear, homogenous polysaccharide backbone (e.g., xylan) containing short sugar or acetate branches.⁹ Sugars from both 6-carbon (cellulose) and 5-carbon (hemicellulose) sugars can be fermented into fuels;¹⁰ however, the focus of this study is the conversion of cellulose into biofuel. Lastly, lignin is a complex three-dimensional polymer of lignols, and is not used for biofuel production. Lignin is referred to as the 'glue' that holds the tree together, and makes cellulose inaccessible for enzymatic digestion.⁹

As mentioned previously, the method for producing corn-based ethanol makes use of the easily accessible starch from corn kernels. Lignocellulosic ethanol uses cellulose, a structural isomer of starch, to convert into ethanol. Although starch and cellulose only differ in the linkage between glucose monomers, β -linkages allows for higher-order interactions (specifically, hydrogen bonding) between each cellulose strand—this generates microcrystalline microfibrils (Figure 1-2) that do not occur in α -linked glucose.⁹

In addition to the different linkages, the organization of the cellulose within biomass material increases the difficulty of conversion into fuels. The current model for biomass organization is illustrated Figure 1-3. Briefly, hemicellulose coats the cellulose microfibrils, and lignin 'surrounds and strengthens cellulose-hemicellulose framework'—lignin is often referred to as 'glue' that holds cellulose and hemicellulose together.⁹ In order to disrupt the interactions between lignin, hemicellulose and cellulose, a pretreatment step prior to enzymatic digestions is necessary for the conversion of cellulose into ethanol.¹¹ Although the current pretreatment processes work,

lignocellulosic ethanol remains a research focus in order to improve the understanding and efficiency of pretreatments, helping to decrease the cost and make lignocellulosic ethanol a viable fuel source.

Lignocellulosic Pretreatment

The pretreatment process is designed to ‘unwrap’ the lignin and hemicellulose coating from cellulose, leaving behind greater surface area for enzymatic digestion of cellulose to occur. The first step in pretreatment is size reduction, which breaks down the biomass into pieces that are compatible with the pretreatment step—this often is performed by a chipping or grinding process. After size reduction, numerous pretreatment steps have been proposed and explored, including steam explosion (autohydrolysis),¹² ammonia fiber explosion (AFEX),¹³ acid hydrolysis,¹⁴ organosolv pretreatment¹⁵ and biological pretreatment.²

The most common pretreatment method of LCMs is steam explosion.¹⁶ Pieces of LCM (e.g., wood chips) are exposed to high-pressure (~0.69–4.83 MPa), saturated steam (~160–260°C) for seconds to several minutes, followed by exposure to atmospheric pressure. The pressure differential causes an ‘explosive decompression’ transforming the lignin and degrading the hemicellulose, which leaves the cellulose accessible for enzymatic digestion (i.e., enzymatic hydrolysis).⁹ Studies have shown that steam explosion pretreated wood chips were 90% enzymatically hydrolyzed, compared to untreated wood chips that were only 15% enzymatically hydrolyzed.¹⁷ Another common pretreatment method is acid hydrolysis, in which the LCM is treated with dilute acids (e.g., sulfuric or hydrochloric) at high temperatures. Dilute acid treatments are effective; however, they introduce additional costs for chemicals and neutralization, as well as processing difficulties due to the corrosive nature of acids.¹⁴

Although these pretreatment methods have been successful, all the processes still require size reduction prior to pretreatment. Size reduction is limiting due to the high energy (and cost) needed for chipping or grinding, especially for woody material. Developing processes that make use of larger starting material could help to improve the overall cost and efficiency of producing lignocellulosic ethanol. In addition, spatial changes in the chemical compositions between untreated and pretreated wood chips are not well characterized.¹⁸ Monitoring these spatial changes in chemical composition could provide valuable information to help improve the efficiency and reduce the cost LCM conversion into biofuel.

Analytical Approaches for LCM Analysis

In efforts to monitor the chemical changes throughout a pretreatment process, a variety of analytical approaches have been explored,¹⁹ optical and fluorescence microscopy,²⁰ magnetic resonance imaging (MRI),²¹ micro-X-ray computed tomography (μ -X-Ray CT),²² and confocal Raman imaging.^{23,24} Optical and fluorescence microscopy have been used to generate high spatial resolution images that visualize polysaccharides within plant cell walls.²⁵ MRI is used to determine the moisture (i.e., water) content within plant or wood tissues.²¹ In addition, μ -X-Ray CT provides high-resolution images that provide insight into the density of the biomass material.²² Confocal Raman microscopy has been used to generate high-resolution images of lignocellulosic tissue, based on scattering light that is characteristic of functional groups on the carbohydrates.^{23,24} Although these analytical techniques offer high spatial resolution images, the chemical specificity is often limited. A technique that offers structural analysis with increased molecular selectivity and sensitivity over existing

techniques is mass spectrometry (MS)²⁶—applying MS to biomass analysis is the focus of this dissertation.

Mass Spectrometry of Polysaccharides

MS is a common analytical technique used to determine the presence of a compound in a sample and can be used for quantitative measurements. In MS, the analyte is transferred into the gas phase, ionized and introduced into the mass spectrometer for mass analysis and detection. Mass analysis measurements are based on the mass-to-charge ratios (m/z) of the ions generated; thus, if the charge of the ion is known, the mass of the analyte can be determined; furthermore, tandem MS can be implemented to elucidate ion structure. The major advantages that mass spectrometry offers over other analytical techniques is the chemical selectivity, the wide variety of analytes that can be analyzed, and the ability to perform two or more stages of MS for structural analysis.²⁷ MS encompasses a wide variety of techniques characterized by the type of ionization source and/or the mass analyzer used, which will be discussed in detail in this chapter.

Early MS of Polysaccharides

MS of polysaccharides has been performed for several decades, with application papers dating back to the 1970s.²⁸ Early polysaccharide MS experiments were complex, as they involved hydrolysis to break polysaccharides down into smaller oligosaccharides, derivatizations (such as methylation, acetylation, trimethylsilylation) and separations, (such as gas chromatography, GC), prior to MS analyses.^{26,28,29} The need for hydrolysis and separations limited MS of polysaccharides to di-, tri-, and tetrasaccharides. In addition, polysaccharide analyses were time-consuming, in that hydrolysis and derivatizations were performed over several days.²⁹

Although GC/MS is still used for polysaccharide analyses, the need for hydrolysis limits the application to extracts or isolated compounds from tissues (i.e., not whole tissue sections). MS of polysaccharides without prior hydrolysis started after the introduction of fast atom bombardment (FAB) ionization in 1981.^{28,30} FAB was developed to overcome the limitation that required samples to be introduced into the gas phase prior to ionization. Briefly, analytes are mixed with a matrix, and the matrix is bombarded with Ar atoms or ions at 2–8 keV to generate analyte ions.³¹ FAB became the ionization source of choice for oligosaccharide analyses, as it was able to ionize these compounds without hydrolysis or derivatization, as well as generate $[M+H]^+$ ions in positive ion mode and $[M-H]^-$ ions in negative ion mode.^{30,32}

In 1984, electrospray ionization (ESI) was introduced as a soft ionization technique (i.e., limited in-source fragmentation) to transfer large, solution-phase molecules into intact, gas-phase ions,³³ and ESI quickly became an ionization source used for MS analysis of polysaccharides.³² ESI generates ions by passing a solution through a needle under a high electric field, resulting in an aerosol of charged droplets. These droplets undergo evaporation and columbic fission until the charge resides on the dissolved analyte.^{32,33} Despite the widespread application, native polysaccharides are not ionized easily using ESI, due to the lack of an acidic or basic functional group, so native polysaccharides must be derivatized by methylation or acetylation, prior to ESI-MS analysis. ESI also requires analytes to be in solution, which is often difficult for polysaccharides, specifically plant-related materials, such as celluloses and hemicelluloses. In order to perform ESI on the insoluble materials, derivatization is necessary.³²

The above ionization sources are adequate for polysaccharide analyses, but ESI and FAB are not amendable for MS imaging applications. The ionization sources that are most commonly used for MS imaging and will be presented in this dissertation are matrix-assisted laser desorption/ionization (MALDI) and secondary ion mass spectrometry (SIMS) and will be discussed in the MS imaging section of Chapter 1.

MALDI-MS offers several advantages over FAB-MS and ESI-MS for the analysis of polysaccharides: no sample derivatization is needed (i.e., the polysaccharide is analyzed in its native form), MALDI-MS does not require the analyte to be in solution prior to ionization, and MALDI is a soft ionization source, so less in-source fragmentation and higher molecular weight ions (thus more intact ions) are observed compared to FAB-MS. In addition, MALDI offers increased ionization efficiency of carbohydrates over FAB, which increases the sensitivity of the analysis by approximately 10–100 times.³⁴ Furthermore, MALDI typically generates singly-charged ions, as opposed to multiply charged ions that are formed in ESI, which helps reduce the complexity of the mass spectrum.

Tandem MS of Polysaccharides

Tandem MS is a technique in which mass-selected ions are introduced into second (or n) stages of mass analysis. Following isolation of the ion, dissociation is induced using a dissociation techniques include electron-transfer dissociation (ETD), electron-capture dissociation (ECD), infrared multiple-photon dissociation (IRMPD), and collision-induced dissociation (CID),³⁵ the most commonly used dissociation techniques for polysaccharides.²⁷

For CID, ions of interest (precursor ions) undergo energetic collisions with a neutral background gas, dissociating the precursor ions into product ions, which are

then mass analyzed. The product ions observed in the tandem mass spectrum help to identify the precursor ion structure, making tandem MS an indispensable tool for peptide polysaccharide (most commonly N-linked glycans) structural analysis.²⁶ Early tandem MS experiments focused on glycoconjugate structural analysis, which presents a more complex analysis than peptides due to a high order of branching. Fragmentation of highly branched glycoconjugates generate more complex product-ion spectra were more complex than peptide product-ion spectra.

The groundwork for tandem MS analysis of polysaccharides was performed using CID following FAB ionization, despite FAB's high in-source fragmentation and low ionization efficiencies.³² These experiments determined that low-energy CID of polysaccharides favorably broke glycosidic bonds over cross-ring cleavages. In the late 1980s, a polysaccharide CID fragmentation nomenclature was introduced by Domon and Costello³⁶ and is still used today (Figure 1-4). Furthermore, tandem MS studies has revealed polysaccharide structural information, such as stereochemistry of individual sugar residues,³⁷ linkage positions,³⁸ as well as branching structures.^{26,36}

The introduction of softer ionization sources, e.g., MALDI and ESI, has made tandem MS necessary for most polysaccharide analyses since in-source fragmentation is reduced. Polysaccharides are typically composed of similar sugar monomers, so numerous structural isomers possible for each nominal m/z . Tandem MS can determine basic polysaccharide structure (e.g., linear or branched) and can potentially distinguish the linkages between each sugar. Laine et al. demonstrated that isomeric polysaccharides composed of the same monosaccharides but branched differently are easily distinguished using tandem MS.³⁸ Furthermore, it has been determined that

different ions, e.g., $[M+H]^+$ versus $[M+Na]^+$, fragment differently during low-energy CID, which could help to increase structural information about a polysaccharide.³⁴

Instrumentation

Matrix-Assisted Laser Desorption/Ionization

MALDI was introduced in the late 1980s and enabled the ionization of analytes (up to ~100,000 Da) in their native form, without the need for separations or derivatizations.^{39,40} Some of the first reports of MALDI included the analysis of a phytochemical tetrasaccharide, stachyose, showing the viability of MALDI for the analysis of native polysaccharides.⁴¹ Since the late 1980s MALDI of carbohydrates has become the method of choice for the analyses of branched glycans, as well as linear polysaccharides.³⁴

Ionization mechanism

The ionization mechanism of MALDI is illustrated in Figure 1-5. MALDI generates ions by the interaction between a pulsed laser, a MALDI matrix and the analyte. The MALDI matrix solution is applied atop the analyte and allowed to co-crystallize—the laser is then fired at the MALDI matrix/analyte sample. The MALDI matrix, typically an organic acid, is chosen based on the absorptivity at the wavelength of light emitted by the laser.³⁹ The MALDI matrix absorbs energy from the laser, which causes a rapid heating that desorbs both MALDI matrix and analyte into the gas-phase, i.e., the ‘MALDI plume.’ A mixture of analyte and MALDI matrix molecules, excited molecules and positive/negative ions exist simultaneously within the MALDI plume and ionization is believed to occur through gas-phase reactions between excited molecules and ions; however, the exact mechanism is still up for debate. Different MALDI ionization theories are discussed in detail in several review papers.⁴²⁻⁴⁸

MALDI matrix considerations

Prior to any MALDI analysis, a MALDI matrix must be chosen. As mentioned previously, the MALDI matrix absorbs the laser energy for desorption and subsequent ionization; thus, the MALDI matrix must have a strong absorptivity at the wavelength of the MALDI laser. Commonly, pulsed UV lasers, such as N₂ (337 nm) or frequency-tripled Nd:YAG (355 nm), are used, but IR MALDI has also been reported.⁴⁹ Theoretically, any compound that absorbs at the laser wavelength could serve as a MALDI matrix, so exploring all the options would be nearly impossible.

MALDI matrices are typically chosen based on the characteristics of the analyte compounds.⁴⁴ For example, a MALDI matrix that works well for polysaccharides might not work well for protein analysis. Several MALDI matrices have been reported for the analysis of polysaccharides, but 2,5-dihydroxybenzoic acid, α -cyannohydroxycinnamic acid and sinnipinic acid are among the most commonly used and reported.³⁴ After the MALDI matrix is chosen, other parameters to consider include solvent system, matrix additives and MALDI matrix-to-analyte ratio.

The solvent system of the MALDI matrix and the analyte plays an important role in MALDI. The MALDI matrix and analyte are hypothesized to co-crystallize, thus it is important to use a solvent that allows for a saturated MALDI matrix solution, and is capable of dissolving the analyte.⁴³ In addition, the solvent should have high vapor pressure to rapidly evaporate and produce small crystals, as this results in a more uniform coating of matrix. Typical solvents for MALDI include methanol, ethanol, water, acetonitrile and mixtures of these.

MALDI typically produces [M+H]⁺ ions, which may not be the most desirable for analysis (e.g., [M+H]⁺ ions could provide uninformative fragmentation during tandem MS

experiments). Salts or other compounds can be added to the MALDI matrix solution to promote cationization that would otherwise not be observed. Since sodiated species can fragment differently than protonated ions, a sodium salt (e.g., sodium acetate) could be added to the MALDI matrix solution to generate more $[M+Na]^+$ ions than $[M+H]^+$ ions. Another important parameter for MALDI analysis is the matrix-to-analyte molar ratio. Early experiments showed that there must be a large excess of MALDI matrix molecule present for the best ionization to occur.⁴⁴ Common matrix-to-analyte ratios are 500:1–10,000:1.^{27,43}

Secondary Ion Mass Spectrometry

SIMS is a surface analysis technique similar to FAB that has been adapted for biological analyses.^{50,51} For SIMS, a primary ion beam is focused onto a surface sample, and the kinetic energy of the primary ions is transferred to the surface atoms and molecules through a 'collision cascade.'⁵² The energy of surface atoms and molecules exceeds the surface binding energy and are desorbed into the gas phase. Most of atoms/molecules desorbed into the gas phase are neutral; however, some ions (secondary ions) are generated and analyzed using MS.⁵³ Typical primary ion beams include Ga^+ , In^+ , Au^+ , Ar^+ , Xe^+ and Cs^+ .⁵⁴

Two types of SIMS can be performed based on the primary ion doses. Static SIMS is a less invasive technique that only penetrates ~0.1% of the surface monolayer—static SIMS sources have low primary ion doses ($< 10^{13}$ ions per cm^2) and low flux (10 pA – 5 nA).⁵³ Dynamic SIMS is more invasive and penetrates ~ 40 nm into the sample surface—dynamic SIMS sources have high primary ion doses ($> 10^{13}$ ions per cm^2) with high fluxes (μA).⁵⁵ Most SIMS experiments are performed under the static SIMS limits.

A difficulty of SIMS is the rapid, non-linear decrease of secondary-ion yield with increasing m/z value, which limits SIMS experiments to small molecule or fragment analyses.⁵⁴ Recently, polyatomic primary ion sources (as opposed to atomic ion sources) have been shown to improve the secondary ion emission (SIE) yield, increasing the sensitivity of SIMS experiments and decreasing the sample damage. Some of the polyatomic primary ion sources that have been reported include SF_5^+ , SF_6^- , glycerol, Au_3^+ , Au_4^+ and C_{60}^+ .^{52,55}

Mass Analyzers

Once ions are formed, the ions are guided toward a mass analyzer. Many different mass analyzers are available on commercial or homebuilt instruments and each mass analyzer offers advantages and disadvantages over the other. The most common mass analyzers include magnetic and electric sectors, Fourier transform ion cyclotron resonance (FT-ICR), quadrupoles, triple quadrupoles, three-dimensional quadrupole ion trap, time-of-flight (ToF), linear ion trap (LIT) and orbitraps. Magnetic and electric sectors have become less popular due to the high cost and limited tandem MS abilities. FT-ICRs, ToFs, and orbitraps offer high mass resolution, but FT-ICR requires high vacuum and a cryogenic magnetic that is costly to purchase and maintain. Orbitraps are a new technology, resulting in similar resolving power and sensitivity to FT-ICR; however, initial costs are high. ToF are a cheaper alternative for high resolving power, but the tandem MS capabilities are limited. Ion traps, three-dimensional and linear, offer the best tandem MS capabilities, but are limited in mass range and mass resolution.^{27,28,35}

Figures of merit

In order to compare different mass analyzers, there are figures of merit that are considered, including mass accuracy, resolving power, m/z range, scan speeds, tandem MS capabilities and cost. Table 1-1 compares important figures of merit between typical mass analyzers.^{54,56,57}

Mass accuracy is describe as the 'error' in the m/z measurement, typically express in parts per million (ppm). The mass accuracy is determined by Equation 1-1, and measurements made within that 'error' are considered accurately known. High mass accuracy mass analyzers are necessary to determine exact elemental composition and such information is especially useful for database searches. The greater the mass accuracy, the fewer possible compounds allowing for more reliable ion identification. Compared with the other mass analyzers, FT-ICR mass spectrometers and orbitraps provide best mass accuracy.

$$\text{Mass Accuracy} = \left[\frac{\text{Measured } m/z - \text{Theoretical } m/z}{\text{Theoretical } m/z} \right] \times 10^6 \quad (1-1)$$

Resolving power is a property of the mass analyzer and is determined by dividing the m/z value of an ion (M) by the m/z values of ions that can be separated (Δm), shown Equation 1-2. A higher resolving power results in greater the separation between two ions at a certain m/z value,²⁷ which can distinguish between two ions with the same nominal m/z , without the need for tandem MS.³⁵

$$\text{Resolving Power} = \frac{M}{\Delta m} \quad (1-2)$$

Linear ion traps

LITs became widely used in the early 2000s for their tandem MS capabilities. LITs are composed of four hyperbolic, parallel rods divided into three sections, creating a

quadrupolar electric field, as illustrated in Figure 1-6.⁵⁸ The ions are trapped in two dimensions in the center section of the LIT, using radial RF voltages on the parallel rods and DC biased plates.⁵⁸⁻⁶⁰ Stability within the LIT is based on the ion's radial motion governed by the solution to the reduced Mathieu Equations (Equations 1-3 and 1-4),^{58,60,61}

$$a_x = a_y = \frac{-8eU}{mr_o^2\Omega_o^2} \quad (1-3)$$

$$q_x = -2q_y = \frac{-4eV}{mr_o^2\Omega_o^2} \quad (1-4)$$

where e is the charge of the ion, U is the DC potential on the rods, m is the mass of the ion, r_o^2 is the radius of the ion trap and Ω_o is the angular frequency of the RF voltage.

Mass analysis in a LIT can be performed several ways; a common method is mass-selective instability scanning with resonance ejection with a q -value set to $q_x = 0.88$.^{59,62} Mass-selective instability operates in 'RF-only mode', which is achieved by setting the DC component, U , to 0V and $a_x = 0$. This allows an ion's stability within the trap can be described only in terms of the Mathieu parameter, q_x , shown in the Mathieu Stability diagram (Figure 1-7).⁵⁹ Once ions are inside the trap, an RF excitation voltage applied across an opposite pair of rods is increased. When the RF frequency is equal to the secular frequency of an ion at particular m/z , the ion is excited and axially ejected through slits in these rods. A mass spectrum is recorded by scanning through the oscillation frequencies to eject and detect ions step-wise from the trap.^{59,62}

The LITs advantage over other MS imaging mass analyzers is the tandem MS capabilities. Tandem MS experiments in a LIT are performed tandem in time,⁶³ so there

is no limitation on the stages of MS that can be performed (other than the number of ions within the trap). Disadvantages of the LIT compare to other MS imaging mass analyzers include limited mass range (vs. ToF) and limited mass spectral resolution (vs. FT-ICR and orbitrap). Commercial LIT instruments typically have an upper mass range of m/z 4000, but studies have shown that this can be extended.⁶⁴ Under standard parameters, the LIT offers unit resolution. Slower scan speeds can be used to obtain higher mass resolution (e.g., zoom scan and ultra zoom scan); however, this is not practical for an entire imaging experiment. The LIT has been interfaced with the high-resolution orbitrap, and its use for imaging has been discussed.⁶⁵

Tandem MS with LIT

LITs perform tandem-in-time MS experiments, which is advantages since they can perform MS^n stages of mass spectrometry.⁶³ Tandem-in-time denotes that the processes involved in tandem MS (ion accumulation, ion selection, dissociation and mass analyses) occur in the same volume, sequentially in time. This process can theoretically be repeated n times, but is often limited by ion abundance and dissociation efficiency.³⁵

Tandem MS in a LIT ion trap involves a user-set m/z isolation window, where only ions within the m/z window are stable inside the LIT. Typically, an isolation width of 1.2–1.5 amu is used to trap the precursor ion efficiently, without the presence of unwanted ions. After trapping, the ions are excited using an excitation, or ‘tickle,’ voltage—this increases the kinetic energy of ions and induces collisions with the neutral background gas, typically He. The collisions cause dissociation, typically along the lowest energy pathway, and is termed low-energy CID. Low-energy CID is one of the most commonly used dissociation technique, specifically in LITs.²⁷

MS/MS or MS² spectra are recorded by scanning product ion out of the trap following dissociation of the precursor ion—this step can be performed multiple times within the LIT. For example, after the first precursor ion is fragmented, one of the product ions can be mass-selected and CID is performed again. The product ions are then scanned out for a MS³ spectrum. The number of stages is typically limited by the number of ions capable of being stored initially within the trap, as well as the dissociation efficiency.

A disadvantage of tandem-in-time MS is the observed ‘low-mass cutoff’. As shown in Figure 1-7, if precursor ions are stored at $q_x = 0.3$ for CID, product ions that fall at a q_x value greater than the low-mass cutoff ($q_x = 0.9$) will not be stored.⁶⁶

Time-of-flight

ToF mass analyzers were introduced in 1946 and first commercialized in 1955 for gas chromatography/MS (GC/MS) analyses.²⁷ The advantage of ToF over other mass analyzers during that time was the spectral acquisition rate. ToF mass analyzers are relatively simple, as they are composed of a field-free region, also called a drift tube, and a detector. The mass analyzer works based on the principle that ions introduced into the field-free region at the same time and with the same kinetic energy will be separated based on their m/z values (i.e., lighter ions will travel more rapidly and heavier ions will travel more slowly).⁶⁷

After ionization, ions are accelerated toward the field free region. The energy (E_{el}) imparted upon an ion of mass, m , through a voltage, U , is converted into the kinetic energy (E_{kin}) and expressed as

$$E_{el} = ezU = \frac{1}{2}mv^2 = E_{kin} \quad (1-5)$$

Where z is the number of electron charges, e (assuming zero kinetic energy prior acceleration). Equation 1-5 is rearranged to solve for velocity.

$$v = \sqrt{\frac{2ezU}{m}} \quad (1-6)$$

The velocity is determined by dividing the distance the ion travels, l , by the time it takes the ion to travel that distance, t_{drift} . Through a series of substitution and rearrangements, the ToF equation reduces to

$$t_{drift} = \frac{l}{\sqrt{2eU}} \sqrt{\frac{m}{z}} \quad (1-7)$$

Thus, the ToF of an ion is proportional to the square root of the m/z value. In addition to t_{drift} both acceleration time, t_a , and ionization time, t_0 , must be accounted for the total time-of-flight, t_{total} .

$$t_{total} = t_0 + t_a + t_{drift} \quad (1-8)$$

Early ToF instruments suffered from poor mass resolution because the speed of the detector electronics was not adequate to distinguish small differences in flight times. The electronics were improved in mid-1990s, which allowed for high-resolution ToF mass analysis.⁶⁷ Furthermore, early ToF mass analyzers had a linear geometry, i.e., the ionization source, drift tube and detector were aligned on the same axis. A reflector geometry was later introduced to ToF mass analyzers to improve the mass resolution; ions travel through a reflector until they reach zero kinetic energy, at which time they reverse directions. Ions with higher kinetic energy fly deeper into the reflector section than less energetic ions, so the reflector serves to correct the kinetic energy distribution of the ions—this dramatically increases the resolving power of ToF.²⁷

Since ToF requires all ions to enter the drift tube simultaneously (with the same kinetic energy), a pulsed ionization source is necessary. Although ToF provides high mass resolution, the tandem MS capabilities, which are need for polysaccharide analyses, are limited and described in detail below.

Tandem MS with ToF

In contrast to LITs, tandem MS experiments using a ToF analyzer is performed tandem-in-space. For a tandem-in-space analysis, a precursor ion is mass-selected, moved into a different region of space for dissociation and the product ions are moved to another region of space for analysis. The most common tandem-in-space mass spectrometer is the triple quadrupole, which is composed of a mass analyzer quadrupole (Q_1) a collision cell (q_2) and a product-ion mass analyzer (Q_3).⁶³ Tandem mass spectrometers using a ToF are typically hybrid instruments, meaning two different mass analyzers are used tandem in space (e.g., quadrupole-ToF, QIT-ToF); in these instruments, the quadrupole and QIT perform MS1 and the ToF performs MS2.

More recently, ToF-ToF instruments have been introduced with the primary application to rapid protein identification for proteomic analyses.³⁵ ToF-ToF instruments are composed of an ion source (most commonly MALDI), directly followed by one ToF, a gated precursor ion selector, a collision cell, a second ToF and a detector. The first ToF is used to separate the packets of ions into approximately 1–3 m/z value groups for passage into the collision cell using a timed gate. These precursor ions are decelerated (to a user-determined value) to reduce the ions' kinetic energy prior to entering the collision cell. The gas within the collision cell acts as the collision gas to induce CID. The energy of the collisions is controlled by electric fields, the mass of the collision gas (the mass of the collision gas alters the energy imparted during collisions) and the

pressure of the collision gas. The pressure of the collision cell is typically $\sim 10^{-4}$ – 10^{-5} Torr, and is typically composed of N₂, He, Ne, Ar, Kr or Xe.³⁵ After exiting the collision cell, the ions are reaccelerated for the second ToF analysis, typically a reflectron ToF.

ToF-ToF analyses offer advantages, such as fast analysis times that allow for high-throughput analyses. Also, ToF-ToF allows for control over the CID energy, and furthermore allows for high-energy CID, which is unavailable for ion trap instruments. Unfortunately, precursor ion resolution is typically poor and the kinetic energy spread of the product ions produced by CID decreases the resolving power of the second ToF. However, the second ToF is still able to provide high mass accuracies (although lower than a single-stage ToF experiment).³⁵ Since, both tandem-in-time and tandem-in-space MS methods offer advantages depending on the analysis, using both methods should provide the most comprehensive analysis of polysaccharides.

Mass Spectrometric Imaging

MS imaging is a powerful analytical technique that combines the chemical selectivity of MS with two-dimensional spatial information of a sample surface.⁵⁴ MS imaging can be performed in two different modes, microscope imaging and microprobe imaging. For microscope MS imaging, the spatial position of ions (relative to each other) generated from a surface is conserved and detected by a position-sensitive detector. The intensity of the ions is then plotted versus the spatial position at which they were detected to generate the MS image. Early microscope MS imaging was performed using an ion-optical collection system coupled to a SIMS ionization source.^{68, 69} For microprobe MS imaging, the sample is mounted on an x-y stage and the sample (or source) is moved to analyze the region of interest. The ion intensities from the mass spectra are recorded at each analytical region and plotted versus the position to generate the MS

image.⁷⁰ Early microprobe imaging experiments were performed using laser microprobe mass analysis (LAMMA), which coupled laser desorption ionization (LDI) to a ToF mass analyzer.^{70, 71}

Microprobe Mass Spectrometric Imaging of Tissue

The field of microprobe MS imaging has rapidly expanded with the introduction of new ionization sources capable of transferring large biomolecules into the gas phase. A general workflow for a MALDI microprobe MS imaging of tissue (Figure 1-8) starts with slicing tissue sections into thin (~10–20 μm thick) sections. The tissue is then mounted onto a microscope slide and coated with MALDI matrix. The slide is introduced into the instrument and the plate is rastered underneath the laser beam at a user-determined raster step size (~50-100 μm). A mass spectrum is recorded at each laser stop, and ion intensities are plotted versus the position to generate an MS image.⁵⁴ The spatial resolution of the MS image is determined by the laser spot size, discussed below, and raster step size.

Tissue Sectioning

The quality of the MS image obtained is highly dependent upon with the quality of the sample preparation.⁷² There are several considerations to address during the tissue sectioning to ensure high quality MS images. For MALDI-MS imaging, it is important that the sample surface is free of contaminants that could ionize easily and compete with analyte ionization, resulting in analyte ion suppression. Tissues prepared for optical and fluorescence microscopy are routinely embedded in an optimal cutting temperature (OCT) compound for rigidity during slicing; however, these embedding media can smear across the sample surface and compromise the chemical images obtained.⁵⁴ Instead, animal tissue is flash-frozen and cryosectioned to obtain thin sections without using

embedding media for MS imaging experiments. In addition to embedding media, common surface contaminants are introduced from oils on the cryotome blade.⁷² It is important to wash the sectioning blade with organic solvent thoroughly prior to sectioning tissues for analysis.

Another common technique used to remove ion interferences is washing.⁷² Washing the tissue helps to remove contamination that can occur during sectioning tissue and excess salts. Animal tissues typically have high concentrations of natural cations, such as sodium and potassium. Excess salts can interfere with adequate MALDI matrix crystallization, thus reducing the ionization efficiency from atop the tissue section.⁷³ High abundance of salts can also compete for charges during the ionization process, thus reducing the ionization efficiency of analyte compounds. For MALDI-MS imaging, methanol and ethanol are typical washing solvents; however, other solvents or detergents can be used based on the analyte.⁵⁴ The limitation of washes is the solubility of the analyte, as it is important that the analyte is not washed away. After the tissue section is mounted onto the glass slide and the appropriate washes are performed, the tissue is coated with MALDI matrix.

MALDI Matrix Application

The MALDI matrix choice, solvent choice and the application method are all important parameters to consider for optimal MS imaging experiments. It is important that the MALDI matrix/analyte co-crystals are smaller than the laser spot size to obtain the best possible spatial resolution.⁵⁴ As discussed previously in this chapter, the MALDI matrix is chosen based on the classification of analytes, but some matrices (α -cyannohydroxycinnamic acid, CHCA), generate smaller crystals than other matrices, (2,4-dihydroxybenzoic acid, DHB). If both matrices result in efficient ionization of the

analyte, it is beneficial to use CHCA over DHB to generate smaller, more-uniform crystals.

Another factor that affects MALDI matrix crystal size is the solvent. The MALDI matrix solvent is determined based on matrix and analyte solubility. Since MALDI involves the co-crystallization of the matrix and analyte, it is important that the solvent used can dissolve the analyte. The rate of evaporation of the solvent is also important for generating uniform MALDI matrix crystals. More rapid evaporation generates smaller, more uniform MALDI matrix crystals that are ideal for MS imaging experiments. The most commonly used solvents include a water methanol mixture (30:70, 50:50, or 70:30) or organic solvent mixed with 0.1% trifluoroacetic acid (TFA) in DI water. Typical organic solvents used are acetonitrile (ACN), methanol, ethanol, acetone and chloroform.⁷²

The MALDI matrix coating method perhaps has the largest effect on the MS image quality,⁷² as it is crucial that the MALDI matrix is applied evenly over the entire tissue section. Some the methods used for coating include electrospray deposition, nebulization, artistic airbrushing and ink-jet printing.⁷⁴ Electrospray deposition generates uniform coating of small crystals; however, electrospray deposition does not work well on insulating sample mounts, such as glass slides. A Meinhard nebulizer can be used to generate small droplets of MALDI matrix to coat the tissue. This technique is discussed in more detail in the experimental sections of Chapter 2. Despite variety of reported techniques for MALDI matrix deposition, it is important to note that MALDI matrix coating is more of an art than a science; determining the exact amount of matrix to apply to could vary from sample to sample. Typically, coating with a nebulizer uses

~8 mL of MALDI matrix solution, but it is possible to need only 6 mL or as much as 12 mL, depending on the sample.

Mass Spectrometric Imaging Ionization Sources

MS imaging experiments are performed using variety of different ionization sources, such as MALDI, SIMS and desorption electrospray ionization (DESI) and each method offers advantages depending on the analyte and sample type.⁵⁴

SIMS

SIMS is most commonly combined with ToF, referred to as ToF-SIMS. More specifically, the ToF-SIMS ion microscope is a unique instrument developed for microscope MS imaging and is discussed in more detail in Chapter 5. An advantage of SIMS ionization source, is that no sample preparation is needed (e.g., no matrix is need) for tissue section analysis, and the primary ion source diameter is small (~ 1 μm), thus, high spatial resolution images are generated.^{75,76}

Previously, liquid metal ion gun (LMIG) Ga^+ or In^+ sources were commonly employed for imaging applications,⁷⁵ but have recently been replaced with polyatomic primary ion sources, e.g., Au_3^+ , Au_4^+ and C_{60}^+ . The polyatomic primary ion sources have shown to improve the poor desorption efficiency of the previous LMIG.⁵⁵ Polyatomic primary ion sources have also increased the applications of ToF-SIMS MS imaging for analysis of large compounds, such as lipids in tissue sections (~ m/z 600–800).⁵⁴

DESI

DESI is an atmospheric pressure soft ionization source developed in 2004.⁷⁷ DESI generates ions by aiming an electrospray toward a sample surface at a particular angle. The charged droplets from the electrospray interact with the sample causing desorption/ionization of the analyte.⁷⁸ Soon after its introduction, DESI was used as an

MS imaging ionization source by mounting the sample on an XYZ stage and moving the sample relative to the stationary DESI probe, generating a 9 x 19-pixel image.⁷⁹ A unique feature of DESI imaging is that the ionization source is continuous (as opposed to pulsed like SIMS and MALDI)—the sample plate is typically rastered at a velocity of 200 μm per second and mass spectra are recorded every 0.67 seconds.⁷⁸

A major advantage of DESI over other ionization techniques (e.g., MALDI and SIMS) for MS imaging is that little to no matrix or sample preparation is required, i.e., after slicing, the tissue can be directly analyzed using DESI-MS. This also helps to eliminate irreproducibility of ion signals introduced by inconsistent (but necessary) sample preparation, especially for MALDI. Another advantage is that the sample is probed at ambient pressure. Disadvantages of DESI include poor spatial resolution and limited analytes. Since DESI uses solution spray of droplets, it is difficult to determine a 'spot-size' analogous to a MALDI laser or a primary ion beam, but it is known that the DESI spray is larger ($\sim 200 \mu\text{m}$) than a MALDI laser ($\sim 75 \mu\text{m}$) or primary ion beam ($< 1 \mu\text{m}$), and as a result, DESI offers lower spatial resolution.⁷⁸ DESI is also limited to lower mass ions, but has recently been effective for lipid imaging.⁸⁰

MALDI

MALDI has perhaps been the most widely used ionization source for MS imaging experiments due to capabilities of ionizing intact biomolecules, including both small molecules (for drug and metabolomics analyses) and large molecules (for protein analysis). The spatial resolution offered by MALDI-MS imaging is still less thanToF-SIMS imaging, but improvements have been made and the spatial resolution of MALDI-MS images has been reported down to 10 μm .⁵⁴

Mass Spectrometric Imaging Mass Analyzers

The majority of MS imaging experiments are performed using a ToF mass analyzer, as they offer higher sensitivity, higher mass resolution and higher repetition rates over quadrupole and ion trap mass analyzers.⁷⁶ In addition, the pulsed nature of MS imaging ionization sources, such as MALDI and SIMS make coupling to ToF mass analyzers easy. However, the disadvantage of ToF analysis are limited tandem MS capabilities, discussed previously; this is perhaps less important for SIMS analyses due to the high degree of in-source fragmentation.^{75,76}

Time-of-flight for imaging

ToF imaging experiments are performed either using linear or orthogonal extraction ToF. Linear extraction experiments accelerate the ions directly into the mass analyzer. For orthogonal acceleration, the ions are accelerated orthogonally to the direction of mass analysis. Linear extraction ToF is more commonly employed for MALDI imaging applications due to the higher sensitivity offered. To obtain the highest mass resolution, reflectron ToFs are often employed.

It has also been shown that including a short time delay after MALDI, prior to ion extraction into the ToF, reduces kinetic energy broadening through collisional cooling. Reducing the kinetic energy distribution ultimately improves the mass resolution and sensitivity of the experiment.⁸¹ Delayed extraction is not necessary for SIMS experiments, as the distribution of kinetic energy of ions generated by SIMS is inherently narrow.⁸²

Another parameter for MALDI-MS imaging experiments to consider is the number of laser shots needed to obtain one mass spectra. For a MALDI-ToF imaging experiment, typically 100–200 laser shots are used at each laser stop on the tissue;

thus, a large number of laser shots is used for one imaging experiment. Consider an MS imaging experiment for a 1 mm x 1 mm square (1000 μm x 1000 μm). Using 100 laser shots per stop and 50- μm raster step size, there are 20 laser stops across the square and 20 laser stops down the square, resulting in 400 laser stops for the experiment. If 100 laser shots and eat laser stop, 40,000 laser shots are used to image the image the 1 mm square. In order to make the experiments feasible, a high repetition laser with a long lifetime, along with high-speed data acquisition is needed. For these reasons, a solid-state laser (Nd:YAG) is often used for MALDI-ToF experiments.

In addition, the sample surface must be considered for ToF experiments. To perform ToF analyses, ions must be generated from the surface with the same kinetic energy (mass resolution is lowered as the kinetic energy distribution is broadened). Thus, samples must be prepared on conductive surfaces such as stainless steel plates or indium tin oxide (ITO) coated glass slides. Conductive surfaces do not limit the analyses, but this could cause complications in sample preparation for samples that do not adhere directly to the conductive surface.

Linear ion traps for MS imaging

Due to the complexity of intact biological tissues, the need for MS imaging coupled with tandem MS has been recognized, and a MALDI source was coupled to a quadrupole ion trap⁸³ and later a linear ion trap⁸⁴ for the analysis of intact tissue sections. Due to the large m/z range offered, proteins were often the compounds of interest for MALDI-ToF-MS imaging analyses. In contrast, the limited mass range of ion traps introduced a new area of imaging small molecules, particularly lipids and small drug molecules and their metabolites, for MALDI ion trap MS imaging.⁸⁴

An advantage LITs offer over ToFs is the capability for tandem MS experiments. Since no separations are performed prior to MS imaging analysis, tandem MS helps to reduce spectral complexity, confirm identity of ions and aid in unknown ion identification by isolating and dissociating analyte ions. Another advantage of the LIT is the small amount of laser shots needed to generate a mass spectrum, compared to ToF mass analyzers. For a LIT MS imaging experiment, typically 1–3 laser shots are required at each laser stop (compared to the 100–200) for ToF experiments. Thus, for the same 1 mm square, using 50 μm raster step-sizes and 3 laser shots per stop, only 1200 laser shots are needed (compared to the 40,000 for ToF). Furthermore, the 1200 laser shots are capable of generating MS, MS² or even MS³ images.

In addition to prolonging the lifetime of the laser, using fewer laser shots allows for repeat experiments of the same tissue section. The high number of laser shots needed for MALDI-ToF typically allows for only one analysis per tissue section. It has been shown that several MALDI-LIT MS imaging experiments (up to 30) can be performed on the same section of tissue. Thus, after collecting MS spectra, subsequent scans can record MS² or MS³ spectra of different analytes for more selective analyses.⁸⁵

It is also important to note the ion source differences between the MALDI-ToF-MS and MALDI-LIT-MS. MALDI-ToF-MS imaging experiments are typically performed at high vacuum ($\sim 10^{-6}$ Torr), which requires samples to be completely dry prior to analysis. Since biological tissues are primarily composed of water, it can take approximately 2 hours to dry a 10 μm thick sample. In addition, MALDI at higher vacuum (lower pressure) often induces in-source fragmentation, particularly with phospholipids.⁸⁴ It has been shown that increasing the pressure of the MALDI source allows for collisional

cooling, which reduces the in-source fragmentation observed.⁸⁶ The MALDI-LIT source is operated at intermediate pressure, typically 10^{-2} to 1 Torr, thus less in-source fragmentation is observed for these experiments.

Another advantage of MADLI-LIT-MS imaging is that a conductive surface is not needed for sample mounting.⁸⁵ Instead, samples can be mounted on common microscope slides used for other techniques, such as histological and fluorescence staining. Furthermore, these common glass microscope slides are less expensive than the conductive ITO coated slides and stainless steel slides. Stainless steel sample plates must be washed and re-used; however, washing the surface might not be adequate to remove all contaminants from the surface, so cross-contamination could be observed for frequently used sample plates. Instead, new glass slides can be used for each sample for an unadulterated sample surface and allowing samples for sample to be archived for future analyses.

Orbitraps for MS imaging

The newest mass analyzer used for MS imaging is the orbitrap, which was introduced in 2000⁸⁷ and coupled to an ESI source in 2003.⁸⁸ The orbitrap was designed as a more practical alternative to FT-ICR, i.e., offer the similar high mass resolution as FT-ICR without the need for a cryogenically-cooled, superconducting electromagnet. Orbitraps use orbital trapping fields to trap the ions. While ions are stored in the trap, they undergo axial oscillation, which are dependent on the m/z of the ion. The axial oscillations are measured using a Fourier transform of the image current detected from the motion of the ions, yielding mass resolving power around 150,000.⁸⁸

The orbitrap has been integrated into a LIT instrument design, for a hybrid linear ion trap/orbitrap mass analysis. The advantage of combining these two mass analyzers

is that the tandem MS capabilities of the linear ion trap can be used prior to high-resolution mass analysis by the orbitrap. The high-resolution of the orbitrap is useful in distinguishing between isobaric ions, such as two different lipids at the same nominal m/z value.⁶⁵ It is evident that the orbitrap offers advantages of both tandem MS and high-resolution imaging; however the technology is still new and the applications are starting to be realized.

MS Image Generation

MS imaging experiments record a mass spectrum and position at each laser stop—this generates large data sets for whole-tissue imaging experiments (the size is affected by the raster step size). Typically, commercial instruments provide imaging software, which plots the ion intensity versus the position to generate an MS image. A smoothing/interpolation technique is typically used to generate MS images, so that the images are not displayed as square ‘pixels.’ Interpolations are commonly performed in any imaging technique—very simply, interpolation uses the ion intensity at the data points to predict the ion intensity between data points, thus smoothing out the square pixels. There are different types of interpolation that can be performed, but triangulation with linear interpolation is commonly used for imaging software.⁸⁹ This technique is a complex mathematical algorithm that generates triangles using three original data points to interpolate the data between the original data points.⁸⁹ The ‘pixel’ size (i.e., resolution) of the MALDI-MS images is controlled by the raster step size.

Normally, the first image generated in MS imaging data processing is the total ion current (TIC) image, showing the TIC at each laser stop. Although this image does not show any specific compound, the TIC image displays where ion signal was observed from the tissue section. To generate compound specific images, the software allows the

user to choose an ion of interest or a range of ions (e.g., m/z 100 \pm 1 amu or m/z 600–800) to plot. The software then plots the intensity of the user-determined range versus the position. The compound-specific image allows for evaluation of the intensity of a certain compound over the sample, but there are considerations for MALDI that could affect the image observed.

Due to the variability of the MALDI-MS ion signal (and perhaps non-uniform sample coating), the variation of ion signal intensity in some regions could arise from the quality of MALDI matrix crystallization. Methods used to correct for the variable MALDI signal include normalizing to the TIC, normalizing to the base peak intensity, or normalizing to a MALDI matrix ion signal. Although these methods are commonly used, it is difficult to determine the best overall method. To obtain more control of image generation, MS imaging data can be exported from the instrument software to produce a spreadsheet with three columns of data, x-position, y-position and ion intensity. From this spreadsheet, the data can be imported into different imaging or graphing software to generate an image map and manipulate the data as needed.

Overview of Dissertation

Improvements in current LCM analysis methods are necessary to improve the efficiency of conversion into biofuels. The purpose of this research was to develop new methods to analyze and image LCMs to provide a more comprehensive understanding of the composition and organization of compounds within LCMs

Prior to imaging intact tissue sections, plant-related standards were first characterized. Chapter 2 reports the development of a MALDI tandem MS method for the analysis of microcrystalline cellulose (MCC), Birch xylan extract and Spruce lignin

extract. Standard characterization identified ions to analyze in wood tissue, and determined neutral losses to monitor for tandem MS experiments of intact wood tissue.

After standard characterization, Chapter 3 reports a MALDI tandem MS imaging method developed for the analysis of intact *Populus* stem cross-sections. The ions identified in Chapter 2 were monitored in tissue, providing MS and MS² ion images of cellulose, hemicellulose and lignin ions identified previously. To further validate the imaging method and obtain higher spatial resolution images, fluorescence microscopy and ToF-SIMS image experiments were performed.

Chapter 4 reports the use of a polychromic dye, calcofluor white and acridine orange as a way to provide more information about cellulose and lignin localization in wood tissue. The fluorescence microscopy images showed high correlation with the MALDI tandem MS images generated. Furthermore, Chapter 5 reports the adaptation of ToF-SIMS methods for the analysis of *Populus* tissue. The high spatial resolution images offered complementary information to fluorescence microscopy and MALDI tandem MS images.

One of the difficulties of ToF-SIMS is that the high in-source fragmentation limits ion identification. In order to help identify ions that were observed in ToF-SIMS experiments, multivariate analyses were performed. Chapter 6 reports PCA and cluster analysis of ToF-SIMS image data sets. Moreover, the multivariate analysis provided a list of ions that could distinguish between lignified and non-lignified tissues. Chapter 7 provides a conclusion and insight into future experiments that could be used to improve the analysis of LCMs.

Appendix A was added to report experiments performed on a MALDI traveling wave ion mobility (TWIM)ToF mass spectrometry at the FOM Institute on Matter and Physics (AMOLF). The MALDI experiments performed on the MALDI-TWIM-ToF mass spectrometer were not comparable to experiments performed on the MALDI-LIT mass spectrometer. However, LDI was performed and Bucky balls were observed from intact wood tissue.

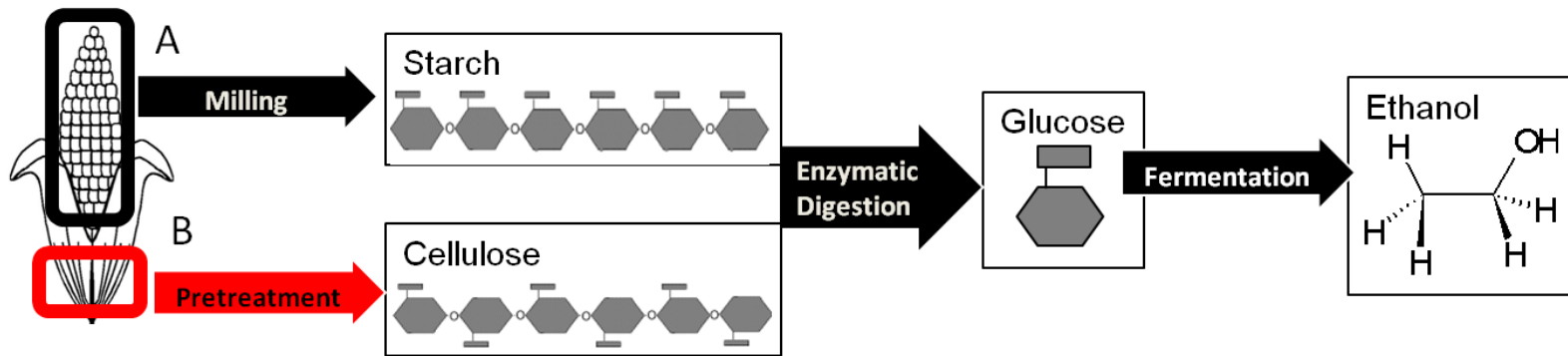


Figure 1-1. Schematic of biomass conversion into ethanol. A) Steps involved converting corn kernels into ethanol B) Steps involved with converted lignocellulosic materials, such as cornhusks, into ethanol.

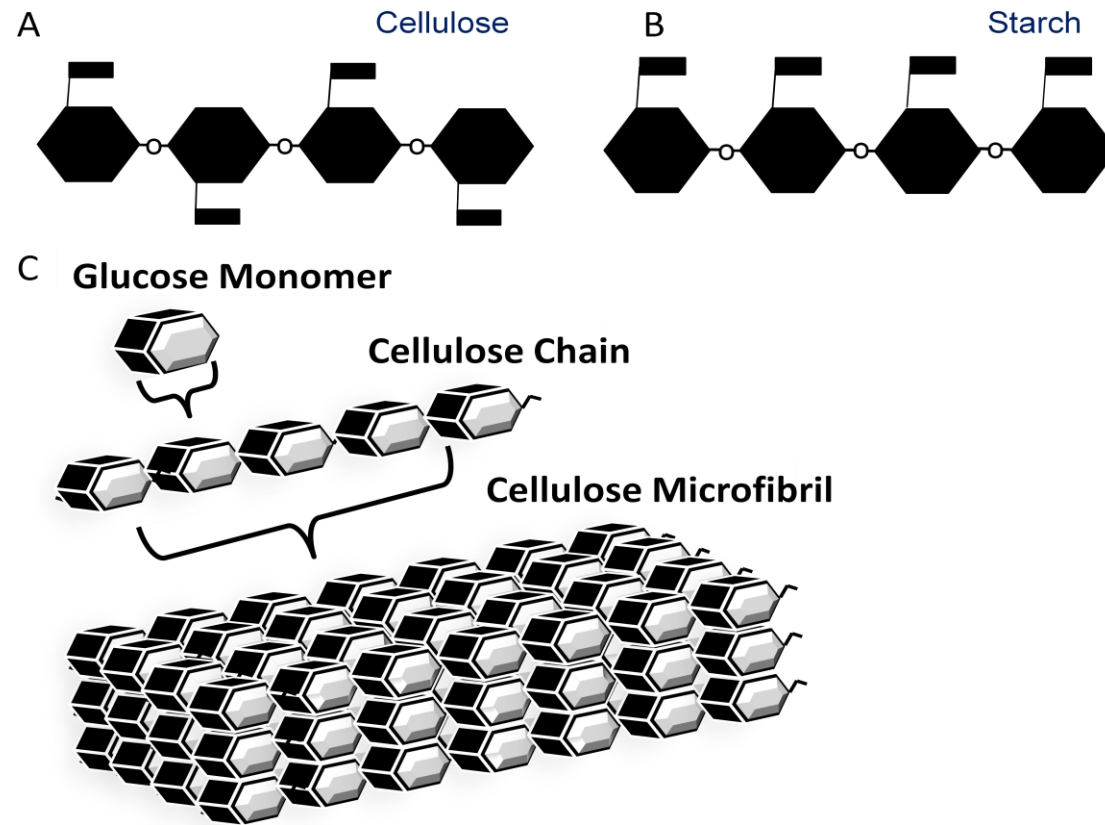


Figure 1-2. Cartoon illustration of cellulose and starch. A) Structure of cellulose showing 1,4- β linkages between glucose monomers. B) Structure of starch, showing 1,4- α linkages between glucose monomers. C) Composition of cellulose microfibrils. β -linkages allow for strong interactions between cellulose strands, creating microcrystalline structures called microfibrils.

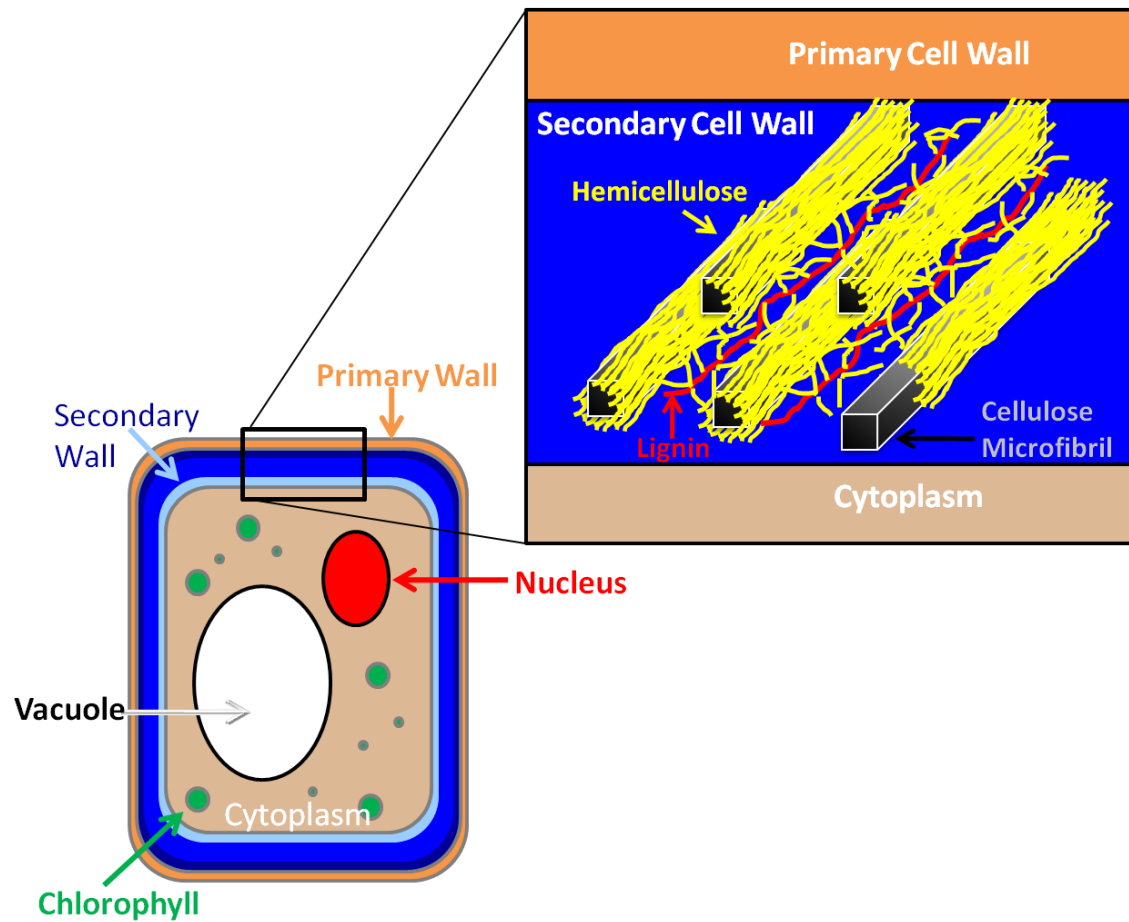


Figure 1-3. Cartoon illustration of plant cell and zoomed-in portion of cell wall cross section. Plant cells have a primary cell wall, in addition to a secondary cell wall that is split into three different regions (depicted by three different shades of colors). The zoomed-in figure shows the hypothesized organization of cellulose microfibrils, hemicellulose and lignin within the secondary cell wall. The hemicellulose coats the cellulose microfibrils, and is linked together with the lignin.

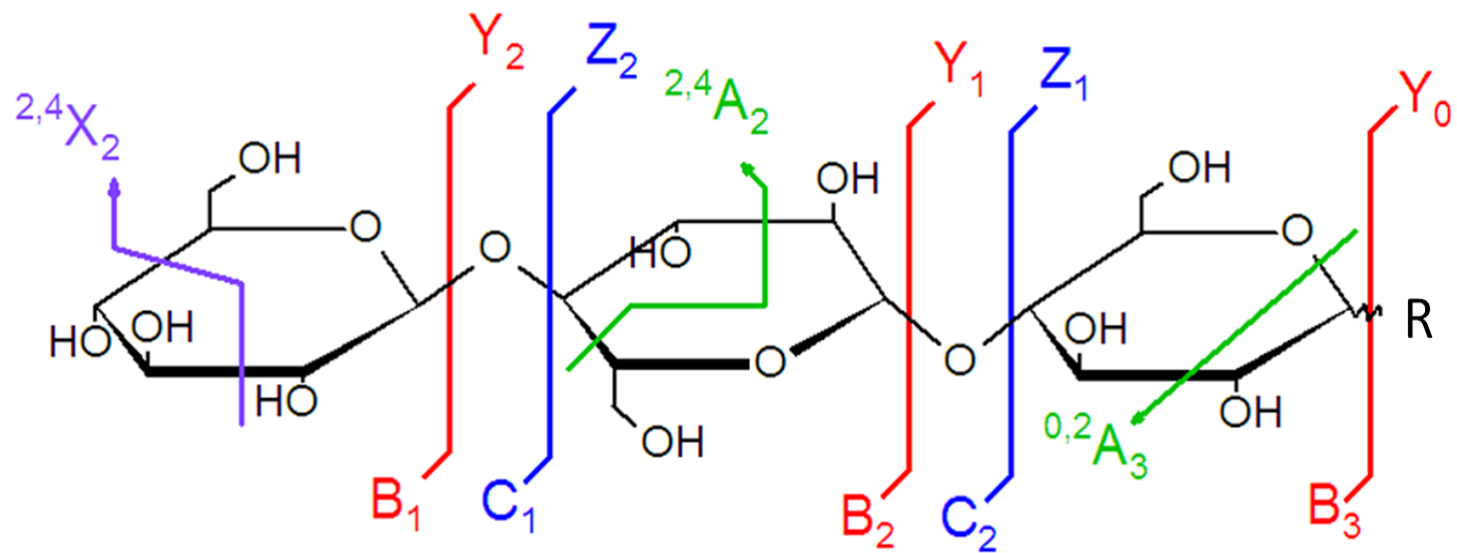


Figure 1-4. Domon and Costello nomenclature of polysaccharide fragmentation, where the 'R' represents the reducing end. Note that for cellulose, the ends are identical, so Y/C ions and Z/B ions cannot be distinguished.

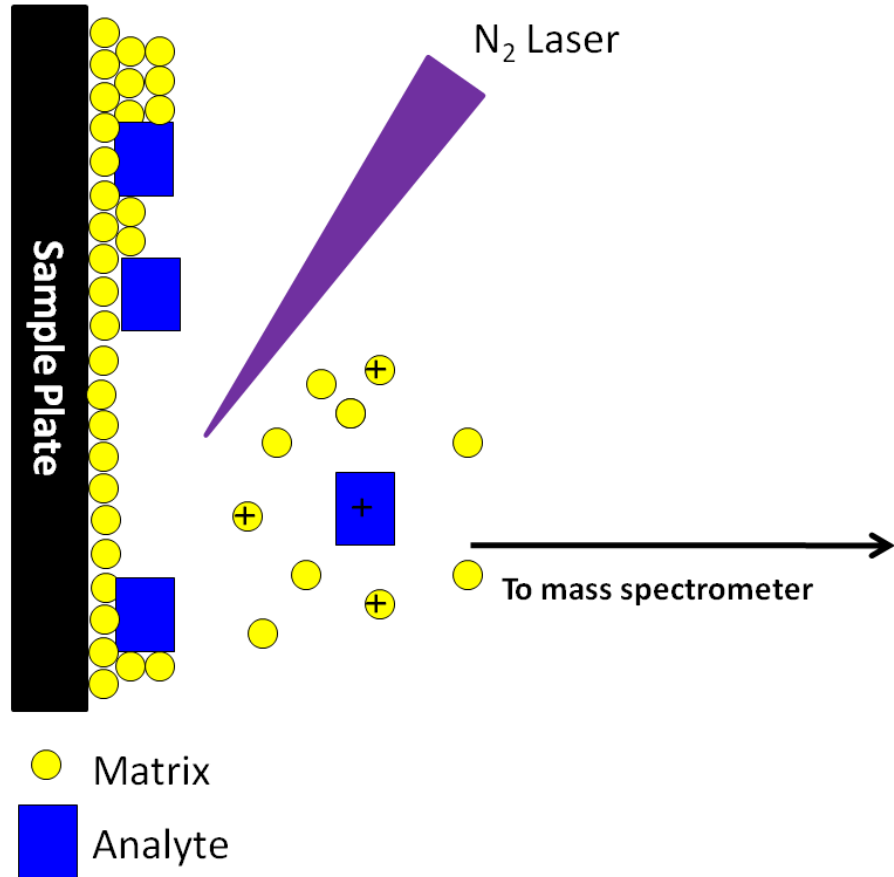


Figure 1-5. Cartoon schematic of the MALDI process. MALDI matrix and analyte solution are applied to a MALDI sample plate and allowed to co-crystallize. A laser irradiates the sample surface and the MALDI matrix absorbs the energy, desorbing both matrix and analytes into the gas phase (i.e., MALDI plume). The ionization is believed to occur in the MALDI plume through proton transfer reactions.

Table 1-1. Figures of merit for common mass analyzers.^{54,56}

Mass Analyzer	Quadrupole	Ion Traps	Time-of-Flight	Time-of-Flight Reflectron	Magnetic Sector	FT-ICR	Quadrupole-ToF	Orbitrap ⁵⁷
Mass Accuracy	100 ppm	100 ppm	200 ppm	10 ppm	< 5 ppm	< 5 ppm	10 ppm	1-2 ppm
Resolving Power	4000	4000	8000	15,000	30,000	100,000	10,000	60,000
Typical m/z Range	4000	4000	>300,000	10,000	10,000	10,000	10,000	5,000
Scan Speed	1 s	1 s	1 ms	1 ms	1 s	1 s	1 s	1 s
Tandem MS	MS ² (triple quad)	MS ⁿ	MS	MS ²	MS ²	MS ⁿ	MS ²	MS ⁿ
Cost	Low	Low	Low	Med	High	High	Med	High

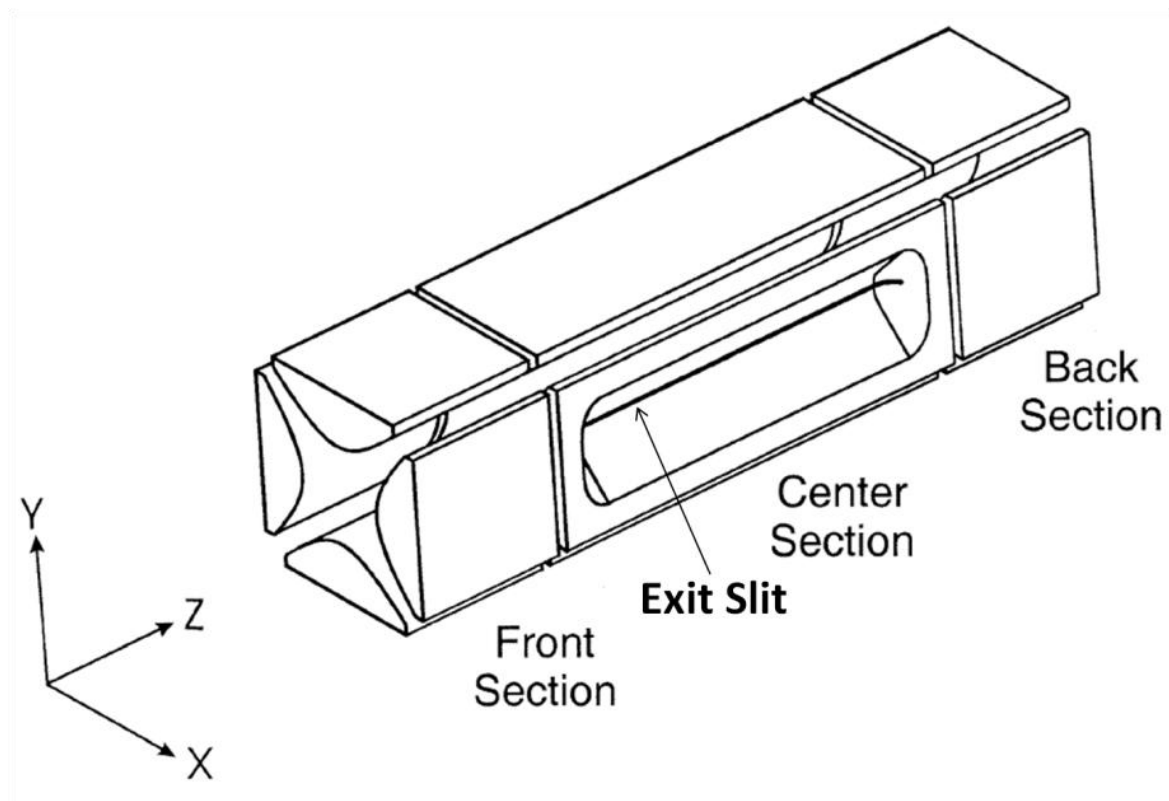


Figure 1-6. Schematic of linear ion trap adapted from Schwartz, J. C.; et al. *J. Am. Soc. Mass Spectrom.* **2002**, *13*, 659-669. Ions enter the trap along the z-axis and are 'trapped' in the center section. The ions are ejected to detector through slits in the center section along the positive and negative x-axis.

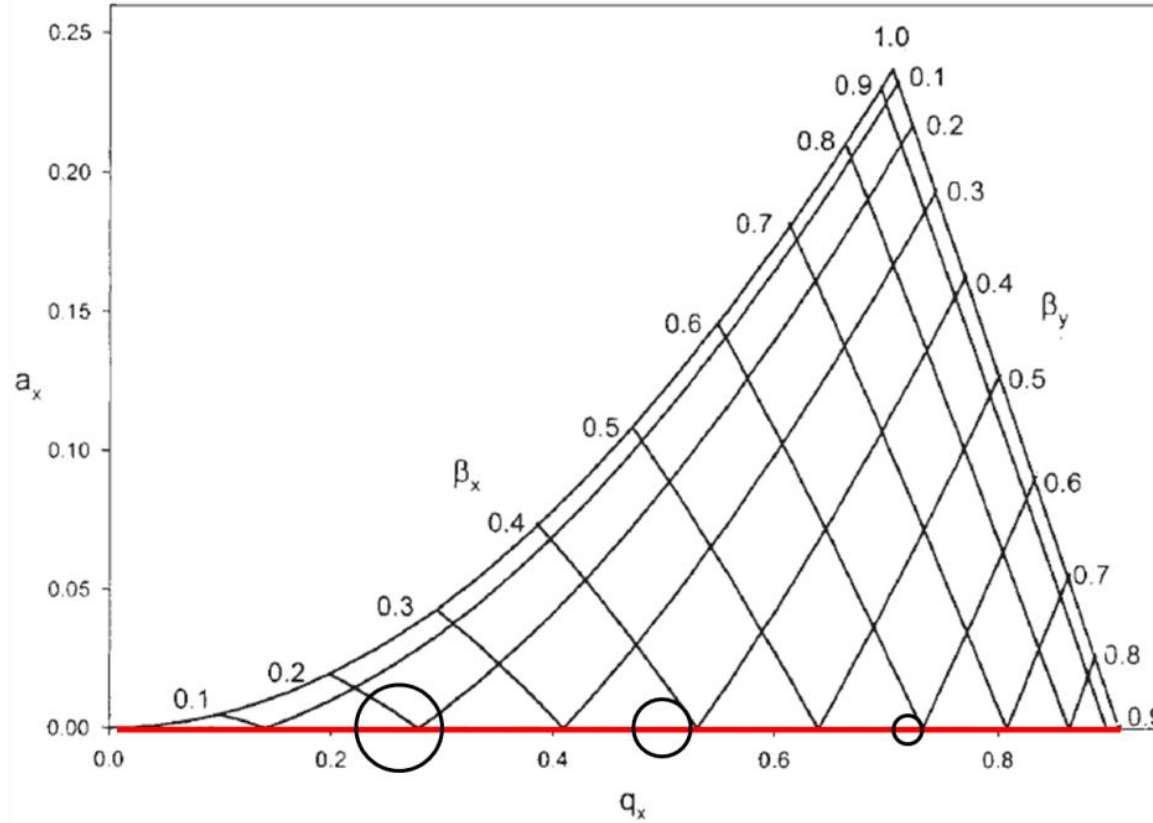


Figure 1-7. Mathieu stability diagram of the LIT adapted from Douglas, D. J. et al. *Mass Spectrom. Rev.* **2005**, 24, 1-29. Typically, LITs are operated in RF only mode, thus ions are stable along the q_x axis with a low mass cut off $q_x = 0.9$. Ions are scanned out in q -space from low mass to high as, represented by the circles.

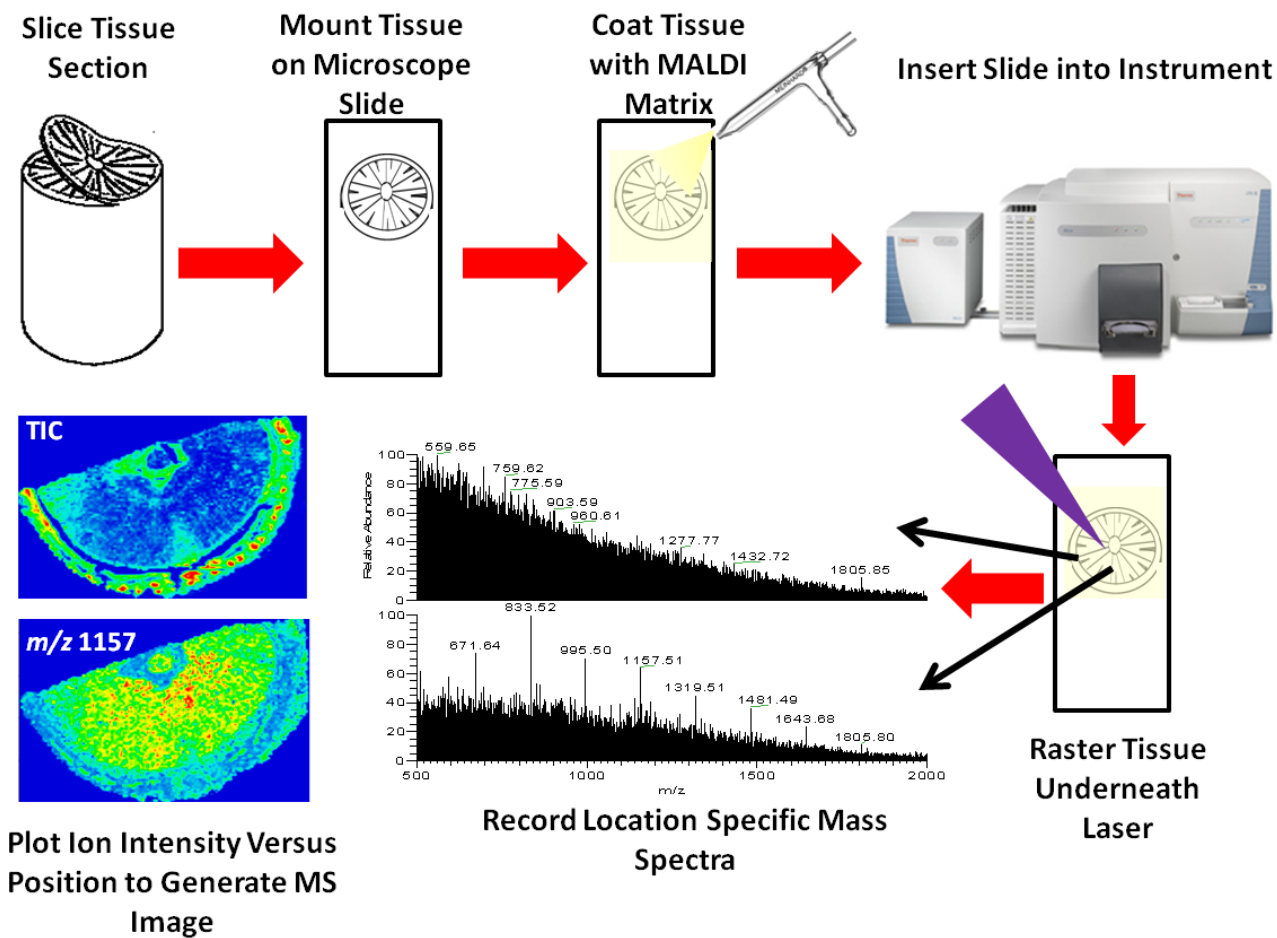


Figure 1-8. Workflow for MS imaging experiment. The tissue is sectioned and mounted onto a microscope slide. The tissue is then coated with MALDI matrix and inserted into the instrument. The tissue is rastered beneath the stationary laser and a position specific mass spectrum is recorded at each laser stop. An ion's intensity is then plotted versus the position to generate a MS image.

CHAPTER 2
MALDI LINEAR ION TRAP TANDEM MS TECHNIQUES FOR THE ANALYSIS AND
CHARACTERIZATION OF LIGNOCELLULOSIC STANDARDS: POTENTIAL FOR
MALDI-MS ANALYSIS OF INTACT TISSUE

Introduction

Biofuel production is a process that converts crops, such as corn and sugar cane, to fuel. However, inefficient processing and increasing food prices have led scientists to a more practical solution—converting plant ‘waste’ (biomass) into fuel has been under investigation. This process is termed cellulosic ethanol and has become a promising new idea for renewable energy.^{1,55}

Cellulosic ethanol is similar to corn-based ethanol in that glucose monomers are fermented to generate carbon dioxide and ethanol; however, the conformation of the glucose monomers of cellulose is different from starch (Figure 1-2).⁹¹ The conformational change results in recalcitrance to enzymatic digestion and requires a pretreatment step prior to fermentation. Pretreatments are typically a high temperature acid baths, which weaken and break interactions between cellulose chains, ultimately making enzymatic digestion possible. Although current pretreatments work, the process is still inefficient and not completely understood.⁹² A molecular understanding of the pretreatment could help increase efficiency of ethanol production and make cellulosic ethanol a more practical energy alternative.

Mass spectrometry is an analytical tool with high chemical selectivity that could be applied toward understanding chemical changes throughout a pretreatment process. Advances in ionization sources have increased the capabilities of mass spectrometric (MS) analyses of plant materials, particularly, matrix-assisted laser desorption/ionization

(MALDI).³⁴ MALDI creates gas phase ions from large biomolecules, (e.g., oligosaccharides and carbohydrates), for MS analysis.³⁹

Although MALDI is typically coupled to a TOF-MS for large biomolecule analysis, tandem MS is limited, thus the tandem MS capabilities of the linear ion trap (LIT) can overcome these limitations. Tandem MS provides more structural information and increases confidence of ion identification.^{85,93}

Furthermore, a MALDI tandem MS method for biomass materials is necessary to lay the groundwork for the MS imaging of intact biomass materials. This chapter reports MALDI tandem MS characterizations of β -glucan, microcrystalline cellulose (MCC), Birch xylan, and Spruce lignin as standards to m/z values as well as characteristic fragmentation pathways for ion identification in MS analysis of LCMs.

Experimental

Chemicals

MALDI matrices, dihydroxybenzoic acid (DHB), trihydroxyacetophenone (THAP), α -cyannohydroxycinnamic acid (CHCA) and 3-Aminoquiniline (3AQ) were purchased from Acros Organics (Geel, Belgium). The β -glucan was purchased from Fischer Scientific (San Jose, CA). The MCC (~20 μ m) and Birch xylan were purchased from Sigma-Aldrich (St. Louis, MO). Spruce lignin extract and Kraft pulp were obtained from Dr. Gary Peter's laboratory in the School of Forest Resources and Conservation.

Preparation of MALDI Matrices

The various MALDI matrices were dissolved in different solvents, including water, acetonitrile, methanol, acetone, and mixtures of the solvents. Details of exact compositions will be reported in the results section. The matrices were prepared at varying concentrations (~5–30 mg/mL) in the different solvents. Literature reports

carbohydrates favor cationization³⁴ (as opposed to protonation) thus different cations, in the form of salts, were added to the MALDI matrix solution to determine the highest ionization efficiency. The salts tested were lithium chloride, sodium acetate, potassium iodide, cesium iodide and ammonium chloride and were dissolved to a final concentration of 100 mM in the MALDI matrix.

MALDI Sample Plate Preparation

The standards were suspended in water at a concentration between 5 and 25 mg/mL and spotted using a modified dried-droplet method. As opposed to mixing the standard and MALDI matrix solutions together, 1 μ L of the standard was pipetted onto the stainless steel MALDI sample plate, immediately followed by 1 μ L of the MALDI matrix solution. Since the solvents used did not evaporate quickly, this allowed for adequate time of interaction between the MALDI matrix and the analyte.

Untreated and Holocellulose Tissue

For lignin analyses, radial slices of untreated *Populus* wood tissue (~20 μ m) were prepared using a Leica 2010 R sliding microtome (Wetzla, Germany). The slices were mounted on tape CryoJane Tape[®] (Instrumedics Inc., Richmond, IL), and the tape was mounted onto a glass slide using scotch tape for MALDI-MS analyses.

Holocellulose tissue was prepared by removing from *Populus* wood tissue using a sodium hypochlorite⁹⁴ treatment. Radial sections of the holocellulose were prepared for MALDI-MS using the process described above.

The tissues were coated with 25 mg/mL DHB+NaOAc aqueous solution using a Meinhard nebulizer. The nebulizer passes the MALDI matrix solution through a small hole, with a nitrogen flow gas to create small droplets of MALDI matrix solution. The MALDI matrix in solution phase interact with the analytes, and as the solvent

evaporates, small, relatively uniform MALDI matrix crystals coat the top of the tissue. The MALDI matrix solution wets the tissue and it is necessary to allow the tissue to dry completely between coatings—rapid evaporation (thus smaller crystals) was promoted by a stream of warm air. Tissues are coated by spraying the solution for 30 seconds, followed drying for 4 minutes; this is repeated until about 8 mL of the MALDI matrix solution is used.

Instrumentation

The dissertation researched spanned an upgrade to the instrument used. Early studies were performed on a Thermo MALDI LTQ, whereas later studies were performed on a Thermo MALDI LTQ XL, both equipped with a 337 nm 60 Hz N₂ laser. Although the instrument used was simply replaced by the updated version, it is important to note the small differences between the two instrumental designs—the source pressure, laser set-up and laser parameter control. The Thermo MALDI LTQ source operates at a pressure of 170 mTorr and used fiber optics to transfer the laser light to the MALDI plate. The user controlled the ‘laser power,’ which was given as a percentage of maximum power. The Thermo MALDI LTQ XL (upgraded instrument) source operates at a pressure of 70 mTorr and uses lenses to direct the laser light toward the MALDI sample plate. The user controls the ‘laser energy’ in μJ . No major differences between the spectra obtained from the two different instruments were observed, and a more thorough discussion of the differences are discussed in the MCC section of this chapter.

For standard analyses, three laser shots were used per laser stop and approximately 50 scans were averaged to generate one spectrum. The laser energy used was varied based on matrix, analyte and nature of MS analysis (i.e., MS versus

tandem MS), and typically fell between 20 and 35 μJ . Collision-induced dissociation (CID) was performed in the LIT with an isolation width of 1.5 m/z and the CID parameters varied between 80–120 (arbitrary units, normalized to 400). Data files were analyzed with Qual Browser (v.2.0.7, Thermo Fischer Scientific).

Results and Discussion

The results are divided into the different standard categories, β -glucan, MCC, Birch xylan, Spruce lignin extract and Kraft pulp. All experiments were performed on the Thermo MALDI LTQ XL, unless otherwise specified.

β -Glucan

Cellulose is a β -1,4-linked polymer of glucose, usually with a degree of polymerization $\sim 10,000$ and can be present in two different forms, crystalline or amorphous. As discussed previously, the orientation of the $-\text{CH}_2\text{OH}$ group allows for strong interactions between different polymers of cellulose. Crystalline cellulose, as the name suggests, has highly order hydrogen bonding between strands of cellulose, which creates a rigid secondary structure. The amorphous regions of cellulose have less ordered bonding between cellulose polymers, generating a weaker secondary structure, as depicted in the cartoon (Figure 2-1) of the different secondary structures of cellulose. Due to the possibilities of highly ordered secondary structures of MCC, β -glucan, a β -linked polymer of glucose similar to cellulose, was used as a model for optimizing MALDI parameters for further analyses.

Choosing the optimal matrix

Optimizing experimental conditions is based on different parameters, such as the response function and signal-to-background ratio (S/B). In analytical chemistry, the response function refers to the analytical signal, and for optimization, experimental

parameters are adjusted to maximize the analyte signal.⁹⁵ However, generating a maximum signal is not the only consideration. If optimizing the analyte signal increases the sum of the background signals from other species (*B*), then the experiment is not optimized. Both the analyte signal and background signal are needed to determine an optimal experimental parameter.⁹⁵

The *S/B* is important (and difficult to calculate) for MALDI-MS analyses since excess of background compounds (MALDI matrix) is added to the sample prior to analyses. Due to the inherent high background in MALDI-MS, the *S/B* was the focus for determining optimal experimental parameters.

Since MALDI matrix serves to transfer energy and ionize the analytes, it is important to start experimental optimization with determining the best MALDI matrix for the analyses. Based on previous studies, MALDI matrices evaluated for β -glucan (4 mg/mL) were DHB, CHCA, THAP, 3-AQ, sinnapinic acid (SA), and a mixture of 3-AQ and SA.⁹⁶ However, 3-AQ, SA and the 3-AQ/SA mixture did not ionize β -glucan and were ruled out as possible MALDI matrices. Starting concentrations of the matrices were chosen to be 25 mg/mL for DHB, 25 mg/mL for THAP and 5 mg/mL for CHCA. The MS spectrum from *m/z* 200–1000 is displayed in Figure 2-2. As predicted, ions 162 *m/z* apart were observed, due to the 162 Da repeating unit of glucose (Glc) in the β -glucan polymer. The spectra clearly show that DHB as a MALDI matrix generated the highest analyte signals and the lowest background signals, thus the highest *S/B*. From this, it was determined that 25 mg/mL DHB was the optimal matrix and used for the remainder of the experiments.

Optimization of MALDI matrix additives

The most abundant analyte ions of β -glucan in the MS were sodiated; relatively less potassiated and no protonated ions were observed (Figure 2-2). This suggests that carbohydrates favor cationization, in agreement with previous work.³⁴ In order to increase the analyte signal, it is often beneficial to promote a certain type of cation by adding cations (in the form of salts) to the matrix solution. Figure 2-3 shows the MS of β -glucan with five different salts, LiCl, NaOAc, KCl, CsI, NH₄Cl, added to the matrix in equal molar amounts (0.100 mM). Although the anions are different for sodium and cesium, this should have little effect on the availability of the cation, since these ionic compounds completely dissolve in solution. The five spectra display, in all cases, that the sodiated species is formed (even without the addition of extra sodium), which further suggests that the sodiated species are favored over the other cations. Sodium acetate was chosen as the optimal matrix additive and used for the remainder of the experiments.

Tandem MS characterization of β -glucan

After determining the optimal matrix, matrix additive and the m/z of analyte ions formed, tandem MS experiments were used to characterize fragmentation. The tandem MS spectra are labeled using Domon and Costello nomenclature.³⁶ It is important to note that distinguishing between C/Y, B/Z, and A/X fragment ions is not possible due to identical terminal sugar groups of β -glucan (as well as MCC and xylan), so the C, B and A nomenclature will be used for the remainder of the dissertation. The fragment ions are labeled by the type of glycosidic fragment (B, C) as well as the position of the fragment denoted by subscripts. Further, cross-ring cleavages are denoted by the letter A, where

the subscripts refer to the sugar residue and the superscripts refer to the position of the bonds breaking.

The MS² 689→..., ([Glc₄+Na]⁺) ion, spectrum using CID 85 is displayed in Figure 2-4. The most abundant fragment ion observed is the C₃ fragment, which is a result of a neutral loss (NL) of 162 (Glc) Cross ring cleavages, NL 60, 90 and 120, were also observed corresponding to ^{0,2}A₄, ^{0,3}A₄, and ^{2,4}A₄, respectively. The NL of 90 could also be due to ^{1,4}A₄, but is more likely ^{0,3}A₄ since the oxygen-carbon bond is more likely to break than a carbon-carbon bond. The B series ions are observed, B₄ (*m/z* 671), B₃ (*m/z* 509) and B₂ (*m/z* 347), which are 18 *m/z* units lower than the C series ions. Tandem MS of β-glucan provided diagnostic fragment ions, which will be useful in the identification of compounds within wood tissue.

Although NaOAc was chosen as the optimal matrix additive, it is possible that other cationized ions offer more diagnostic fragmentations. Tandem MS of lithiated, sodiated and potassiated ions were explored to test the effects of cation size on fragmentation as well as determining the cation that provides the most diagnostic fragmentation. Figure 2-5 displays the MS² spectra of *m/z* 673, 689, and 705, corresponding to [Glc₄+Li]⁺, [Glc₄+Na]⁺, and [Glc₄+K]⁺, respectively. The most abundant fragment for all three ions is the C₃ ion (NL 162) and no other fragment ions were observed for the lithiated and potassiated ions. Cross-ring cleavages occur during CID of the sodiated species, which offers more structural information about the ion from the MS² spectrum.

Since it was already determined that NaOAc was the optimal matrix additive, these results support that choice. It is interesting to note that there seems to be no trend in

fragmentation according to the cation size; however, this experiment only analyzed the four sugar polymer. Since the cations are different sizes, the length of the polymer could affect the strength of the adducts, thus affecting the fragmentation pathways.

Microcrystalline Cellulose (MCC)

After the MALDI parameters were optimized with β -glucan, MCC was characterized using MALDI tandem MS. Although β -glucan and MCC have similar properties, there are some differences that made MCC analyses more difficult. The major difference is the solubility— β -glucan is soluble in common matrix solvents and MCC is not soluble, without the addition of concentrated acids or bases, which break glycosidic bonds. Having an analyte that is not soluble is difficult for MALDI-MS since the proposed ionization mechanisms rely on analyte/matrix co-crystallization. Despite the inability to dissolve MCC in solvents, MALDI-MS analyses were successfully performed.

Figure 2-6 compares an ideal MALDI sample spot where the analyte and MALDI matrix co-crystallize completely to MCC and DHB crystals. Note the small, homogeneous crystal sizes of the ideal spot, as opposed to the heterogeneous, larger crystals of the MCC and DHB MALDI sample spot. Since the MCC is not in solution, the DHB crystals tended to gravitate away from the MCC, which caused large 'hot spots' within the MCC MALDI sample spot. The 'hot spots' produced quality spectra and areas around the 'hot spots' produced spectra dominated with MALDI matrix ions, which increases the ion background signal when spectra are averaged. Despite complications, the sample preparation developed for these analyses allowed for quality spectra that were readily analyzed.

MALDI-MS of MCC

The MCC standard was suspended in water at ~4 mg/mL and a range of concentrations from 5–25 mg/mL DHB NaOAc was used to determine the optimal MALDI matrix concentration (Figure 2-7). Literature suggests the optimal MALDI matrix-to-analyte molar ratio from 1,000–10,000; however, the molarity of MCC is difficult to determine. For example, MCC is a polymer, with a wide range of sugar chain lengths, thus only an average molecular weight can be calculated. Furthermore, MCC is not soluble, so determining the molarity of the MCC standard solution is problematic. Instead of calculating the molar ratios, different concentrations of the MALDI matrix were tested with a constant concentration of suspended MCC to determine the optimal concentrations for MALDI-MS.

MALDI-MS of MCC generated intense ions 162 amu apart, similar to the β -glucan, and the highest intensity analyte ions with the lowest MALDI matrix ion background signal occurred between m/z 500–2000. Since the analyte ions signal to background is a major concern for MALDI-MS analysis, this mass range was used for the majority of the studies. Similar to the β -glucan, the analyte ions observed from the MS of MCC were sodiated, however, the most intense ions were also dehydrated and represented in the form $[\text{Glc}_n\text{-H}_2\text{O}+\text{Na}]^+$. Figure 2-7 illustrates that 20 mg/mL DHB has a low analyte ion S/B, and was ruled out as the optimal matrix concentration. The other three spectra are similar. The 10 mg/mL DHB spectrum has the highest analyte signal, but the ion background signal is also higher. The 5 mg/mL DHB spectrum produced the best S/B ratio, so it was used for the remainder of the MCC standard experiments.

Several different approaches were used to try to improve sample spot quality, for example, ethylenediaminetetraacetic acid (EDTA) was added to the solution. Adding

EDTA to the MALDI matrix solution aggregated the MCC with DHB crystals (Figure 2-6). Since the EDTA seemed to cause an aggregation of MCC and DHB crystals, the 'hot spots' were closer together, thus more reproducible spectra, with a lower MALDI matrix ion background signal were observed

It is interesting to note the ion intensity distributions of the MCC analyte ions. MS of polymers use the ion intensity distribution to determine molecular weight of polymer as well as the degree of polymerization (DP). However, this might not be the case for the MALDI LIT MS analyses of MCC. MCC is known to have a DP ~10,000, which far exceeds the mass range of the LIT. Despite the high mass of the analyte, ions in the range m/z 500–2000 were observed, suggesting that smaller polymers are naturally present within the MCC or in-source fragmentation of larger polymers occurs. Since MALDI uses a laser, it is likely the energy put into the analyte could induce in-source fragmentation, which makes the m/z distribution of analyte ions not necessarily representative of the MW distributions of MCC.

The stability of analyte ions within the ion trap is also important to consider as this could also affect the ion intensities. Figure 2-7 displays that the most intense ions occur around m/z 1157, which is close to the middle of the mass range scanned. If the ion intensity distribution were a property of the MCC, then shifting the mass range should have little to no effect on the ion intensity. However, when the mass range is increased to m/z 500–3000, the distribution shifts to make the ions around m/z 2000 the most intense. This is not problematic, as the length of the cellulose is not a focus of this study, instead, determining the presence and spatial distribution of cellulose within a tissue section is the goal of these experiments..

In addition to optimizing the MALDI matrix concentration, the effect of varying the laser energy was also explored. Figure 2-8 illustrates the effect of the laser energy on MALDI matrix ion and MCC ion intensity in the mass spectrum. MCC was spotted on a MALDI sample plate, immediately followed by 5 mg/mL DHB+NaOAc and EDTA. Three laser shots were used and 25 spectra were averaged and the standard deviation of the mean was calculated for each data point. The laser energy was increased from 5–50 μJ in five μJ increments. The plot illustrates that from 5–20 μJ , the MALDI matrix ion intensity is significantly larger than the MCC analyte ion intensity, and 25–30 μJ , and the intensities are similar. Laser energies greater than 30 μJ show a larger intensity analyte ion and lower MALDI matrix ion intensity, which is optimal for the experiments. Figure 2-9 displays the MS spectrum of MCC after all parameters were optimized, showing very little MALDI matrix ion signal.

It is also interesting to note that the analyte ion intensity steadily increases over the range of laser energies tested; however, the MALDI matrix analyte ion signal shows more variability, and there is a decrease in ion signal around 20 μJ . Although the scope of this research was not the MALDI mechanism, these data suggest that the ionization mechanism for MCC differs from typical MALDI experiments.

Tandem MS of MCC

Tandem MS is often necessary for in vivo tissue analyses, so characterizing fragmentation of standards is important. The most abundant ions in the MALDI-MS of MCC were the sodiated, dehydrated species— m/z 1157, $([\text{Glc}_7\text{-H}_2\text{O}+\text{Na}]^+)$ ion. For tandem MS experiments, m/z 1157 ions were isolated and fragmented. Figure 2-10 displays the MS^2 spectrum lower abundance of background ions compared with the MS spectrum. The most abundant fragment ions were the B series ions resulting from

sequential NLs of 162 (Glc), due to glycosidic bond cleavages. In addition, NL of 18, a non-specific loss of water, NL of 60, $^{0,2}A_7$ cross-ring cleavage and NL of 144, a C_6 fragment were also observed in the MS spectrum.

The difference between CID of sodiated MCC versus the sodiated dehydrated MCC also was explored. Figure 2-11 displays four stages of MS of the sodiated species m/z 1175, $[Glc_7+Na]^+$. The most intense fragment of the sodiated species is the $^{0,2}A_7$ cross-ring cleavage, which is different from the sodiated dehydrated species (most intense fragment is the C_6 ion). In addition, the sodiated species shows both B and C series fragment ions, resulting from NL of 162 and 180, indicative of NL of the glucose repeating unit and glucose molecules. Further, the fragment ion m/z 1115, resulting from a cross-ring cleavage, was isolated and fragmented for MS³ (m/z 1175→1115→...). CID of m/z 1115 resulted in NL of 60, possibly another cross ring cleavage, as well as NL of 120, which results in the C_6 fragment—the other C fragment ions are observed as well. The MS⁴ of m/z 1175→1115→1055→... results in NL of 60, likely a cross ring cleavage, to form C series ions. Additionally, NL of 162 from m/z 1055 are also observed, which is indicative that there is still an intact terminal glucose monomer.

Tandem MS analyses of MCC show that there are diagnostic fragment ions for both a sodiated and sodiated, dehydrated species to monitor in wood tissue analyses. If the most abundant fragment ion is a NL of 60, then it can be assumed that the ion is sodiated, and if the most abundant fragment is a NL of 162, then the ion can be assumed to be sodiated, dehydrated. One of the most important advantages of tandem MS, is that analyte ions can be isolated from a high background ion signal to increase

the analyte ion S/B, which is very important for in vivo analyses, where the background ion signal is hypothesized to be very high. Increasing the S/B improves the sensitivity of the experiment, and isolating the analyte ion helps to improve the selectivity of the experiments.

Xylan

Xylan is a classification of hemicellulose that is a polymer of xylose, a five-carbon sugar with MW of 150 amu. The major difference between xylan and MCC (and β -glucan), is that xylans can be branched and/or substituted. Figure 2-12 illustrates the common forms of xylan, linear, glucuronic acid (GlcA) substituted, and 4-O methyl glucuronic acid (O-MeGlcA) substituted, as well as the mass differences from the linear xylan. For example, the linear Xyl₄ polymer has a mass of 546 amu (each xylose, Xyl, repeating unit has a mass of 132). Glucuronic acid has a mass of 194 amu, 44 amu more than a xylose monomer, thus the Xyl₃GlcA polymer is 44 amu more than Xyl₄. Since xylan can be branched and substituted, there is a possibility of more ions, thus more complex mass spectra. Although xylan is more soluble in water than MCC, the same parameters that were optimized for MCC were used for xylan.

MS of Birch xylan

Approximately 4 mg/mL Birch xylan was dissolved in water and 1 μ L was spotted on a MALDI sample plate, immediately followed by 1 μ L of 15 mg/mL DHB with NaOAc. The MS of 23 averaged spectra is displayed in the inset of Figure 2-13, which shows intense ions 132 amu apart (mass of repeating Xyl residue) and intense background ions in between the intense ions. The most intense ions were identified as sodiated, dehydrated linear xylan ions, represented in the form $[Xyl_n-H_2O+Na]^+$, where n is the number of Xyl residues. Focusing on a smaller portion of the spectrum (Figure 2-13)

illustrates a repeating pattern of ions between the linear xylan ions that were identified as substituted xylans, $[\text{Xyl}_6\text{GlcA-H}_2\text{O+Na}]^+$ (m/z 991) and $[\text{Xyl}_6\text{MeGlcA-H}_2\text{O+Na}]^+$ (m/z 1005).

One of the difficulties of xylan analysis is trying to determine an accurate analyte *S/B*. MCC is a linear polymer, so only one m/z was observed for each length of the polymer—it was determined the ions in between the analyte signal were the MALDI matrix background ions. In contrast, xylans can be substituted and branched, so ions in between the linear xylans are not necessarily MALDI matrix background. Instead, the ions are the different variations of the polymer, making the calculation of analyte *S/B* difficult, thus optimization was based primarily on analyte signal of the linear polymers.

Tandem MS of Birch xylan

Tandem MS is necessary for Birch xylan analyses due to the abundance of analyte ions at nearly every m/z value. Tandem MS isolates one xylan ion for analyses, which helps to not only positively identify the ion, but also to increase the *S/B* for the analysis. Figure 2-14 shows three tandem MS spectra of the linear, GlcA substituted, and MeGlcA substituted sodiated, dehydrated species, m/z 947, 991, and 1005, respectively.

The major fragment ions from CID of the $[\text{Xyl}_7\text{-H}_2\text{O+Na}]^+$, similar to MCC, are B_{7-4} ions, resulting from NL of 132, a Xyl repeating unit (Figure 2-14). Another major fragment is the C_6 ion, the hydrated counterpart to the B_6 ion. Tandem MS is capable of distinguishing the monomers that make up the polymer; however, there are several different structures (i.e., linear or branched) that are possible for a particular m/z value. The ion at m/z 947 is only composed of xylose sugars; however, determining the location of the branching or substitution on the polymer backbone is more difficult.

Tandem MS of m/z 991 \rightarrow , $[\text{Xyl}_6\text{GlcA-H}_2\text{O+Na}]^+$, shows abundant NL of 44, carboxylic acid from the GlcA sugar (m/z 947), NL of 176, GlcA (m/z 815) and NL 132, xylose residue (m/z 859). In addition, NL of 264, due to losses of two Xyl residues and NL of 308, due to losses of Xyl and GlcA were also observed. This again demonstrates that tandem MS is capable of determining the sugar composition of polysaccharides; however, the exact location of the GlcA along the sugar cannot be determined from tandem MS alone. The tandem MS spectrum of m/z 1005 \rightarrow , $[\text{Xyl}_6\text{MeGlcA-H}_2\text{O+Na}]^+$, is very similar to the tandem MS of m/z 991. The difference between the two is 14 amu, due to the methyl group on the MeGlcA (as opposed to the GlcA).

Lignin

Lignin is a complex, three-dimensional polymer composed of a variety of different aromatic monolignols connected with a variety of different linkages. Lignin is found the plant cell walls and acts as 'glue' to hold the secondary structure of hemicellulose and cellulose intact, providing mechanical strength for the plant. Lignin is derived from three common monolignols, *p*-coumaryl alcohol, coniferyl alcohol and sinapyl alcohol (Figure 2-15) that undergo extensive condensation polymerization—this results in a variety of different linkages and a degree of polymerization around 10,000.⁹⁷

MALDI-MS of lignin

Mass spectrometric characterization of lignin is difficult due to the variety of building blocks, strong inter- and intra- molecular interactions and no standard materials (lignin used for this research was a spruce lignin extract obtained from the School of Forest Resource and Conservation). Since lignin monomers encompass a variety of different compounds (thus molecular weights), MS analysis results in ions at nearly every m/z value, without a repeating pattern (as observed in cellulose and

hemicellulose). This complicates the spectra, making it difficult to identify and characterize 'lignin' in intact tissue sections.

Lignin analyses are commonly performed using pyrolysis mass spectrometry. Pyrolysis MS breaks the lignin polymer apart into the building blocks, and the most common ions monitored in these analyses are vinyl syringol and vinyl guaiacol, also referred to as S and G lignin.⁹⁸ The vinyl syringol to vinyl guaiacol ratio (S:G) varies depending on hard or soft wood, as well as different species. Most wood used for this research is *Populus*, which has an S:G ratio greater than one, indicating more S lignin is present in the tissue.⁹⁹

The monolignols are similar in structure and chemical properties to common MALDI matrices, specifically the aromatic benzene rings. Since it is likely that lignin absorbs the wavelength of the laser used for MALDI (337 nm), lignin analyses with and without MALDI matrix were performed (Figure 2-16). As Figure 2-16 displays, MALDI matrix is not necessary to generate ions; however, both analyses are complicated, and choosing an ion to be a 'lignin marker' using MALDI-MS could be difficult. In order to find a diagnostic ion for lignin analyses, tandem mass spectrometry is necessary. As a starting point, m/z 181 ($[M+H]^+$ of vinyl syringol) was isolated for MS^2 analysis to determine if tandem MS can identify a diagnostic ion for lignin in wood tissue.

Characterizing low molecular weight ions using MALDI can be complicated due to interferences from the MALDI matrix (specifically, DHB, 154 Da). Figure 2-17 displays MS^2 of m/z 181 \rightarrow ... from DHB+NaOAc (alone) and untreated *Populus* wood tissue without MALDI matrix. The two spectra show common fragment ions, m/z 163, 153 and 137, so these were not chosen as diagnostic ions of lignin. The most abundant ion,

separated from the other fragment ions observed from the wood tissue, was m/z 121, resulting from losses of both $-OCH_3$ groups (NL of 60) from the vinyl syringol.

MALDI-MS analysis of lignin in untreated and holocellulose *Populus* tissue

Radial slices of both untreated and holocellulose tissue was placed on the same slide for MALDI tandem MS Imaging analysis. A thin layer of DHB+NaOAc crystals was applied atop the tissues using a Mienhard nebulizer. Details of MALDI matrix coatings are found in the experimental section. Figure 2-18 displays the optical and MS² images of untreated (top) and holocellulose (bottom) tissues. MS² of m/z 181 was performed in the rectangle outlined in blue in the optical image, using 100- μ m laser step sizes. The intensity of the fragment ion from m/z 181 \rightarrow 121 was plotted for the MS² image and displays intense ion signal off the untreated wood, and little ion signal from the holocellulose. There were areas of signal from m/z 181 \rightarrow 121 observed from the holocellulose tissue, which could result from lignin being left behind after the sodium hypochlorite treatment.

In addition, Figure 2-18 confirms that the ion signal from MS² 181 \rightarrow 121 is not due to MALDI matrix alone. The section in between the two tissue sections (the red region in the optical image) is an area of exposed tape, coated with the MALDI matrix. If the ion signal MS² 181 \rightarrow 121 was only coming from the DHB MALDI matrix, than the region between the tissues would show high ion intensity, but this was not observed. It was determined that MS² 181 \rightarrow 121 is a good diagnostic ion for the presence of lignin within wood tissue, and will be used in future experiments.

Summary

The results presented in this chapter laid the groundwork to develop a MALDI tandem MS imaging technique for LCM. Due to the complexity of the compounds, as

well as the organization of the compounds, that comprise LCM, it was necessary to first optimize the experimental parameters using standard materials.

β-glucan and MCC

Experiments with β-glucan were used to determine the optimal MALDI matrix, which included the matrix, solvent as well as additives, for the analyses of LCMs. The highest *S/B* was observed using DHB+NaOAc dissolved in water. MALDI-MS of β-glucan resulted in the formation of sodiated species.

The optimal MALDI parameters determined for β-glucan were applied for the analysis of MCC. The MALDI matrix concentration and laser energy were optimized using the MCC. The plot of laser energy versus a MALDI matrix ion and a cellulose ion illustrated that higher laser energies are needed (> 20 μJ) to obtain higher analyte signal (as the MALDI matrix ion signal remains similar). Despite the difficulties in obtaining uniform MALDI sample spots, MALDI-MS spectra of MCC were obtained, with a high *S/B* ratio. The MALDI-MS spectra displayed ions 162 *m/z* apart, which is consistent with the molecular weight of the glucose repeating unit of the polymer. The ions were identified as sodiated, dehydrated polymers of glucose and represented as $[\text{Glc}_n\text{-H}_2\text{O}+\text{Na}]^+$ where *n* represents the number of glucose monomers. A list of *m/z* values of cellulose to monitor in wood tissue is presented in Table 2-1.

In addition to MS, MCC was characterized using tandem MS. A single cellulose ion, *m/z* 1157 was isolated and fragmented using collision-induced dissociation. The fragmentation observed after dissociation of the sodiated, dehydrated species showed abundant B series fragment ions, resulting from glycosidic bond cleavages. Cross-ring cleavages were also observed; however, they were in low abundance relative to the B series ions.

Hemicellulose

Hemicellulose characterization was more difficult compared to the analysis of MCC. Hemicellulose encompasses linear and branched, as well as substituted polysaccharides. Since cellulose only contains glucose, the molecular weight between each degree of polymer remains the same (162 Da). However, the xylan backbone of hemicellulose, is commonly substituted with GlcA and MeGlcA—this generates several different polymer patterns of ions as well as increases the number of analyte ions observe (thus the spectra complexity). The ions that were observed were the sodiated, dehydrated species in the form $[Xyl_n-H_2O+Na]^+$, where n represents the number of xylose residues.

Tandem MS was used to characterize and identify xylan, GlcA substituted xylan and MeGlcA substituted xylan. The tandem MS of all three compounds displayed NLs of 132, due to glycosidic cleavages of xylose residues. The GlcA substituted was identified by a NL of 176 (GlcA) and MeGlcA was identified by a NL of 190 (MeGlcA). Although the exact composition of the monomers that are in the polymers are known, the structure (e.g., branching and where it is branched) is not able to be determined from tandem MS alone. However, this is not vital to the imaging of LCMs.

Lignin

The MS characterization of lignin was difficult since there are no standard materials commercially available and the inherently high heterogeneity of the polymer. Although lignin can be ionized without MALDI matrix, the MS spectra with and without the MALDI matrix look similar and are complex. Ions at nearly every m/z with similar intensities are observed, making it difficult to choose a diagnostic ion for monitoring in

wood tissue. Since lignin has been shown to have an S:G ratio greater than 1, vinyl syringol (m/z 181) could provide insight into lignin composition in wood tissue.

Tandem MS of m/z 181 of MALDI matrix was compared to *Populus* wood tissue, and it was determined that m/z 181 \rightarrow 121 is an abundant fragment in the wood tissue, but not the MALDI matrix. To determine if tandem MS of m/z 181 \rightarrow 121 could be diagnostic of lignin in wood tissue, analysis of untreated wood tissue was compared to holocellulose tissue. The tandem MS image of MS² of m/z 181 \rightarrow 121 illustrated abundant ion signal from untreated tissue, and less abundant ion signal from the holocellulose, elucidating the m/z 181 as a diagnostic ion for lignin in wood tissue.

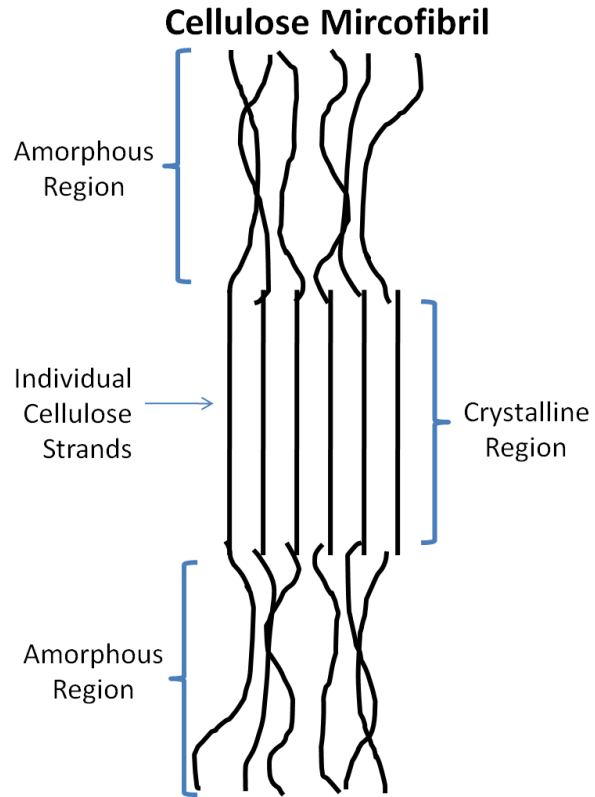


Figure 2-1. Cartoon representation of a cellulose microfibril. Each microfibril is composed of several individual cellulose polymers. Both amorphous and crystalline regions of the microfibril exist, depending on the strength of interactions between cellulose polymers.

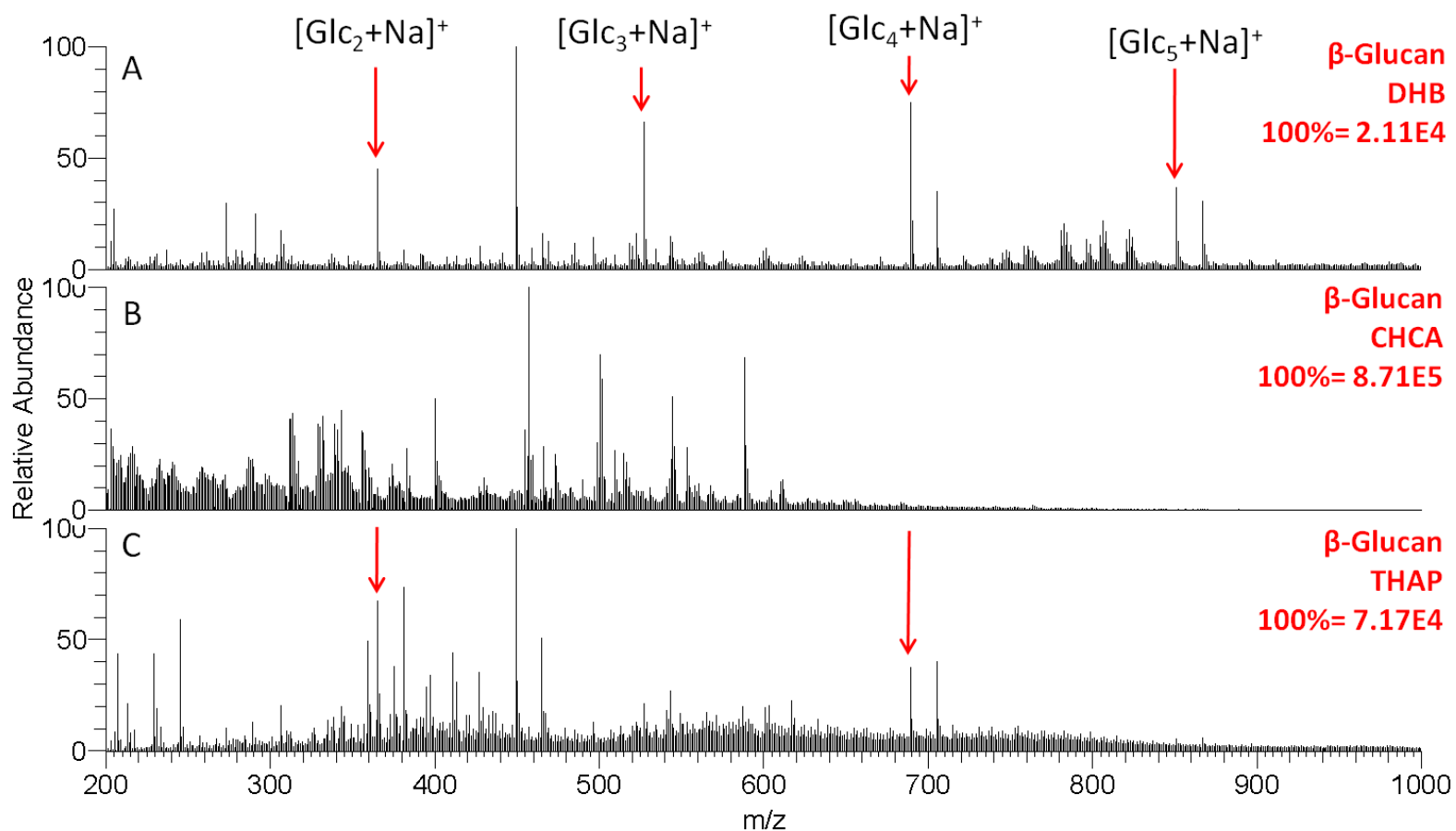


Figure 2-2. MALDI-MS spectra of β -glucan standard using Different matrices. A) 2,5-Dihydroxybenzoic acid (DHB) B) α -cyano-hydroxycinnamic acid (CHCA) C) trihydroxyacetophenone (THAP). The most intense ions observed for the DHB were the $[Glc_n+Na]^+$ ions, where n represents the number of glucose monomers. Note that sodiated ions signals were more intense than the potassiumated ion signals and no protonated ions were observed. Also, no analyte ions were observed for CHCA. The highest analyte ion signal to background ion signal was observed for DHB and was determined to be the optimal matrix.

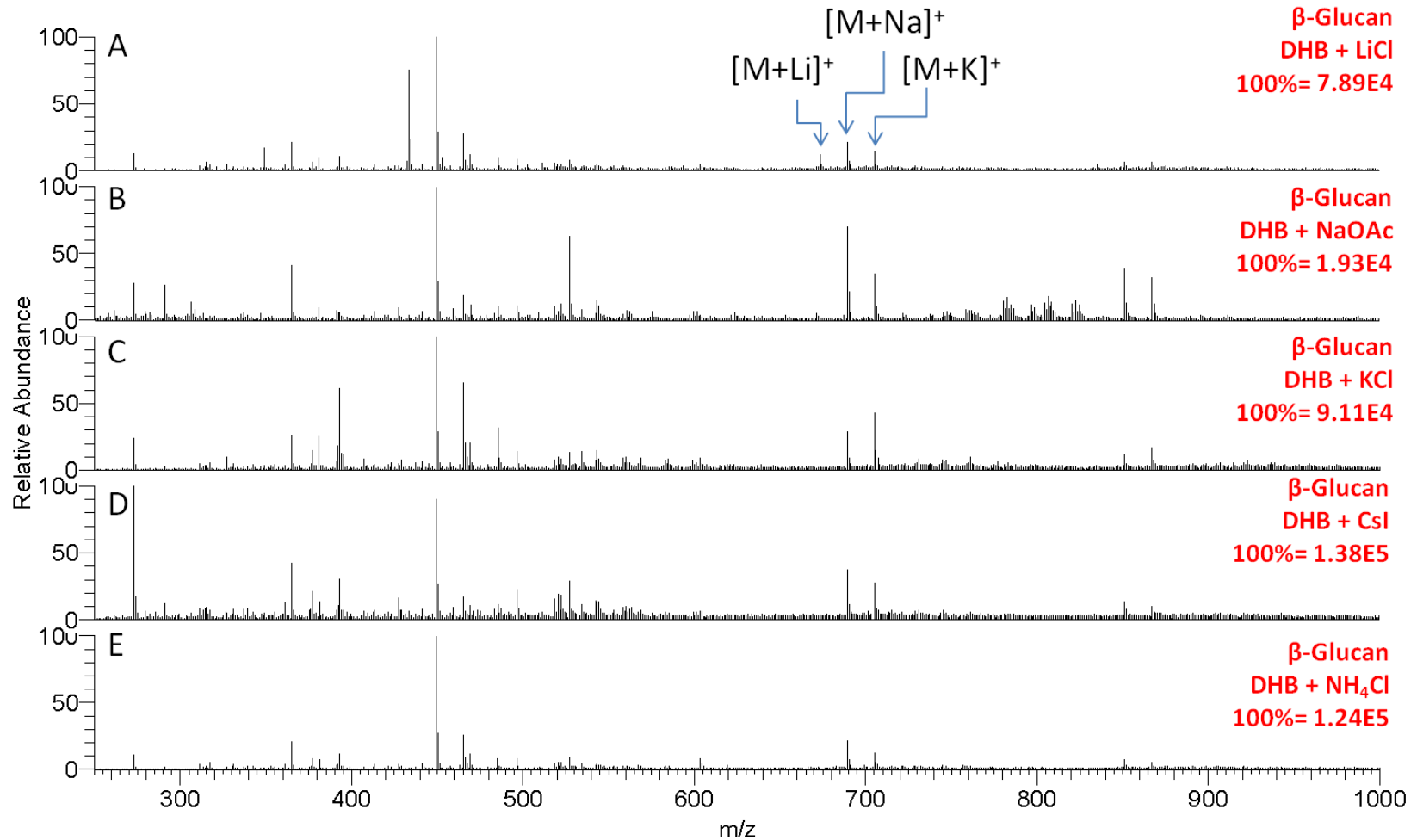


Figure 2-3. MS Spectra of β -glucan standard using DHB MALDI matrix with different salt additives. A) Lithium chloride. B) Sodium acetate. C) Potassium chloride. D) Cesium iodide. E) Ammonium Acetate. Spectra illustrates that regardless of salt added to the MALDI matrix, sodiated species are preferentially formed.

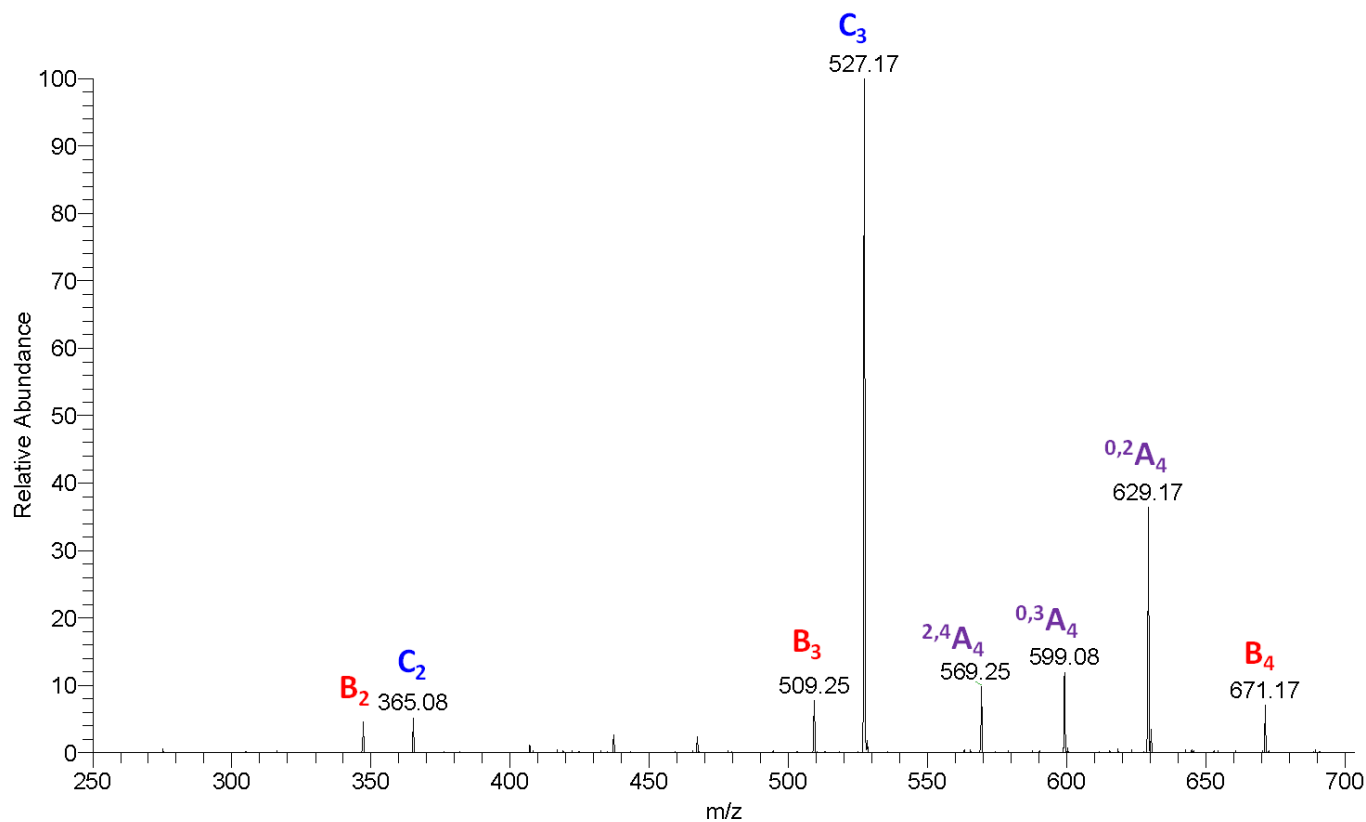


Figure 2-4. MS² Spectrum of [Glc₄+Na]⁺. Collision-induced dissociation of sodiated β-glucan ion labeled with Domon and Costello nomenclature of oligosaccharide fragmentation. The most abundant fragment ion, C₃ results from a glycosidic cleavage, a neutral loss of 162 Da. This corresponds with the mass of a glucose monomer. Also, a NL of 60, due to a ^{0,2}A₄ cross-ring cleavage is observed. Minor losses include other cross-ring cleavages, as well as the B₃ fragment ion.

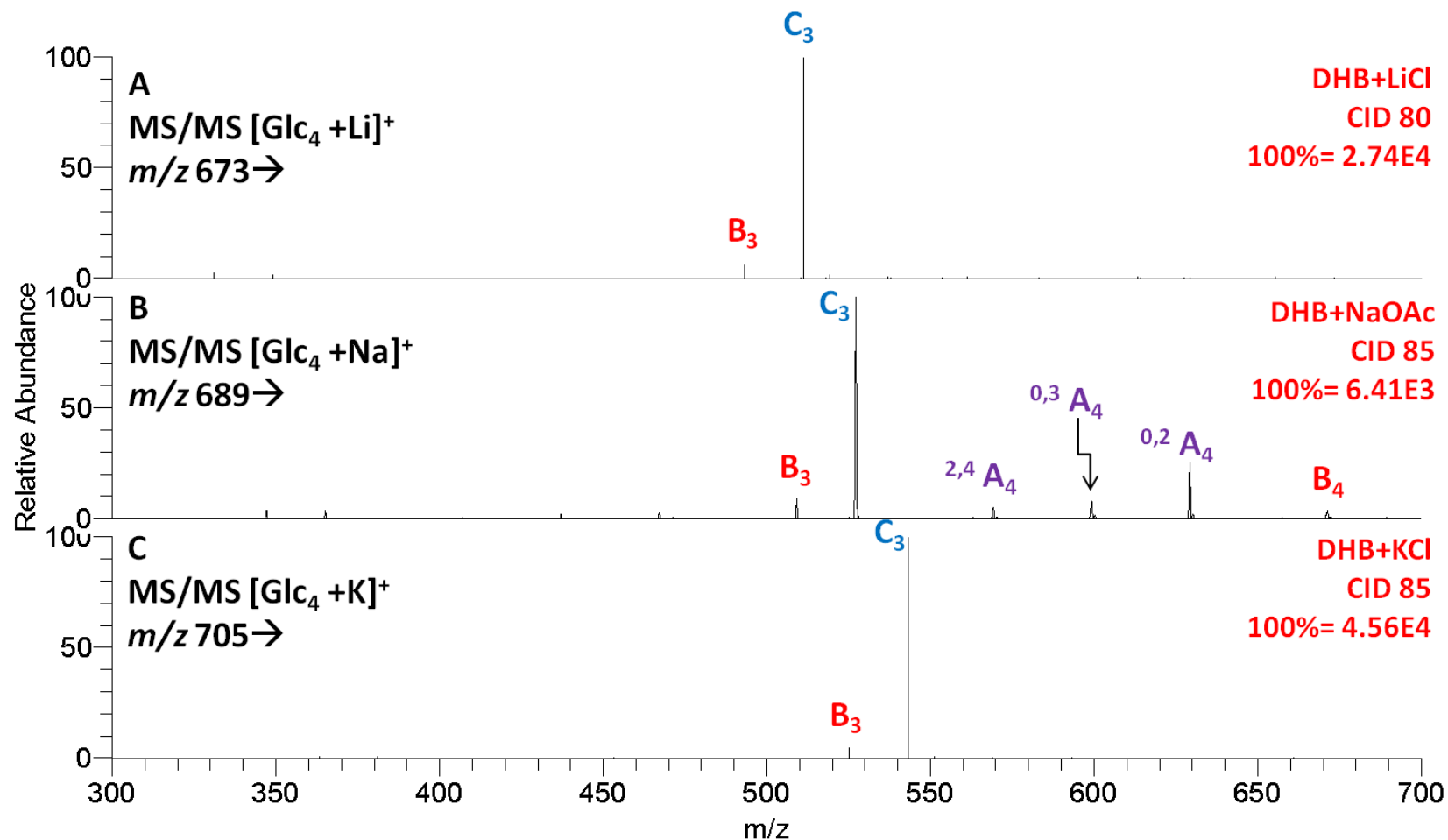


Figure 2-5. MS² spectra of different cationized β-glucan ions. A) Lithiated ion shows NL of 162. B) sodiated species shows NL 162 and cross-ring cleavage. C) potassiated ion shows NL of 162. The sodiated species offers increased fragmentation, which can aid in unknown ion identification.

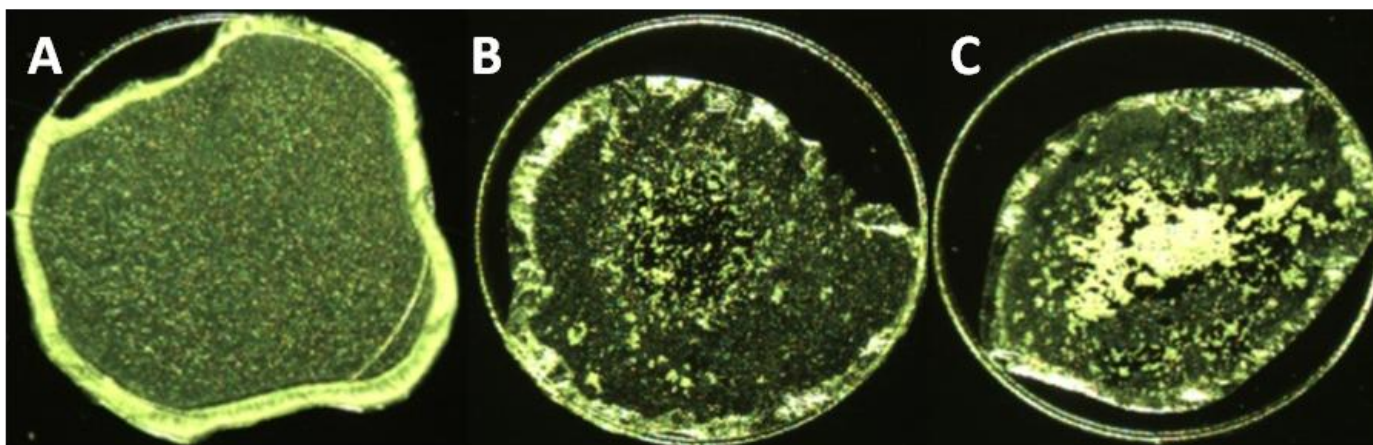


Figure 2-6. Optical images of MALDI sample spots. A) DHB and sodium acetate crystals, illustrating an ideal MALDI sample spot. For optimal MALDI analyses, the MALDI matrix crystals should be uniform. B) MALDI sample spot of MCC and DHB crystals. The sample spot shows inhomogeneous crystals, which causes poor reproducibility of mass spectra between laser shots C) MALDI sample spot of MCC, DHB and EDTA. EDTA caused an 'aggregation' of MCC, which made a region of homogenous spots, increasing MALDI ion signal reproducibility within that region.

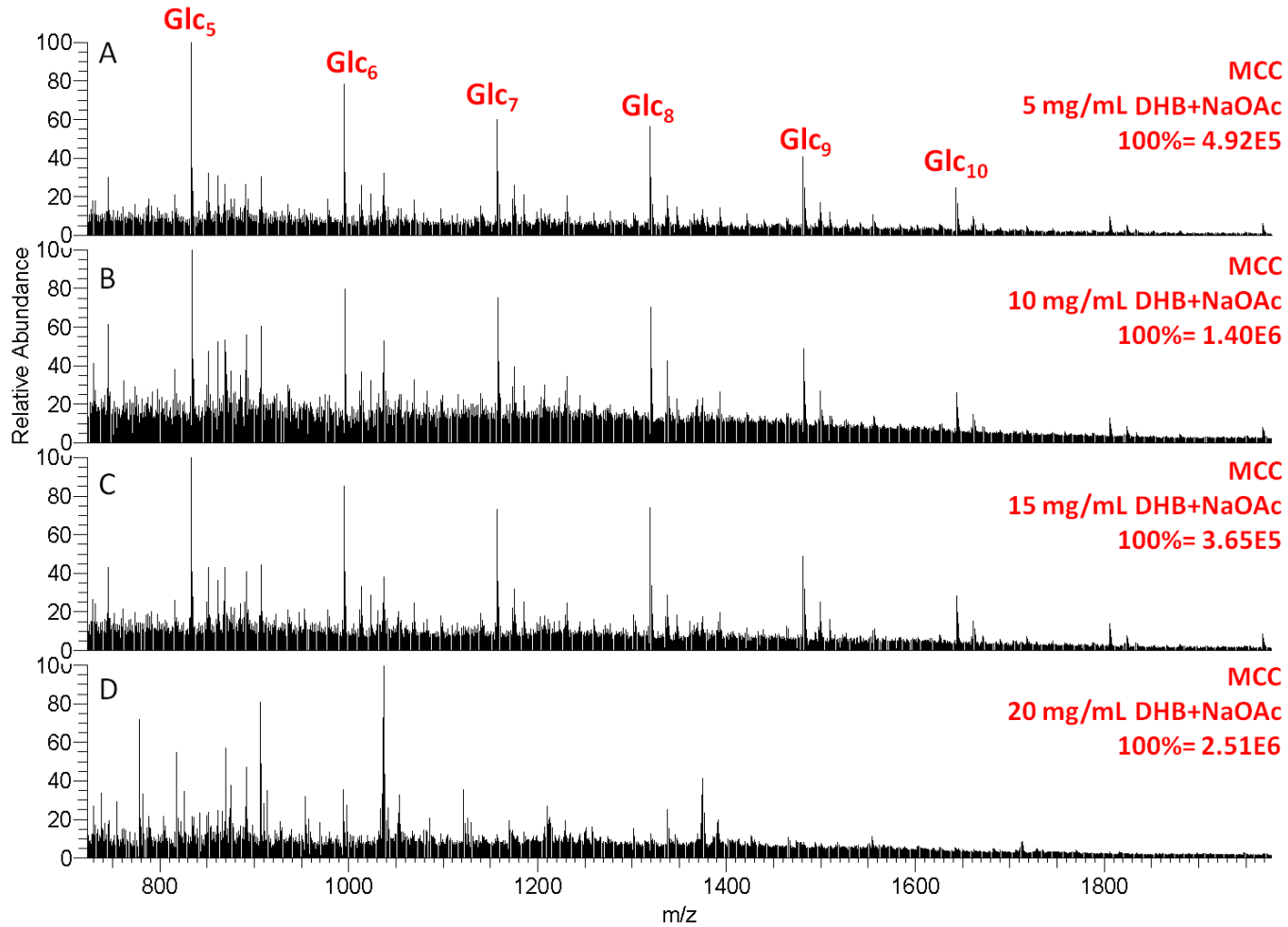


Figure 2-7. Comparison of MCC MS by varying DHB concentrations. A) 5 mg/mL DHB. B) 10 mg/mL DHB. C) 15 mg/mL DHB. D) 20 mg/mL DHB. Analyte ions labeled are in the form $[\text{Glc}_n\text{-H}_2\text{O}+\text{Na}]^+$. It was determined that 5 mg/mL DHB provided the highest signal to background for cellulose ions.

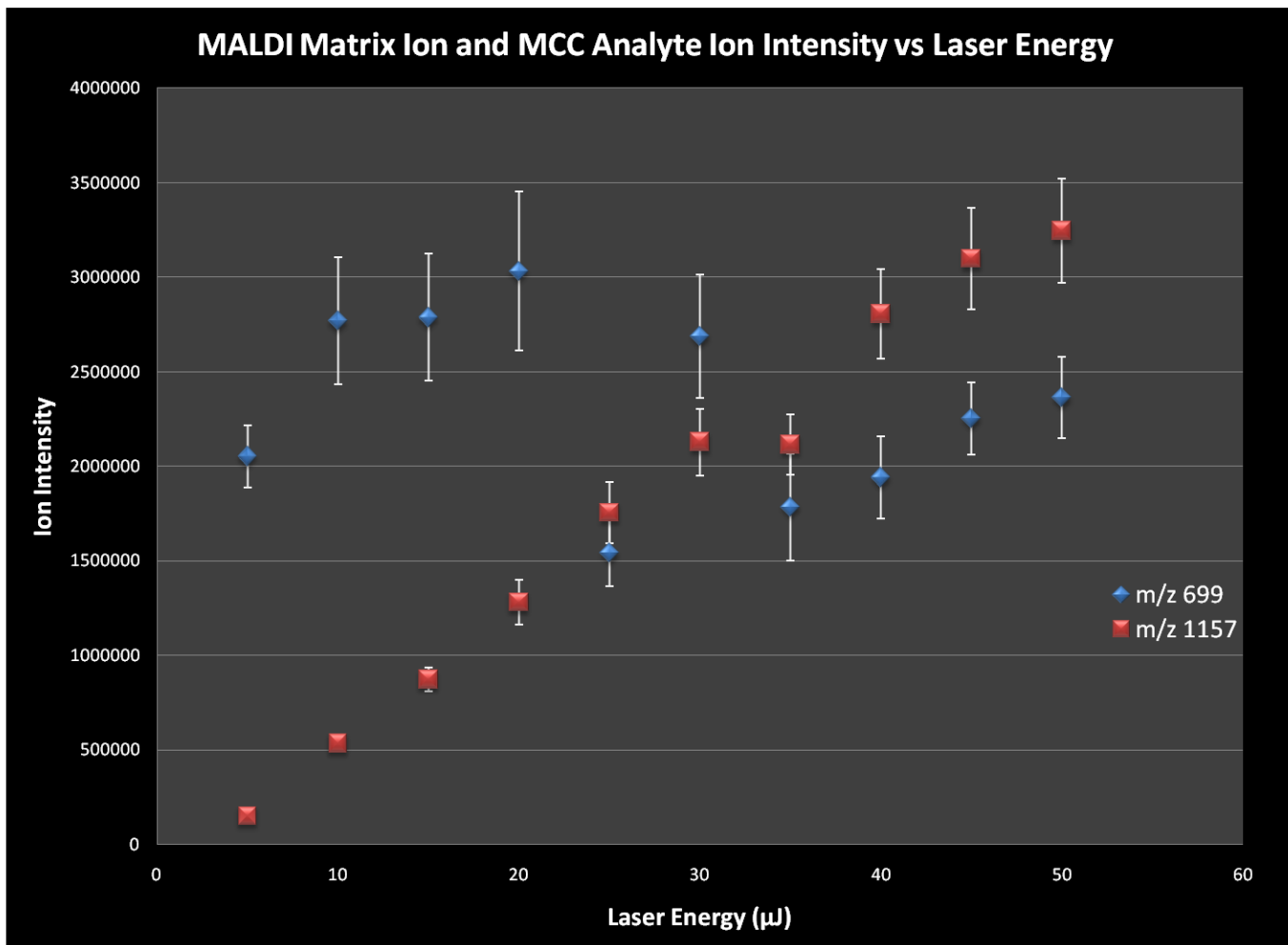


Figure 2-8. Plot of MALDI matrix and cellulose ion intensity versus laser energy. The plot illustrates the analyte ion intensity (m/z 1157) steadily increases with increasing laser energy. Above 30 μ J laser energy, the analyte to matrix ion signal is the highest, which is ideal for experiments. The error bars represent the standard deviation of the mean.

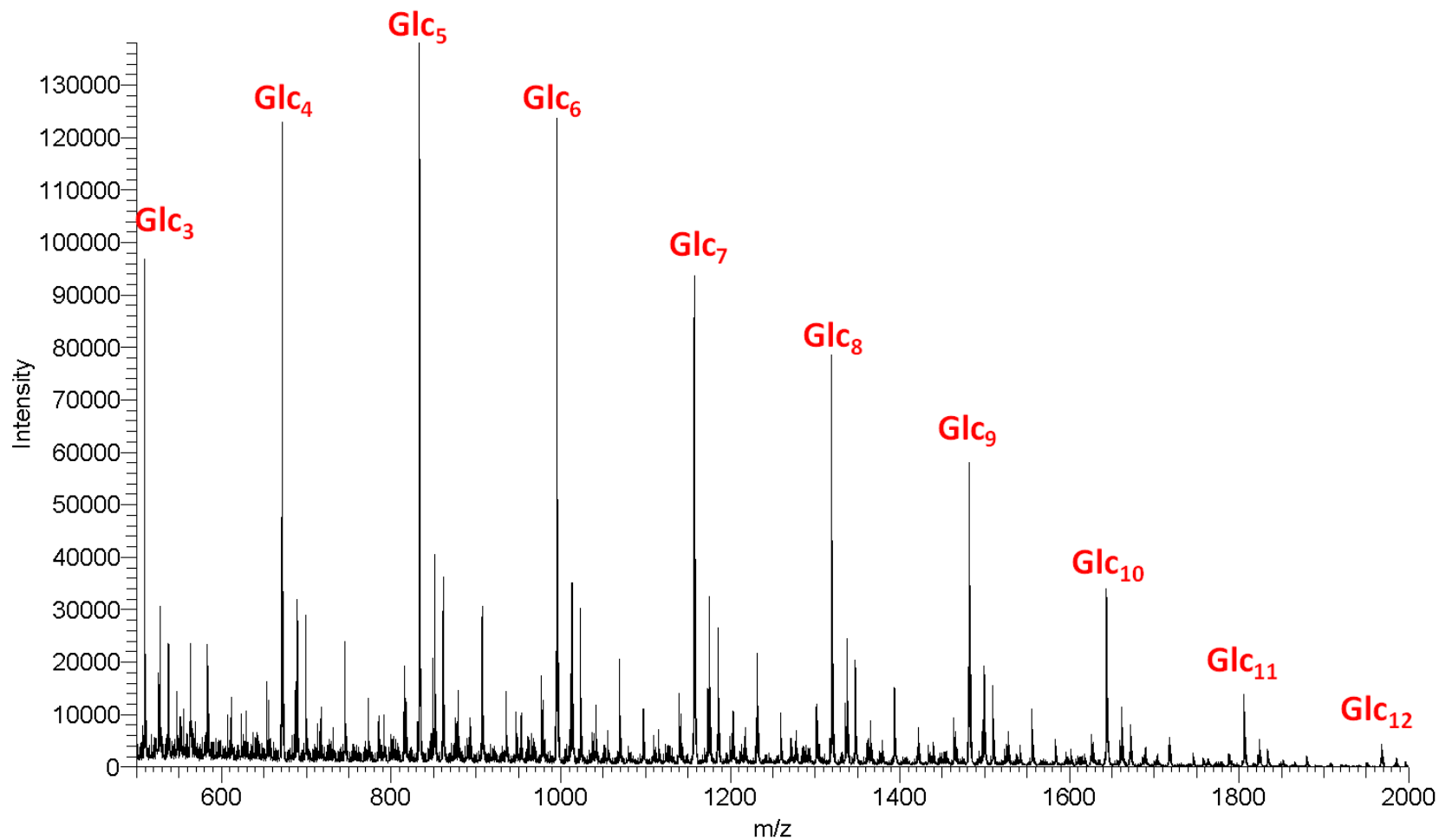


Figure 2-9. MS spectrum of MCC using optimized experimental parameters. Ions labeled are in the form $[\text{Glc}_n\text{-H}_2\text{O}+\text{Na}]^+$. The spectrum shows very low 'background ion' signal. Ions observed in between the majors ions are a repeating pattern, possible due to in-source fragmentation.

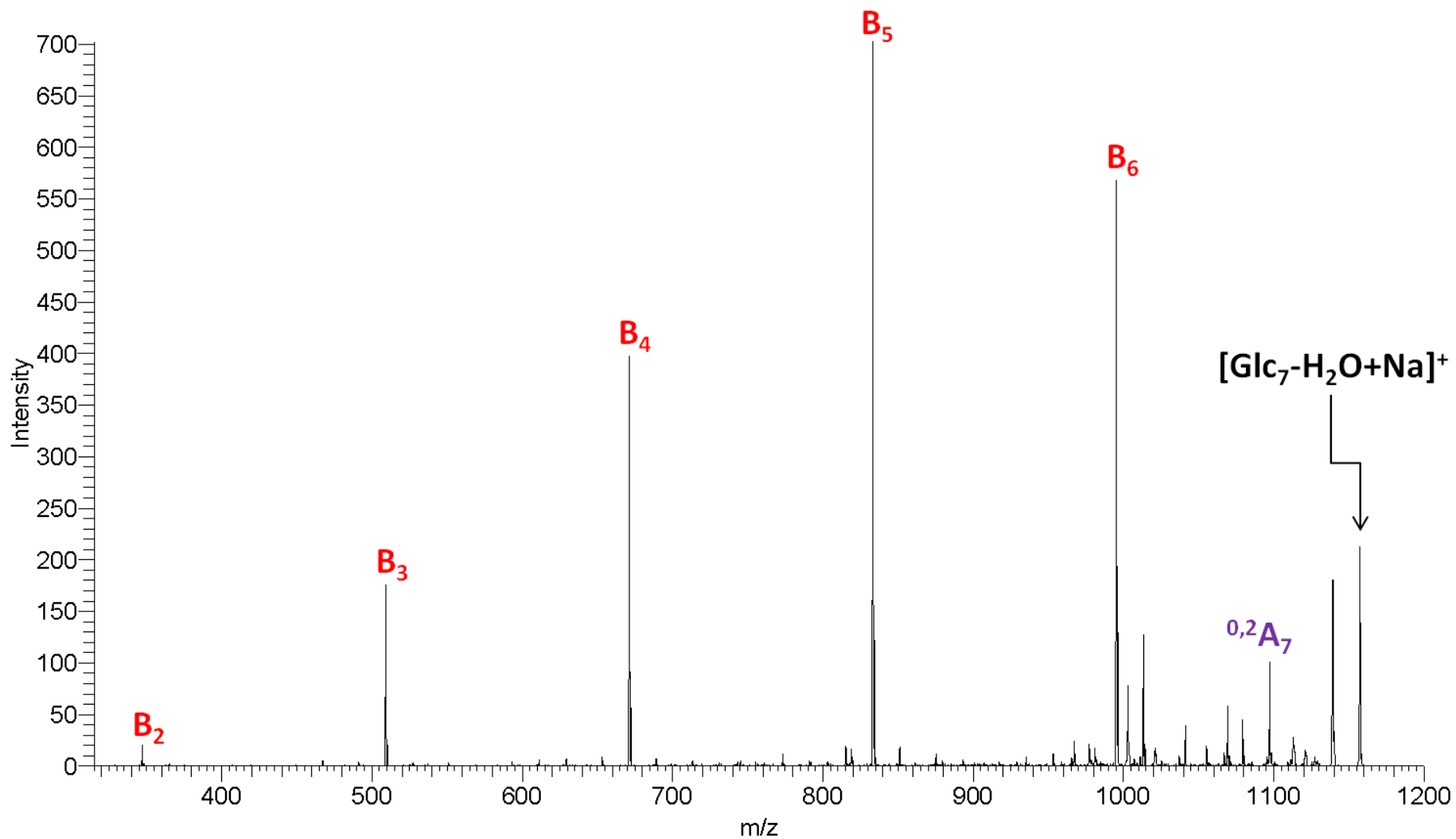


Figure 2-10. MS² spectrum of *m/z* 1157. Similar to the β-glucan standard, MS² of *m/z* 1157 ([Glc₇-H₂O+Na]⁺) results in cross-ring cleave and sequential NLs of 162, due to glycosidic bond cleavages.

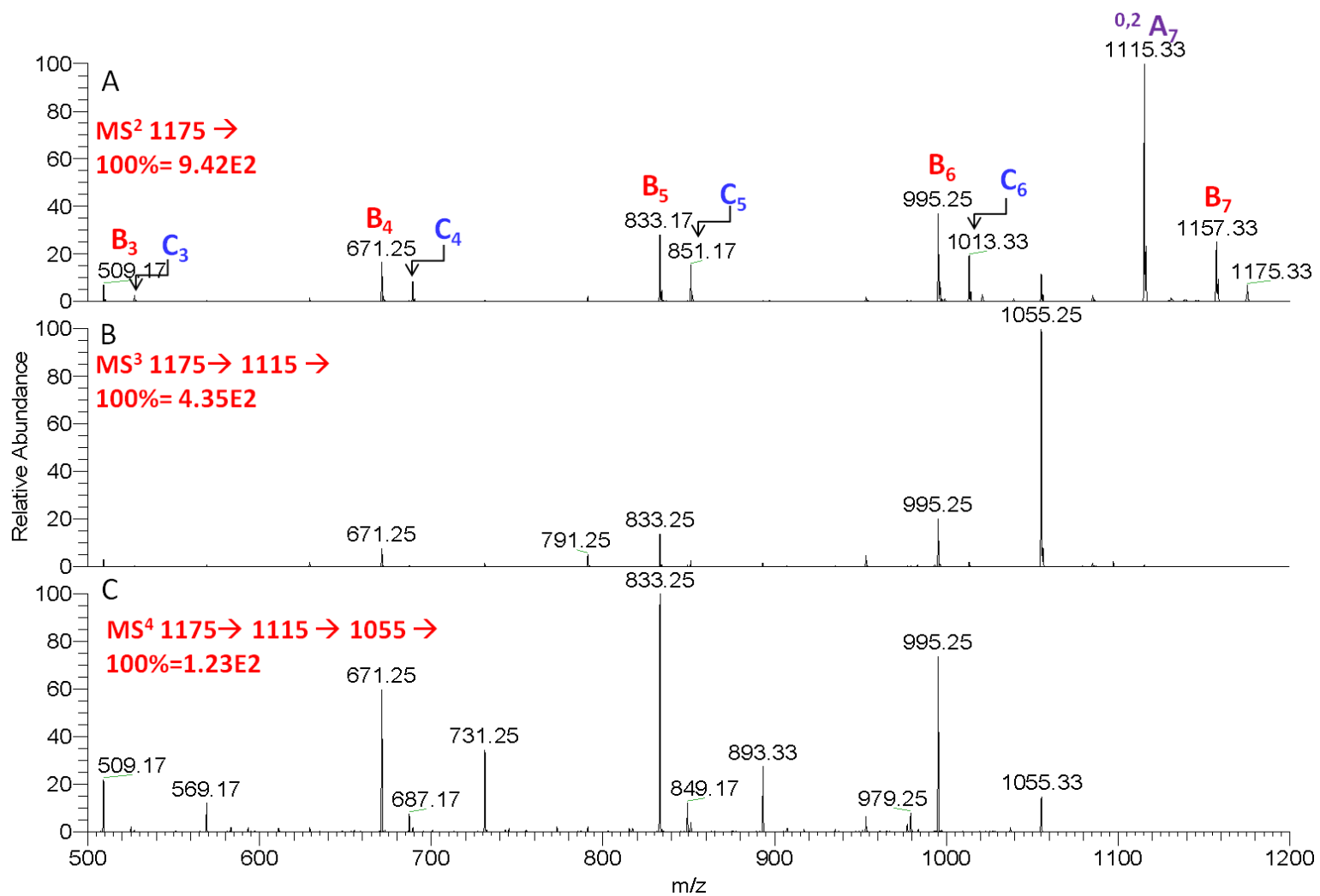


Figure 2-11. MS²–MS⁴ analysis of MCC. A) MS². B) MS³. C) MS⁴. The MS² of *m/z* 1175 ([Glc₇+Na]⁺) shows an abundant NL of 60, due to a cross-ring cleavage (top). The MS³ of 1175→1115, shows NL of 60, as well as NL of 120 (middle). MS⁴ of 1175→1115→1055 shows NL of 60, followed by NL of 162 were also observed.

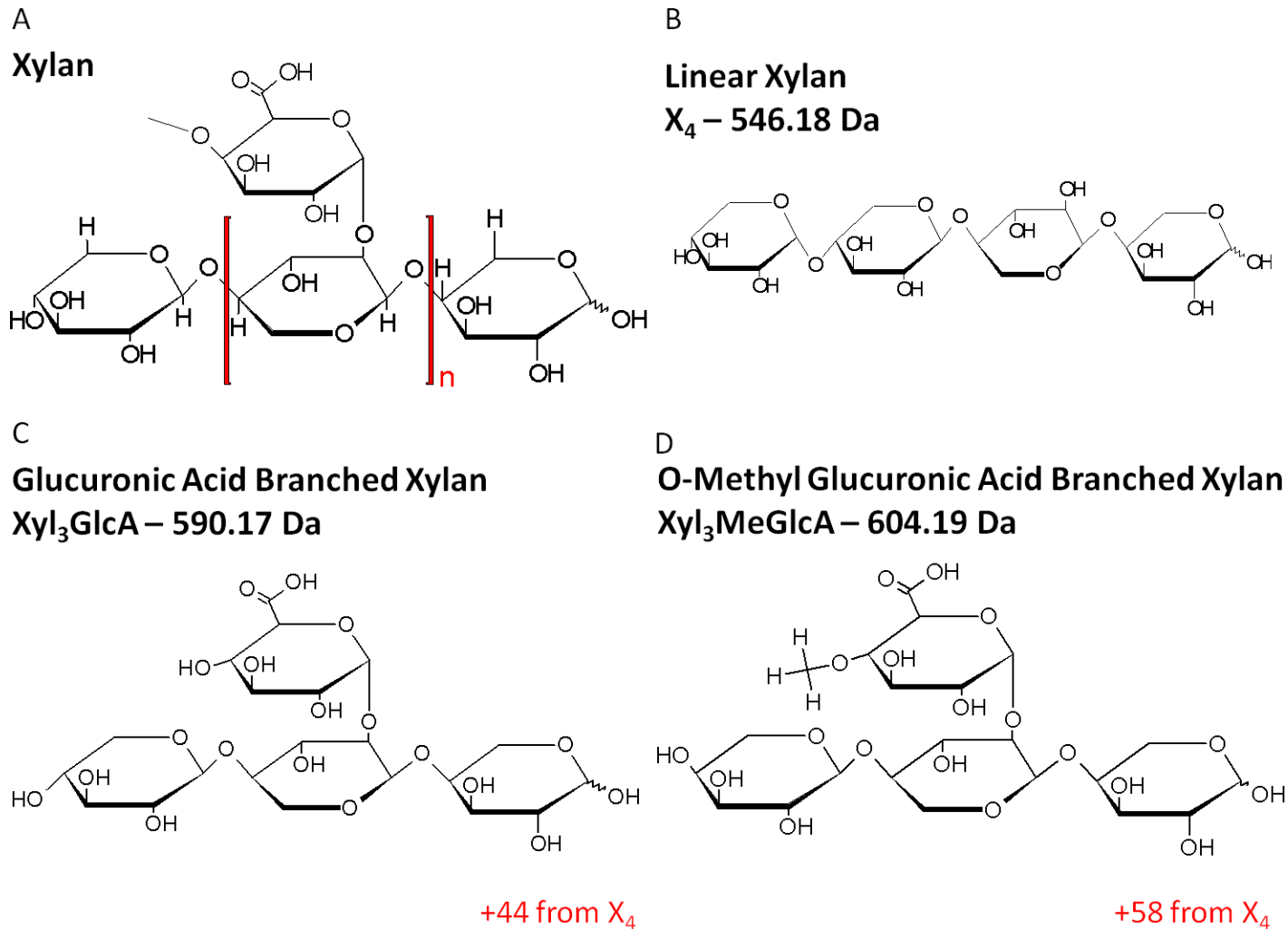


Figure 2-12. Common hemicellulose structures. A) Generic Xylan. B) Linear xylan. C) Glucuronic acid branched xylan. D) O-methyl glucuronic acid branched xylan. The most common substitutions include glucuronic acid and methyl glucuronic acid, which increase the mass of a linear xylan by 44 and 58 Da, respectively.

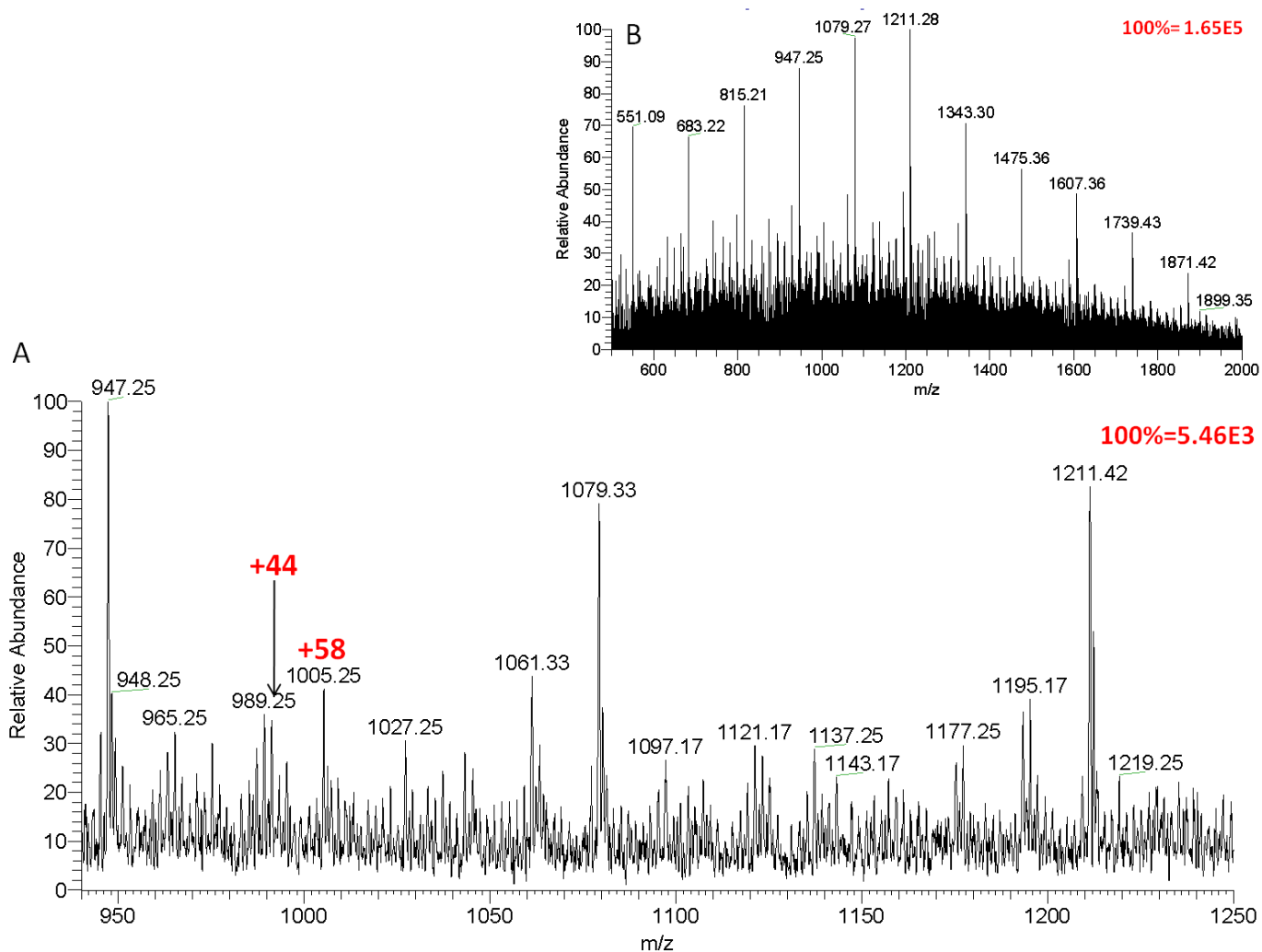


Figure 2-13. MS spectra of Birch Xylan extract. A) m/z 500–2000, with intense ions 132 amu (Xyl residue) apart, which were identified as linear xylan ions in the form, $[\text{Xyl}_n\text{-H}_2\text{O}+\text{Na}]^+$. Abundant ions in between the linear xylan ions are observed as a result of substituted xylans. B) m/z 945–1250, showing the predicted substituted ions were observed.

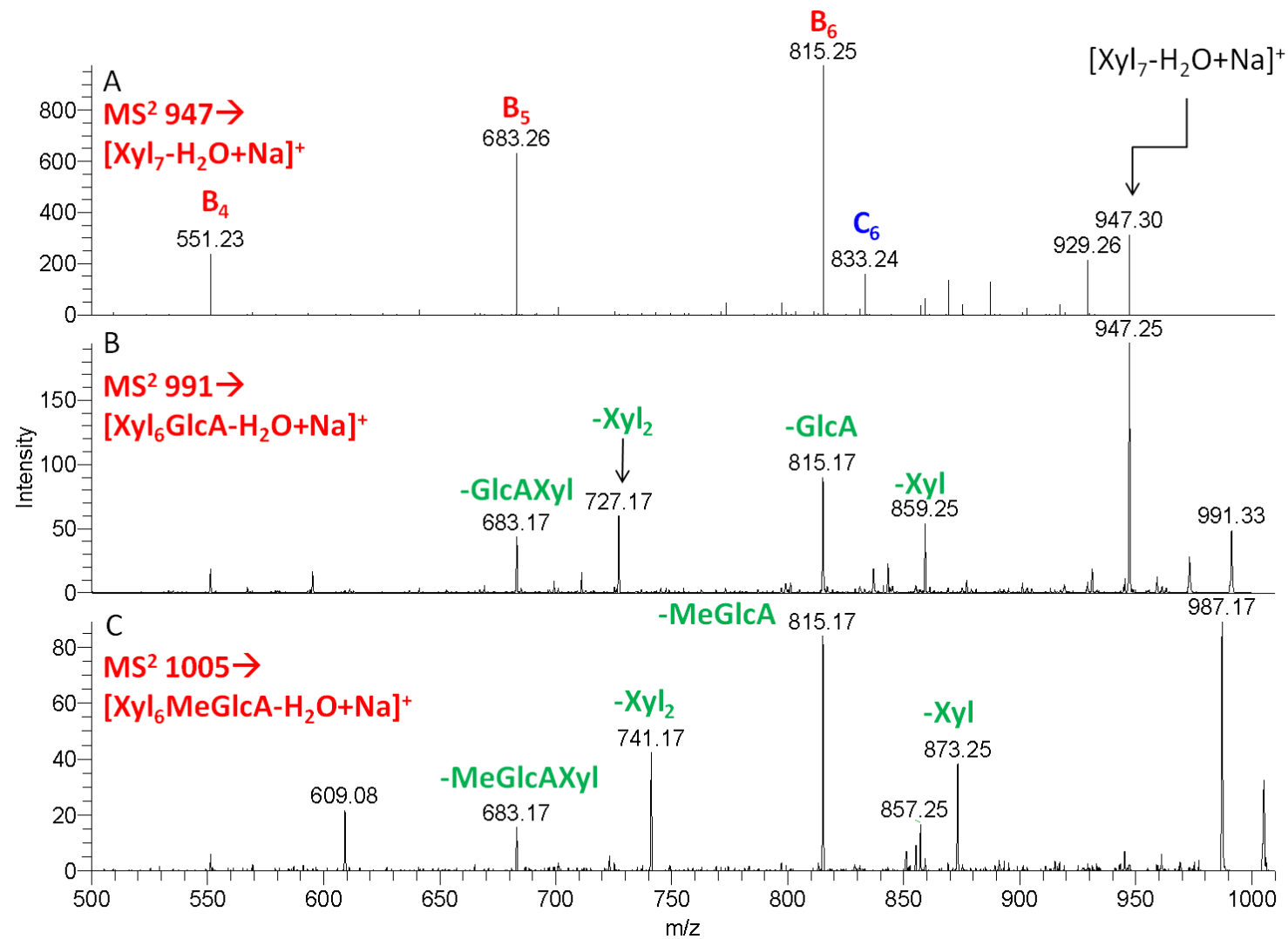
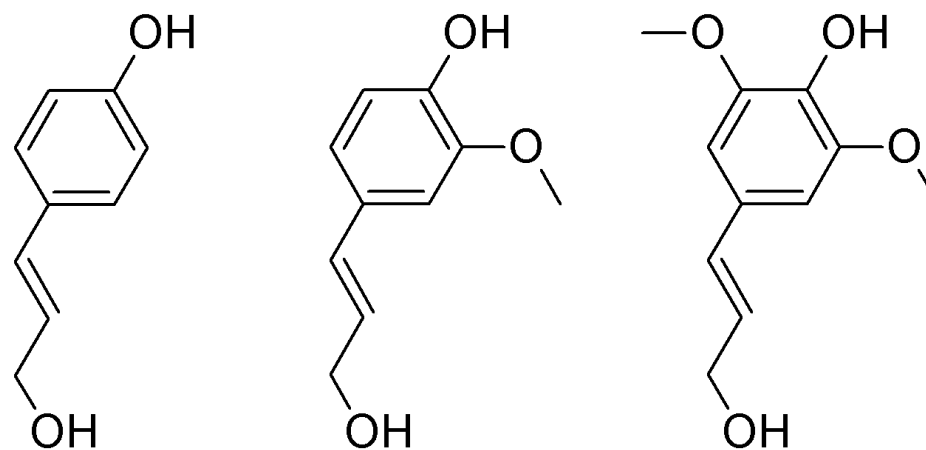


Figure 2-14. MS² analyses of xylans. A) MS² of linear xylan shows sequential NL of 132, xylose residues. B) MS² of GlcA substituted xylan. NL of 176 is indicative of GlcA substitution. NLs of 132 are also observed. C) MS² of MeGlcA substituted xylan. NL of 190 is indicative of MeGlcA substitution



p-Coumaryl Alcohol Coniferyl Alcohol Sinapyl Alcohol

150 g/mol

180 g/mol

210 g/mol

Figure 2-15. Common building blocks of lignin. Lignin is a complex, three dimensional polymer of monolignols, including coumaryl alcohol, coniferyl alcohol and sinapyl alcohol. The structure of monolignols is similar to common MALDI matrices.

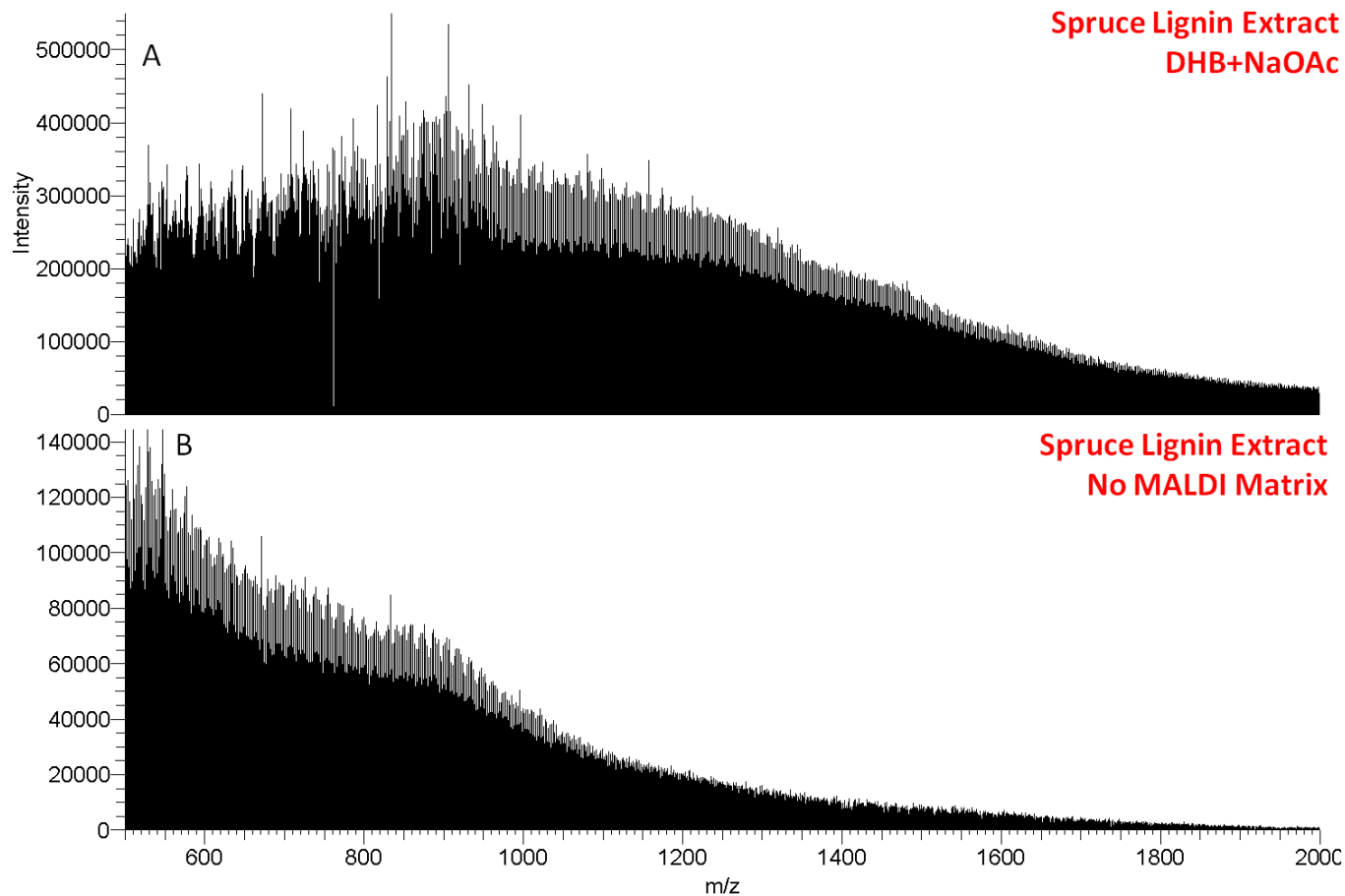


Figure 2-16. MALDI and LDI MS analysis of Spruce lignin extract. A) DHB+NaOAc for MALDI-MS analysis of lignin extract Abundant ions at nearly every m/z value are observed. B) MS without using MALDI matrix (LDI), showing lignin analyses can be performed without MALDI matrix. This is likely due to the highly aromatic monolignols absorbing at the wavelength of the N_2 laser.

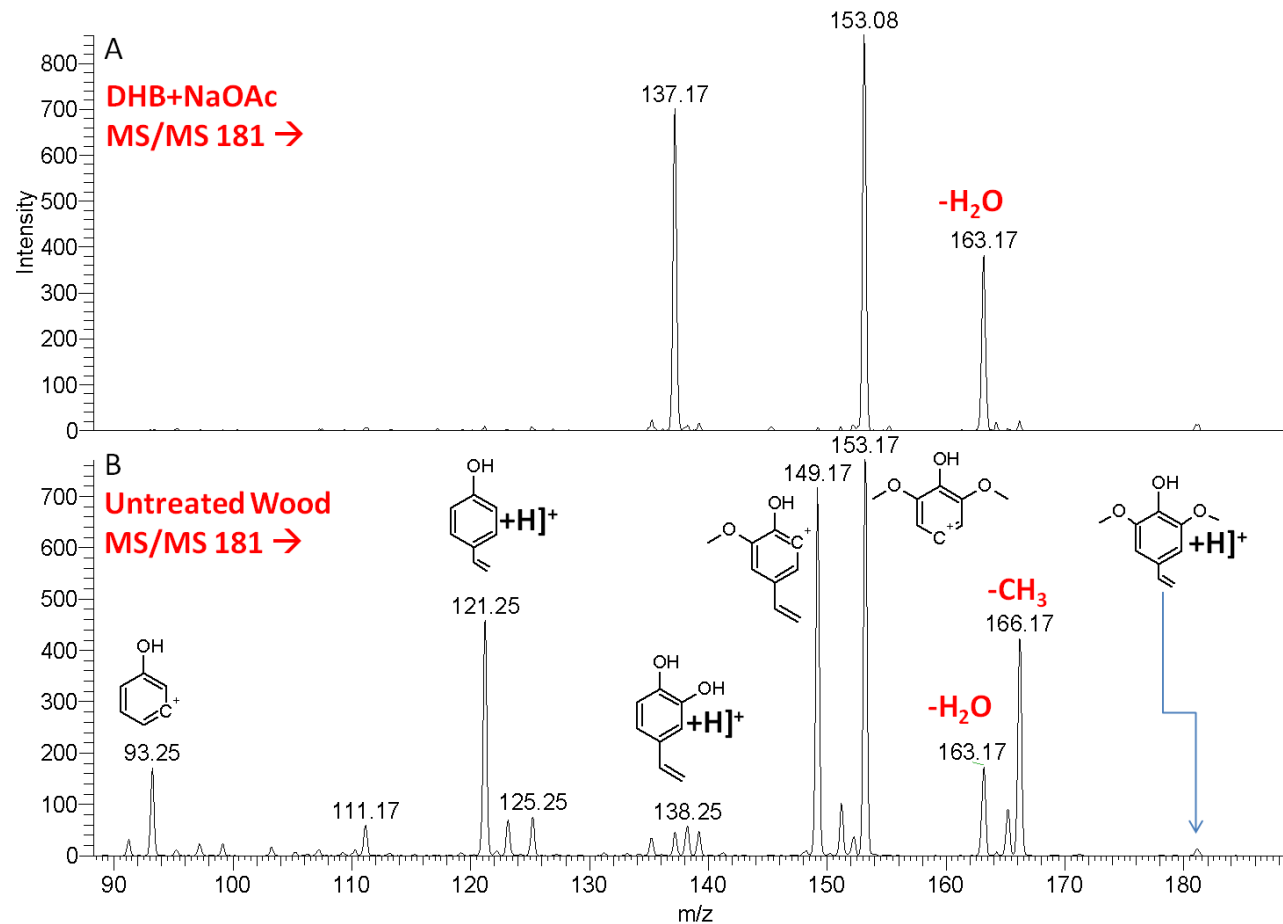


Figure 2-17. MS² analysis of *m/z* 181. A) DHB+NaOAc. B) Untreated wood tissue without MALDI matrix. MS² of DHB displays three major fragment ions. The bottom spectrum preliminarily identified *m/z* as vinyl syringol (a monolignol), with predicted fragment structures. Fragment *m/z* 121 could provide a diagnostic fragment for lignin.

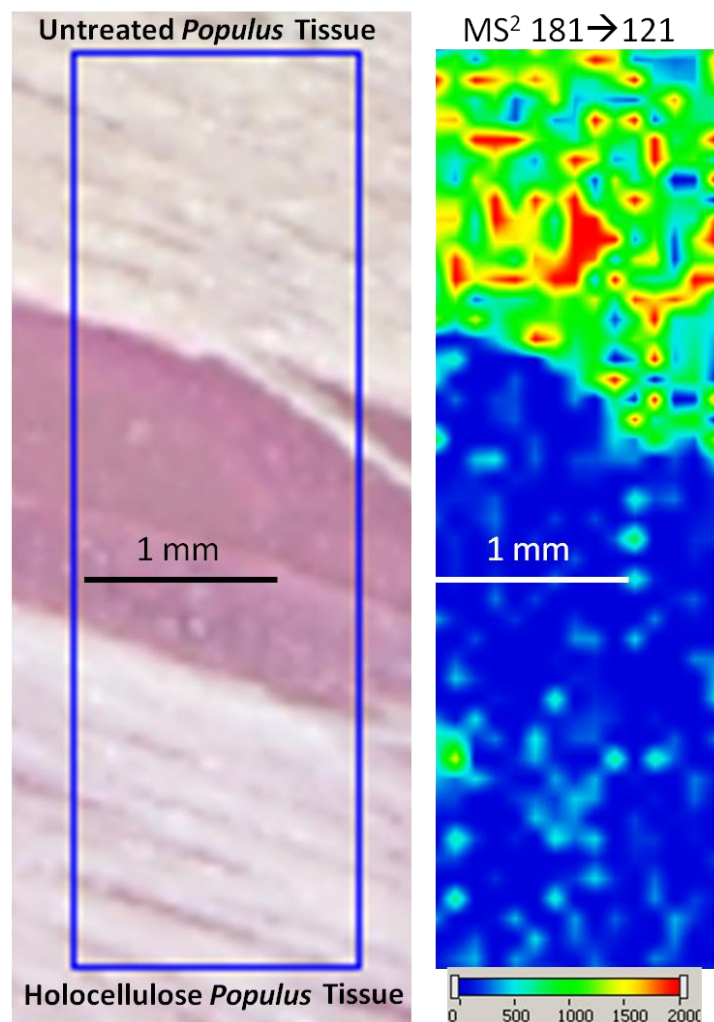


Figure 2-18. Optical and MALDI tandem MS image of untreated and holocellulose *Populus* tissue. Lignin is removed from holocellulose. MS² analysis of m/z 181 \rightarrow 121 illustrates ion signal only from untreated *Populus* tissue.

Table 2-1. List of hypothesized cellulose ion m/z values to monitor in wood tissue.

Number of Glucose Residues	Molar Mass (g/mol)	Hypothesized m/z $[\text{Glc}_n\text{-H}_2\text{O}+\text{Na}]^+$
3	504	509
4	666	671
5	828	833
6	990	995
7	1152	1157
8	1314	1319
9	1476	1481
10	1638	1643
11	1801	1805
12	1962	1967

CHAPTER 3 DIRECT MATRIX-ASSISTED LASER DESORPTION/IONIZATION MASS SPECTROMETRIC IMAGING OF CELLULOSE AND HEMICELLULOSE IN *POPULUS* TISSUE

Introduction

In recent years, alternative energy research has garnered significant attention, particularly research focused on biofuel produced from plant 'waste' or lignocellulosic biomass.^{3,100-102} Unlike the simple sugars and starch of sugar-cane and corn grain, the complex arrangement of cellulose, hemicellulose and lignin in plants naturally resist enzymatic digestion and limits bioconversion of biomass into biofuel.^{100,103} In bioconversion methods, a pretreatment step is performed to overcome some of this natural recalcitrance by increasing accessibility of the cellulose to cellulase digestion, particularly at high enzyme loadings.¹⁰⁰ Despite the success of current pretreatment methods, most are conducted with size-reduced materials to remove anatomical differences. Due to high energies (and cost) required for size-reduction, particularly for woody biomass, the use of larger fragments (e.g., wood chips) is preferred for commercial processes,^{3,101} but the spatial changes in chemical composition in pretreated wood chips are not well characterized.¹⁰² The ability to map spatial changes in chemical compositions within wood tissue should provide valuable information that can be used to improve the efficiency of lignocellulosic bioconversion to biofuel.¹⁰³

A variety of techniques are used to image lignocellulosic material, including optical microscopy with stains, ultraviolet microscopy,²⁰ magnetic resonance imaging (MRI),²¹ micro X-ray computed tomography (μ X-Ray CT),²² confocal Raman microscopy,^{23,24} scanning electron and transmission electron microscopy. Although these techniques provide structural information, their molecular selectivity is quite limited. One approach

that helps to overcome this lack of molecular specificity is mass spectrometry, specifically, time-of-flight secondary ionization mass spectrometry (ToF-SIMS)⁵³ and matrix-assisted laser desorption/ionization time-of-flight mass spectrometry (MALDI-ToF-MS).¹⁰⁴ In addition to molecular selectivity, ToF-SIMS and MALDI-MS are capable of MS imaging experiments.^{53,85,105,106} Despite widespread applications reported for these techniques in animal studies,⁵⁴ ToF-SIMS and MALDI-MS have only recently been used to analyze lignocellulosic compounds.¹⁰⁷⁻¹¹²

SIMS analyzes secondary ions emitted from a surface, which are characteristic of compounds within a sample.^{53,105} ToF-SIMS images of wood tissue and switchgrass have obtained spatial resolution down to 1 μm , the highest spatial resolution offered by MS imaging.¹¹² Although ToF-SIMS imaging provides direct surface analysis and high spatial resolution, extensive analyte fragmentation during ionization limits the chemical specificity.²⁶ Because many plant cell wall carbohydrates are complex and composed of closely related building blocks, e.g., glucose ($\text{C}_6\text{H}_{12}\text{O}_6$), xylose ($\text{C}_5\text{H}_{10}\text{O}_5$), glucuronic acid ($\text{C}_6\text{H}_{10}\text{O}_7$), and methyl glucuronic acid ($\text{C}_7\text{H}_{12}\text{O}_7$), SIMS ionization of different carbohydrates often results in non-specific fragmentation, complicating interpretation.

MALDI is a soft ionization method used to generate biomolecular ions for mass spectrometry¹¹³ and MALDI-ToF-MS has been applied toward lignocellulosic biomass analyses;¹¹¹ however, the molecular specificity of ToF-MS is limited. Due to the similarities of lignocellulosic composition compounds, ions of different analytes are observed at the same nominal mass-to-charge ratio (m/z) (isobaric ions). Tandem mass spectrometry (MS/MS) can overcome this difficulty by dissociating precursor ions and using fragmentation to distinguish between isobaric ions, thereby increasing confidence

in ion identification.^{65,85} Herein, we report direct imaging of cellulose and hemicellulose in intact wood tissue using MALDI-LIT tandem MS.

Experimental

Instrumentation and Data Analysis

All MS experiments were performed using a Thermo MALDI-LTQ XL mass spectrometer (Thermo Fisher Scientific, San Jose, CA), equipped with a nitrogen laser (LTB Lasertechnik Berlin, 337 nm, 60 Hz) with approximately 100- μ m diameter laser spot size. The samples were analyzed at intermediate pressure (70 mTorr). Mass spectra were analyzed using Qual Browser v.2.0.7 and MS images were generated with Image Quest v.1.0.1 (Thermo Fisher Scientific, San Jose, CA).

MALDI Matrix

DHB (99% pure) was purchased from Acros Organics (Geel, Belgium). Although the concentration used for the standards was 5 mg/mL, higher MALDI matrix concentrations are needed for intact tissue section analysis. The MALDI was prepared at 25 mg/mL DHB dissolved in 0.05 mM aqueous sodium acetate (NaOAc).

Wood Samples

One of the difficulties of intact wood tissue analysis is mounting the sample onto the sample plate (or glass slide). Animal tissues are sections while still frozen, and can be thaw-mounted onto a glass slide with the gentle heat of a finger. However, this cannot be done with wood tissue section. The wood tissue does not stick to the microscope slide and also has a tendency to curl on itself. Also, if the wood did stick to the microscope slide, applying the matrix re-wets the sample, thus removing it from the sample plate and curling the edges.

Another obstacle is the 'rigidity' of wood tissue itself, which makes microtome sectioning very difficult. For optical microscopy studies of wood tissue, a tape is mounted directly onto the top of the wood tissue prior to cutting, serving as a 'tape backing.' The section is then sliced, and thus mounted onto the tape. The tape works well to keep the tissue intact, flat and on the sample slide for analysis. However, due to the molecular selectivity (and sensitivity to contamination of sample surfaces), it was possible that the adhesive from the tape could seep through the wood tissue and ionize more readily over the wood compounds. To avoid contamination, great care was taken to ensure the sample surface remained free of the adhesive of the tape. Experiments comparing the ion signal obtained from the tape with MALDI matrix versus the ion signal from the wood tissue with MALDI matrix clearly displayed no contamination problems. Thus, it was determined mounted the wood tissue sections onto tape would provide the highest quality wood tissue sections and highest quality mass spectra.

Untreated, radial pine wood samples were sectioned to ~ 30- μm thickness using a Leica crytome (Instrumedics, Inc., Richmond, IL #475214). and mounted onto a tape. The tape was then mounted onto a glass microscope slide for analysis.

Small wood blocks, 1 cm x 1 cm x 1 cm, were cut from a field-grown, three year-old stem of *Populus deltoides*, and 50- μm thick radial sections were cut on a sliding microtome (Lieca, SM2010R). In a subset of sections, the lignin was removed with sodium hypochlorite treatment⁹⁴ to produce holocellulose. For tissue imaging, the lower stem regions from 10-week-old greenhouse-grown *Populus deltoides* X *Populus trichocarpa* X *Populus deltoides* hybrids were sectioned with a vibratome (Lieca,

VT100S) to obtain 50- μm thick transverse sections. All sections were mounted on CryoJane[®] tape (Instrumedics, Inc., Richmond, IL #475214) prior to analysis.

MALDI Matrix Coating

The MALDI matrix (DHB) was applied to the tissue with a Meinhard nebulizer—the tissue was sprayed for approximately 30 seconds, followed by a 4 minute drying time aided with a warm air stream. This process was repeated until a white crystal layer was observed atop the wood tissue (~8 mL of matrix solution). MS images were generated by rastering the tissue underneath the laser in 50- μm step sizes, using three laser shots per spot and 35 μJ and 40- μJ laser energy for MS and MS² analyses, respectively. A 15 x 15 mm rectangle was imaged at a rate of 131 scans per minute for both MS and MS². The MS² experiments on tissue sections were performed using the same CID energy and isolation width as the standard experiments.

Results and Discussion

Pine Wood Samples

The average of 1549 spectra from m/z 500–2000 of a pine wood sample is illustrated in Figure 3-1. The average spectrum shows abundant ions at nearly every m/z , which was likely due to lignin ion signal. In addition, ions 162 m/z units apart, consistent with the m/z values from MCC standard analysis, confirming that cellulose was observed from the intact wood tissue. It is interesting to note that the average spectrum from the first 180 scans versus the last 180 scans is different (Figure 3-2). The first 180 scans shows ions at nearly every m/z value at similar relative abundances—the last 180 scans displays more signal from the ions identified as MCC. The different spectra correlate well with the different tissue types observed in the optical image (Figure 3-1), which likely have different compositions of cellulose, hemicellulose

and lignin. The difference in MS spectra demonstrates that MS imaging is capable of distinguishing between differences in chemical composition. To investigate different tissue types further, cross sections, which contain various regions of tissue types, were examined.

Tandem MS of Young *Populus* Stem Tissue

To confirm the identity, tandem MS of ions observed from wood tissue were compared with the tandem MS of MCC and xylan standards. MS² analyses of the four most abundant ions observed from wood tissue, *m/z* 833, 995, 1157, and 1319 ([Glc₄₋₇-H₂O+Na]⁺), were compared to MS² of the same ions of the MCC standard. The MS² spectra from both wood tissue and MCC standard displayed major fragment ions resulting from glycosidic bond cleavages (sequential NLs of 162), which confirmed cellulose was observed from wood tissue. The MS² spectra of *m/z* 833, 995, and 1157 displayed an NL of 154 (molecular weight of DHB), suggesting a DHB cluster ion at the same nominal *m/z*, thus *m/z* 1319 was used for further cellulose analysis on wood tissue.

The comparison of MS² of 1319 of the MCC standard with the spectrum from untreated wood tissue is displayed in Figure 3-3. As expected, both spectra show similar fragmentation—the major fragment ions (*m/z* 1157, 995, 833, 671, and 509) result from successive NLs of 162, due to glycosidic bond cleavages. Although the major fragment ions of MCC and untreated wood tissue are similar, *m/z* 1319→1301 and 1319→1275, NLs of 18 and 44 respectively, are more abundant in the MS² spectra from wood tissue. The NL of 18 is likely due to a loss of water and is a non-specific loss, i.e., most ions with an –OH group can lose water during collision-induced dissociation in the ion trap. The NL of 44 from *m/z* 1319 suggests the presence of an acetyl or

carboxylic acid functional group, which is common for carbohydrates other than cellulose present in wood tissue. Thus, the greater abundance of these fragment ions observed in the MS² spectrum of untreated wood tissue strongly suggests the presence of at least two isobaric ions at m/z 1319.

Figure 3-4 displays the MS² spectra of m/z 1079 from purchased Birch xylan and *Populus* wood tissue. Sequential NLs of 132 are observed in the MS² of m/z 1079 of xylan standard, resulting from glycosidic bond cleavages between xylose monomers—this ion was identified as $[\text{Xyl}_8\text{-H}_2\text{O}+\text{Na}]^+$. The MS² spectrum of m/z 1079 from *Populus* tissue shows m/z 1079→917 (NLs of 162) and 1079→875 (NL 204), in addition to m/z 1079→847 (NL of 132). Since these fragment ions are not observed in the standard, at least two isobaric ions are likely present at m/z 1079. Further stages of MS determined that in addition to the linear xylan, another ion is of the form, $[(162)_4(204)_2+\text{Na}]^+$ and preliminarily identified as an O-acetylgalactoglucmannan (another classification of hemicellulose). However, analyses of additional standards, such as galactoglucmannan are needed to confirm this preliminary identification more positively.

MS and Tandem MS Imaging of Young *Populus* Stem Tissue

MALDI-LIT-MS imaging of the young polar stem was performed on a quarter section of the *Populus* stem, to ensure all different regions of the tissue section were examined. Optical, MS and MS² images of a transverse section of young *Populus* stem are displayed in Figure 3-5 and Figure 3-6. The white dotted line in the optical image (a) illustrates the region of MS analysis. The pith is located in the center of the stem and is composed of thin, non-lignified, primary-walled cells. The secondary xylem extends from the pith to the vascular cambium and is composed of living ray parenchyma, as

well as nonliving, lignified, fiber and vessel cells with thickened secondary walls. The vascular cambium is a thin layer (~50 μm) of living tissue between the secondary xylem and secondary phloem where new cells are produced for secondary, or radial, growth. The secondary phloem is composed of living, primary walled parenchyma and companion cells, as well as dead sieve and fiber cells with thickened secondary walls. In contrast to the sieve cells, the fiber walls are lignified.

Abundant ion signal at nearly every m/z value was observed for all the regions; however, different regions displayed characteristic spectra. For example, around the mass spectra from the pith and the secondary xylem, where most live tissue is found, displayed ions at every m/z value at 50% or greater relative abundance. On the other hand, abundant ions 162 Da apart (corresponding to ions observed in the MCC standard) were observed above the background ion signal in the secondary xylem and the center of the phloem. These general differences in the observed spectra were attributed to characteristics of the different tissues present in the different regions of *Populus* stem probed. Although MS analyses are capable of discerning general differences in regions of wood tissue, tandem MS increases the molecular specificity of the experiment to analyze specific analytes in the different regions of wood tissues.

The extracted ion MS image of m/z 1319, identified with standards as a cellulose ion $[\text{Glc}_7\text{-H}_2\text{O}+\text{Na}]^+$, displays uniform ion signal over all tissue regions of the *Populus* wood stem (Figure 3-5b), which is expected for a cellulose ion. Interestingly, the thin, primary walled cells of the pith and intact vascular cambium (arrow) have similar intensity as the secondary xylem and phloem tissues, even though they are known to contain relatively less cellulose.

The MS² images of m/z 1319→1275 and 1319→995, resulting from NL of 44 and two sequential NLs of 162 (Glc monomers) from the precursor ion, (m/z 1319) are displayed in Figure 3-5c and Figure 3-5d, respectively. Figure 3-5c displays more ion signal in the gap around the pith, lacking cells, and the secondary phloem. On the other hand, the MS² image of m/z 1319→995 shows a negative image of m/z 1319→1247. Specifically, m/z 1319→995 illustrates intense ion signal in the center region of the pith with cells, the secondary xylem, and small localized regions in the secondary phloem, which could correspond to fiber bundles.

The other regions, the vascular cambium and secondary phloem without fiber bundles, display less abundant ion signal. Furthermore, the m/z 1319→995 ion signal closest to the pith, which corresponds to older xylem tissue in the sample, suggesting this region could have thicker cell walls, thus increased cellulose composition. However, the difference in cellulose ion signal variation due to inhomogeneous crystal formation atop the wood tissue needs to be ruled out. As previously discussed, the MS² spectrum of *Populus* wood tissue suggests at least two isobaric ions at m/z 1319. This was confirmed by comparing the MS image of m/z 1319 with the drastically different MS² images obtained from plotting m/z 1319→1247 and m/z 1319→995.

The comparison of m/z 1079 (standard analysis identified as a linear xylan ion, [Xyl₈-H₂O+Na]⁺) MS with the MS² images also exemplifies the necessity of tandem MS for wood tissue analyses. Specifically, tandem MS is needed to distinguish between different hemicellulose ions or other interfering ions at the same nominal m/z . The extracted ion MS image of m/z 1079 shows nearly even ion signal over the entire tissue section (Figure 3-6). MS² images of two fragment ions, m/z 947 (NL of 132, 5-carbon

sugar), and m/z 917 (NL of 162, 6-carbon sugar) illustrate different ion intensities in different regions of the stem tissue.

The MS² image of m/z 1079→947 (Figure 3-6b) shows higher ion signal localized in the secondary xylem closest to the pith (similar to the cellulose ion intensity), also consistent with the hypothesis that this region contains thicker cell walls. A localization of m/z 1079→947 is also observed in the secondary phloem and vascular cambium, which is different from the observed cellulose signal. Although no xylan is located in the vascular cambium, this region is thinner than the spatial resolution of the imaging experiment. The MS² image of m/z 1079→917 (Figure 3-6d) shows localized ion intensity in the region of the secondary xylem closest to the pith, but less intense ion signal is observed in the secondary phloem compared to the MS² image of m/z 1079→947. Moreover less signal is observed around the pith, which further demonstrates the need for tandem MS to obtain accurate spatial distributions of ions at a single m/z .

As discussed in Chapter 2, performing MS² on m/z 181 could be used to identify the presence of lignin. Figure 3-7 displays the optical image and MS² images of m/z 181→163 (NL 18) and m/z 181→121 (NL 60). The localization of the non-specific NL 18 shows ion signal over the entire tissue section. This was expected since NL of 18 is a non-selective loss. The image of m/z 181→121 shows ion signal localization in the secondary xylem, the center of the pith and small regions in the secondary phloem. The localization of the ion signal is similar to distribution of cellulose. Since lignin is typically present in the secondary cell walls, which contain more cellulose than primary cell walls, it was expected that the lignin ion signal would show a similar distribution to the

cellulose ion signal. Comparing the two different MS² images also demonstrates that tandem MS can distinguish between two different ions at the same nominal *m/z*. Lignin compounds are similar in structure (thus *m/z*) to MALDI matrix ions, thus it is necessary to use tandem MS to increase the selectivity of the experiment.

Although a complete chemical composition analysis of all the regions of wood tissue was not completed, the experiments show the viability of MALDI-MSⁿ imaging of cellulosic tissue. More specifically, MS alone is incapable of providing accurate spatial distributions of different ions at a single *m/z*. Instead, the necessity and advantages of tandem MS analyses of wood tissue are evident after comparing MS² images with the MS images. Specifically, characteristic fragment ions resulting from collision-induced dissociation of a precursor ion are needed to differentiate between isobaric ions, which are inherent when analyzing a complex tissue, such as *Populus* wood. The MS² images provided more selectivity of cellulose and hemicellulose ion signal, as well as significantly reduce background ion signal compared to the MS spectrum. Furthermore, tandem MS was shown to differentiate between an analytes and interfering ions at one nominal *m/z*.

Conclusions

The direct analysis of cellulose and hemicellulose in *Populus* tissue using MALDI tandem MS was reported. Plotting different fragment ions from MS² experiments resulted in different ion signal localization, thus tandem MS is necessary for separating isobaric species and generated accurate wood tissue MS images. In addition to elucidating isobaric species, tandem MS reduces the background ion signal of wood tissue, improving the signal-to-background of imaging experiments. The combination of MS² and imaging provides specific chemical mapping in intact wood tissue, and this

MALDI-LIT-tandem MS method could be applied toward imaging other intact cellulosic tissues, such as switch grass or sugarcane. Imaging specific compounds within cellulosic tissue will provide further insight into the secondary structure, and furthermore, monitor changes throughout pretreatment for the conversion to ethanol.

Future experiments will focus on comparing MALDI-LIT-MS images to complementary techniques to improve the understanding of chemical changes that occur during the pretreatment process. Furthermore, future experiments will focus on developing a MALDI-LIT-MS technique to characterize lignin in wood tissue.

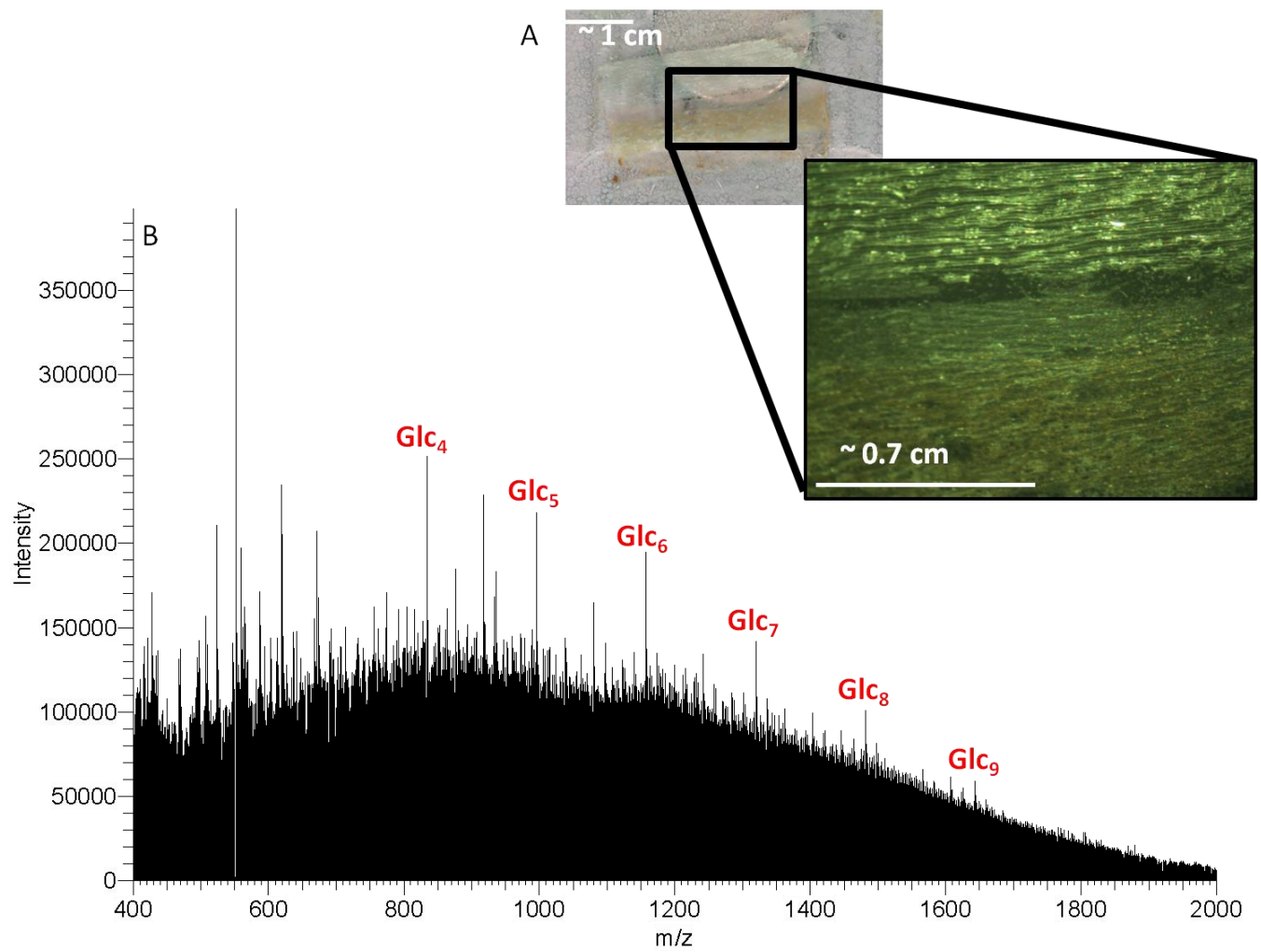


Figure 3-1. Optical image and average MS from Pine wood sample. A) The optical image of the radial pine wood sections shows two different regions of tissue (the region imaged outlined in black). B) The MS spectra averaged over 1500 scans displays spectra representative of a mixture of lignin standard, with ions at nearly every m/z and MCC standard, ions 162 m/z difference and xylan standard, ions 132 m/z difference.

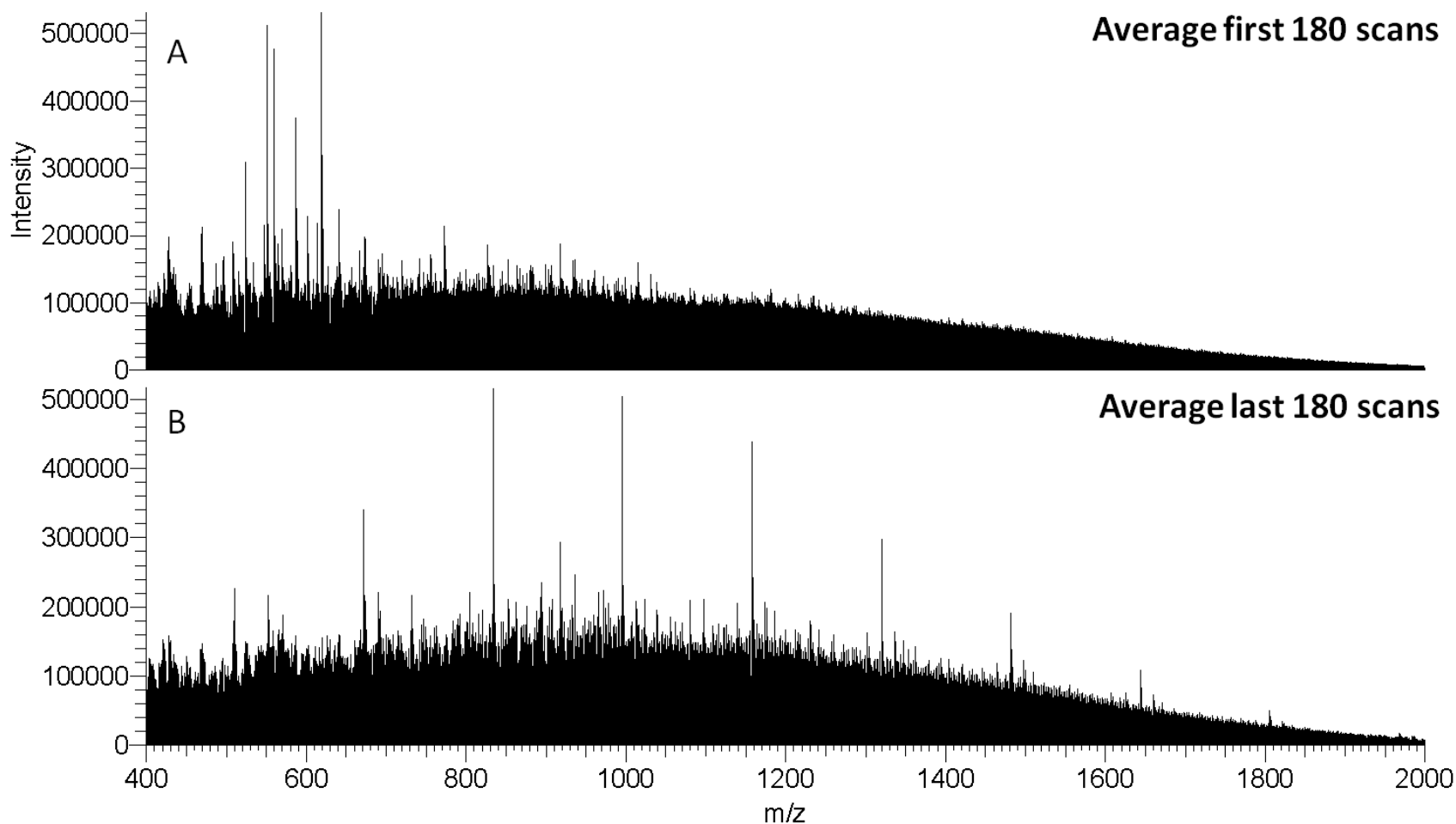


Figure 3-2. Comparison of spectra from different regions of tissue. The optical image (Figure 3-1) clearly illustrated two different regions of tissue in the area analyzed, which resulted in two different MS spectra. A) The first 180 scans average (top) shows a characteristic spectrum from lignin, with even intensity of ions at nearly every m/z . The ions that appear above the background are likely to do MALDI matrix. B) The average of the last 180 scans displays a spectrum more representative of cellulose, with intense ions 162 amu difference.

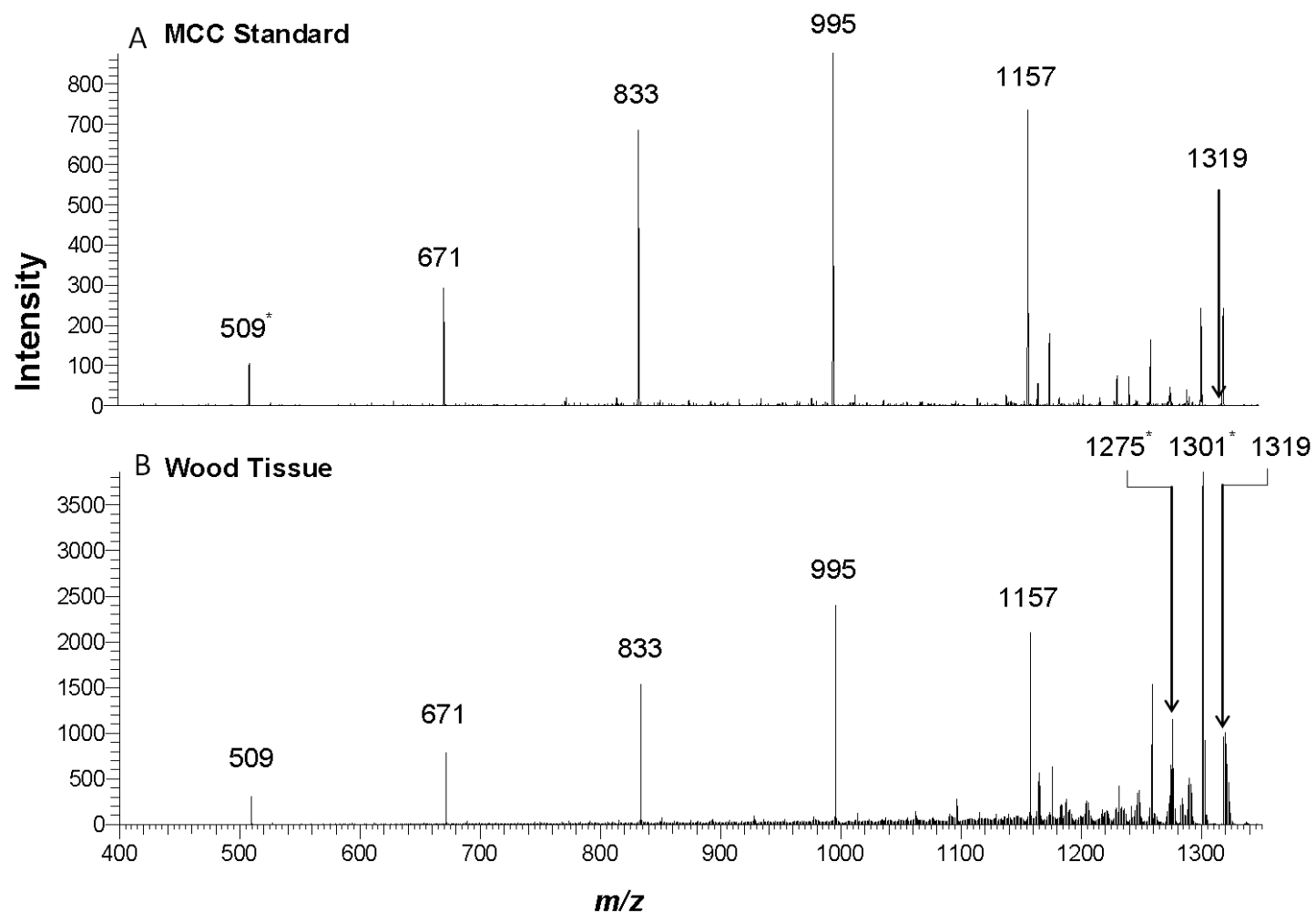


Figure 3-3. MS² of m/z 1319→... A) MCC standard. B) Wood tissue. The comparison of the standard with the wood tissue spectrum confirms that cellulose was detected from wood tissue., as the major fragment ions, NL of 162, are similar. Fragment ions m/z 1301 (NL 18) and m/z 1275 (NL 44) are observed in higher abundance from the wood tissue analysis, suggested isobaric species at m/z 1319, which can be distinguished using tandem MS.

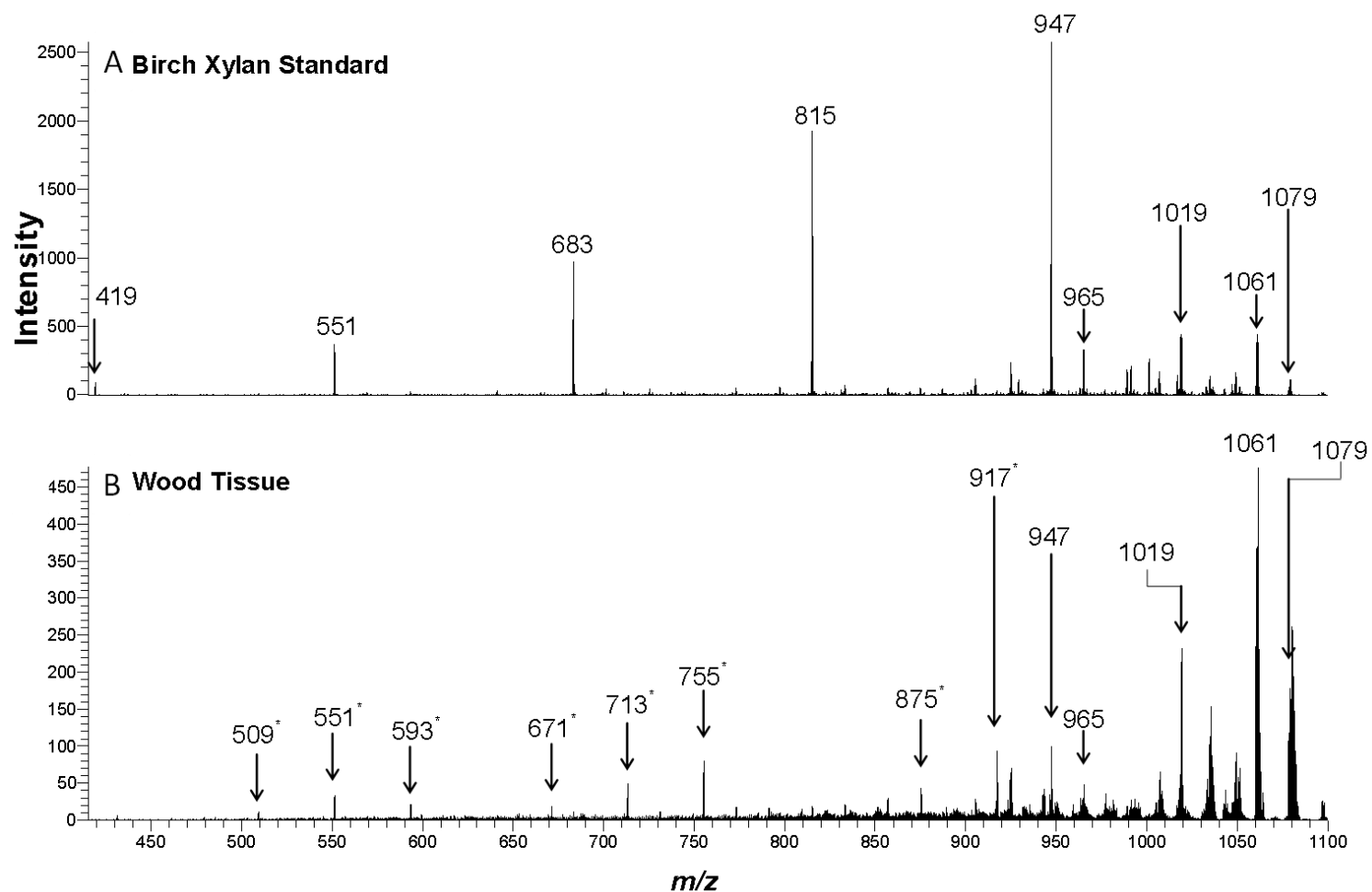


Figure 3-4. MS² of *m/z* 1079... A) Birch xylan standard B) Wood tissue. The comparison of the standard with the wood tissue spectrum confirms that hemicellulose was detected from wood tissue, as similar fragment ions (NL 132) were observed in both analyses.. MS² of *m/z* 1079 → from wood shows a more complicated spectrum indicative of isobaric ions. The starred ions refer to fragment ions not observed in the standard spectrum and were preliminarily identified as O-actylglucomannan, a different classification of hemicellulose

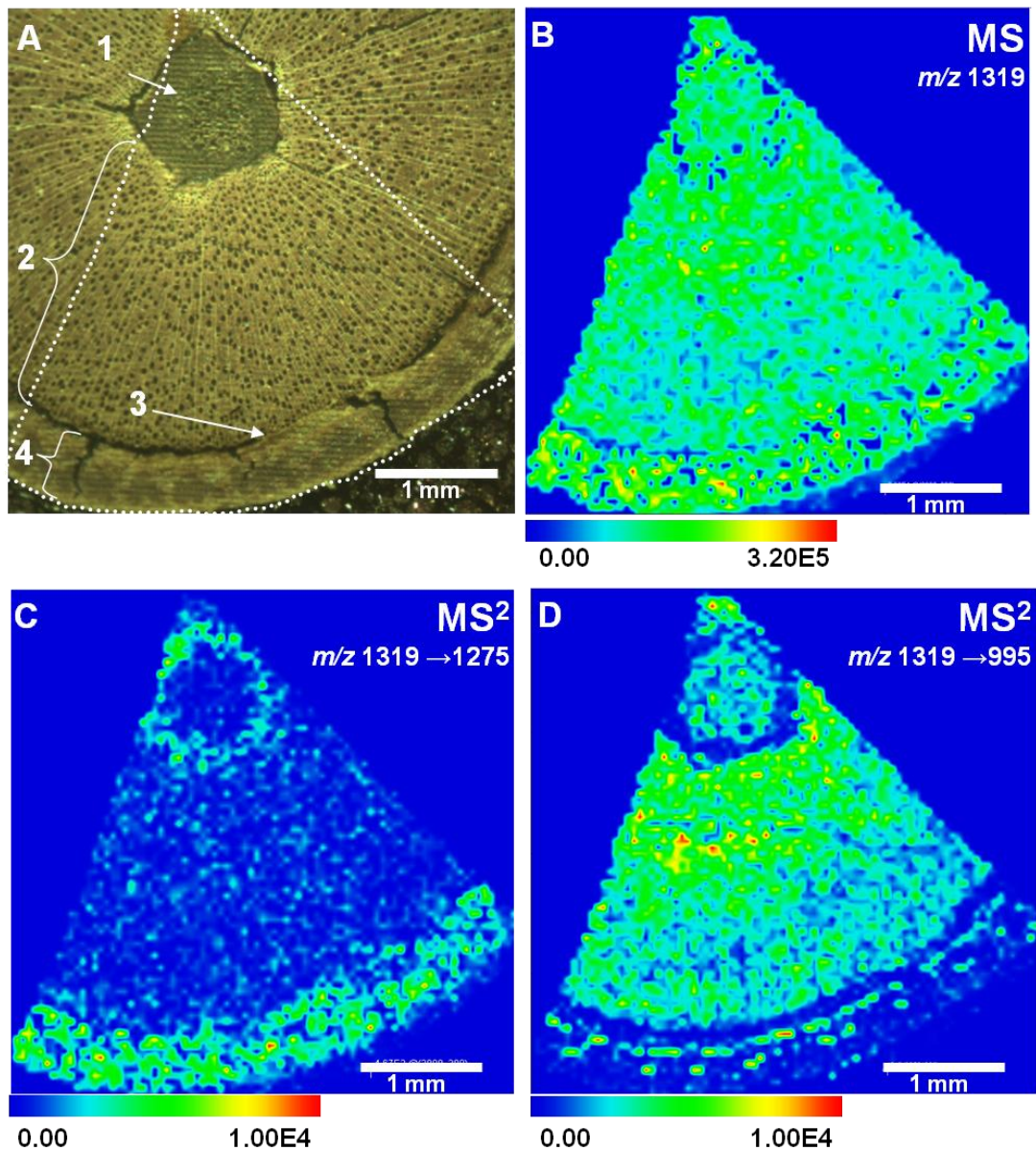


Figure 3-5. Optical and MS images of cellulose ion in *Populus* stem. A) Optical image of *Populus* wood tissue showing the pith (1), secondary xylem (2), vascular cambium (3), and secondary phloem (4). The white outline shows the area of MS and MS² analyses. B) MS image of m/z 1319 ($[\text{Glc}_7\text{-H}_2\text{O}+\text{Na}]^+$) shows ion signal over the whole tissue. C) The MS² image of m/z 1319 \rightarrow 1275 (NL of 44) displays more abundant ion signal in the region around the pith and the secondary phloem, which is consistent with tissue compositions. D) MS² image of m/z 1319 \rightarrow 995, resulting from two NLs of 162, shows localization in the secondary xylem, closest to the pith, and reduced ion signal in the center of the pith, vascular cambium and secondary phloem.

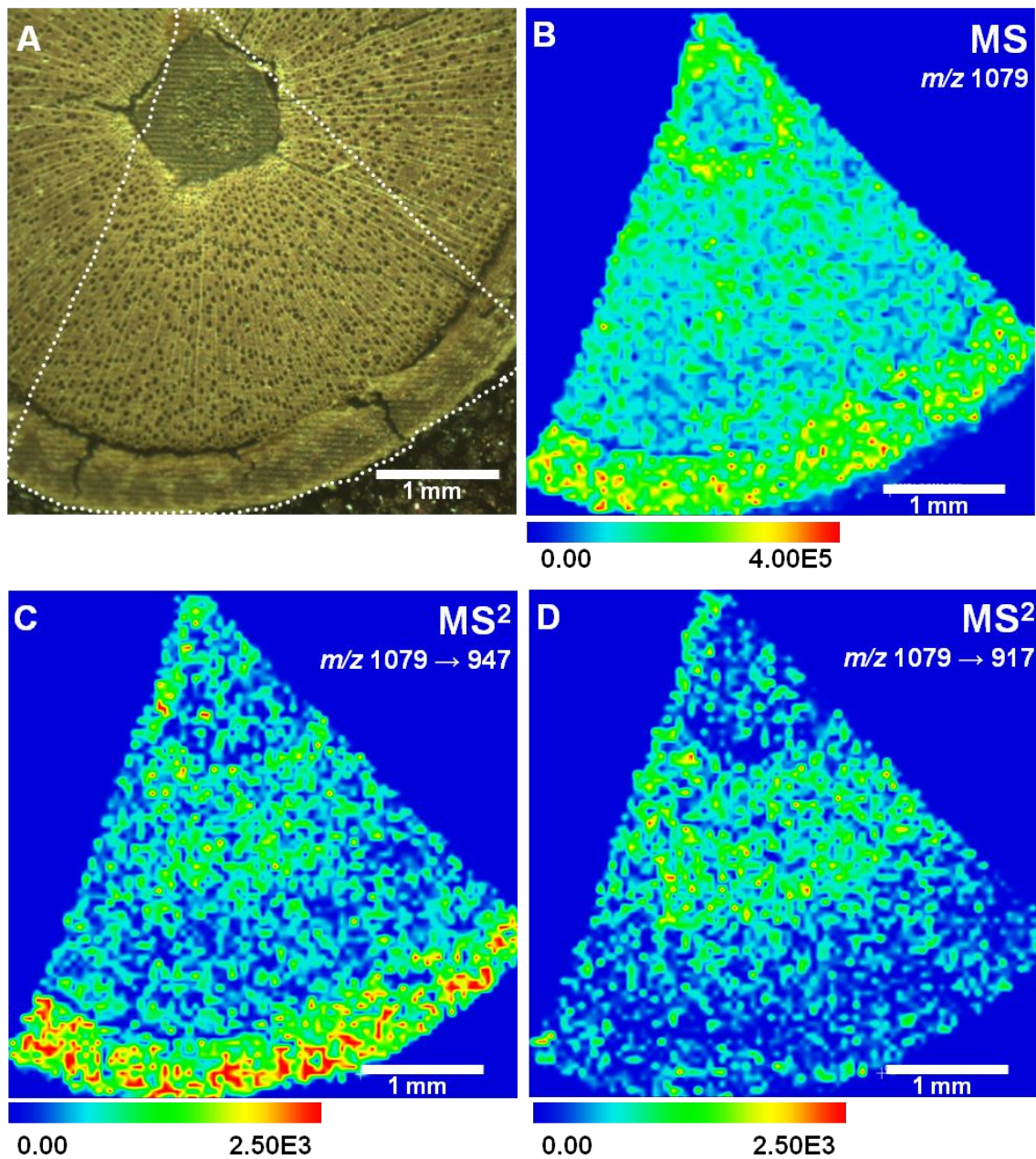


Figure 3-6. Optical and MS images of hemicellulose ion in *Populus* stem A) Optical image of *Populus* wood tissue with the region imaged outlined in white. B) MS image of m/z 1079 (identified as $[\text{Xyl}_7\text{-H}_2\text{O}+\text{Na}^1]$), shows ion signal over the whole tissue section, with more intensity in the secondary phloem and around the pith. C) MS^2 image of m/z 1079 \rightarrow 947 (NL of 132) displays increased ion intensity in the secondary phloem. D) The MS^2 image of m/z 1079 \rightarrow 917 (NL of 162) displayed increased ion signal in the secondary xylem closest to the pith. Comparing the MS^2 images of two different fragment ions illustrates two isobaric compounds are present and tandem MS can distinguish between them.

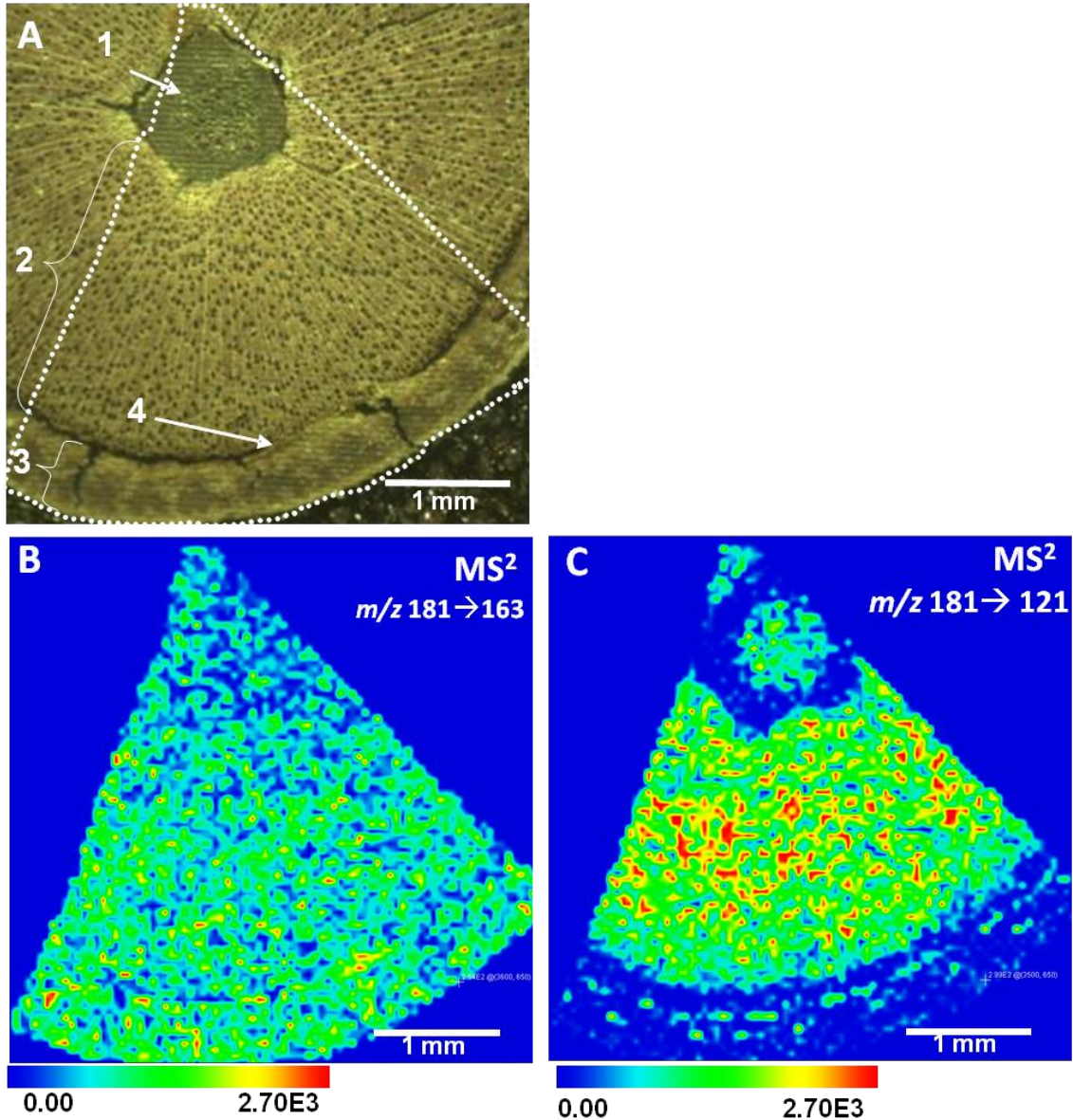


Figure 3-7. Optical and MS images of lignin ion in *Populus* stem A) Optical image of *Populus* wood tissue with the region imaged outlined in white. B) MS² image of m/z 181 → 163 (NL 18) displays ion signal over the whole tissue section. C) MS² image of m/z 181 → 121 (NL of 60) displays increased ion intensity in the secondary xylem and regions of high intensity in the secondary phloem and center of the pith. The transition of m/z 181 → 121 was identified as lignin ion and shows similar distribution as the cellulose ion in Figure 5-4.

CHAPTER 4 IMAGING OF *POPULUS* TISSUE BY FLUORESCENCE MICROSCOPY

Overview

MS imaging provides high chemical selectivity; however, the spatial resolution is inadequate to probe individual plant cells. In contrast, microscopy techniques provide images with superior spatial resolution to MS imaging. Furthermore, fluorescence imaging can offer selective staining techniques to provide high-resolution images. Combining fluorescence microscopy with MALDI-MS imaging could provide a more comprehensive analysis of wood tissue. Moreover, the complementary information of MS imaging and microscopy offers more insight into the spatial positioning of chemical compounds than other techniques alone.

This chapter discusses fluorescence microscopy analysis of *Populus* stem cross-sections. Furthermore, the fluorescence images are correlated with MS imaging to obtain complementary information and aid in method validation.

Microscopy

Microscopy is a technique in biological sciences that uses a microscope to observe the structure, architecture and anatomy of tissues and/or cells.¹¹⁴ The three main types of microscopy include optical, electron and scanning probe microscopy. This chapter discusses optical microscopy techniques applied to plant tissue analyses.

Very simply, optical microscopy is performed by passing light through a series of optics, which can generate a magnified (and focused) image of the sample. Depending on the arrangement of the optics, presence of filters, collection of light (e.g., absorbed or scattered light) within in the microscope, different optical microscopy techniques can be

performed. The most commonly used optical techniques are bright field microscopy, dark field microscopy and fluorescence microscopy.¹¹⁴

In addition to obtaining magnified images of samples, stains and dyes can be implemented for microscopy experiments to contrast of regions of tissue that contain different compounds. For example, the polychromic dye toluidine blue O (TBO) changes color when exposed to lignified cells versus non-lignified cells,¹¹⁵ which helps to identify different regions of tissue to correlate with other techniques (e.g., MS imaging). In recent years, fluorescence dyes, or fluorophores, have become increasingly popular in plant cell biology. Fluorophores are used similar to traditional dyes, in that a solution is placed atop the tissue and the dye or fluorophore selectively binds to specific classes of compounds; thus, the localization of observed fluorescence is indicative of those particular compounds. To increase the selectivity of the experiment, scientists can add fluorescence tags to molecules designed to bind to one particular compound, as opposed to compound classes (i.e., carbohydrates).¹¹⁶

Fluorescence Microscopy

Fluorescence is performed by irradiating a sample with a certain wavelength of light, termed the excitation wavelength (λ_{ex})—this causes the molecule to enter an excited electronic state. The molecule then relaxes to the lowest vibrational state, and then relaxes back down to the ground electronic state by the emission of light (λ_{em})—this light is referred to as fluorescence and is characteristic of certain molecule (Figure 4-1).¹¹⁷ Traditionally, fluorescence spectroscopy (Figure 4-2) was performed in solution for quantitative, as opposed to qualitative analyses, since fluorescence intensity is proportional to concentration and fluorescence can provide low detection limits. Today,

fluorescence is has been incorporated into microscopy techniques and has become a widely used method in biological sciences.¹¹⁸

Fluorescence microscopy experiments involve a fluorescence stain, referred to as a fluorophore, that selectively binds to specific molecule or classifications of molecules, e.g., β -linked glucans. Once the sample is stained, it is placed atop a slide and observed using a fluorescence microscope that is equipped with an excitation UV source. The light emitted from the source can contain several different wavelengths and is typically passed through an excitation filter to select the correct λ_{ex} for the fluorophore. The emitted fluorescence from the excited fluorophore is passed through a barrier filter before detection. The fluorescence can be detected by the eye (as in a typical microscope) and/or a digital camera, which can be connected to a computer to capture and save images. A schematic of a fluorescence microscopy experiment is illustrated in Figure 4-3.

Experimental

TBO Stain

A TBO staining technique was modified for *Populus* stems prepared for MS imaging experiments. A phosphate buffer (pH 6.8) containing 1 M K_2HPO_4 and 1 M KH_2PO_4 was prepared in water, and 0.10 g of TBO blue was dissolved in 100 mL of the phosphate buffer solution.

Fluorescence Stains

Calcofluor white (CW) stain was purchased from Sigma Alridch (St. Louis, MO) and is composed of calcofluor white M2R (shown in Figure 4-4, also referred to as Fluorescence brightening agent 28) (1g/L) and Evans blue (0.5 g/L)—the λ_{ex} is 360 nm and λ_{em} is 460 nm. Evans blue is added to the staining so that the staining solution is

blue (as opposed to colorless) to ensure an even stain across the tissue and to help reduce background fluorescence of tissues. CW has been reported to bind selectively to β -glucans (including 1,3- and 1,4-linked polysaccharides).^{119,120} and was used to identify relative concentrations of cellulose (β -1,4 glucan) in the wood tissue sections.

Due to aromatic monolignols, lignin 'autofluoresces' with a $\lambda_{\text{ex}} \sim 300$ nm and $\lambda_{\text{em}} \sim 490$ nm. Thus, it is possible to observe fluorescence from wood stems without the addition of a fluorophore. However, the fluorescence signal is weak and difficult to observe at higher magnifications. To enhance the fluorescence signal due to lignin in the tissue, the fluorophore acridine orange (AO, Figure 4-4) with $\lambda_{\text{ex}} 497$ nm and $\lambda_{\text{em}} 535$ and 630 nm was used. AO has been reported to interact with lignin inside of cells, thus the presence of lignin can be correlated with the observed green fluorescence.¹²¹

Sample Preparation and Instrumentation

Fifty-micron cross sections of *Populus* stems were cut using a sliding microtome and mounted atop CryoJane[®] Tape (Instrumedics Inc., Richmond, IL), and the tape was mounted onto a glass slide. Some wood tissue samples were coated with 25 mg/mL DHB+NaOAc using a Meinhard nebulizer for MS imaging experiments. MS imaging experiments were performed using a Thermo MALDI LTQ XL with 50- μm raster step sizes and parameters discussed in Chapter 3.

TBO staining was performed by applying approximately 500 μL of the prepared TBO solution atop the 50- μm *Populus* tissue section for approximately 1 minute. The stain was washed off using water and observed under a microscope.

Fluorescence microscopy was performed before and after MS imaging experiments. For CW, approximately 500 μL of the CW stain solution was pipetted atop the *Populus* cross section. After five minutes, the CW stain was washed off with excess

water and a cover slip was applied on to the stem section to observe the fluorescence. AO stained was performed in a similar manner—approximately 1 mg/mL in 50:50 methanol/water solution was pipetted atop the stem and washed off with water after five minutes. The fluorescence was observed and captured using an Olympus Macroscope and high-resolution images were captured with an Olympus x70 fluorescence microscopes.

Results and Discussion

TBO Stain

The TBO stained wood tissue section is illustrated in Figure 4-5. TBO changes colors when the stain interacts with cells of different composition. Specifically, lignified cells appear blue-gray and non-lignified cells appear a bright red-purple color. Figure 4-5 displays the secondary xylem and small regions within the phloem appear blue-gray, which is indicative of lignified cells (thus secondary cell walls). The phloem and intact region of the pith appear a red-purple, illustrating the phloem cells do not contain lignin (i.e., composed of only primary cell walls).

The results of the TBO stain were consistent with the MS imaging results discussed in Chapter 3. Specifically, the blue regions in the phloem confirmed that lignified cells are observed in the phloem—the high correlation between an established staining method and the MS imaging results demonstrate that the MS imaging method provides high molecular selectivity that can distinguish between different tissue types.

CW Fluorescence Microscopy

The stem used for this experiment was first stained with CW, and the fluorescence images were captured with a fluorescence microscope equipped with a digital camera. As Figure 4-4 displays, CW is a highly aromatic molecule with a λ_{ex} similar to

wavelength of the MALDI laser on the LTQ XL. It was hypothesized that the CW could act as a MALDI matrix, thus no additional DHB was added atop the stems for the MS imaging experiments displayed in this section.

Figure 4-6 displays the CW fluorescence stained and MS image of the same *Populus* wood stem cross section. The CW image shows blue fluorescence in the presences of β -1,4 and β -1,3-linked glucans, which can be correlated with the localization of cellulose. Several pictures were taken over the imaged area of the stem and stitched together using photo editing software; therefore, some of the areas of the stem observed in the MS image were not observed in the fluorescence image.

The fluorescence image displays that the most intense fluorescence signal comes from the secondary xylem, which is primarily composed of thickened secondary cell walls. It is also interesting to note the fluorescence signal observed from the center of the pith, as well as from small regions within the secondary phloem. Although the pith is composed of mostly primary cell walls, cellulose is still present but in lower abundance. The intensity of the fluorescence can be correlated to the relative abundance of cellulose between the regions of the tissue. For example, the intense fluorescence observed in the left region of the stem can be correlated with higher relative concentration of cellulose when compared with the center region of the pith.

Figure 4-6 also displays tandem MS images of m/z 1319 (previously identified as a cellulose ion) of the same stem, after CW staining. More specifically, Figure 4-6 b shows the TIC of the MS² of m/z 1319 and Figure 4-6 c shows the MS² of m/z 1319 \rightarrow 995 (NL of 324). The TIC ion signal shows the most intense ion signal around the pith region and in the secondary phloem. CW is believed to act as the MALDI

matrix. Since CW binds selectively to β -glucans, less intense ion signal would be expected in regions where CW (and β -glucans) is not present. Comparing this tandem MS image to the CW fluorescence image demonstrates that the most intense ion signals are localized in the regions with the least intense fluorescence. (Note, the gap between the secondary phloem and secondary xylem is due to a crack in the tissue that occurred after washing, drying and placing the stem into intermediate pressure for MS analysis.) The comparison of these two images shows that CW can be used to generate ions from the surface on the stem and the CW does not appear to ionize β -glucans selectively.

The comparison of Figure 4-6 b and c again demonstrates the necessity of tandem MS imaging for intact wood tissue analysis. Figure 4-6 c shows the NL of 324 (two Glc residues) from m/z 1319. The ion signal localization is similar to that observed in Chapter 3, where the most intense ion signal is localized in the thick, secondary cell walls of the secondary xylem, the center of the pith, and small-localized regions in the secondary phloem. The localization of the ion signal is similar to the fluorescence observed with the selective fluorophore. This comparison helped to validate the developed tandem MS imaging method of intact plant tissue, and could be used to generate relative quantitative methods for MALDI tandem MS imaging.

Traditionally, MALDI-MS is a more qualitative method, since the ion intensities observed could be affected by several different parameters (i.e., ion intensity does not always correlated with analyte concentration) for example, heterogeneous MALDI matrix crystal and/or topographic differences of the stem surface. Fluorescence microscopy coupled with MALDI-MS could be used to increase quantitative information.

For example, the most intense fluorescence signal is observed in the left and right hand regions of the xylem, with a region of less intense fluorescence in the bottom center of the secondary xylem and around the pith region. The relative intensities from MALDI tandem MS imaging are opposite—the most intense ion signal is observed in the bottom region of the secondary xylem and around the pith region and less intense ion signal is observed in the right and left sides of the xylem. However, this information could still be used to help increase quantitative information obtained from MALDI-MS experiments.

Although no absolute quantitation was obtained, the difference in ion intensity correlated with the difference in the fluorescence signal. Although the correlation was inversely related (i.e., higher fluorescence correlated with lower ion signal), this suggests that the variation in the ion signal is a result of relative changes in cellulose concentration and/or accessibility, which could help to improve the understanding of pretreatment processes for cellulosic ethanol.

Acridine Orange Fluorescence Microscopy

Primary and secondary cell walls both contain cellulose (cellulose is more concentrated in the secondary cell wall), thus distinguishing regions of primary versus secondary cell walls could be difficult using a cellulose fluorophore alone. Lignin, however, is more representative of the secondary cell wall, since primary cell walls do not contain any lignin. AO was used to stain lignin and the fluorescence images are displayed in Figure 4-7. The green fluorescence signal is observed across the secondary xylem and intense regions in the phloem. This confirms the regions are lignified phloem fiber cells that contain secondary cell walls and higher concentrations of cellulose compared with the rest of the phloem.

It is also interesting to note that the fluorescence within the xylem is not an even signal (i.e., there are regions of more intense fluorescence). These areas were observed with higher magnification and displayed in Figure 4-7 b-c and demonstrated smaller structures within the xylem, specifically the xylem vessels and the cell walls, were able to be observed. Xylem vessels are long tubes that extend the length of the stem and are larger in diameter than the plant cells, approximately 30 μm . As previously mentioned, the secondary cell walls are identified by green fluorescence of the AO and Figure 4-7c illustrates the cells are approximately 12- μm in diameter and the cell wall approximately 2- μm thick.

Figure 4-7c clearly shows the difference between the regions of high fluorescence intensity, high lignin content (bottom left) and the lower fluorescence intensity, low lignin content (top right). The cell walls in the bottom left region shows more regularly shaped, less 'curvy' cell wall structure, which is typical for xylem tissue. The cell walls in the top right region are less regularly shaped, more 'curvy' and appear 'squished.' These cell shapes are characteristics of 'tension wood'—other characteristics of tension wood include thicker secondary cell walls, increased cellulose concentration and lower lignin concentration, which is consistent with the observed fluorescence of the cellulose. Tension wood forms when plants are exposed to 'stress' as cells are developing. The cellular composition (i.e., cellulose, hemicellulose, lignin concentrations) changes to alleviate the stress induced on the plant.

The fluorescence image of the same stem stained with CW is displayed in Figure 4-8 to contrast the two fluorescence signals. In the regions less intense AO fluorescence signal is observed, greater CW signal is observed (relative to the signal

across each respective tissue)—these regions are indicated by the arrows in Figure 4-8. Contrasting the fluorescence signals of CW and AO signal helps to identify these regions of tension wood. It is also interesting to note the difference in the CW fluorescence signal in the phloem between Figure 4-6 a and Figure 4-8 b. Figure 4-6 shows little CW fluorescence signal in the phloem, relative to the lignified phloem fiber cells. In contrast, Figure 4-8 b shows similar CW signal in both the phloem and the lignified fiber cells; this difference in fluorescence signal could be explained by the age of the stem. The stem displayed in Figure 4-8 is younger than the stem in Figure 4-6, which could explain the differences in cellulose content within the phloem. The differences observed between these stem demonstrate that different techniques are needed for full characterization of LCM tissue.

The advantage of analyzing regions of tension wood is that the regions of cellulose and lignin concentrations differences can be observed within one tissue section, and thus can be analyzed in one analytical scan. These analyses could help lead to develop quantitation methods using MS imaging; however, three main difficulties need to be overcome. Since tension wood is a natural reaction to stress, there is not a way to guarantee that every section prepared (or every stem analyzed) will contain tension wood areas. Also, the regions of tension wood are difficult to identify without fluorescence stains, so probing the correct regions with MS imaging could be difficult. Lastly, tension wood areas within these stem sections are small, which is difficult to analyze with the current spatial resolution limitations of MALDI-MS imaging (Figure 4-8c).

Figure 4-8c shows the MS² image of m/z 1319→833 stem after CW and AO staining and shows increased cellulose signal in the top region of the stem. This could possibly be correlated with the region of tension wood observed; however, the quality of the MS after both fluorescence stains were applied to the tissue was poor. Also, the region of tension wood displayed in Figure 4-8b is approximately 200- μ m wide. The laser spot size is > 75- μ m in diameter. Without large over-sampling, only four laser stops would probe the region of tension wood, limiting the analysis of that area. A higher spatial resolution technique is needed to probe these regions and to show more structural features of LCMs.

In addition, the cellulose ion signal was observed in the phloem region, which is consistent with the CW fluorescence microscopy signal. It is important to note that the older stem (Figure 4-6) displayed little CW fluorescence signal in the phloem and was also observed in the MALDI-MS image of a cellulose ion. These results further validate the method of MALDI-MS imaging for the analysis of intact tissue. Furthermore, these images demonstrate that the selectivity of MALDI tandem MS imaging is needed for accurate analysis of LCMs.

Conclusions

This chapter discussed the ease and viability of obtaining high-spatial resolution images of intact wood tissue sections using fluorescence microscopy. The staining protocols are easy to follow and offer more insight into the chemical composition than traditional microscopy or polychromic dyes. In addition, it was shown that CW can be used as an 'internal matrix,' which could be further implemented developing a more quantitative method for the analysis of cellulose within intact LCM tissue sections.

Correlating fluorescence microscopy with MALDI-MS imaging validated the developed MALDI-MS imaging method and illustrated the need to improve spatial resolution of MALDI-MS imaging experiments. Coupling fluorescence staining with MALDI-LIT-MS imaging was shown to produce a more comprehensive analysis of the *Populus* stem..

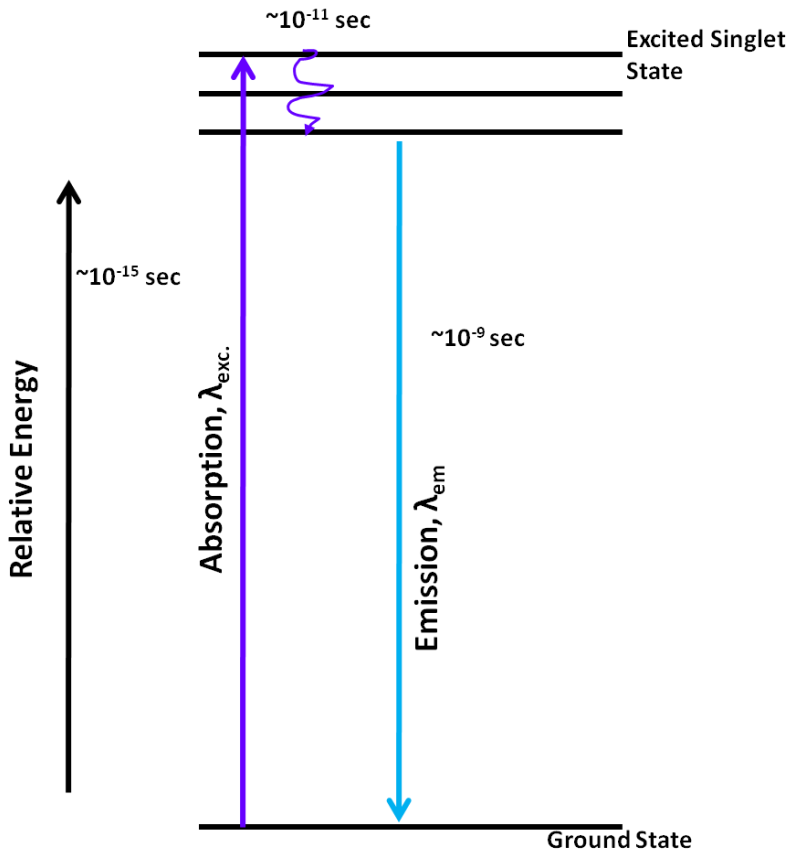


Figure 4-1. Jablonski diagram representing energy level transitions involved in fluorescence emission. The molecule absorbs a certain wavelength of light, which raises the energy to an excited electronic state. The molecule undergoes vibration relaxation, and electronic relaxation by the emission of light (fluorescence). The energy of the emission is always less than the energy of absorption.

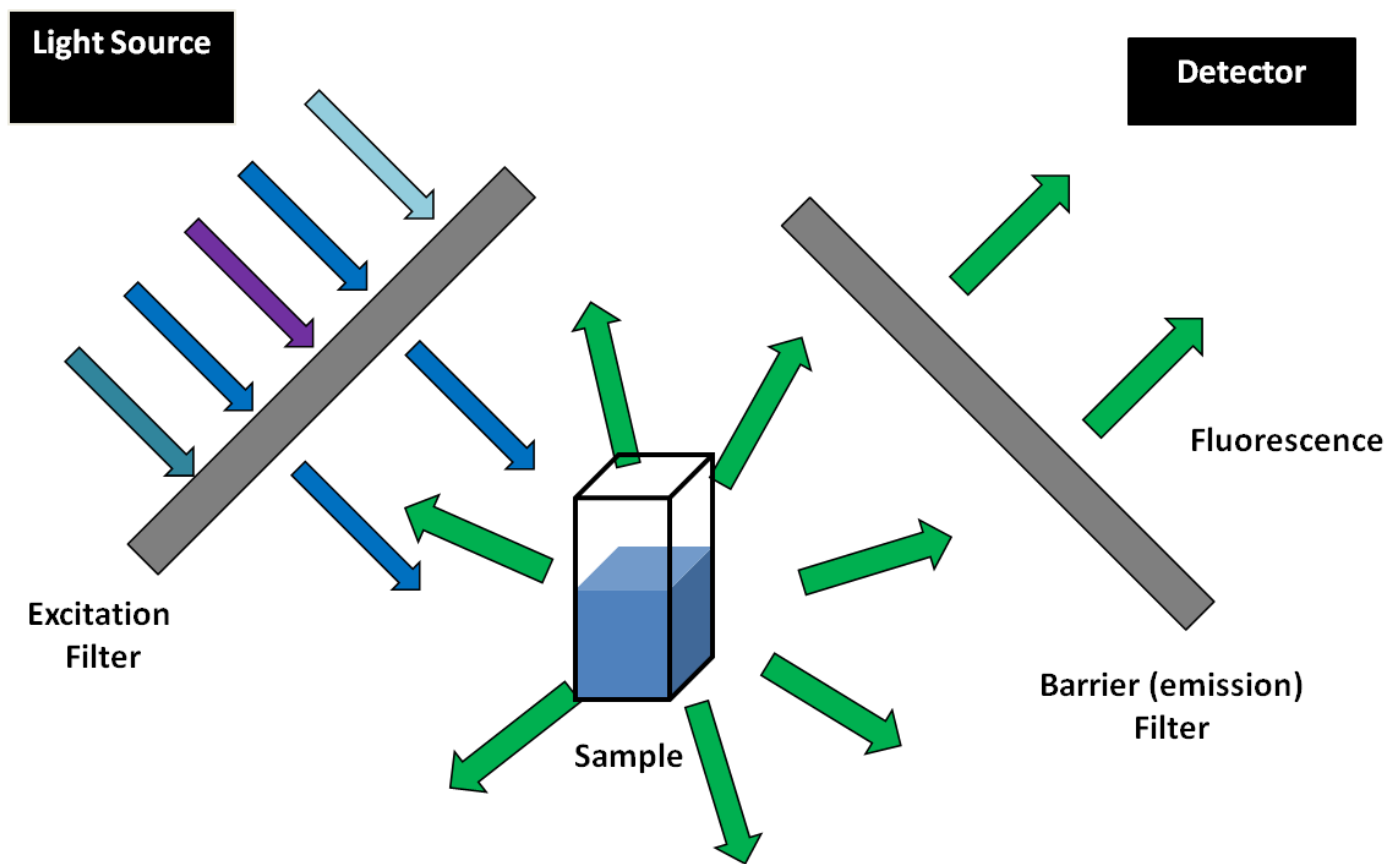


Figure 4-2. Schematic of a general fluorescence experiment. The light from an emission source is passed through and excitation filter, and only the excitation wavelength reaches the sample. The fluorescence emitted from the sample passes through a barrier filter before detection.

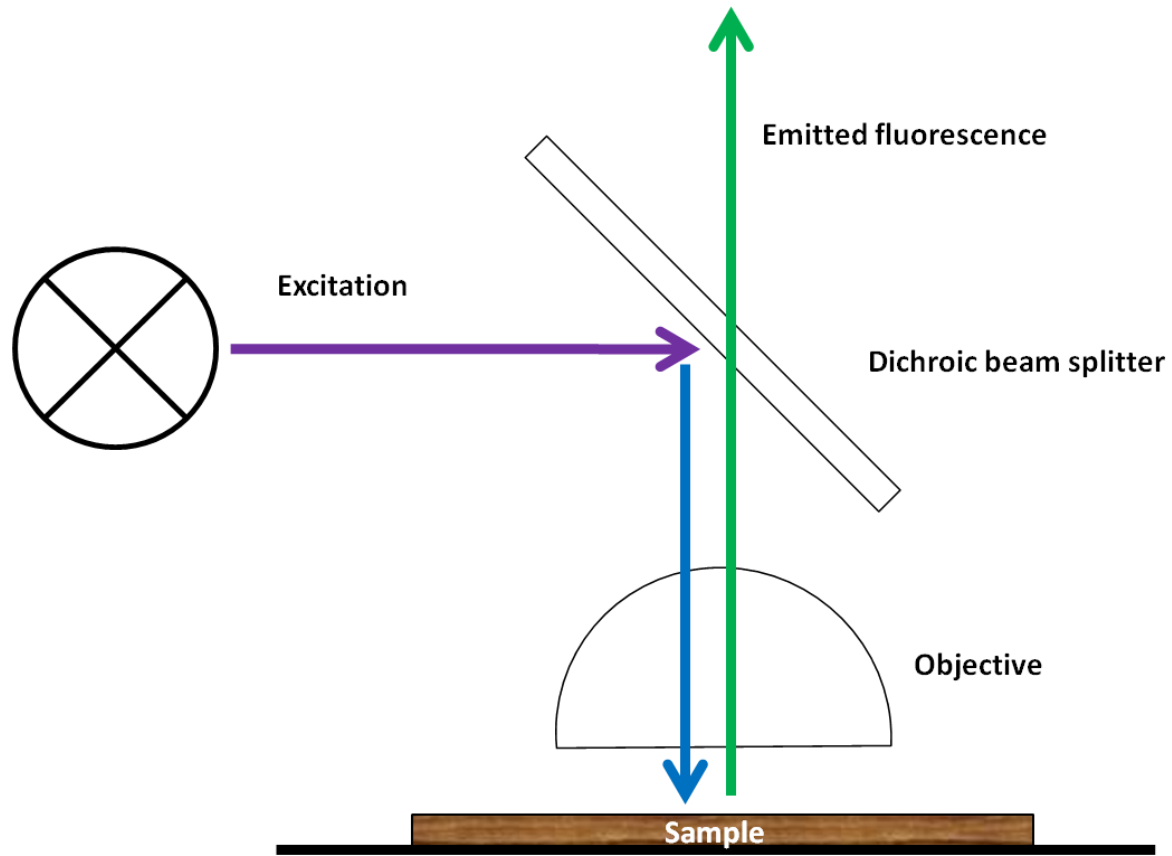


Figure 4-3. Schematic of fluorescence microscopy. The excitation source is reflected toward the sample by a dichroic beam splitter. The fluorescence emitted from the sample is passed through objective lens for magnification and lastly to the detector (eyes or digital camera).

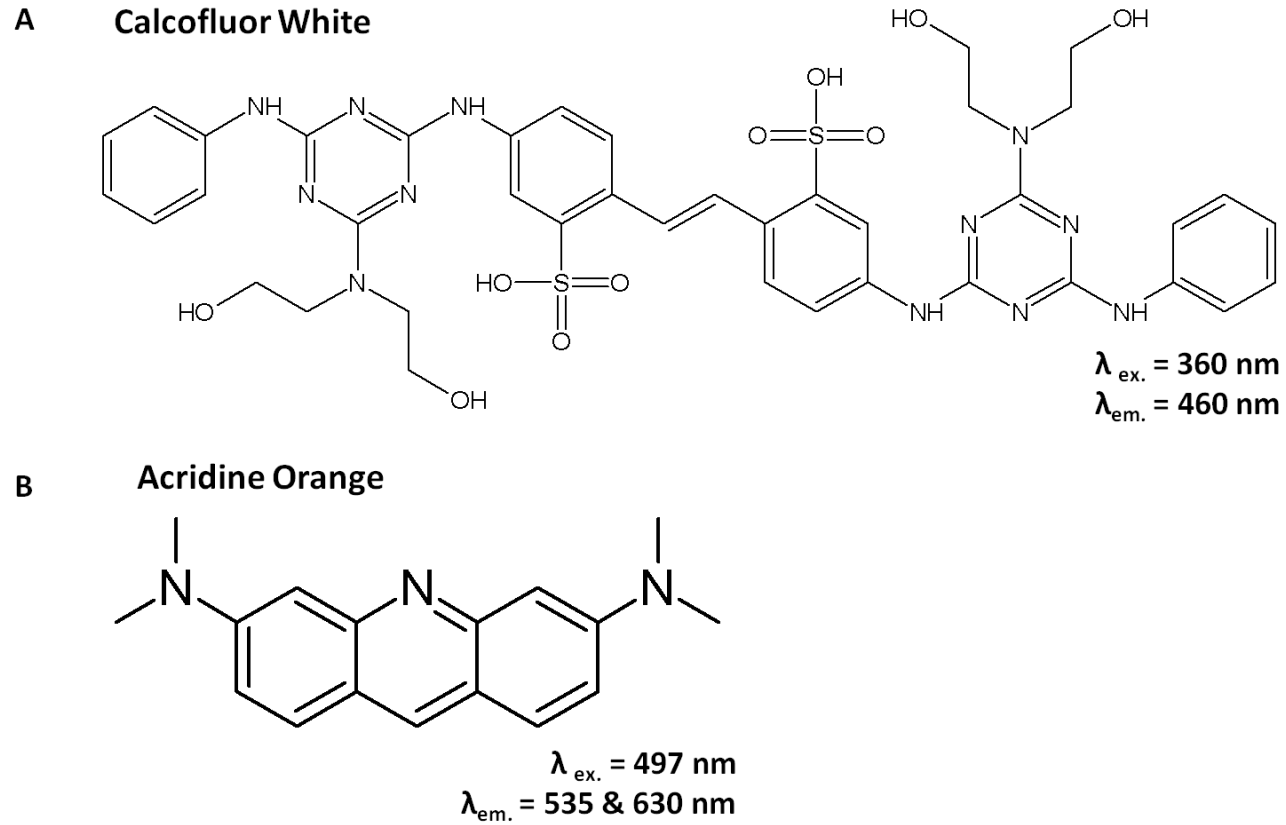


Figure 4-4. Chemical structures of fluorescence stains used. A) Calcofluor white. B) Acridine orange. Note the highly aromatic structures and wavelength of excitation is similar to the N₂ MALDI laser.

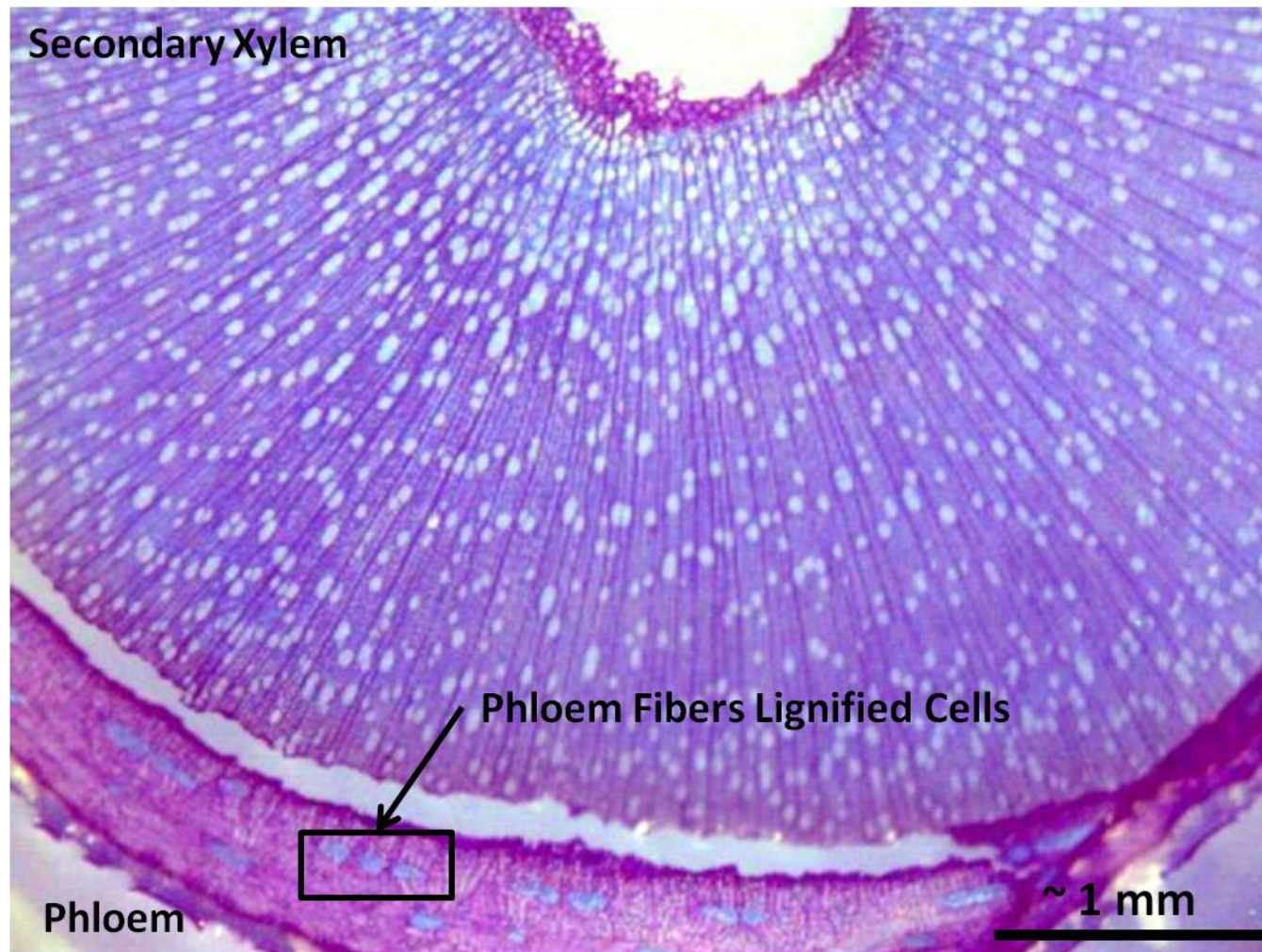


Figure 4-5. TBO Stained *Populus* stem. TBO is a polychromatic stain used to determine lignified cells. In the presence of lignin, TBO appears a blue-gray color and in the absence of lignin, appears a red-purple color

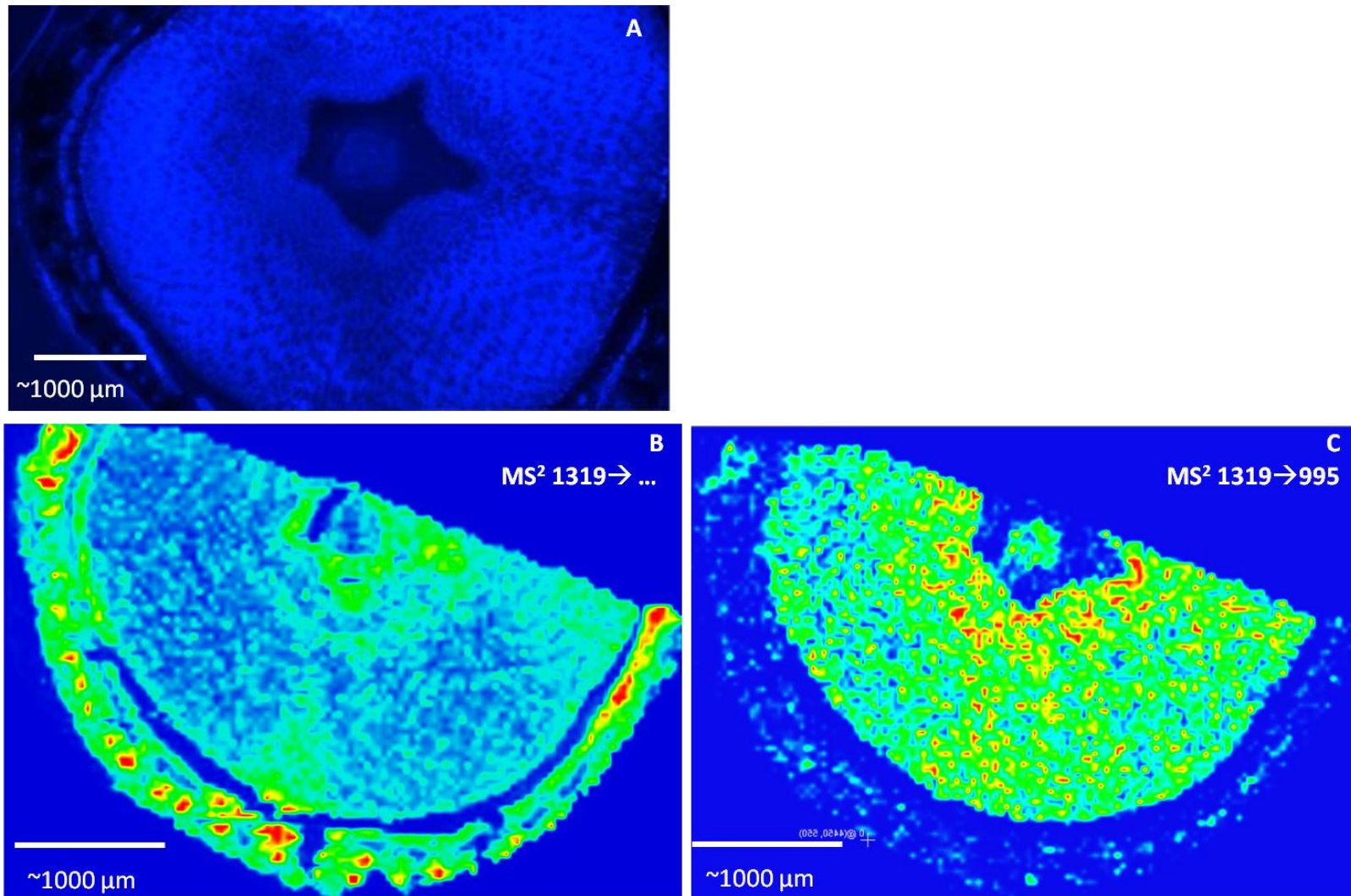


Figure 4-6. CW stained and tandem MS images. A) The CW image shows fluorescence signal localized in the secondary xylem and in regions within the phloem. B) The MS² image shows ion signal was not affected by the CW stain. C) The MS² 1319→995 (NL 324) displays high correlation between ion signal and CW fluorescence.

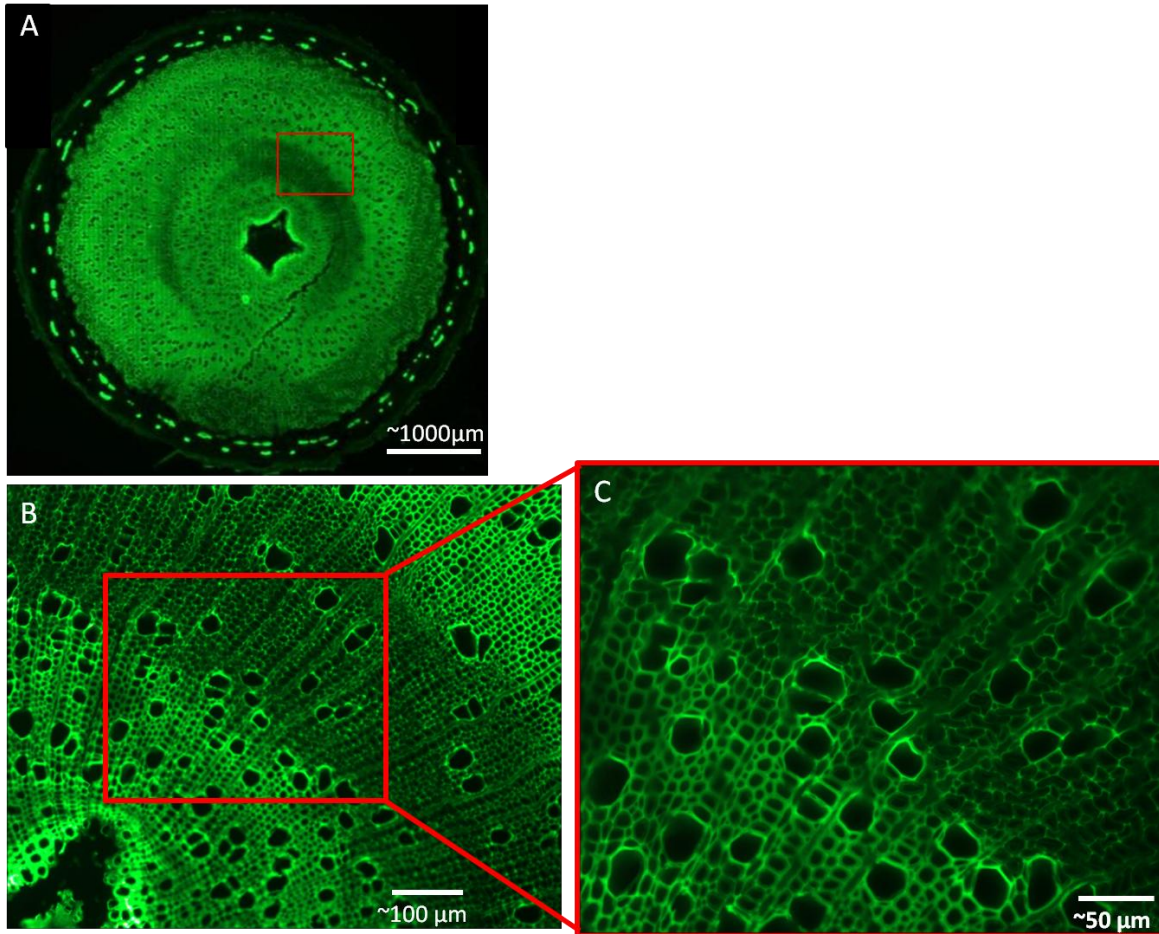


Figure 4-7. AO stained *Populus* stem. AO fluoresces in the presence of lignin and is indicative of secondary cell walls. A) AO signal is localized in the secondary xylem and intense regions in the phloem, indicative of the phloem fiber bundles. B) High magnification reveals areas of high and lower fluorescence intensity and was determined to be representative of tension wood. C) Further magnification illustrates the irregularly shaped cell walls of the tension wood.

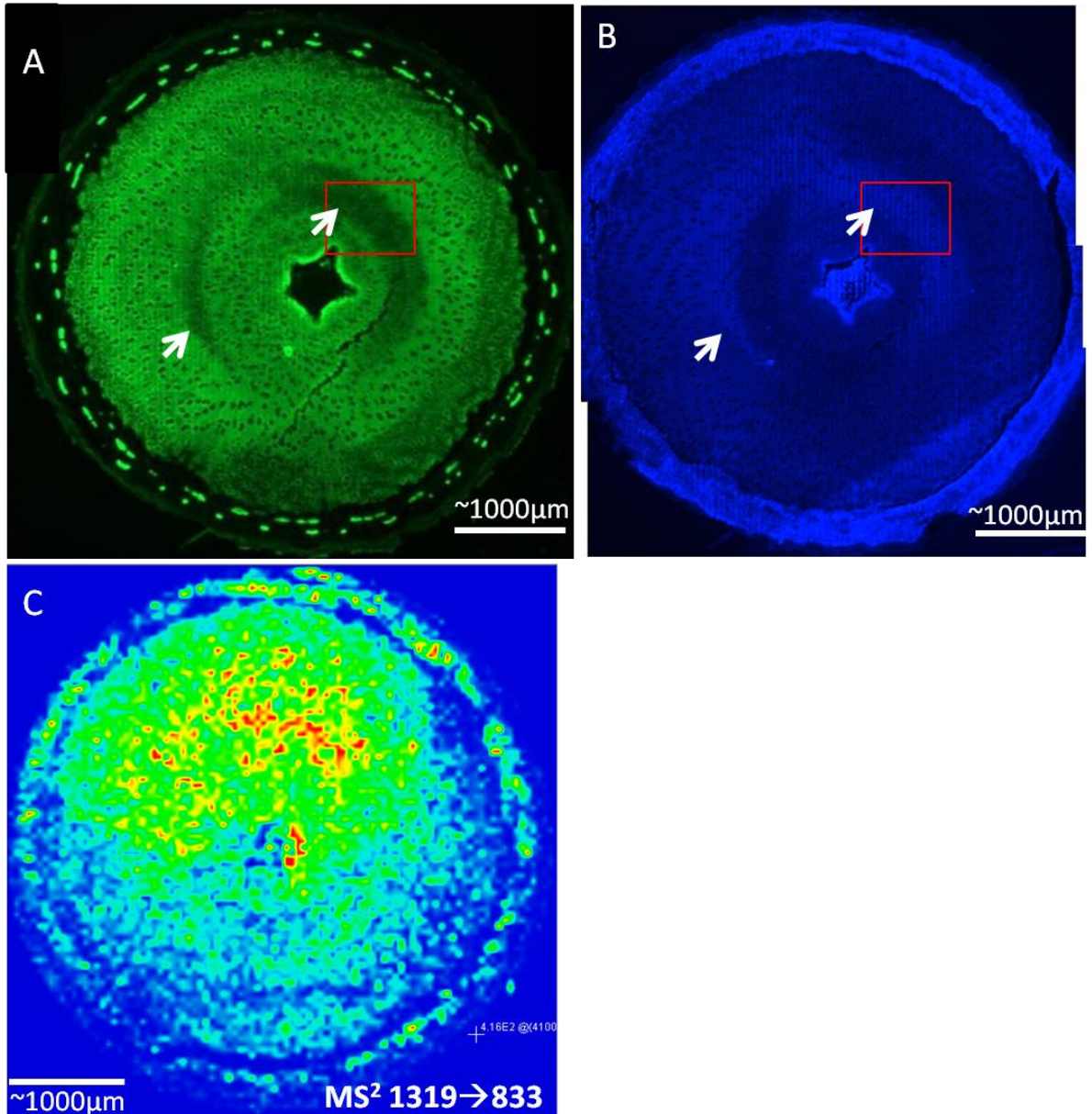


Figure 4-8. Comparison of AO, CW stain and MS image of same *Populus* wood stem. A) AO fluorescence. B) CW fluorescence. C) MS² 1319→833 image. Contrast of AO and CW illustrates the lower AO fluorescence signal (identified as a region of tension wood) shows increased CW signal. MS image illustrates increased cellulose ion signal at the top of the stem; however, the spatial resolution is not adequate for the analysis of tension wood regions. Also, the AO and CW stain appeared to reduce the quality of MS spectra from the stained wood tissue.

CHAPTER 5 HIGH SPATIAL RESOLUTION IMAGING OF *POPULUS* TISSUE USING TOF-SIMS

Overview

As in any field of study, using one analysis technique could limit the information obtained about the sample. For example, MS imaging techniques that provide high molecular selectivity typically lack spatial resolution and vice versa. Thus, performing a variety of different techniques on the same sample offers complementary information to allow for a more comprehensive understanding of the sample. This chapter focuses on employing complementary imaging techniques to verify and compare with the developed matrix-assisted laser desorption/ionization linear ion trap MALDI-LIT tandem MS imaging method for the analysis of lignocellulosic materials (LCMs). These techniques include ToF-SIMS and fluorescence microscopy.

ToF-SIMS Microscope Imaging

As previously described in Chapter 1, ToF-SIMS is a sensitive surface analysis technique that offers superior spatial resolution over other MS imaging techniques. Thus, the goals of these experiments were to obtain higher spatial resolution ToF-SIMS images and to correlate the MALDI-MS analyte ion signal with the SIMS analyte ion signal. The two major differences between MALDI imaging and ToF-SIMS imaging are the ionization mechanism and the image generation.

MALDI relies on interactions between analytes and the MALDI matrix during laser desorption to generate analyte ions. The MALDI matrix is designed to absorb most of the laser energy, which makes MALDI a soft ionization technique capable of introducing intact biomolecules into the gas phase. SIMS generates secondary analyte ions by bombarding the sample with a high-energy primary ion beam—the high energy causes

intense fragmentation, which produces complex spectra of ions typically lower than m/z 1000. In addition to the different ionization sources, the ToF-SIMS instrument used in this chapter is operated in the microscope-imaging mode (versus the microprobe imaging of MALDI experiments). Instead of rastering the sample beneath the laser (in the case of MALDI LIT experiments), the spatial distribution of ions generated from the surface is conserved through the mass analyzer, focused through ion-optics and directed toward a position sensitive detector. The spatial resolution of the images generated is determined by the magnification of the microscope, the quality of the ion-optics and the resolution of the position sensitive detector.⁵⁴

A general schematic of the Physical Electronics TRIFT II (Chanhessen, MN) instrument used for these experiments is displayed in Figure 5-1. The instrument is operated under high vacuum (10^{-10} torr) to increase the mean free path, thus mass resolution, of the ToF-SIMS experiments.

Ionization

Liquid metal ion guns (LMIGs) are the most common primary ion source for SIMS experiments. The gun operates by heating the metal (gold for the experiments reported) until it reaches the liquid phase. The liquid metal is passed through a needle induced with a large electric field, as the liquid moves further down the needle, the electric field strength increases and ionization is induced. Parameters controlled to start the LMIG include the heater and the extractor voltage (tips of LMIG are fragile, so great care must be taken to not damage the ion gun needle). The ion current at the tip is monitored for proper operation and must be stable before measurements can be obtained. The gold primary ions (Au^+) are guided through deflector plates and a focusing lens toward the sample surface.⁷⁶

The point-size (i.e., sample spot) of a SIMS source is much smaller than the MALDI laser spot diameter. Atomic ion sources (e.g., Au⁺) routinely produce 50 nm spot sizes and have been reported smaller.¹²² The impact of the primary ions causes a ‘collision cascade’ that transfers kinetic energy from the primary ions to the surface, which releases ions, neutrals and clusters within 10 Å of the surface (assuming static SIMS limits, Figure 5-2).

The ‘damage cross-section’ measures the surface area damaged by the primary ion beam and is an important parameter of SIMS. If significant surface damage is induced, the measurement is no longer of the pristine sample surface; instead, the secondary ions generated will be characteristic of the damaged surface. The primary ion dose can be altered to change the amount of surface damage induced on the sample. Typically, low primary ion doses (< 10¹³ ions per cm²) are used for static SIMS experiments; thus, it can be assumed that the secondary ions are generated from the monolayer.⁵⁴

Mass Analysis and Detection

The secondary ions generated from the surface are electrostatically extracted through an immersion lens followed by two transfer lenses—these magnify the secondary ion profile prior to entering the mass spectrometer. The magnified ion packet is then focused through three, identical 90° electrostatic analyzers (ESAs), which help to compensate for the kinetic energy distribution. Illustrated in Figure 5-1, the secondary ions also pass through a contrast diaphragm to limit the lateral energy distribution and an energy slit to limit the axial energy distribution.⁷⁶ The secondary ion image is then projected onto the position sensitive detector.

The TRIFT II instrument uses a dual microchannel plate (DMCP) for detection. As the secondary ions hit the first MCP detector, electrons are generated and amplified for detection, and the time of detection is used for ToF mass analysis. The image is generated by setting a time (mass) window for collection, and each mass spectrum is correlated to the position of the detector. The detector is a 256 x 256-array detector and the counts for each ion at each position are summed to generate the ion image and mass spectrum at each location.⁷⁶

Experimental

Instrumentation

Experiments reported in this chapter were carried out at the FOM Institute AMOLF, in Dr. Rob Heeren's Biomolecular Imaging Mass Spectrometry laboratory. The ToF-SIMS experiments were performed on a TRIFT II by Physical Electronics (Chanhessen, MN) within the static SIMS limit ($< 10^{13}$ ions cm^{-2}). The primary ion source was a LMIG of Au^+ .

Fluorescence microscopy was performed using a Leica DMRX microscope equipped with a Nikon DXM1200 camera and filters from Chroma Technology.

Sample Preparation

Microcrystalline cellulose (MCC), Birch xylan and Spruce lignin were prepared as described in Chapter 2 and 1 μL of the suspensions were dropped onto an ITO coated glass slide and allowed to dry. Half of the sample spots were coated with 1 nm of gold using a sputter coater (SC7640 Quorum Technologies, Newhaven, UK) to determine the best sample preparation.

10-week-old *Populus* hybrids were grown under high nitrogen conditions and portions of the stem were subjected to carbohydrate and lignin analyses. Approximately

50- μm thick cross sections were sliced on a sliding microtome and mounted onto a glass slide with a cover slip. The wood sections were then floated in acetone, transferred onto double-sided conductive tape and mounted onto an ITO coated glass slide.

For method development studies, different sample coatings were used. Four stems were prepared as follows: a) no gold, no DHB, b) DHB only, c) DHB and gold, and d) gold only. The DHB was applied using the ImagePrep, an automated MALDI matrix coating device (Bruker Daltronics, Billerica, Mass.) with 25 mg/mL DHB dissolved in 50/50 methanol:water. A 1 nm thick layer of gold was deposited onto the surface using a sputter coater (SC7640 Quorum Technologies, Newhaven, UK).

Imaging Experiments

Mosaic imaging experiments were set-up to determine the optimal sample preparation. Mosaic images are generated by piecing together tiles, which have a set resolution of 256 x 256 pixels. The dimensions of each tile are user-determined and were set to 87.5 x 87.5 μm for these experiments. The spatial resolution can be approximated by solving for the dimensions of 1 imaging pixel using the ratio,

$$\frac{1 \text{ Mosaic Tile}}{256 \text{ pixels}} = \frac{87.5 \mu\text{m}}{1 \text{ Imaging Pixel}} \quad 5-1$$

However, due to the large amount of data sets, under the normal settings, the software reduces the 256 pixels into 8 pixels; thus, the actual spatial resolution observed from the software is lower than the physically measurement. The full resolution images can be observed using different software, but needs a high performance computer, as some data files can take days to convert and open.

The spatial resolution and mass resolution can also be altered by operating in 'bunched' or 'unbunched' mode. Bunched mode offers higher mass resolution, as the ions are bunched together in shorter pulses to generate more ions per time. This shorter ion pulse results in a smaller kinetic energy distribution and higher mass resolution. Unbunched mode increases the ion pulse time, thus increasing kinetic energy distribution, lowering the mass resolution, but increasing the spatial resolution dramatically (Figure 5-3).

Results and Discussion

ToF-SIMS spectra are more complex compared the MALDI spectra, due to extensive fragmentation of the high-energy ionization source. Also, ions observed from MALDI experiments are not expected in SIMS, since cationization (or adduction) may not occur due to the high-energy ionization. Thus, no comparisons between ions observed in MALDI-MS and ToF-SIMS were made. Another difficulty of ToF-SIMS analyses is the sensitivity to surface contaminants. Despite great caution taken for sample preparation, phthalates and silicones are commonly observed in ToF-SIMS spectra, more specifically, poly(dimethylsiloxane) (PDMS). Since PDMS is a polymer, a series of ions (as opposed to just one ion) can be monitored for the presence of PDMS and the commonly observed series of ions includes, m/z values 28, 43, 59, 73, 147, 207 and 221.¹²³

Standards

ToF-SIMS analyses were performed on MCC, Birch xylan extract and Spruce lignin extract. The best spectra were obtained from coating the standards with a 2 nm layer of gold prior to analysis. An example of ToF-SIMS spectrum recorded from the birch xylan standard is displayed in Figure 5-4 and demonstrates the intense

fragmentation characteristic of SIMS. Some predicted ion identifications were made based on the known composition of xylans; however, positive identifications could not be assigned. One of the difficulties of adding gold to the sample surface prior to analysis is that the gold ions and cluster ions observed become the base peaks of the MS. Despite this obvious disadvantage, no analyte ionization was observed without the gold coating.

The ToF-SIMS analysis of the three different standards (MCC, Birch xylan extract, Spruce lignin extract) resulted in similar mass spectra, demonstrating the difficulties of ToF-SIMS as an exploratory method. Since these standards are all similar in composition (i.e., all contain carbon, hydrogen and oxygen), the m/z values of many fragment ions are likely to be isobaric making, it difficult to differentiate between different compounds at the same nominal mass.

***Populus* Tissue**

The optimal sample preparation method for wood tissue was determined by comparing the spectra obtained from four different sample preparation methods, a) no gold coating, b) DHB coating, c) DHB and gold coating and d) gold coating. This comparison revealed that 1 nm of gold coating gave optimal spectra of wood tissue. Briefly, the intensity of ions was increased and higher mass ions were observed—all wood tissue samples reported in this chapter were coated with a 1 nm layer of gold prior to ToF-SIMS analysis (the gold layer was increased to 2 nm for standard analysis). The focus of this section was to compare/contrast different regions within one tissue section in order to determine characteristic ions of a particular region, e.g., regions of lignified versus non-lignified cells.

Positive ion mode

Positive ion ToF-SIMS mass spectra from regions of interest are displayed in Figure 5-5. The regions of interest are identified by the color of the corresponding MS spectrum. Briefly, red is from the phloem, green is from the lignified phloem fiber cells and blue is from the secondary xylem. The spectra from the three different regions of the tissue are all similar; however, some differences were observed. For example, in the top spectrum, the red line (phloem) is more abundant at m/z value 23 and 39, which are identified as Na^+ and K^+ , respectively. The salts are interesting to observe in intact wood tissue because the localization of salts can be correlated with regions that are more characteristics of living cells, i.e, only primary cell walls and the vascular cambium, unlike the dead cells of the secondary xylem.

The similarities observed in the ToF-SIMS spectra between the different regions of interest result from the similarities of the carbohydrates that compose the primary and secondary cell walls, which tend to fragment similarly. Significant differences are observed, specifically, m/z value 265, 266 and 607; however, some of the differences could be subtle and more in-depth analysis to distinguish between the regions is required. For example, a multivariate analysis technique could be used to determine ions that are significantly different, thus representative, of certain tissue regions; this approach will be discussed in Chapter 6.

The optical, autofluorescence, calcofluor white (CW), total ion current (TIC) and extracted ion images of the secondary phloem, vascular cambium and secondary xylem regions are displayed in Figure 5-6. The autofluorescence image (Figure 5-6b) identifies the regions of lignified cell walls, specifically located in the secondary xylem and the phloem fiber cells—the lack of green fluorescence observed in the secondary phloem

identifies the regions containing only primary cell walls. The CW white image (Figure 5-6c) displays that cellulose is present in both the secondary xylem and phloem. The fluorescence signal appears less intense in the secondary xylem, which could be a result of the interaction of the cellulose with lignin. The fluorescence images are used as markers for the different regions and are useful in ion identification.

The TIC image (Figure 5-6d) illustrates the higher spatial resolution when compared with MALDI-MS imaging and shows that ion signal is observed over the whole tissue section. The image of m/z 39, K^+ , (Figure 5-6e) shows intense ion signal in the bottom part of the phloem, which is more characteristic of living cells and less intense signal in the secondary xylem, which is more characteristic of dead cells. It is also interesting to note the intense K^+ ion signal observed in the region between the secondary xylem and phloem. This is consistent with the location of vascular cambium, which is more representative of living cells. This demonstrates that ToF-SIMS has adequate spatial resolution and selectivity to distinguish between these areas, as the spatial resolution of MALDI-MS imaging could not.

Another ion observed localized in the vascular cambium region (which also showed increased K^+ signal) was m/z 331, displayed in Figure 5-6f— m/z 331 is consistent with the m/z value of a radical cation on of a classification of compounds called Gibberellins (GA). GA are plant hormones that has been associated with cambial growth and has been reported to be present in low abundance in healthy stems and aids in the differentiation of phloem and xylem cells during wood formation.^{124, 125} The ion intensity observed was low, which is expected due to the width of the region (~50 μm), as well as the relative abundance of GA expected in vascular cambium tissue.

Although the identification cannot be confirmed in the present study, the evidence suggests that m/z 331 could be tentatively identified as GA.

Figure 5-6g displays the ion image of m/z value 85, which has been previously identified as a non-specific polysaccharide fragment, $C_4H_7O_2^+$.¹²³ and shows relatively even signal across the entire tissue. In contrast, Figure 5-6h (m/z 69) and Figure 5-6i (m/z 607) display distinct localization in the phloem fiber cells and the secondary xylem, similar to the lignin autofluorescence signal (Figure 5-6b). The ion, m/z value 69, has been previously reported as both $C_4H_5O^+$, resulting from a non-specific polysaccharide fragment and $C_5H_9^+$, resulting from a lignin fragment.¹²³ However, the localization of the ion signal suggests that the m/z value 69 is indicative of lignified cells, but the presence of ions originating from polysaccharides cannot be ruled out. The extracted ion image demonstrates that more intense ion signal is observed in the presence of lignified cells. These results are also consistent with that MALDI-LIT tandem MS analysis that showed localization of lignin (m/z 181) in the phloem fiber cells and secondary xylem (Figure 3-7).

Furthermore, m/z 607 shows similar ion signal localization, also suggesting an ion indicative of lignified cells. Although it appears that m/z 607 is more selective (i.e., no ion signal is observed in the phloem, suggesting no isobaric carbohydrate ions), the absolute intensity of m/z 607 is an order of magnitude lower than m/z 69. The lower observed ion signal could be a result of the inherent decrease with m/z value in secondary ion yield of ToF-SIMS experiments, but can still be informative about relative lignin composition within the intact tissue section.

Analyzing the phloem and the xylem region using ToF-SIMS, and comparing the results to fluorescence microscopy, aided in identifying ions representative of different regions of tissue. To help to validate ion identifications reported above, the same m/z values were monitored in different sections, as well as different areas of the tissue, and showed consistent data. Figure 5-7 displays the optical, fluorescence microscopy and ion images of the pith and secondary xylem region of the stem, and corresponds to the same ion images displayed in Figure 5-6. Briefly, the autofluorescence shows more lignified cells in the secondary xylem. The ion image of m/z 39 (K^+) shows localization in the pith, which is more characteristic of living cells.

The ion signal of m/z value 331 is localized only in the pith region and was not observed in the secondary xylem—these results are still consistent with the identification of GA. Since GA is a plant hormone, it would not be expected to be observed in dead cells (e.g., the secondary xylem). The pith, on the other hand, is primarily composed of primary cell walls, and a higher concentration of salts were observed, thus is expected to have more characteristics of living cells.

Figures 5-7g and Figure 5-7i demonstrate similar trends to those discussed for Figure 5-6. The ion m/z value 85 shows even ion intensity over the tissue, and identified as a non-specific carbohydrate fragment. The ion image of m/z value 69 shows ion signal over the whole tissue, but displays an increase in ion signal where lignified cells are observed in the autofluorescence image. Lastly, the ion image m/z 607 shows highly localized ion signal in the secondary xylem (lignified cell walls). Observing the autofluorescence of the lignin more closely (Figure 5-7b) shows a gradient of green fluorescence signal—the most intense signal is observed closest to the pith and the

least intense signals are observed in the bottom of the ion image. This same trend can be correlated with the ion signal of m/z value 607, where more intense ions signal is observed in the region nearest the pith and decreased ion signal is observed further away from the pith. This further suggests that m/z value 607 can identify regions lignified tissue and furthermore provide the relative lignin concentrations.

Comparison of ToF-SIMS with MALDI-LIT-MS

Figure 5-8 compares microscopy, MALDI tandem MS imaging, ToF-SIMS imaging and fluorescence microscopy of *Populus* stem. To make a better comparison, the raster step size of the MALDI tandem MS image displayed in Figure 5-8 b was reduced from 50 μm (as used in Chapter 3) to 10 μm (which introduces a large amount of oversampling). The tandem MS image of m/z 1319 \rightarrow 995, identified as a cellulose ion, displays intense ion signal in the secondary xylem and the lignified phloem fiber cells. Figure 5-8 c shows ToF-SIMS image of m/z 69 (different stem), which was identified to be characteristic of cellulose ions and Figure 5-8 d displays a CW fluorescence image of the same stem.

Comparing the MALDI-MS image with ToF-SIMS image illustrates the dramatic increase in spatial resolution achieved with ToF-SIMS imaging (even when a significant amount of oversampling was performed for MALDI imaging). Specifically, the ToF-SIMS image can resolve cell walls within the lignified phloem bundles; the MALDI-MS image displays a large region of intense ion signal in the phloem fiber bundles. Since biomass research focuses on the thickened secondary cell walls, ToF-SIMS is valuable to obtain information about the cell wall thickness; however, identifying only one classification of ions to a particular m/z value is less informative than the chemical information provided by MALDI-MS imaging.

Another difference observed between MALDI-MS imaging and ToF-SIMS imaging is selectivity of the experiment. As discussed in Chapter 3, MALDI generates more intact ions, which helps to provide a more accurate identification. In addition, tandem MS imaging provides for selectivity by generating product ion spectra, which can distinguish between isobaric ions. ToF-SIMS, The small fragment m/z 69 could result from fragmentation of cellulose, hemicellulose and/or lignin; fluorescence microscopy helps to provide a different approach to provide more positive compound identification.

Negative Ion Mode

The same tissue sections describe above were also analyzed in negative ion mode; the results are displayed in Figures 5-9 and 5-10. For negative ion mode analyses, the same ionization parameters are used and negative ions are analyzed by switching the polarity of the ion extraction, ion optics and ESA voltages. Negative ion mode analysis, in general, resulted in less characteristic ions and lower absolute abundance of the ions observed; however, some ions displayed localization that corresponded with lignified cell walls.

As observed in Figures 5-9c and 5-10c, ion signal is observed over the whole tissue and the image quality is similar to positive ion mode. The extracted ion image of m/z value 35, identified as a chloride ion (Cl^-), displays ion signal over the whole tissue, but appears to be more abundant in the phloem regions. Since chloride is a common anion of salts, the localization is expected to be similar to the cations, K^+ , displayed in the previous figures. However, the sensitivity of negative ion mode is likely lower than the sensitivity in positive ion mode due to the decrease in TIC.

Extracted ion images of m/z 80 and 97 (Figures 2-9 e-f and 2-10 e-f) are localized in the regions of lignified cells, tentatively, m/z value 80 could be identified as $[\text{SO}_3]^-$ and

m/z value 97 can be identified as $[\text{H}_2\text{PO}_4]^-$, however the identification cannot be verified without MS/MS or accurate mass data. In addition, the localization of these particular ions cannot be explained based on known composition of wood tissue in literature searches.

Negative ion mode analyses were more exploratory in nature, and the results were not conclusive. However, despite the lack of identification, the localization of some ion signal was consistent with regions containing lignified cells identified by fluorescent microscopy. Further studies, such as increasing the acquisition time at each tile, could be performed to increase the sensitivity of the experiment to help identify ions and possibly determine other characteristic ions of the different regions of wood tissue.

Conclusions

This chapter reported the successful analysis of intact *Populus* tissue sections using a ToF-SIMS microscope imaging method. Different sample preparation techniques were used and the optimal spectra were observed when the sample (or standard) was coated with a thin layer of gold. Since wood tissue is a non-conductive surface, the gold coating helped to decrease charge build-up on the sample surface, generate ions at the same initial potential energy and increase secondary ion yield of higher mass ions, which ultimately increased the sensitivity of the experiment.

Extracted ion images demonstrate the ability of ToF-SIMS to provide high spatial resolution, chemically selective images of intact wood tissue sections. Several ions, although not positively identified, were localized in different regions of tissue and showed high correlation with fluorescence microscopy—these ions can be considered characteristic of these tissue regions to be monitored. In addition, further data

processing could help to increase the chemical information obtained from ToF-SIMS imaging.

In conclusion, the ability to correlate ToF-SIMS images with other imaging techniques will help to provide a more comprehensive analysis of wood tissue. ToF-SIMS imaging provides the spatial resolution needed to provide more insight into spatial changes in chemical composition of pretreated wood tissue. Ultimately, this technique could help to visualize the changes of LCM throughout pretreatment processing.

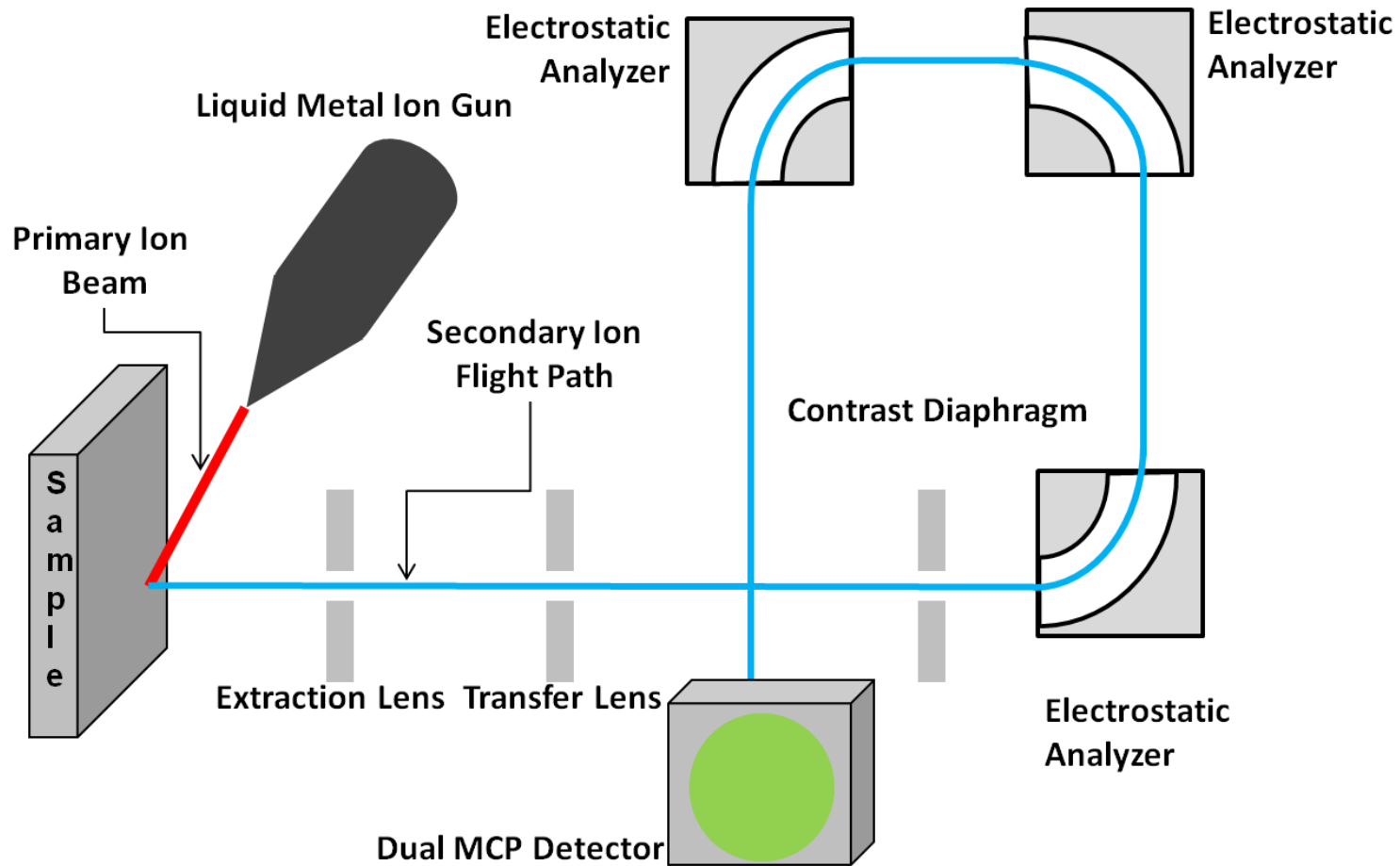


Figure 5-1. Schematic of Physical Electronics TRIFT II ToF-SIMS instrument. The secondary ions generated from the sample are guided through series of optics and three electrostatic analyzers (ESA). The spatial position of the secondary ions is conserved and detected with an MCP detector.

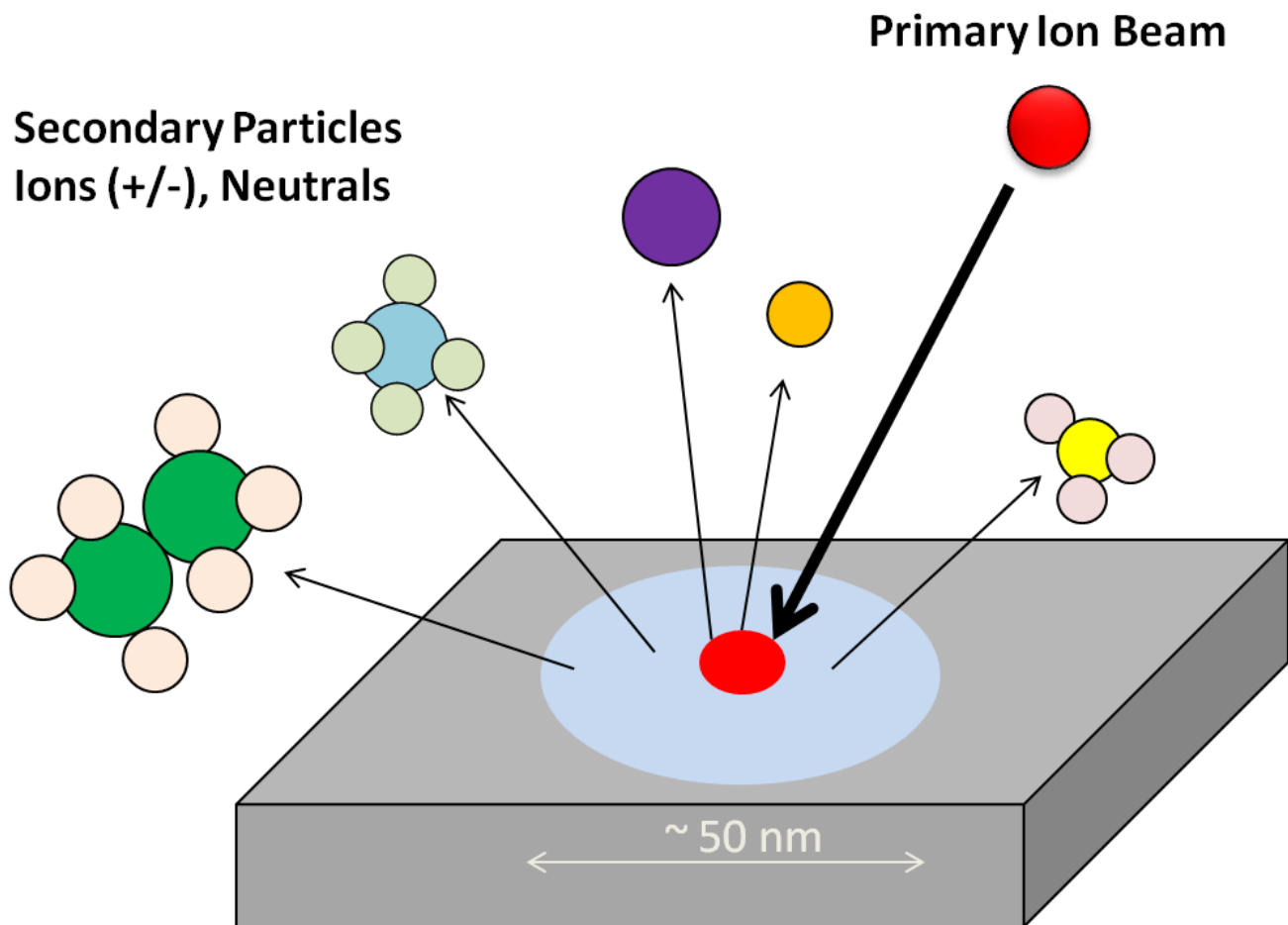
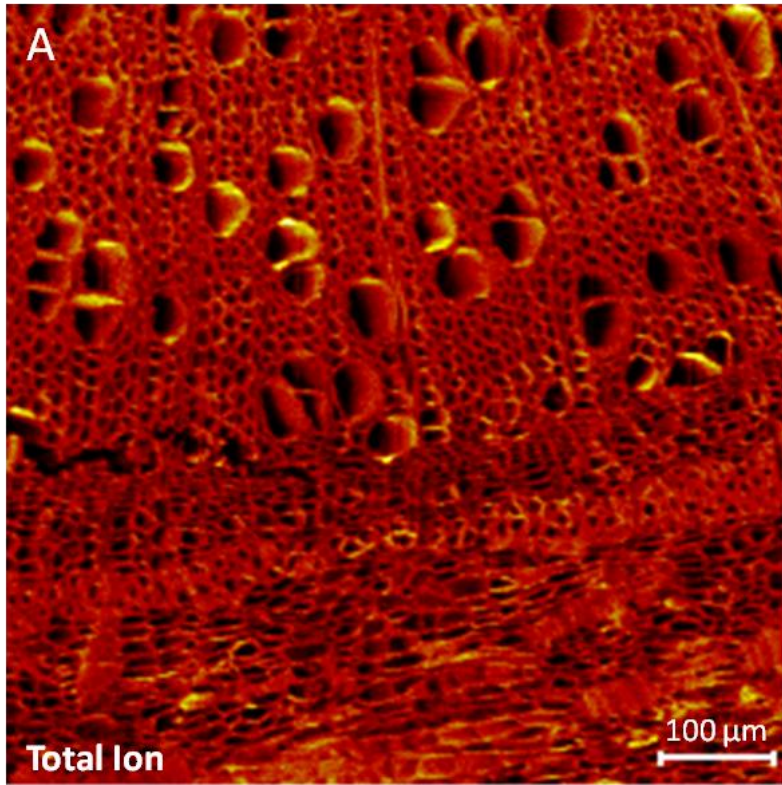


Figure 5-2. Cartoon illustration representing secondary ionization. The high energy primary ion beam bombards the sample surface to release secondary particles, including positive/negative ions and neutrals.

Unbunched



Bunched

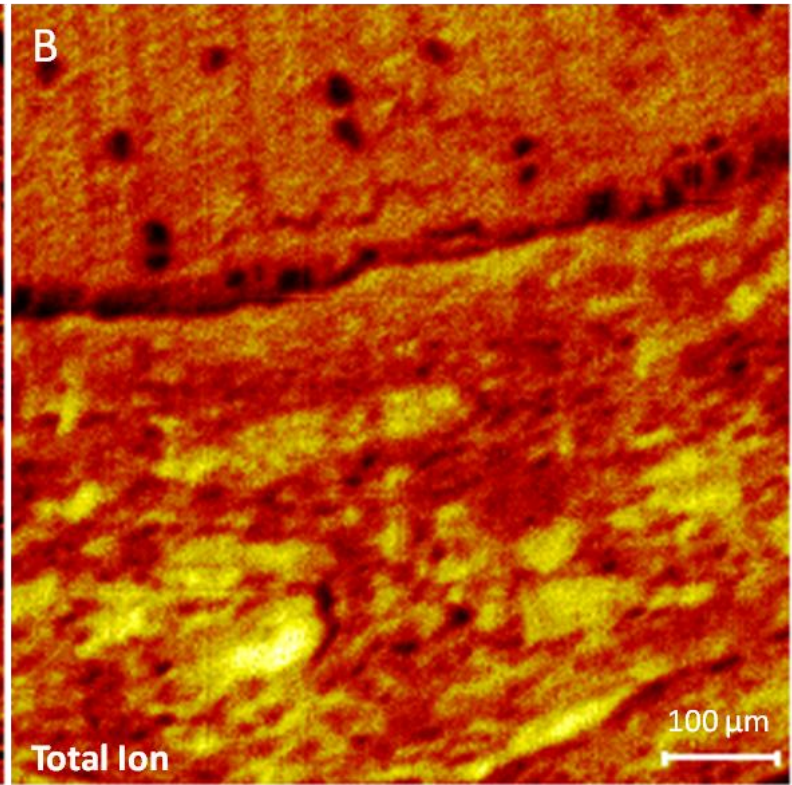


Figure 5-3. Comparison of ToF-SIMS imaging modes. A) Unbunched. B) Bunched. The unbunched mode offers superior spatial resolution at the cost of poorer mass resolution

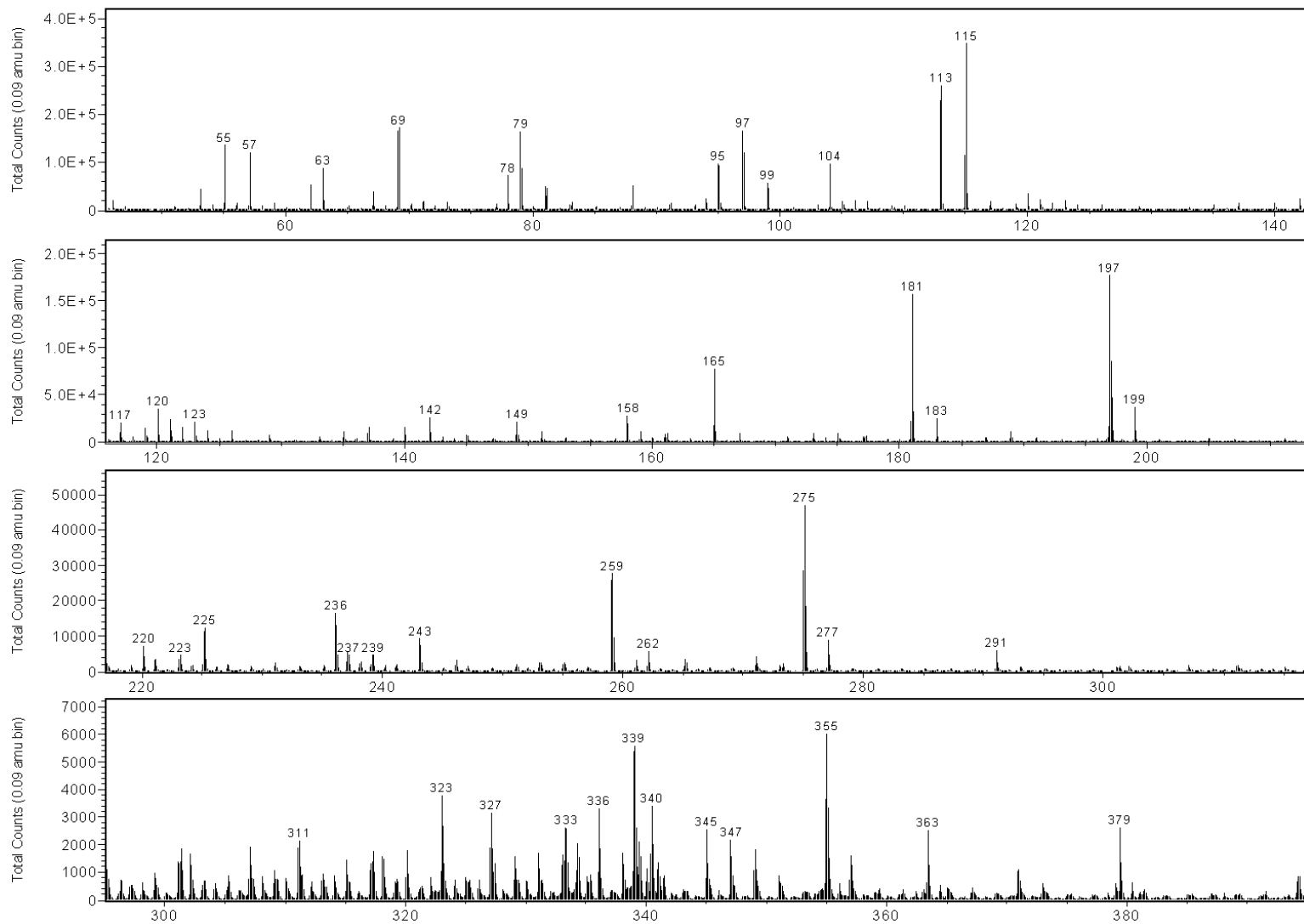


Figure 5-4. ToF-SIMS spectrum of Birch Xylan extract coated with 2 nm gold. Spectra were split to show lower abundance ions. SIMS is a high-energy ionization source, which results in high fragmentation, and thus higher m/z ions are typically lower in abundance, as seen here.

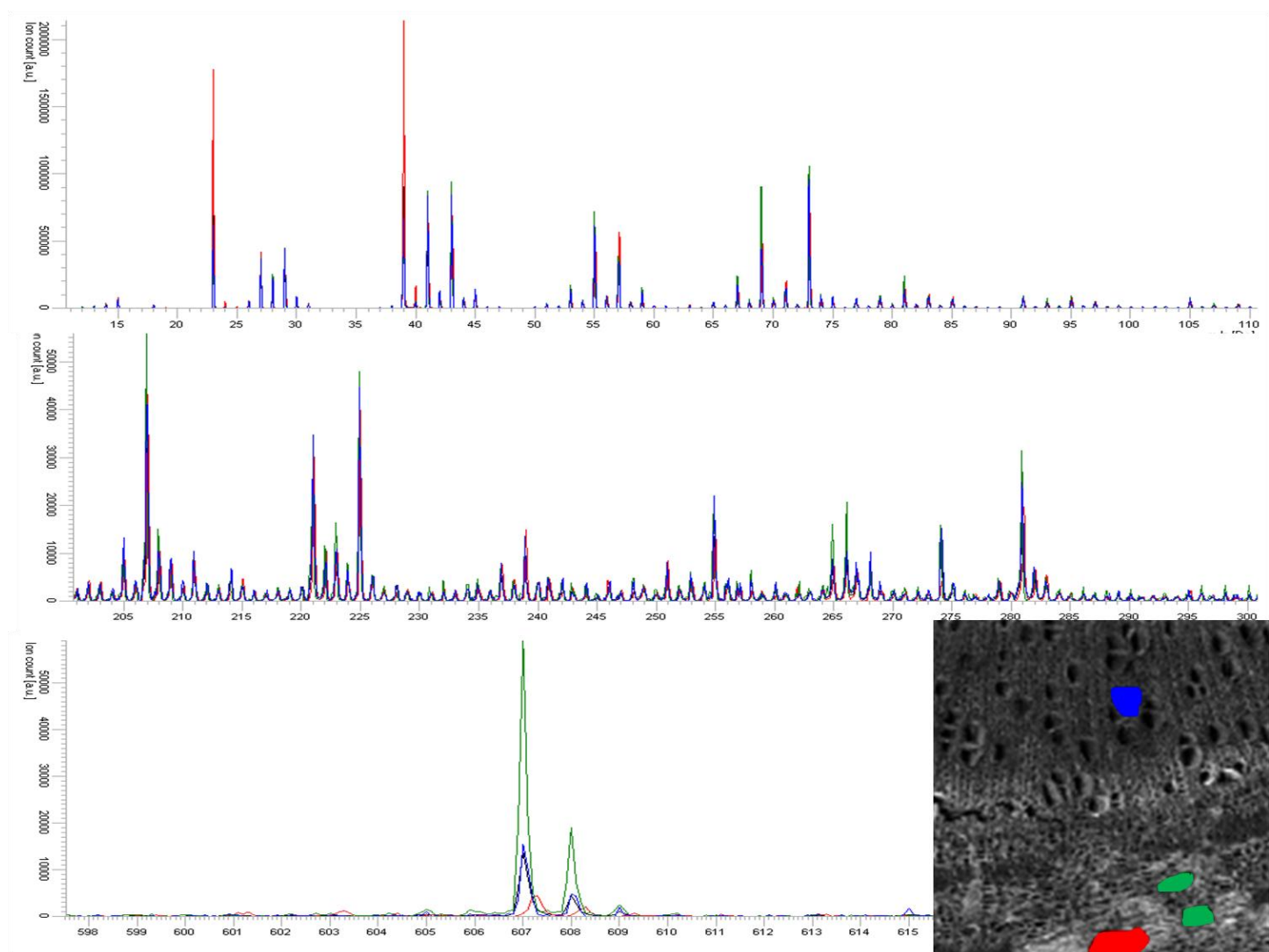


Figure 5-5. ToF-SIMS spectra from different regions of interest in wood tissue. Colors correspond to the regions outlined in the optical image. Despite the different regions, most ions are similar showing the difficulties in identifying chemical markers for distinctive regions of wood tissue.

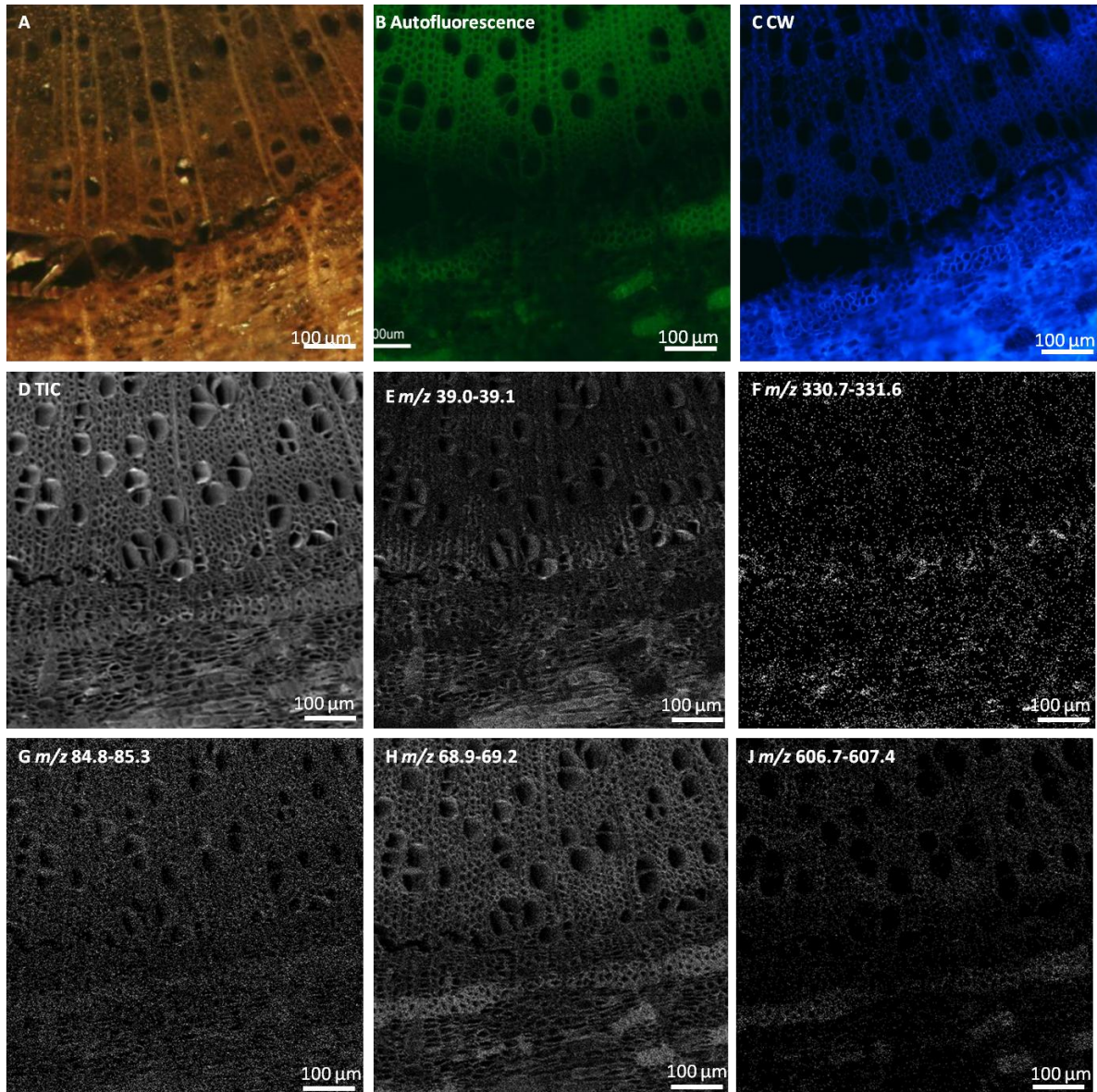


Figure 5-6. Optical, fluorescence and positive ion ToF-SIMS images of phloem and xylem of *Populus* wood stem. Images show localization of different ions in different regions of wood tissue.

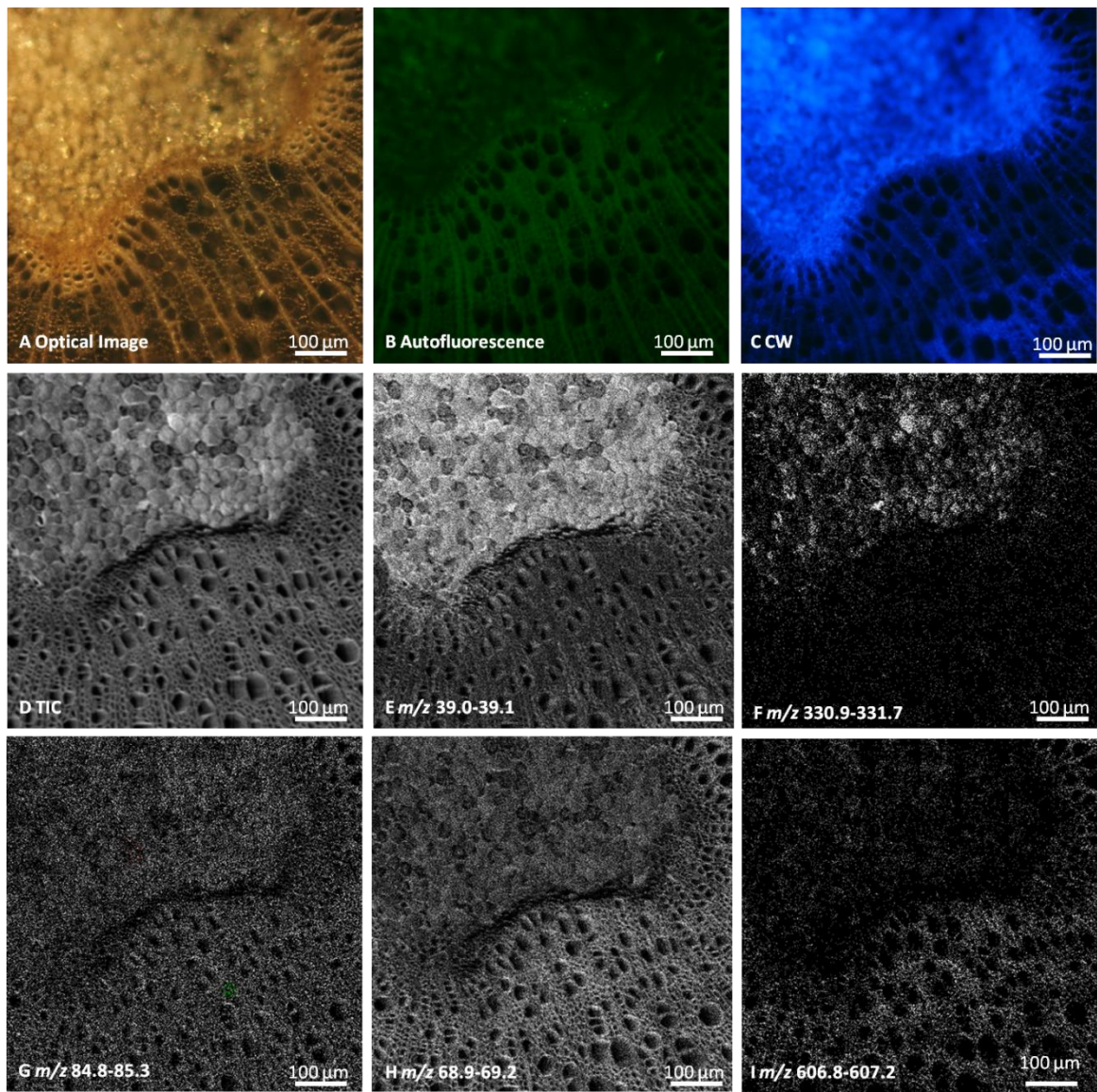


Figure 5-7. Optical, fluorescence and positive ion ToF-SIMS images of pith and xylem of *Populus* wood stem. Images show localization of different ions in different regions of wood tissue.

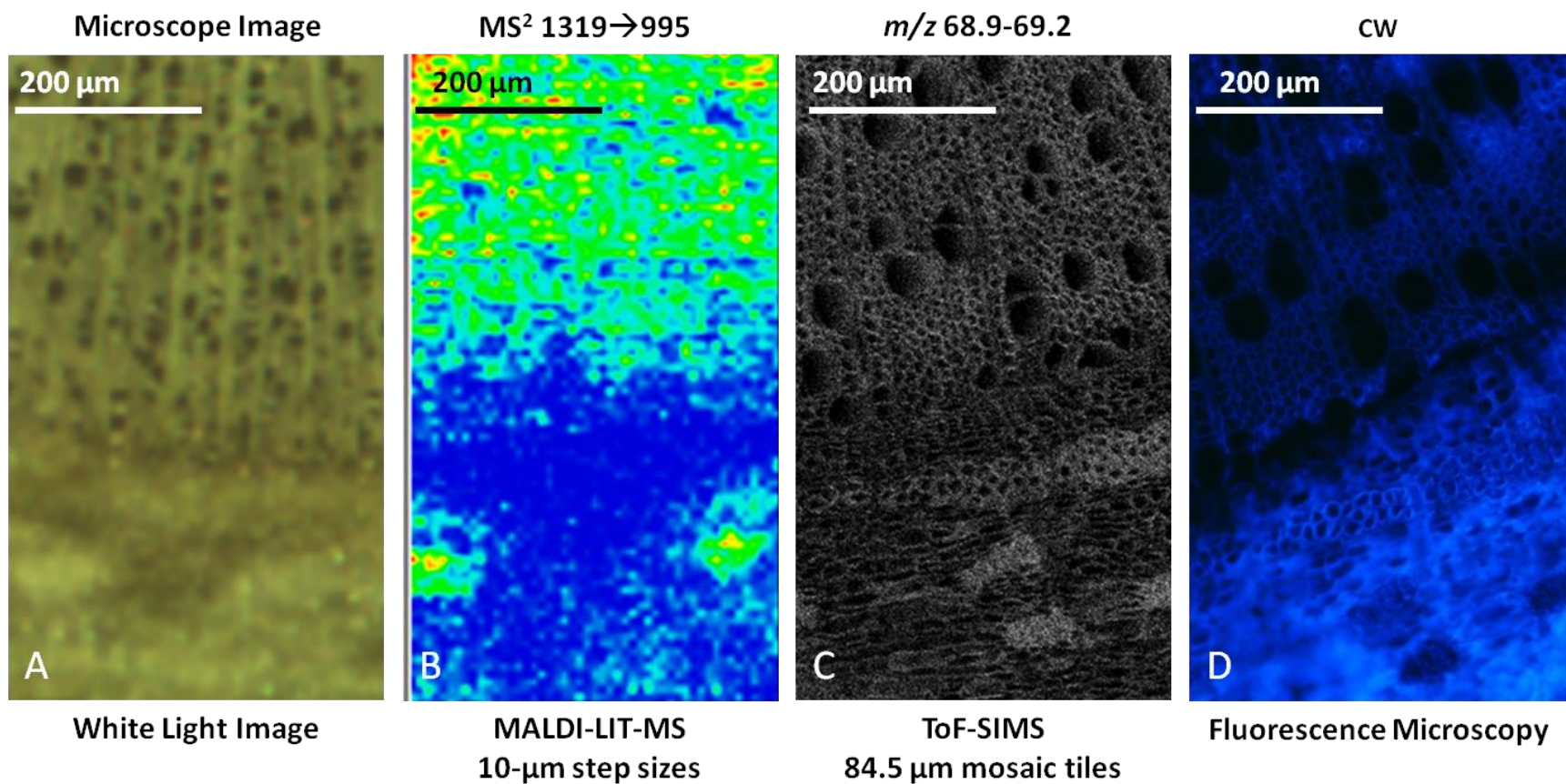


Figure 5-8. Comparison of different imaging techniques. A) The microscope image. B) MALDI-LIT-MS image of a cellulose ion. C) ToF-SIMS image. D) CW fluorescence image. Reducing the raster step size to 10- μ m shows intense ion signal in the region of the lignified phloem fibers.. Note A and B are images of the same stem. C and D are the same stem, but different from A and B.

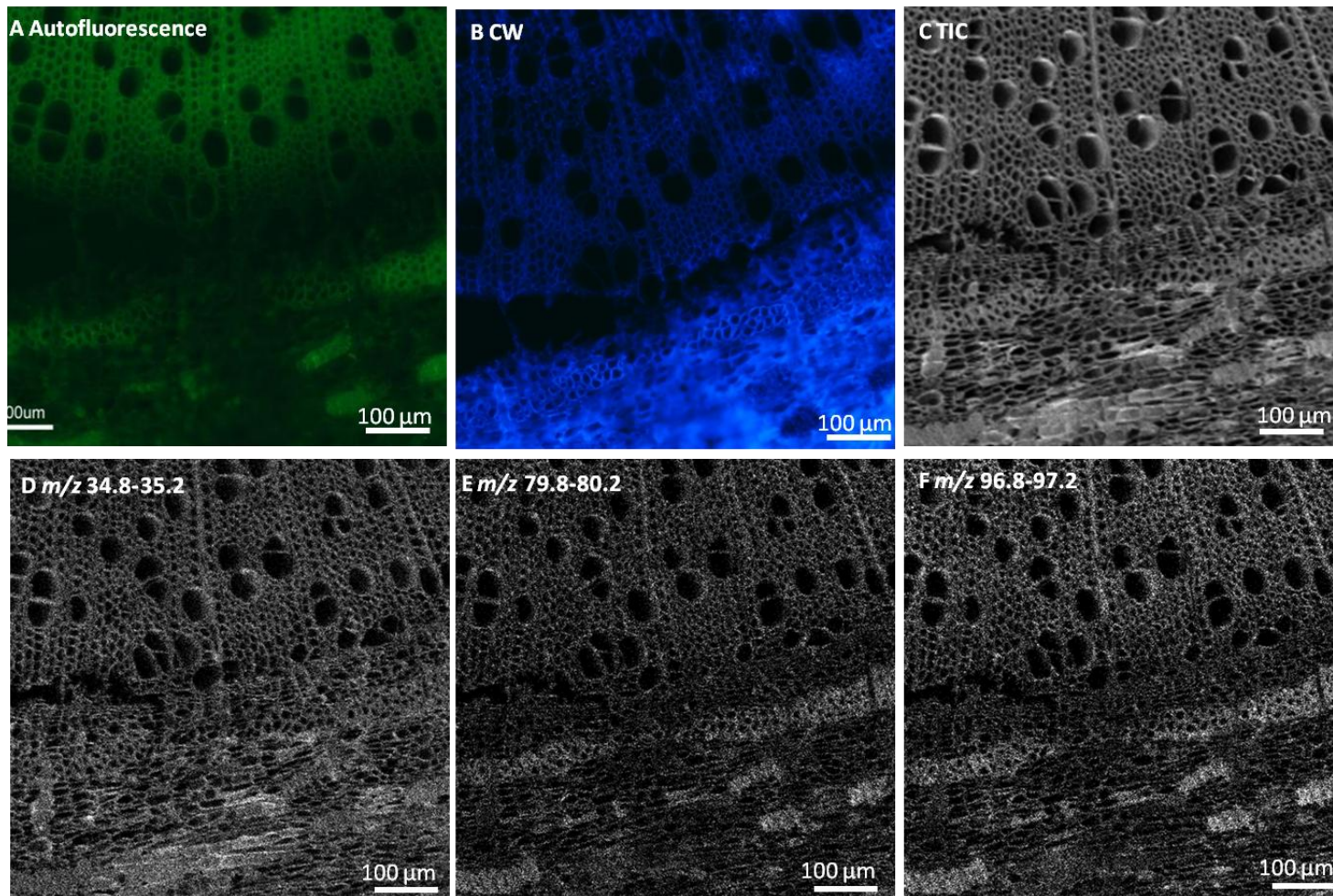


Figure 5-9. Optical, fluorescence and negative ion ToF-SIMS images of phloem and xylem of *Populus* wood stem. Images show localization of different ions in different regions of wood tissue.

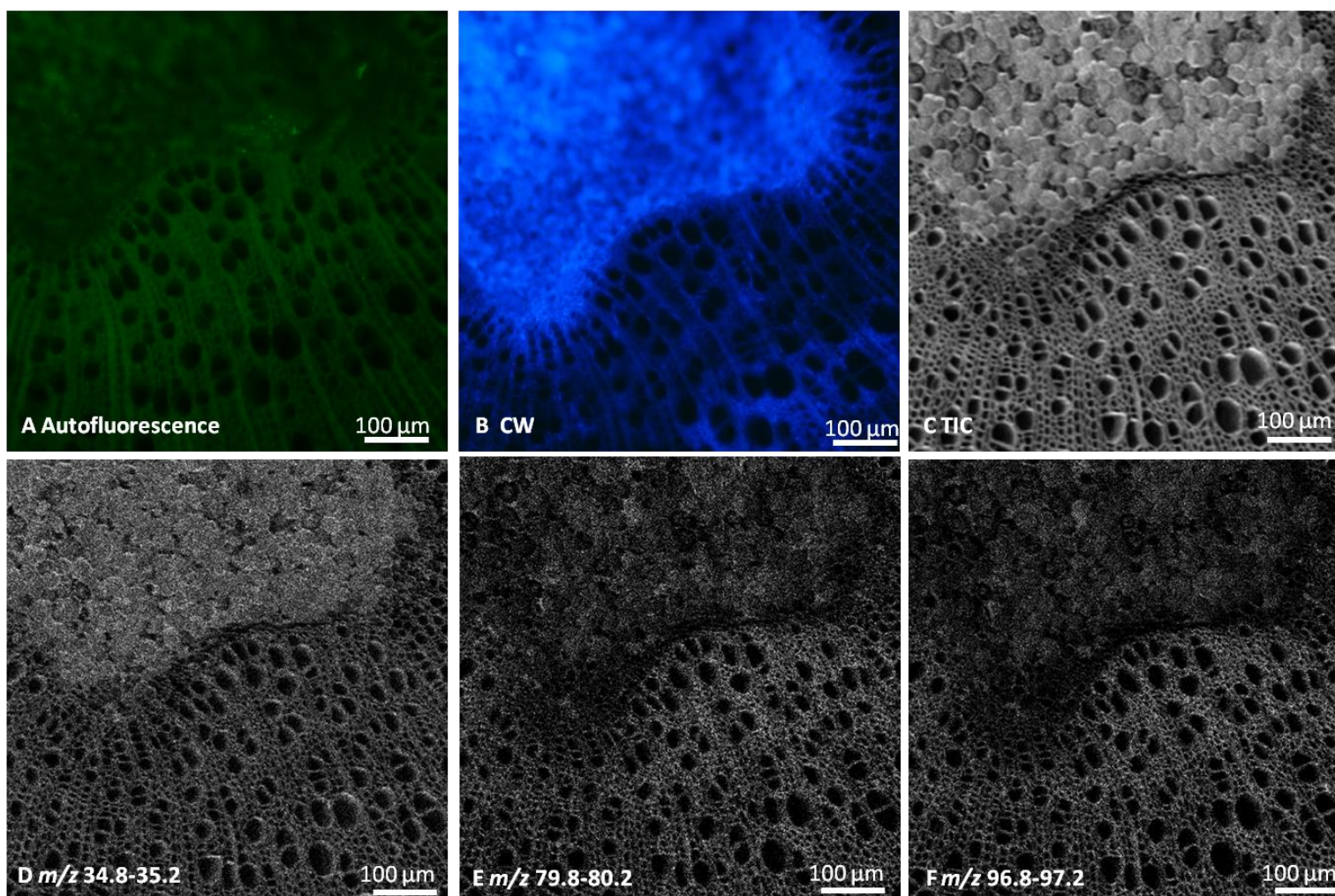


Figure 5-10. Optical, fluorescence and negative ion ToF-SIMS images of pith and xylem of *Populus* wood stem. Images show localization of different ions in different regions of wood tissue.

CHAPTER 6 MULTIVARIATE ANALYSIS OF MALDI-MS AND TOF-SIMS IMAGING DATA

Overview

The large data sets generated by MS imaging experiments make a complete data analysis difficult, i.e., a large portion of the data is discarded or overlooked. Multivariate and/or statistical analyses can overcome this difficulty by analyzing larger portions of the data set in a timely manner. In addition, multivariate analyses helps reduce the data set to explain differences observed in mass spectra in fewer variables. This is especially useful for a more comprehensive analysis of the complex mass spectra observed in MS imaging of tissue sections.

Using multivariate analysis in chemistry is not a new idea. In the 1980s, multivariate analyses were developed to analyze the complex spectra of pyrolysis mass spectrometry (Py-MS) data. Many multivariate analysis methods required reference spectra from standards and/or 'pure mass' peaks; however, this is not feasible for Py-MS data analysis of biological samples, such as yeasts and extracts.¹²⁶ To overcome these limitations, multivariate methods that do not require calibrations were applied to chemical and biological data sets, e.g., factor analysis and principal component analysis (PCA).^{127,128}

Factor analysis and PCA are unsupervised methods that efficiently describe differences between samples within a data set, which can be used to identify and quantify the components of a mixture. In contrast to supervised methods, unsupervised statistical methods are performed without prior grouping (or assumptions) of the input data.¹²⁹ Multivariate analysis of Py-MS data extracted differences within a data set of related samples;¹²⁷ this is consistent with the goal of matrix-assisted laser

desorption/ionization mass spectrometry (MALDI-MS) and time-of-flight mass spectrometry ToF-MS analysis of intact *Populus* tissue. This chapter discusses the adaptation of multivariate statistical methods for the analysis of MALDI-MS data of the plant-related standards discussed in Chapter 2. The statistical method provides the groundwork for using MALDI-MS to determine cellulose, hemicellulose and lignin concentrations in intact lignocellulosic material (LCM). Further, an in-house written statistical software program was used to analyze ToF-SIMS imaging data to aid in identifying ions that are observed in different regions within an intact tissue section.

Principal Component Analysis

PCA has been a popular unsupervised, multivariate analysis technique for chemists since the 1970s due to the multivariate data collection inherent in many chemistry experiments. In the broadest scope, PCA is considered a pattern recognition technique, and specifically within mass spectrometry, PCA compares mass spectra within a data set to determine patterns in the mass spectra that describe the most variance between the samples.¹³⁰ Two important parameters of PCA include, (1) the number of principal components (PCs) that account for the variance within data set and (2) the *scores* and *loadings* of a PC, which is discussed in detail below.¹³⁰

Briefly describing the mathematics behind PCA, the data is arranged in a data matrix, $X_{i,j}$ where the rows (i) represent different samples and columns (j) represent different variables, such as m/z values.¹³¹ Using linear algebra and abstract transformations, PCA describes data matrix $X_{i,j}$ as a product of column matrix, $T_{i,a}$ and row matrix $P_{a,j}$, represented by

$$X_{i,j} = T_{i,a} \bullet P_{a,j} \quad (6-1)$$

Where $T_{i,a}$ is the scores and $P_{a,j}$ are the loadings (Figure 6-1). The PCA scores represent the projection of the data set on the determined PCs, and the PCA loadings are used to determine the contribution of the variable on each PC. The number of rows observed in T and the number of columns observed in P are limited by the number of rows (i) and columns (j) in the original data matrix $X_{i,j}$. The common dimension (a) represents the PCs and are linear combinations of the original variables calculated from PCA.¹³⁰ The PCs determined are chosen so that PC1 accounts for the most variability, PC2 accounts for the second most variability, etc, which helps with data deconvolution and identification of representative markers. Furthermore, PCA determines the variance accounted for by a PC and often only 10 PCs (as opposed to hundreds or thousands of variables) can account for > 99% of the variability in the data set.¹²⁹

PCA results are typically displayed in two (or three) dimensional 'PCA scores plots,' where the scores of each data point, representing separate experiments, are plotted for the different PCs.¹³⁰ An ideal PCA scores plot of three entirely different samples (three replicates of each) is displayed in Figure 6-2. PCA analysis should group together the replicates, thus all of the 'A's' should be close to each other, and should separate the different samples—the plot in Figure 6-2 illustrates that B's and C's are separated by PC1 and A is separated from B and C by PC2.

In addition to scores plots, 'PCA loadings plots' are also useful in PCA analysis. PCA loadings plots are generated by plotting the Eigenvalue (loading) for each vector (representing each variable) for a particular PC. Loadings can be both positive or negative and the absolute value of the loading represents the contribution to variance of the analysis (e.g, higher absolute value loading scores accounts for more variability).

For example, Figure 6-2 illustrates that B has a positive loading on PC1 and a negative loading on PC2; thus, it is determined that PC1 is characteristic of sample B. Plotting the positive loadings of PC1 provides ‘mathematically derived’ mass spectra that display ions contributing to the variance of PC1. These loadings plots should ideally resemble the raw mass spectrum of sample B.¹²⁶

These types of analyses have been reported to determine the composition and concentration of complex mixtures.¹²⁶ In the example above, if a MALDI-MS analysis of an unknown mixture contain A, B and/or C was performed, the position of the unknown mixture data on the Scores Plot should be indicative of the composition. For example, if the unknown mixture is plotted more closely to the C group, than it could be concluded that the unknown mixture contains more of compound C than the other compounds—if the mixture was composed of 33.3% of each A, B and C, than the mixture would appear in the center of the ‘triangle.’

In addition to analysis of standards and mixtures, PCA has been applied to both ToF-SIMS microscope imaging data^{132,133} and more recently, MALDI-MS imaging data.¹³⁴⁻¹³⁶ Due to the high fragmentation (in the case of ToF-SIMS), high complexity of the spectra of any tissue analysis, PCA is often necessary to analyze the MS imaging data to help differentiate regions of tissue.^{133,137} More specifically, PCA ‘scores images’ are generated to visualize the differences between the regions.^{133,136} Once differences are recognized, the loadings can be used to identify characteristic ions.

PCA is a complex series of mathematical manipulations and an entire PhD project could be aimed toward developing PCA for the analysis of MS imaging data; thus, PCA is often performed using purchased software packages and/or open-source programs.

Data preprocessing, such as mean centering or normalization, is often necessary prior to any statistical analysis, which may or may not be included in the software package. These steps, as well as other pre-processing techniques, can alter PCA results dramatically and are important for successful PCA analyses. The techniques used for these analysis will be discussed later in the chapter.

PCA of Lignocellulosic Material Standards

Since lignocellulosic materials (LCM) are primarily composed of cellulose, hemicellulose and lignin, PCA experiments aimed to determine the composition of each classification of compound within a tissue section were designed. Three replicates of an average of 50 scans from an analysis of 'pure standards,' MCC, Birch xylan extract and lignin extract, were used for the experiments reported below.

Software

PCA performed on MALDI-MS data used Tanagra v 1.4.36 (Lyon, France) and open-source free DATA MINING software available for download (<http://eric.univ-lyon2.fr/~ricco/tanagra/index.html>).¹³⁸ Prior to analysis in the software, the raw data were exported from Qual Browser v. 2.0 (Thermo Scientific, Inc.) into Microsoft® Excel to generate the original data matrix (Figure 6-3) and data preprocessing.

MetaboAnalyst,¹³⁹ an online webserver metabolomic data analysis system was also explored, but no results from those experiments are reported in this chapter.

Data Preprocessing

One of the biggest challenges in data preprocessing was manipulating the data to ensure that the m/z values in each sample were in line with each other. When exporting data from Qual Browser, only the m/z values with ion intensities are exporting, leaving gaps where ions are not observed. Since different samples have different ions that are

not observed in the mass spectrum, adjusting the data to have the m/z values in the proper columns to complete the matrix was difficult. To overcome this difficulty, a Macro program was used in Excel to insert the missing values in a series of m/z .

When inserting m/z values that are not observed in the mass spectra, an intensity value for that m/z value must also be inserted. One of the solutions is to insert a zero for the missing intensity; however, this could lead to false representations of the PCA data. For example, if there is an ion that is not observed in any of the samples, then the intensity of that certain m/z will be zero and will be highly correlated to each other. In mass spectrometry, zero intensity is not always indicative of the absence of an analyte, thus PCA describing correlation between the samples based on the zero intensity is not a valid result. Different methods have been developed to insert missing values (other than zero) to alleviate this challenge. Some of the common methods that are used include inserting random values, inserting a small value (half of the minimum value observed) and inserting the mean value of the observed intensities.¹³⁹ For these experiments, m/z values that were not present in 2/3 of the samples were discarded and small values were used for the intensities of inserted m/z .

Due to the irreproducibility of ion intensities between different MALDI-MS analyses, a normalization procedure is important to help to increase the quality of the PCA analysis, i.e., without normalization the variations determined by PCA could be due to intrinsic MALDI differences. Some normalization methods include: (1) normalizing to the sum of the absolute value of all the variables, (2) normalizing to the sum of the square value of all variables for a given sample and (3) normalizing to the maximum value observed for all variables for the given sample.¹³⁹ These experiments normalized

all the intensities to the maximum value observed for a particular sample, e.g., each intensity value of a m/z value was normalized to the average TIC of those spectra.

PCA Results

The optimized PCA scores plot of three replicate spots of MALDI-MS analysis from three different 'pure' standards, MCC, Birch xylan extract and Spruce lignin extract are displayed in Figure 6-4. As expected, the three replicates of each compound grouped closely together, and the three different groups formed a triangle. The plot also demonstrates that the variance of PC1 is due to the differences between lignin and cellulose—the score of Birch xylan extract on PC1 is nearly zero, indicating PC1 is not affected by Birch xylan extract. The variance of PC2 describes the difference between Birch xylan from MCC and lignin.

As discussed earlier, PCA loading plots give insight into the 'weighting' of variables on the PCs determined. Figures 6-5 through 6-7 displays the comparison between PC loading plots (purple) and the raw mass spectra (black). The PCA loading plots were prepared by extracting the loading values from the Tanagra program and exporting into excel. The values were then multiplied by the average value for each m/z in order to put the intensities on a similar scale as the mass spectra.¹²⁶ The loadings plots were prepared using the Microsoft[®] Excel graphing tool, and the loading value is plotted versus the m/z , so a direct comparison can be made with the mass spectra.

Figure 6-5 displays the positive loadings on PC1, which should be characteristic of lignin extract based on the scores plot in Figure 6-4. The comparison of the PC1 loading plot (positive y-axis) with the MALDI-MS of lignin shows high correlation, with ions observed at nearly every m/z and the distribution of the ions are similar. It is interesting to note, that in the MALDI-MS of lignin, MCC ions are observed (since this is an extract,

other compounds are present); however, in the PC1 loadings plot, the MCC ions observed are removed by the PCA. This shows the ability of PCA to determine small differences between samples.

Similarly, Figure 6-6 shows the PC1 negative loadings plot, compared with the MALDI MS spectrum of MCC. Again, the PC factor spectrum is similar to MALDI-MS spectrum, showing abundant ions 162 mass units apart, indicative of a polymer of a six-carbon sugar. In addition, the PC1 loadings plot also shows similar ion abundance distributions. Another example displayed in Figure 6-7, is the Birch xylan MALDI MS spectrum compared with the positive loadings of PC2, which shows similarities. The similarities between the PC loadings plots and the MALDI-MS analysis of the standards show the ability of PCA to determine PCs that are highly correlating with the ions observed in the MALDI-MS of LCMs.

After the analysis was optimized for the standards, PCA was used to analyze the standards, as well as MALDI-MS spectra of intact wood tissue (data not shown). The PCA scores plot showed that most of the wood samples were grouping close to the lignin. This was not expected since lignin is least abundant classification of compounds in wood tissue (when compared to cellulose and hemicellulose). However, after analyzing the data, the observed results were logical due to several reasons. For example, the 'standard' for lignin results in ions at nearly every m/z , which is similar to the wood tissue analysis, even though wood is not primarily composed of lignin. PCA is an unsupervised, pattern recognition technique, thus it is reasonable that the analysis would group these together. In the future, these experiments will be performed using a supervised technique, such as discriminant analysis (DA) or partial least squares DA

(PLS-DA). In supervised techniques, the chemist provides information to the program on the identity of the classifications of compounds, which could help to correct for the intense ion signal of lignin in LCMs.

Another difficulty with PCA analyses of MALDI-MS is the ionization efficiency of each classification of compounds may be very different from each other. For example, hemicelluloses are more easily ionized than cellulose, thus, the ion signal from hemicellulose could be observed higher than cellulose. This would cause the PCA scores of the tissue to be more closely related to the xylan, even if the tissue is composed of more cellulose. Differences in ionization efficiency could be corrected by using standards more representative of the samples, using a supervised method or perhaps modifying the program so that it could consider ionization efficiencies.

Despite the inability to apply MALDI-MS spectra from intact tissue into the PCA analysis, the groundwork has been prepared for a multivariate analysis method for the analysis of LCM. PCA is capable of distinguishing between the different standards with high correlation of the factor loadings to the MALDI-MS spectra. However, for intact tissue, other multivariate analysis methods could provide a more accurate analysis of components within the mixture.

PCA and Hierarchical Cluster Analysis of ToF-SIMS Imaging Data

Chapter 5 reported localizations of ions from ToF-SIMS imaging that were consistent with regions of different wood tissue. However, the raw data from ToF-SIMS is difficult to analyze due to the high fragmentation observed from the primary ion gun and the low ion signal (at higher m/z values). PCA analysis and hierarchical clustering (HC) was performed on the large imaging data sets to help determine ions that are

characteristic of different regions of wood tissue, thus improving the characterization of LCM.

Hierarchical Clustering

PCA is an unsupervised method that effectively displays variations of a large data set in fewer PC images; ¹³⁵ however, PCA does not allow for exploration of the data set based on spectral similarities, which limits the detail of analysis. HC methods overcome this limitations by generating groupings of similar spectra without prior knowledge of the sample (as in the case of supervised methods, such as DA). Moreover, HC allows for interactive exploration of the data set that generates images based on mass spectral similarities. Clustering methods in combination with PCA has been shown to provide more insight into histological of MS imaging data. ¹³⁴⁻¹³⁶

HC groups together similar mass spectra and builds a dendrogram of nodes from the bottom up; the more similar spectra are, the closer they are grouped together. An illustration of a simplified HC analysis of five elements is displayed in Figure 6-8. The first step in HC groups together two elements with the smallest different between them (i.e., most similarities); this group is now considered a new element. The next step groups together the next two elements with the smallest distance between them, and his grouping becomes a new element. This process is repeated until all the elements have been clustered together.

For MS imaging data sets, HC groups together imaging pixels based on the position in the multidimensional PCA space. ¹³⁴ After HC, the images are regenerated by plotting the mass spectra present at the selected node. The image changes as the different branches are selective, which allows for interactive exploration of the imaging data set. ¹³⁶

Software and Data Preprocessing

Raw ToF-SIMS imaging data were converted from WinCadence (Physical Electronics) into a MATLAB[®] (The Mathworks, Inc.) format using a MATLAB program. The were loaded into an in-house written statistics software, ChemomeTricks[®] v 0.99993 beta (FOM Institute, AMOLF Amsterdam, The Netherlands) for PCA and cluster analyses. HC analysis was performed using the first 5 PCs and was used to remove silicone contaminants observed at m/z 73 and 147. After the silicone ions were removed from the data set, PCA was performed, and PC scores images were generated.

Imaging PCA Results

The PCA scores images of a *Populus* wood tissue section are displayed in Figure 6-9 and compared with the ToF-SIMS TIC and fluorescence images. The PC scores image suggests that PC2 separates the lignified from the non-lignified cells. Specifically, the positive scores on PC 2 (PC2+) image correlates well with the lignin autofluorescence image; thus, PC2 could be used to determine the ions that distinguish between lignified and non-lignified cells. Figure 6-10 displays the positive and negative PC2 loadings plot (the PC scores images are displayed next to each loading plot). The PC2+ loadings, which are localized in lignified cells, are dominated by m/z values 69, 81, 133, 344 and 607. Although these ions are not positively identified, predicted structures are also displayed in Figure 6-10.

In addition to determining representative ions of different tissue regions, the PC scores images help to cluster different ions together. The low ionization efficiency, especially with higher molecular weight ions, requires long analyses and large data sets to obtain quality spectra for higher m/z value ion. Instead, PCA can help to identify the

lower intensity, higher mass ions that would otherwise be overlooked, as well as distinguish series of ions that could be indicative of different regions (as opposed to plotting as single ion as in the case with most MS imaging experiments).

The negative PC2 (PC2-) loadings plot shows the vascular cambium and the phloem are dominated by the salts, Na⁺ and K⁺ (Figure 6-10). The salts should be more abundant in the living cell region of the vascular cambium, which is observed in the PC image. Also observed in the PC loading plot is *m/z* 331 with a series of ions similar in *m/z* values, which could be identified as different Gibberellins (GA) in the vascular cambium region. In addition, cellulose ions could be observed in these regions of the tissue, since cellulose is present in the phloem (just at lower abundance). The ions *m/z* values 102, 130 and 140 have all been reported as degradation products of cellulose during pyrolysis,¹⁴⁰ so could be indicative of cellulose ions. It is also important to note the loading values of these predicted cellulose ions are smaller than the salts and the Gibberellins, which is to be expected.

The positive and negative scores image of PC1 are illustrated in Figure 6-9 b-c. The PC1+ scores are localized in the regions where higher cellulose concentrations are expected, specifically, in the xylem and the lignified phloem fiber cells. The PC1+ loading plot (data not shown) is dominated by *m/z* values 130, 140 and 274—as previously mentioned, *m/z* values 130 and 140 have been reported as possible cellulose fragment ions. The ion *m/z* values 274, is 144 Da higher than *m/z* 130, which is a commonly observed sugar fragment, thus would be consistent with the cellulose ion identification. The *m/z* value 607, which shows localization in lignified cells and dominated the PC2+ loading plot, is also present in the PC1+ loading plot; however, the

relative loading value is lower than the other ions observed. These results further suggest that PC1+ is more characteristic of cellulose ions, and PC2+ is more characteristic of lignin ions.

Another example of the PCA analysis on ToF-SIMS imaging is presented in Figure 6-11. The PC1 scores images show an efficient distinction between the pith, non-lignified cells, and the xylem, lignified cells. The PC1+ loadings plot (Figure 6-12) is similar to the PC2+ loading plot (Figure 6-9), where m/z values 69 and 607 dominate the spectrum. This helps to further validate the PCA method, as well as validate the ions that have been assigned to a certain classification of compounds. Furthermore, the PC2 scores image (Figure 6-11) shows a distinction between the xylem cells and pith, and the PC1 loading plot is displayed in Figure 6-12. The positive loadings plot is dominated by the m/z value 130, 140 and 274, which are the same ions observed in the previous example. In addition, the ions more characteristic of lignin, m/z value 69 and 607, are observed, but in lower relative abundance.

Conclusions

The analysis reported above showed the viability of PCA to distinguish between regions of different tissue composition within intact plant tissue. The lignified versus the non-lignified cells were efficiently separated. Furthermore, the PC loading plots provided series of ions to monitor for different classifications of compounds. In general, the non-lignified, living regions of tissue were dominated by the Na^+ and K^+ (m/z value 23 and 39) as well as m/z value 331, 389, which were identified as GAs. The lignified regions of tissue were dominated by m/z value 69, 81, 334, and 607—these ions provided a localization that was most similar to the lignin autofluorescence.

Taking a closer look at the PC loadings plots, the m/z values 130, 140 and 102 were present in both the lignified and non-lignified regions, which is consistent with known composition of plants. Cellulose is present in non-lignified cells, but believed to be in lower abundance and is consistent with the observations of the low loadings on the PCs characteristic of these cell types.

In conclusion, PCA offers insight into the MS analysis of different regions. Due to the high fragmentation and complex ToF-SIMS spectra, PCA helps to reduce the data set and determine differences that can otherwise be overlooked. In addition, PCA can also help to identify between different fragment ions at the same m/z . This is important since cellulose, hemicellulose and lignin often result in the same molecular weight fragment ions, and plotting only one particular m/z at a time could result in uninformative, non-selective images. Furthermore, PCA could become a useful tool to analyze differences between chemically pretreated and untreated wood samples. Since ions are abundant and nearly every m/z ratio, PCA can identify ions at lower abundance that change as a result of the pretreatment, which can optimistically provide insight to develop a more efficient pretreatment process.

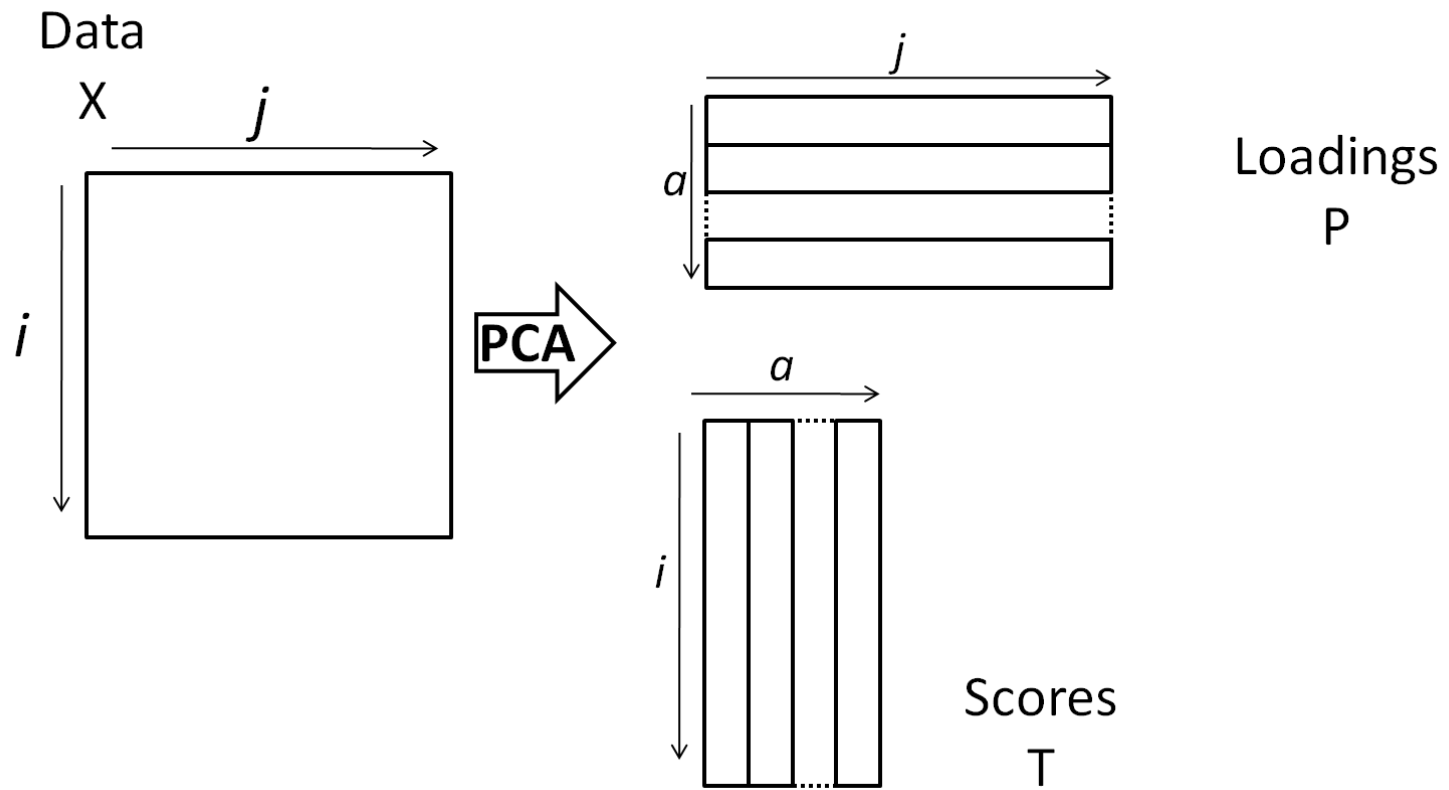


Figure 6-1. Graphical representation of PCA analysis. Original data matrix is transformed into two different matrices, called the loadings and the scores matrix.

PCA Scores Plot

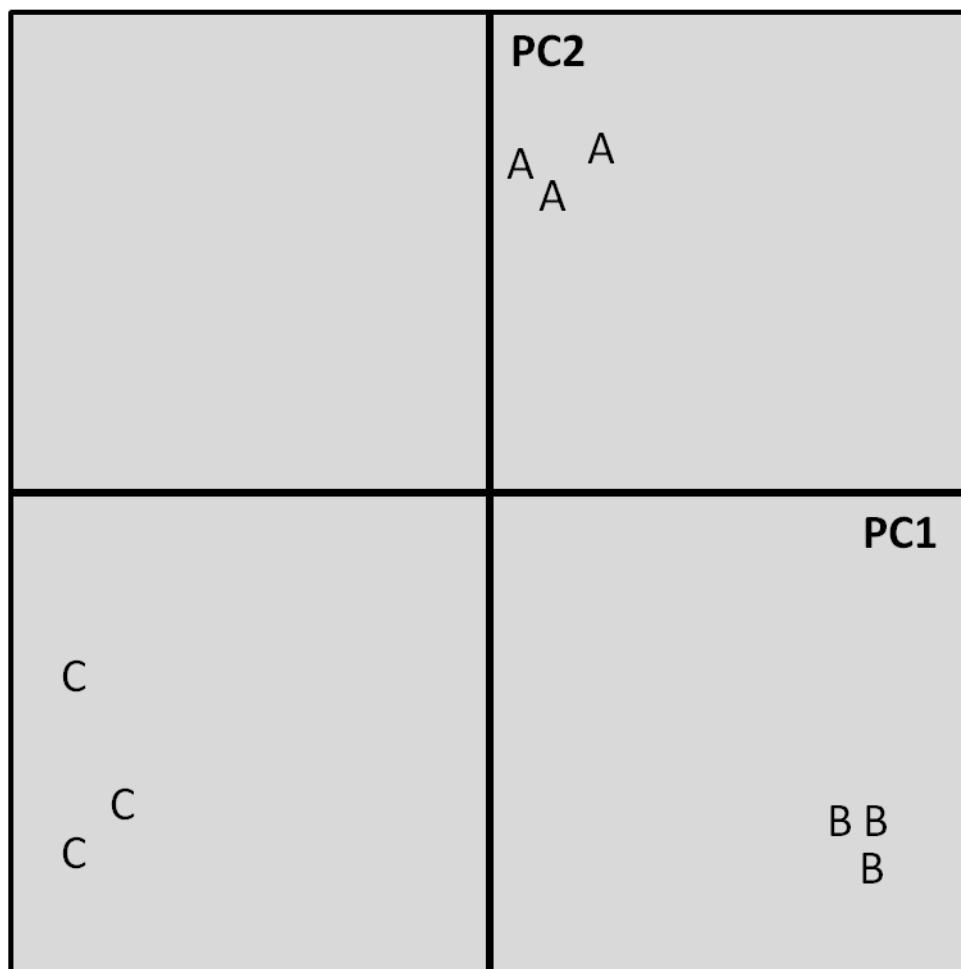


Figure 6-2. Ideal PCA plot of three pure standards. PCA analyses of pure standards will help to determine the components and concentrations within unknown mixtures.

j

	Sample	501	→	2000
i	MCC	Intensity	Intensity	Intensity
	MCC	Intensity	Intensity	Intensity
	MCC	Intensity	Intensity	Intensity
	Xylan	Intensity	Intensity	Intensity
	Xylan	Intensity	Intensity	Intensity
	Xylan	Intensity	Intensity	Intensity
	Lignin	Intensity	Intensity	Intensity
	Lignin	Intensity	Intensity	Intensity
	Lignin	Intensity	Intensity	Intensity

Figure 6-3. Data matrix set-up for PCA analysis. Three replicates of each standard are in the rows and each column represents a different m/z.

PC1 & PC2 Scores Plot

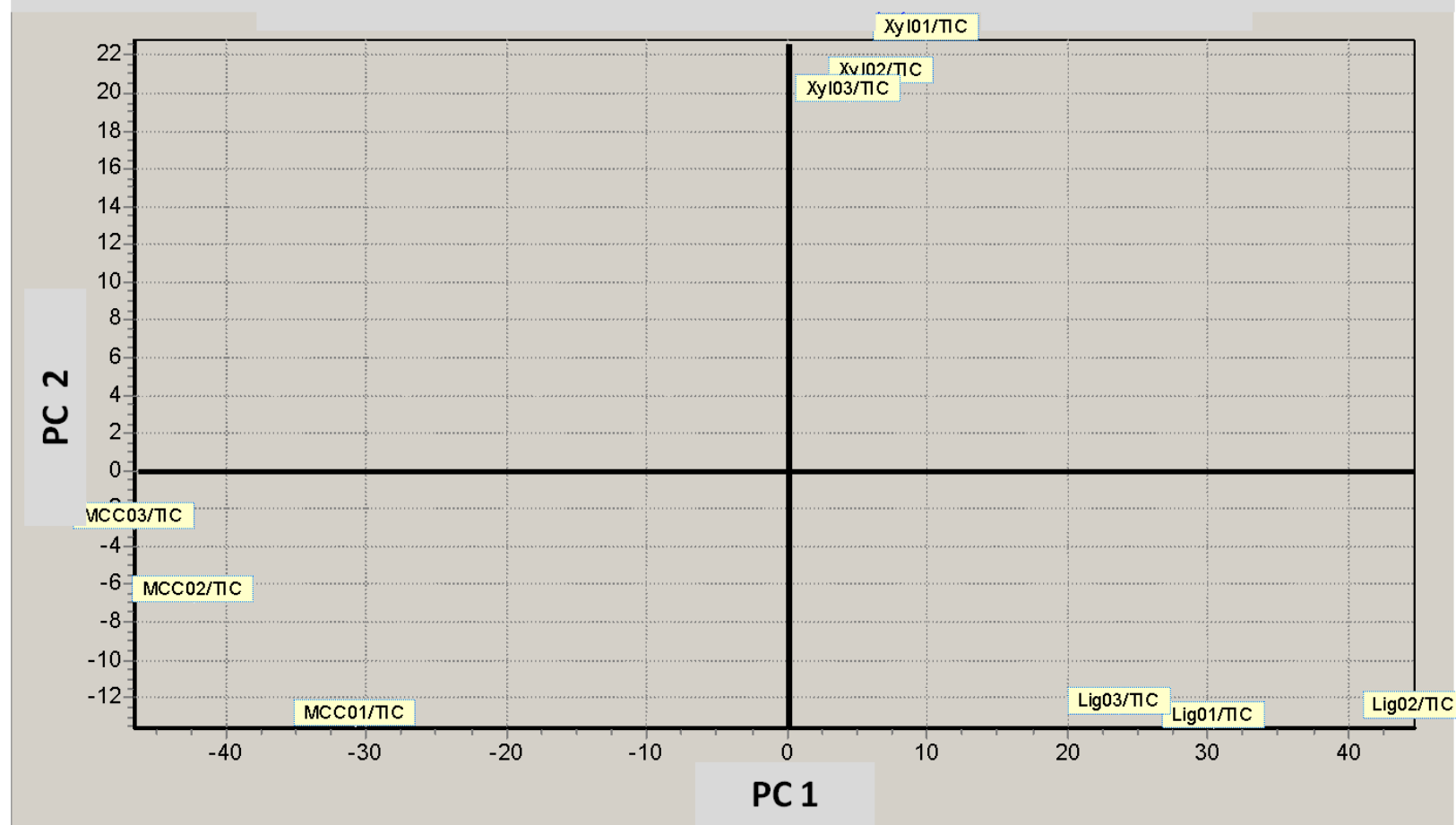


Figure 6-4. PCA Scores plot of MCC, xylan and lignin analysis by MALDI-MS. The three replicates of the same standard group together and PCA analysis forms a triangle, which is consistent with the 'ideal' PCA analysis displayed in Figure 6-2. Data points are located in the center of each square label.

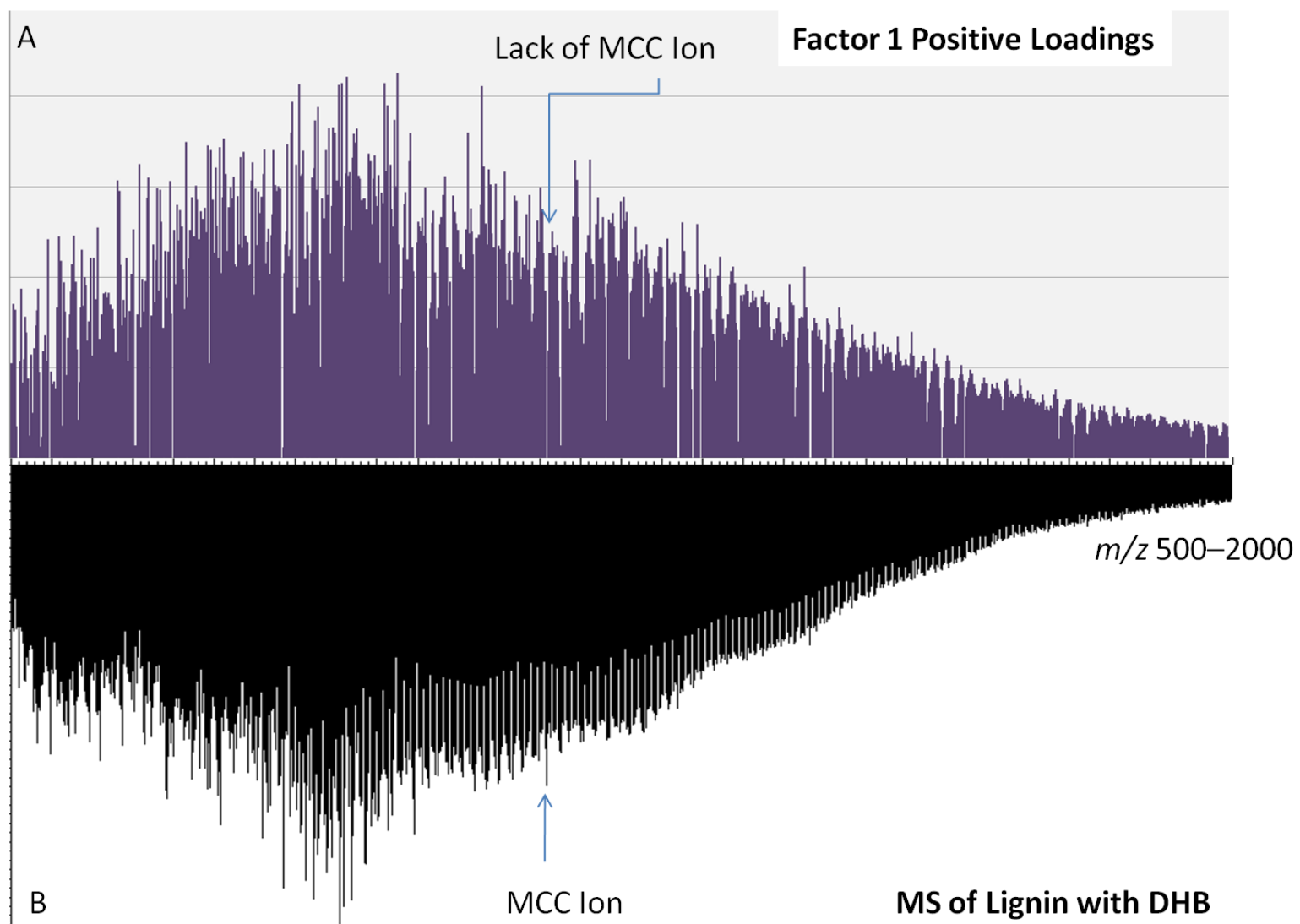


Figure 6-5. PC loadings plot compared with MALDI-MS spectrum of lignin. A) Positive PC1 loadings plot. B) MALDI-MS of lignin. The loadings scores are representative of the MALDI-MS of the lignin, which shows PCA is separating based on the correct ions.

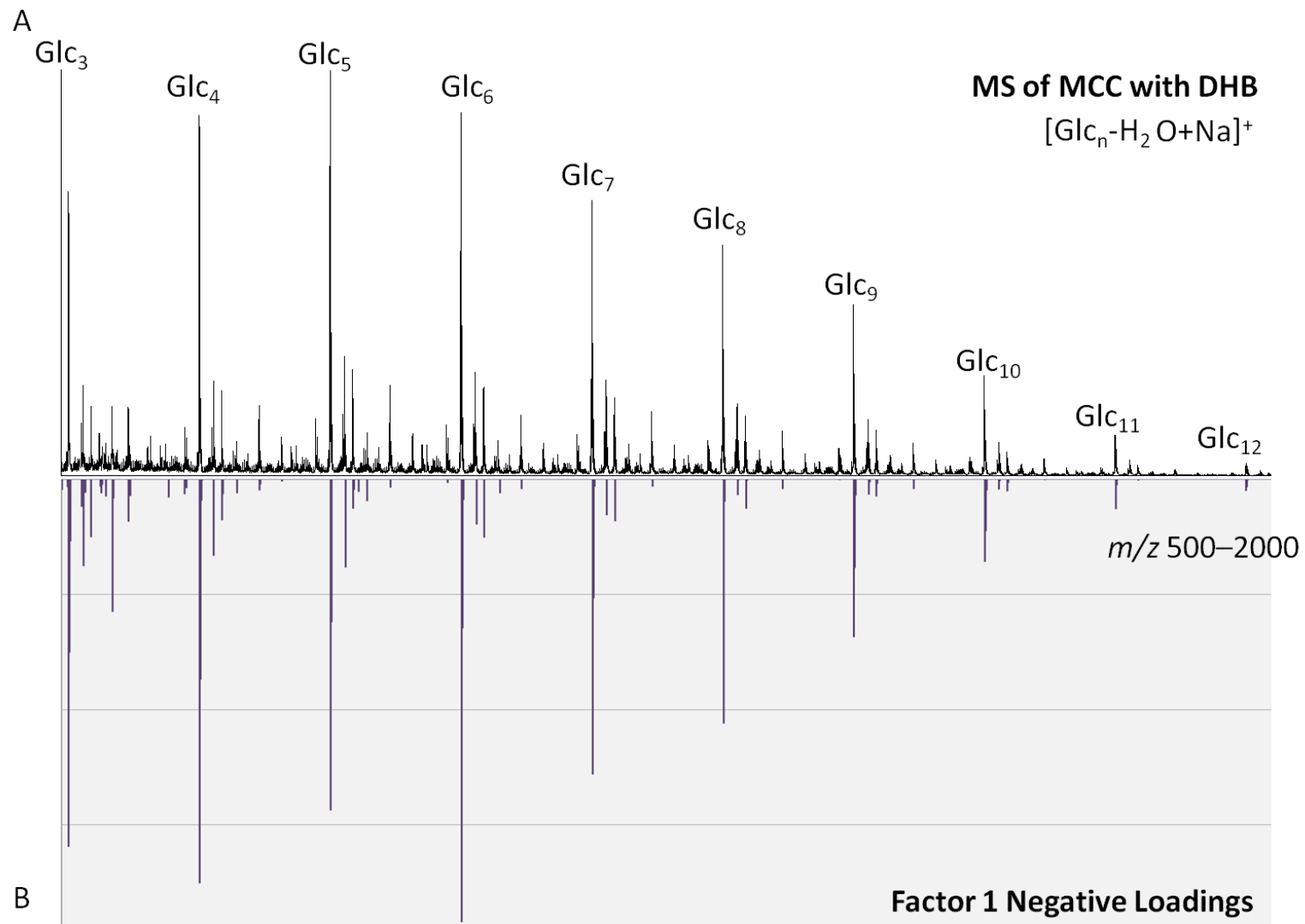


Figure 6-6. PC loadings plot compared with MALDI-MS spectrum of MCC. A) Negative PC1 factor loadings. B) MALDI-MS of MCC. The negative loadings show characteristic ions that are observed in the MALDI-MS of the pure standard.

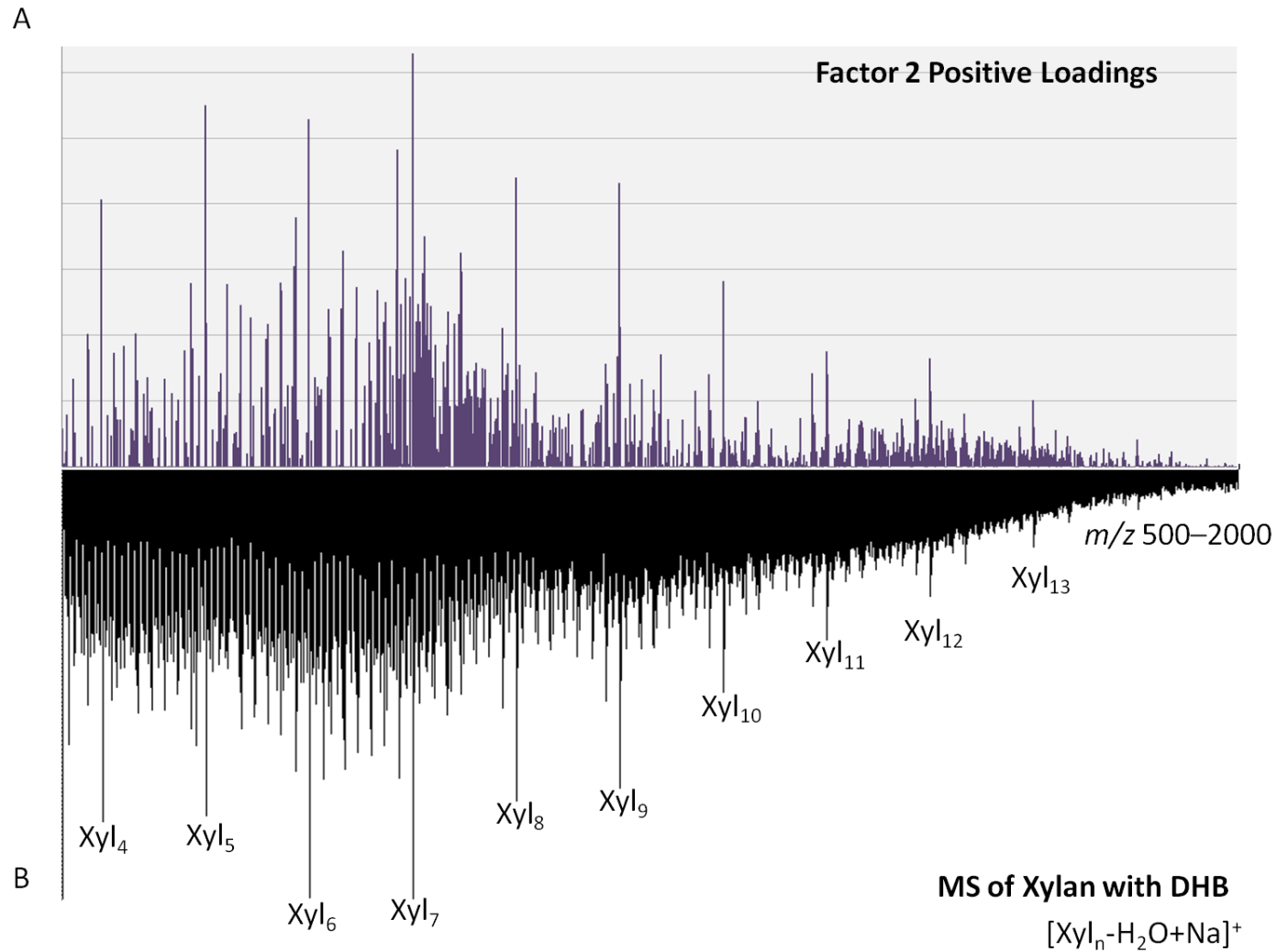


Figure 6-7. PC loadings plot compared with MALDI-MS spectrum of Birch xylan. A) Positive PC2 factor loadings. B) MALDI-MS of Birch xylan. The PC2 loading show similar abundant ions as the MALDI-MS analysis and appears to reduce the number of ions between the linear xylans.

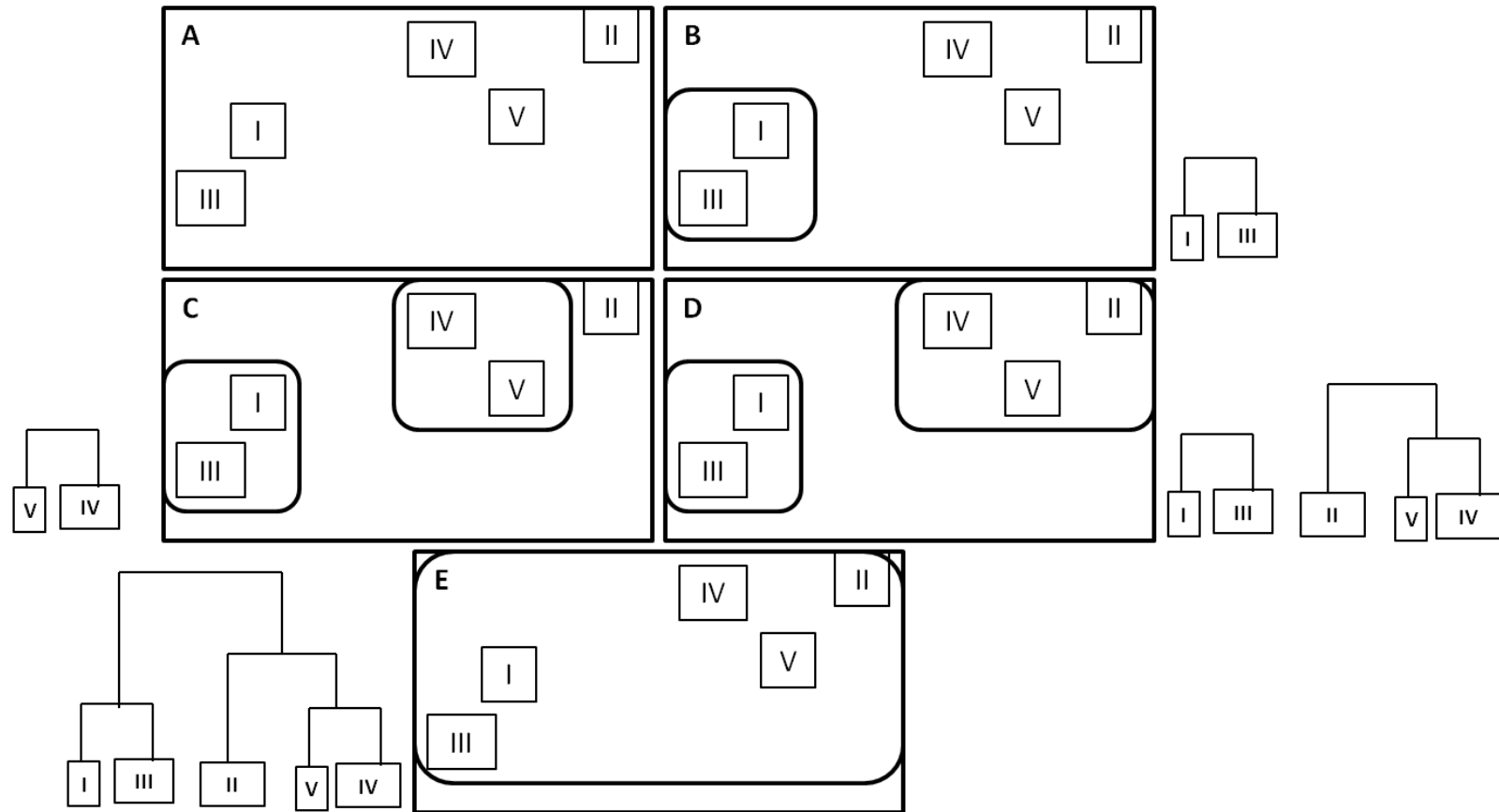


Figure 6-8. Illustration of hierarchical clustering adapted from Deininger, S. et al. *Proteome Res.* **2008**, 7, 5230-5236. A) Five elements subjected to HC. B) Two closest elements are grouped together and are now considered one element. C) The next two closest elements are grouped together and considered one element. D) The next closest elements are clustered together, forming another cluster. E) Complete HC of the five elements.

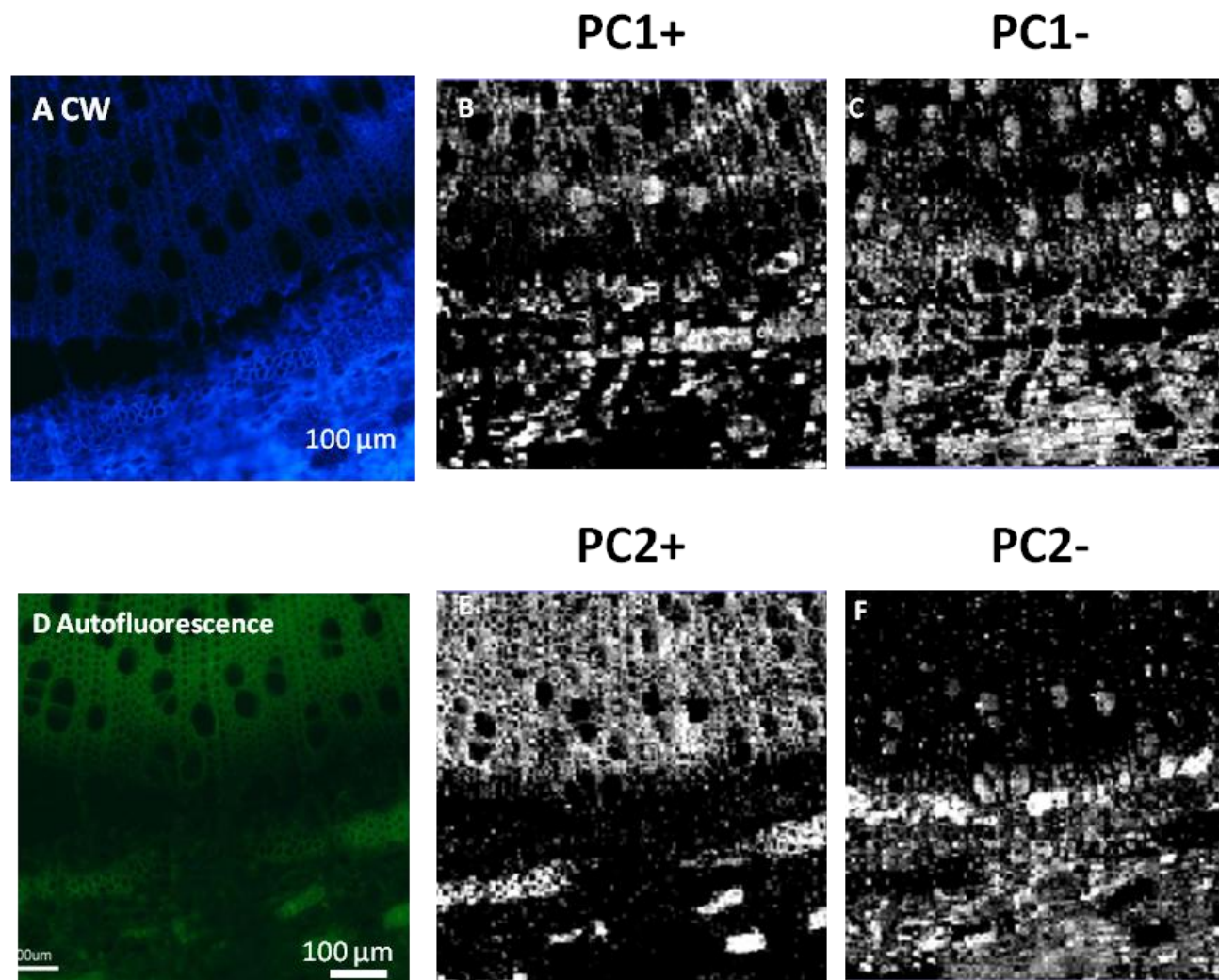


Figure 6-9. Fluorescence images compared with PCA images generated by plotting the positive and negative loadings of PC1 (top) and PC2 (bottom) of ToF-SIMS imaging data. PC1 differentiate between cellulose ions and other primary cell wall material. The PC2 separates effectively between lignified and non-lignified cells.

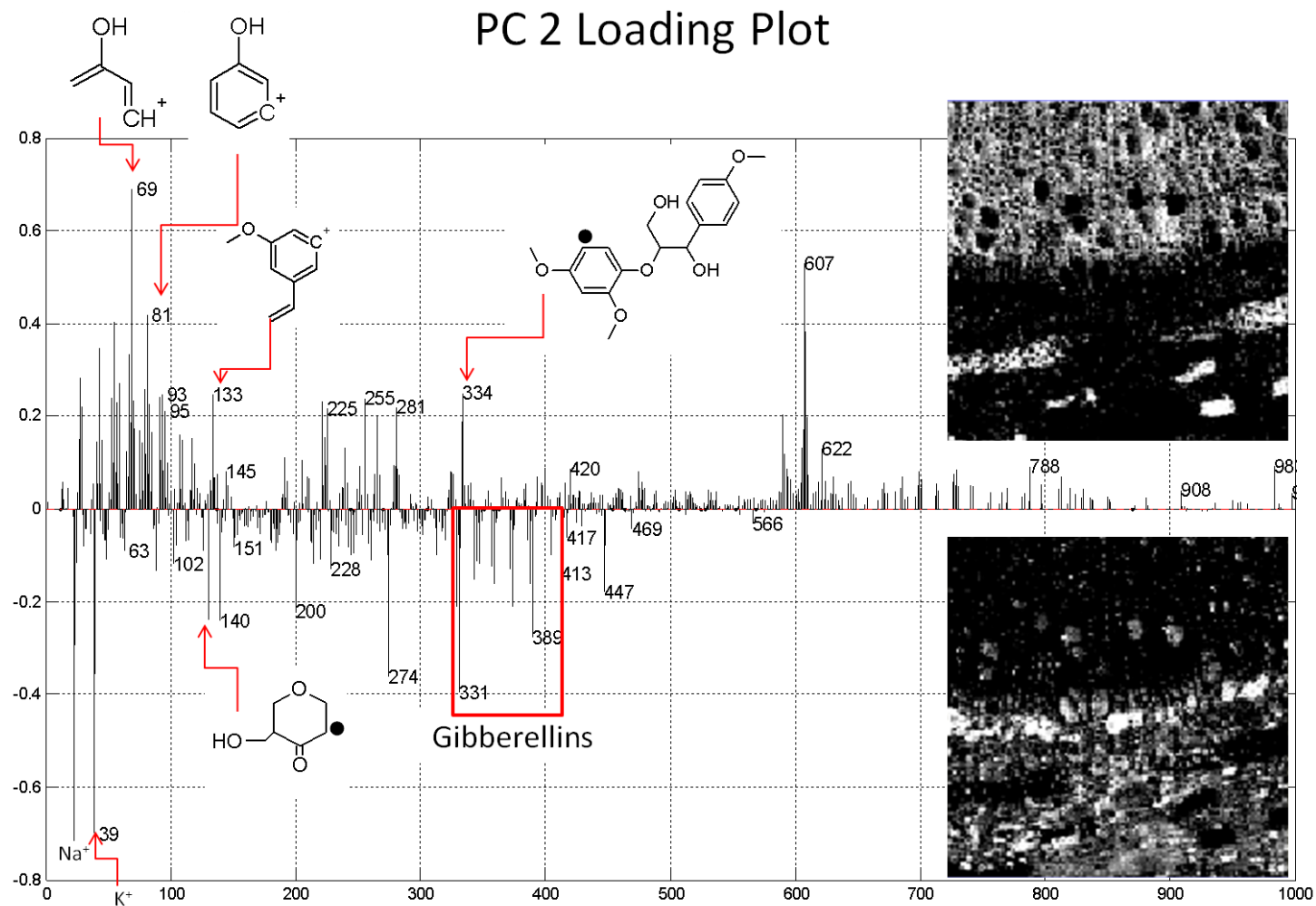


Figure 6-10. PC2 loading plot and corresponding images. PC1+ is more characteristic of lignified cells and provides series of ions that are characteristic of lignin ions. Structures drawn are predicted structures; however, they could not be positively identified. PC2- shows more salt signal and ions that are consistent with the m/z of Gibberellins

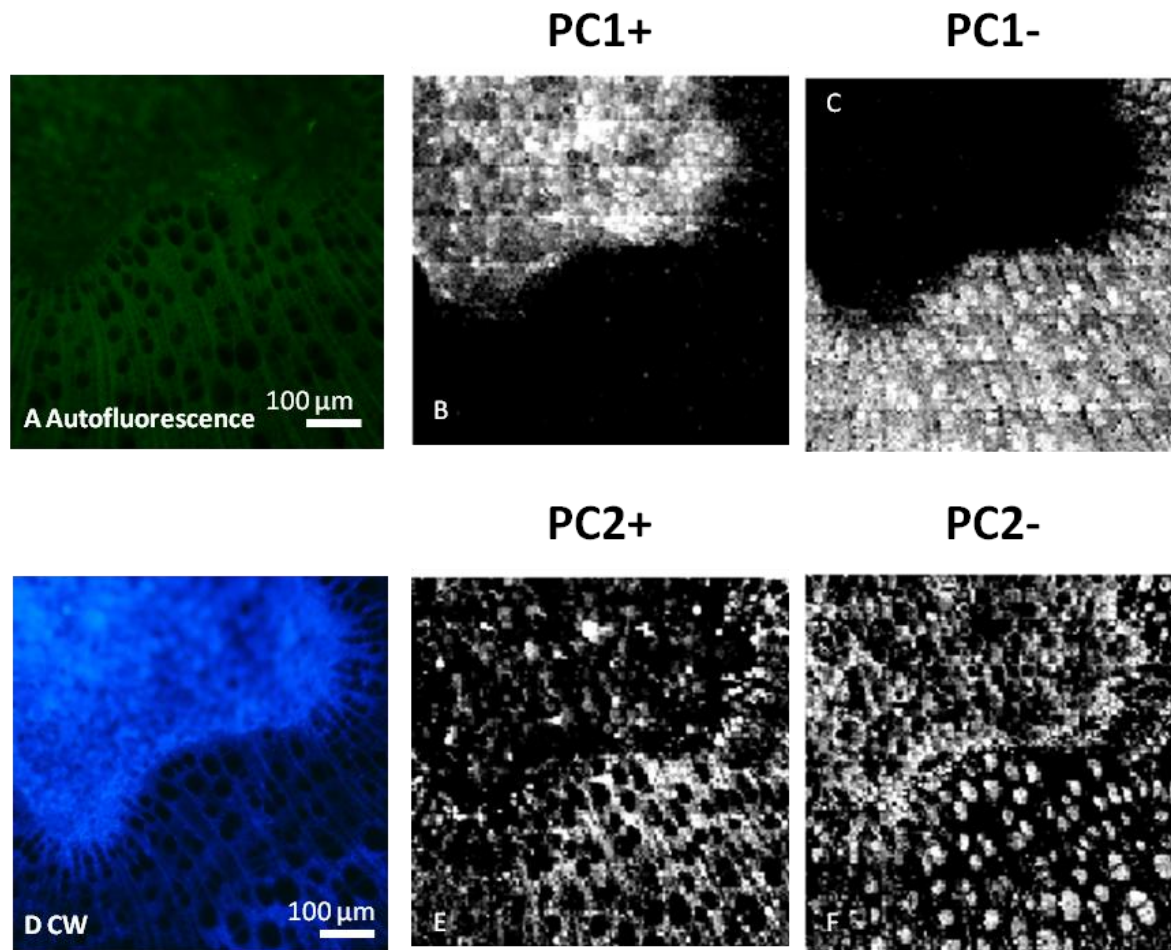


Figure 6-11. PCA images of the pith and xylem. PC1 efficiently distinguishes the regions of the pith and the xylem. PC2 identifies signals characteristic of cellulose.

PC 1 Loading Plot

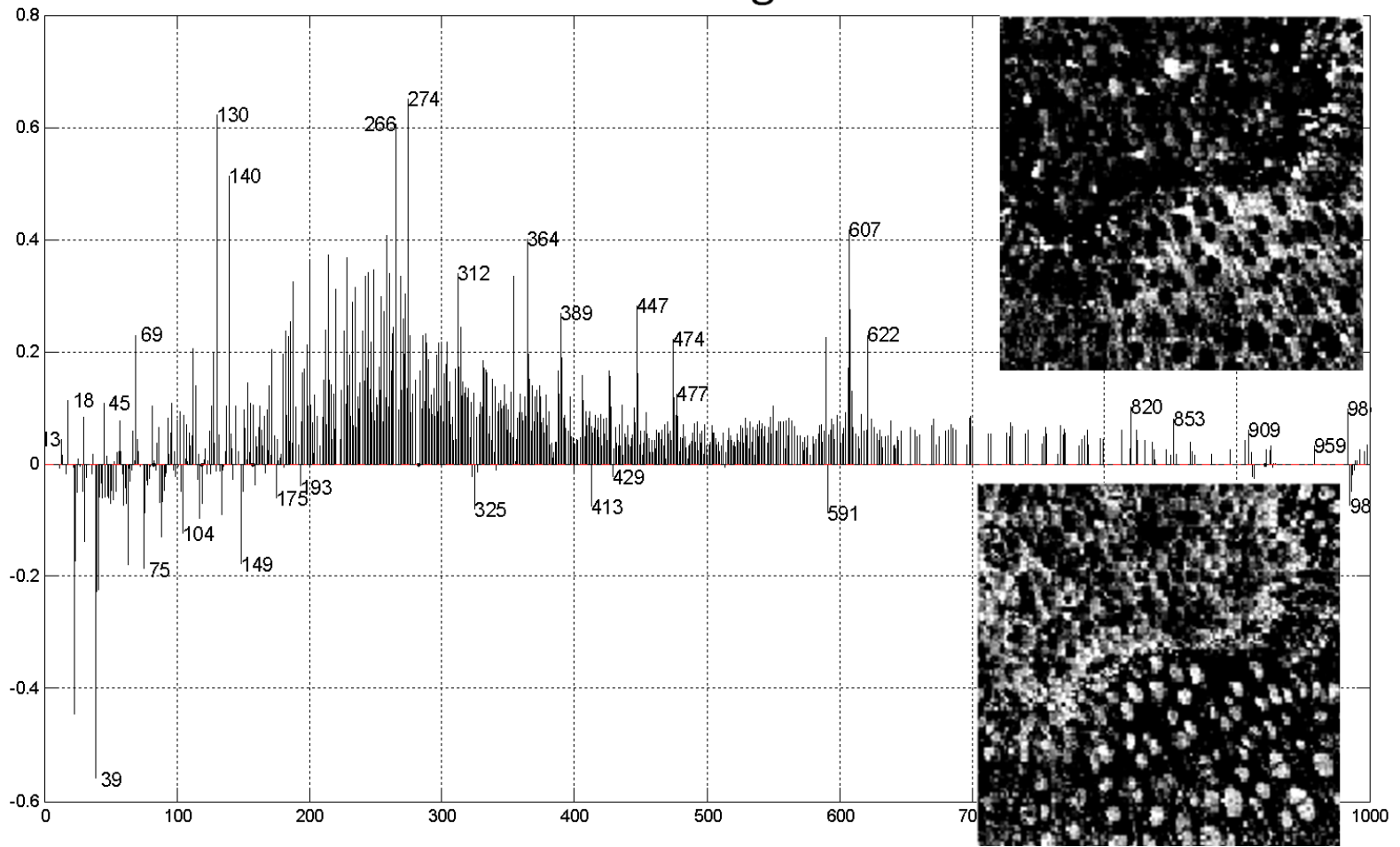


Figure 6-12. PC1 loading plot and corresponding images. The positive loadings show more characteristic of cellulose ions.

CHAPTER 7 SUMMARY AND FUTURE DIRECTIONS

The analysis of LCMs is difficult due to the number and complexity of the compounds as well as the spatial organization of these compounds. This dissertation reports the development of methods that reduce the complexity and offer high chemical selectivity for the analysis of intact LCMs; specifically, mass spectrometric imaging (MS imaging) techniques were utilized in the imaging and characterization of intact *Populus* wood tissue sections.

Prior to intact tissue analysis, a matrix-assisted laser desorption/ionization linear ion trap mass spectrometric (MALDI-LIT-MS) method was developed to characterize standard materials that were anticipated to be present within the wood tissue sections, microcrystalline cellulose (MCC), Birch Xylan and Spruce lignin. The MALDI tandem MS method ionized these compounds and determined the m/z values to monitor in the intact tissue section studies. Furthermore, tandem MS was useful in identifying common NLs and common fragment ions observed for each classification of compounds.

Although these standards were adequate for method development, future work should include a larger library of standards, specifically, standards that are directly related to tissue type. For example, *Populus* was used for all intact wood tissue analyses; however, the hemicellulose standard that was used was from Birch and the lignin standard was from Spruce. It is not anticipated that the hemicellulose and lignin varies greatly between species, but differences may occur, which could affect the intact tissue analysis. In addition, the standard analyses were more difficult since two of the 'standards' used were extracts that can contain other plant material, in addition to the compound of interest. It is difficult to overcome this limitation, but perhaps a purification

step, prior to MS analysis, could result in higher purity standards, especially in the case of lignin.

In addition to standard analyses, a MALDI tandem MS imaging for the analysis of intact LCMs was developed. Other analytical methods used to ionize LCM may suffer higher spatial resolution than MALDI-MS imaging, but the chemical selectivity is typically less. MS imaging provides a way to display the localization of specific compounds with confidence in compound identification. A major advantage of the developed technique over the existing techniques is the ability to perform tandem MS experiments. It was demonstrated that tandem MS improved the sensitivity and selectivity of the experiment by isolating a small range of ions, distinguished between isobaric species and identified unknown ions observed from wood tissue.

Despite the advantages of this technique, future work could improve the data obtained from the analysis. The major drawback to MALDI-MS imaging is that the spatial resolution is inadequate to map distinct features within the wood tissue sections. Future experiments will aim to improve the spatial resolution of the MS imaging experiment by reducing the laser spot size. Reducing the laser spot size is practical in a physical sense, but could lead to MALDI-related challenges. For example, reducing the laser spot size ultimately reduces the 'sampling area.' Thus, the amount of analyte that is present in a single sample spot will be lower, and could be below the limit of detection of the experiment. This is problematic, especially in MALDI, due to the high MALDI matrix ion signal observed. Fortunately, MS/MS will provide lower limits of detection. Furthermore, reducing the spot size increases the fluence of the laser and could adversely affect the measurements.

Since this dissertation was not aimed toward reducing the spot size, the limited spatial resolution was circumvented by implementing other analytical methods that offer superior spatial resolution, e.g., fluorescence microscopy and ToF-SIMS imaging. Fluorescence microscopy is commonly used for the analysis of wood tissues and offers high spatial resolution. However, the fluorescence labels provide less chemical selectivity and are can also be expensive. In this dissertation, fluorescence microscopy was used to validate the MALDI-MS imaging method, as well as to make comparisons to help increase the comprehensive understanding of the chemical composition of intact wood tissue.

Fluorescence microscopy also aided in determining differences in cellulose concentration within one intact tissue section, which could be useful in later developing a semi-quantitative method. One of the experiments that could be performed is to develop a way to quantify the cellulose ions observe in MALDI by using CW fluorescence microscopy. For example, the fluorescence signal observed from CW is directly correlated with the abundance of cellulose present in the tissue. Correlating the fluorescence signal with the observed MALDI analyte ion signal could prove to be useful in generated a 'calibration' to determine relative abundance of cellulose (or available cellulose). This information could ultimately be used in the analysis of LCM to determine the accessibility of cellulose before and after a chemical pretreatment.

ToF-SIMS imaging produced high spatial resolution MS images in which features not resolved in the MALDI-MS image were observed. Despite the superior spatial resolution, the identification of the ions was difficult due to extensive fragmentation observed in SIMS spectra, making it difficult to distinguish between different

classifications of polysaccharides. However, ToF-SIMS was successful in distinguishing between different regions of tissue, specifically lignified versus non-lignified tissues. This is useful in the analysis of LCMs because this differentiation is important during pretreatment for LCM conversion into fuel.

As analytical chemists, it is important to identify ions that are observed in spectra, but with ToF-SIMS, ion identification is limited. However, in LCM analysis, the ability to determine different regions, chemically and spatially, could provide more insight into the pretreatment process than what is already known. In other words, knowing the exact identification of the compound observed is not necessary to analyze the material. Ions that are characteristic of certain compounds were identified, specifically lignin ions. Since one of the biggest difficulties in understanding pretreatment is the spatial changes of lignin in the tissue after pretreatment, ToF-SIMS could prove to show chemically specific information, without knowing the exact identity of the ion. Future experiments will be aimed toward analyzing both untreated and pretreated wood tissue samples to help determine spatial changes in the ions identified in this dissertation.

MS and more specifically, MS imaging, generates large data sets with many variables that can easily be overlooked. Multivariate analyses are often useful in analyzing data with a large amount of variables. Principal component analysis (PCA) was used to analyze pure standards, as a way to develop a semi-quantitative analysis for intact plant tissue sections. Future experiments should be aimed toward analyzing intact wood tissue sections and perhaps generating internal calibrations of different regions of tissue that are known to having different concentrations of cellulose, hemicellulose and lignin.

Lastly, PCA proved to be an invaluable tool identifying ions or series of ions that are characteristic of different regions of wood tissue. Specifically, the lignified and non-lignified cells were easily distinguishable using PCA analysis. In addition, PC loadings were used to generate PC images, which also correlated well with fluorescence microscopy.

In conclusion, this dissertation outlines different analytical techniques that can be used for the analysis of LCM. It is clear that one method does not provide all the characterization needed for LCM analysis. Instead, correlating the strengths of each technique proved to provide a more comprehensive understanding of LCM. Ultimately, these can be used to characterize the materials that are useful for processing into fuel sources and aid in improving the efficiency of the overall process.

APPENDIX A
DIFFICULTIES OF MALDI TIME-OF-FLIGHT ION MOBILITY SPECTROMETRY
OF PLANT-RELATED STANDARDS AND *POPULUS* TISSUE

Overview

A goal of the research presented herein was to compare MALDI-LIT-MS with MALDI quadrupole time-of-flight (Q-ToF)-MS of plant-related standard and intact tissue. However, generating trends and correlations were difficult due to the unexpected results obtained from MALDI ToF-MS experiments. This Appendix briefly reports the experiments performed and results that were obtained from MALDI-QToF-MS and LDI-ToF-MS analysis performed on the Waters Synapt mass spectrometer.

Experimental

Standard Analysis

Standards and MALDI matrices used were prepared as described in Chapter 2. Briefly, the suspensions of the plant-related standards were prepared at 4 mg/mL in water. The MALDI matrix, DHB, was prepared at varying concentrations (~0.5 – 20 mg/mL) to determine the optimal matrix-to-analyte ratio. The standards were prepared for MALDI analysis by pipetting 1 μ L of the standard, followed by 1 μ L of the MALDI matrix onto a stainless steel MALDI sample plate.

Instrumentation and Traveling Wave Ion Mobility Parameters

A Waters Synapt G1 (Waters Corp., Milford, MA) was used for MALDI-QToF-MS analyses. The MALDI source is equipped with a frequency-tripled, solid-state, Nd:YAG laser (355 nm) with an adjustable repetition rate up to 250 Hz. The laser energy was adjusted from about 200-350 au, which were values typically used for experiments with

this instrument. The number of laser shots per spot was adjusted from about 200–300. The MALDI-source pressure approximately 10^{-2} mTorr.

The traveling wave velocity and height are parameters that can be altered using the software provided to operate the instrument. The wave velocity was 500 m/s and the wave height was 12 volts peak-to-peak.

Results and Discussion

The analyses of the qplant-related standards that were discussed in Chapter 2, repeated on the MALDI-QToF mass spectrometer, were not successful. The spectra obtained showed mostly MALDI matrix (DHB) ions (data not shown). In addition, the m/z values that were hypothesized to be present in the samples were isolated within the quadrupole and fragmented for MS/MS, but the data again was not comparable to MALDI-LIT-MS experiments.

The major different between the instruments is the MALDI laser source, which could explain the discrepancies between the results. The MALDI LTQ XL is equipped with a 60 Hz, N_2 (337 nm) laser and the Synapt is equipped with a 250 Hz, solid-state, tripled Nd:YAG laser (355 nm). The biggest differences between the lasers are the repetition rate, laser profile and fluence—the effects of these parameters on MALDI-ToF-MS sensitivity has been discussed in the literature.¹⁴¹ It is reported that N_2 lasers generate higher total ion intensity at the same laser fluence when compared with the frequency-tripled Nd:YAG laser. This ultimately leads to improved MALDI-ToF-MS sensitivity when using a N_2 laser, assuming all other parameters are equal. In addition to these parameters, there is a small difference in the laser wavelength; however, this is unlikely to cause such a dramatic difference in the spectra. Although these differences

are present, there is not an obvious reason as to why the fluence and different wavelength would have such a dramatic effect on the spectra observed.

For intact *Populus* tissue analyses, the sample preparation discussed in Chapter 3 was followed for analysis on the Synapt mass spectrometer, but conductive, double-sided tape was used instead for the QToF-MS analysis. A comparison of the MALDI spectra obtained from the two different instruments from m/z values 500–1300 is displayed in Figure A-1. The top spectrum in Figure A-1 displays ions that were above the background in the MALDI-QToF-MS analysis; however, these ions could not be identified. The m/z differences between the peaks were not consistent across the whole spectrum and did not correspond to the masses of sugar ions that were observed in MALDI LTQ spectra. The ions observed in the MALDI-QToF-MS analysis might have been assigned as MALDI matrix (DHB) cluster ions, but the m/z values were not consistent with DHB cluster ions observed with the MALDI LTQ instrument. The ions observed in the MALDI-ToF-MS analysis were isolated within the quadrupole and fragmented for MS/MS to aid in ion identification. The NLs observed were not consistent with previous analyses, and were likely due to DHB cluster ions, and thus remaining unidentified despite tandem MS capabilities.

One of the main goals of using the Waters Synapt instrument was to perform an ion mobility separation prior to MS analysis, which was hypothesized to reduce spectral complexity. However, for MALDI analysis of the intact tissue section, the ion mobility plot only had one grouping, thus no separation was observed. Ion mobility parameters were altered to try to obtain better separation; however, this was still unsuccessful in trying to separate the ions generated from the wood tissue.

After the unsuccessful attempt to compare MALDI-MS between the two instruments, LDI (i.e., with no additional MALDI matrix was applied atop the tissue) experiments were performed on the *Populus* tissue. For these experiments, the laser energy was increased and the laser raster step-size was decreased from 200 μm to 50 μm . In contrast to the MALDI analysis, the ion mobility plot from LDI showed separation resulting in four different mobility regions (Figure A-2). This ion mobility plots ion intensity at each m/z value vs. the drift time; thus, isobaric ions can potentially be separated by their drift times, which differ with differences in collisional cross-sections. The mass spectra from regions outlined in white are displayed in Figure A-3.

The top spectrum in Figure A-3 corresponds to the highest drift time mobility line (farthest right in Figure A-2) and displays ions at nearly every m/z value, but with a dramatic increase in ion intensity above m/z 700. The center mass spectrum corresponds to the middle mobility line and shows an intense ion at m/z 720, as well as a distinct pattern of ions with a mass difference of 24. After further investigation, it is believed that this is due to the formation of carbon clusters (similar to a Buckminsterfullerene¹⁴²) from the tissue surface. The ions observed at m/z value 720 corresponds to the radical cation of C_{60} and the difference between the other ions observed is 24, which the mass of C_2 . In one of the original reports of fullerenes, C_{60} clusters were formed by focusing a second harmonic (532 nm) Q-switched Nd:YAG laser onto a graphite sample and the ions produced were detected with ToF-MS.¹⁴² The most stable configuration of the clusters observed was C_{60} , and only even numbered carbon clusters were observed, which explains the difference of 24 mass units. In the bottom spectrum (Figure A-4c) from the left ion mobility regions, ions that are 12 m/z

units apart were observed. After a closer look at the isotope distribution, these ions were identified as doubly charged carbon clusters ($\Delta m=24$, $z=2$, so $\Delta m/z=12$).

Since wood tissue is composed of mostly carbon, oxygen and hydrogen, it would be possible that a carbonization can occur as a result of the rapid heating and increased energy from the Nd:YAG laser used for LDI. It is also interesting to note that more abundant carbon-cluster ion signal is observed when the laser raster size is reduced; at 200- μm raster step sizes, little carbon cluster ion signal was observed, but at 50- μm step sizes, a significant increase of carbon cluster ion signal was observed. Rastering at 50- μm step sizes results in oversampling, increasing the heat and energy that is imparted on one area of tissue, which should lead to an increase the formation of the carbon clusters.

In order to confirm that the ions observed at m/z 720, and the subsequent ions observed 24 m/z units higher, corresponded to carbon clusters, the wood sample was analyzed with a MALDI-FT-ICR to obtain high mass resolution data. The 7T FT-ICR was equipped with an Nd:YAG laser and a home-built sample stage. The LDI analysis produced the same carbon clusters that were observed on the MALDI-ToF-MS. The recorded m/z value of 720 confirmed that the ion observed contained only carbon atoms, thus confirming that this was a C_{60} cluster.

Although the MALDI-QToF results reported have no immediate implications, it is interesting, nonetheless, to report the laser-induced formation of carbon clusters from wood tissue. Furthermore, it would be interesting to perform MS imaging using these instruments to plot the localization of the C_{60} ion to determine the regions of tissue that produce the most carbon clusters. One of the difficulties of converting biomass into fuel

is the need to remove the high oxygen content of the carbohydrates present in wood tissue. Observing the localization of carbon clusters from wood tissue might help to identify the characteristic tissues that could most efficiently produce biofuels.

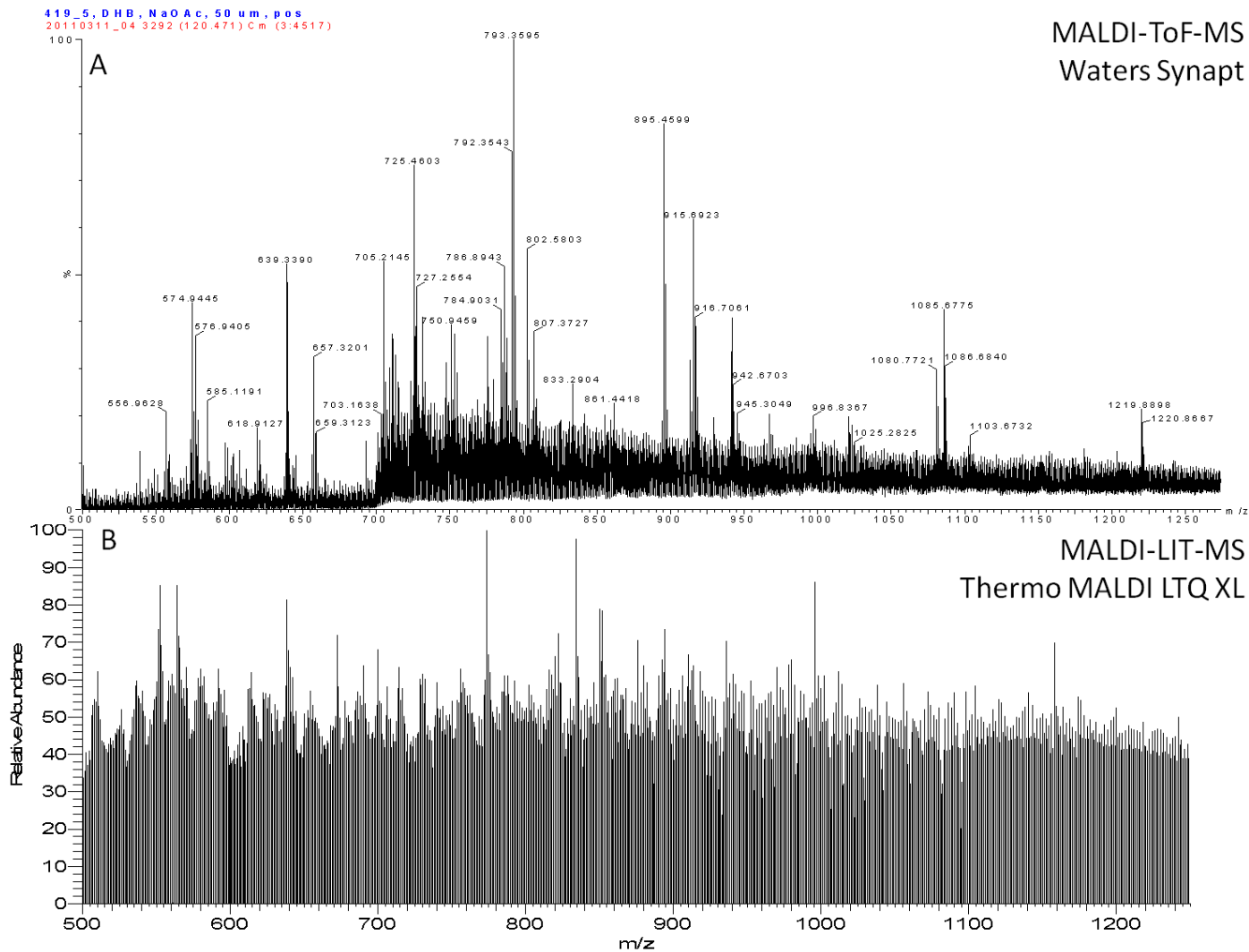


Figure A-1. Comparison of MADLI MS of wood tissue from two different instruments. A) MALDI-QToF-MS on Waters Synapt. B) MALDI-LIT-MS on Thermo MALDI LTQ XL. The dramatic increase in ion signal above m/z 700 is observed in all spectra.

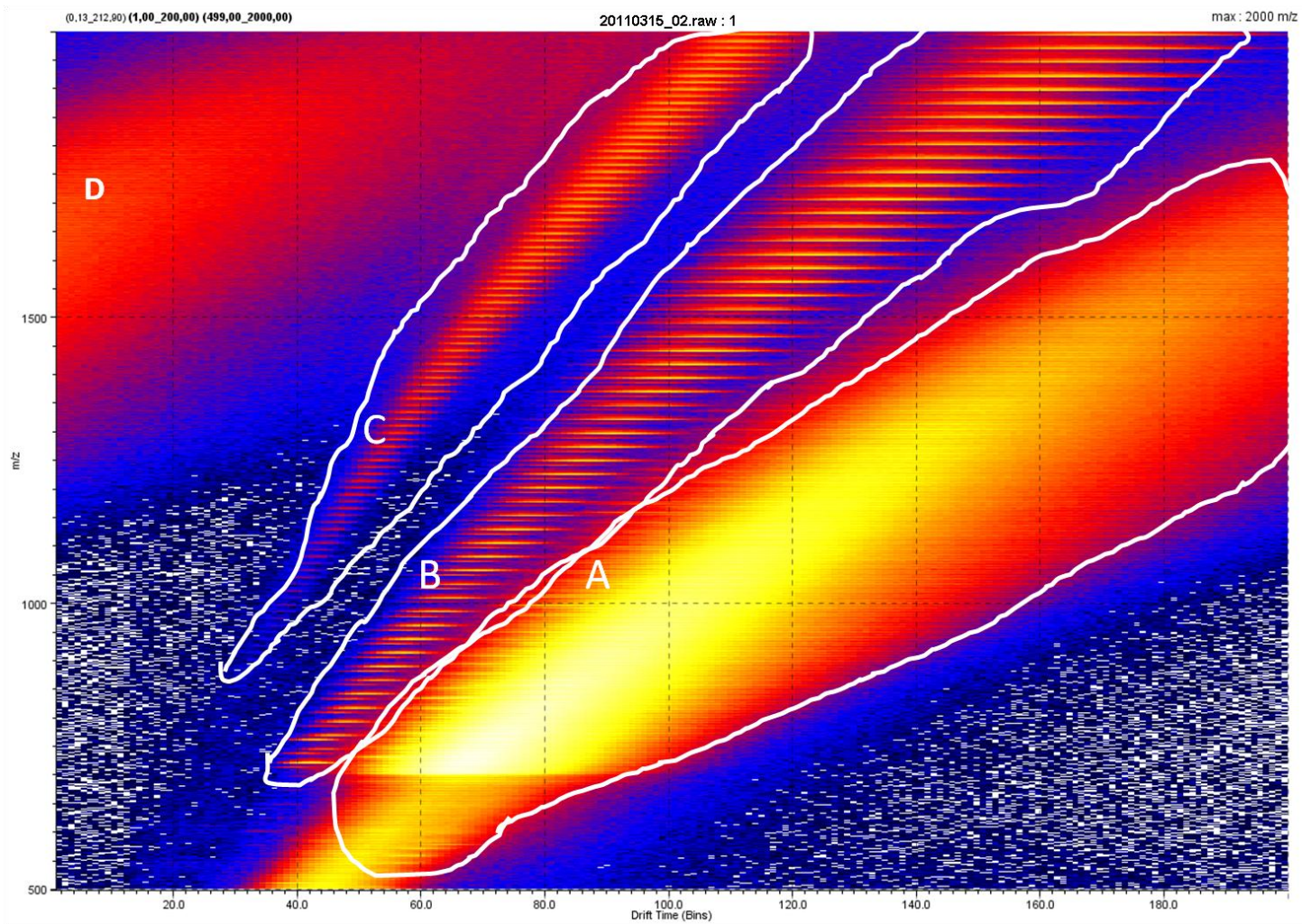


Figure A-2. Ion mobility plot of LDI analysis of intact wood tissue sections. The different regions outline represent compounds with different drift times, which may be related to the collisional cross-section.

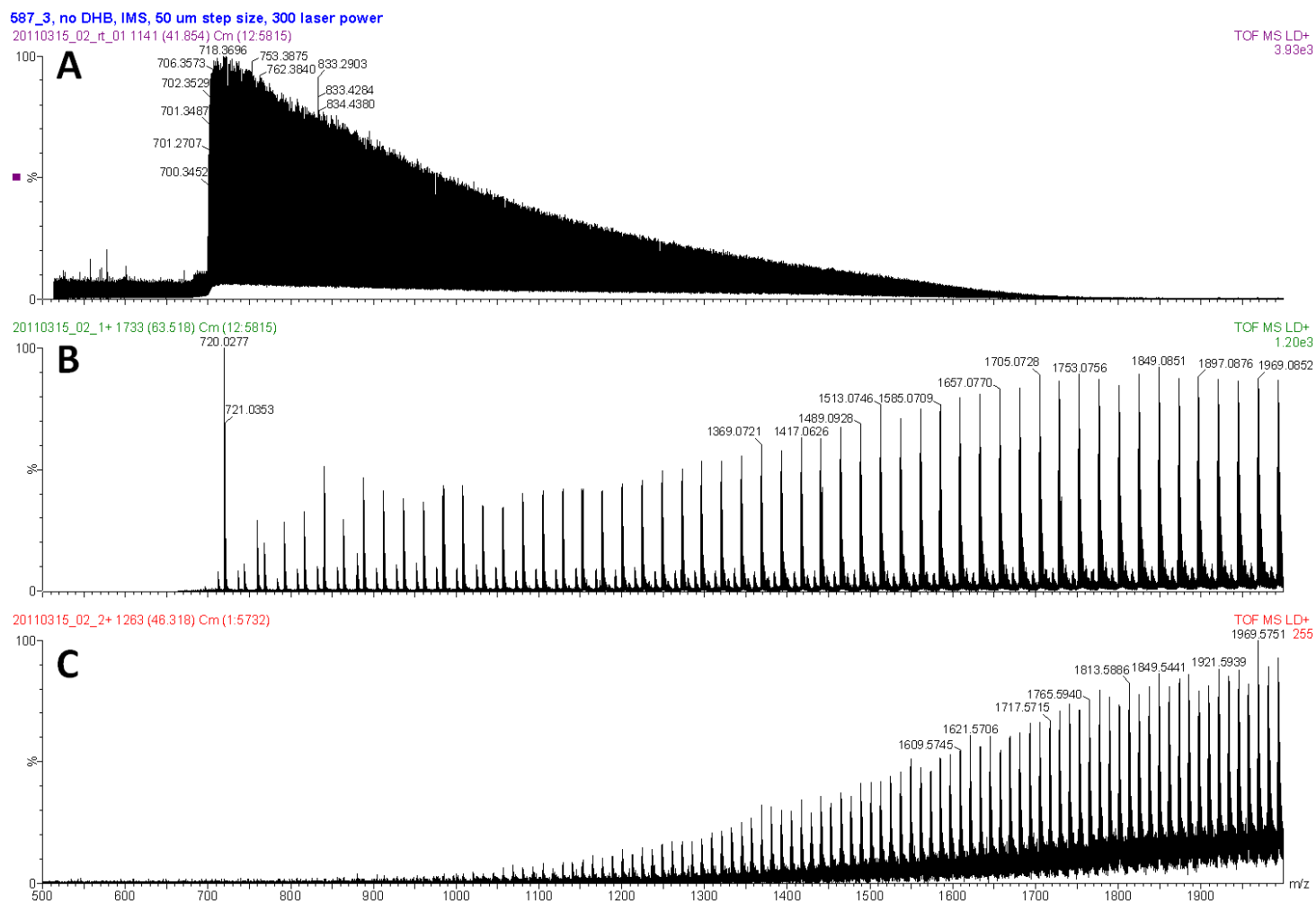


Figure A-3. Mass spectra from the different regions of the ion mobility plot from Figure A-2. A) Spectrum that looks similar to LDI spectrum from MALDI LIT. B) Intense ion at m/z 720, which was identified as C_{60} cluster. The ions observed at higher m/z values are 24 mass units apart. C) doubly-charged carbon cluster

LIST OF REFERENCES

- (1) Himmel, M. E.; Ding, S.; Johnson, D. K.; Adney, W. S.; Nimlos, M. R.; Brady, J. W.; Foust, T. D. *Science* **2007**, *315*, 804-807.
- (2) Sun, Y.; Cheng, J. *Bioresour. Technol.* **2002**, *83*, 1-11.
- (3) Wooley, R.; Ruth, M.; Glassner, D.; Sheehan, J. *Biotechnol. Prog.* **1999**, *15*, 794-803.
- (4) Biofuels—Solid, liquid or gas Fuels made from Biomass. (accessed December 7, 2010).
- (5) Service, R. F. *Science* **2007**, *315*, 1488-1491.
- (6) Sluiter, J. B.; Ruiz, R. O.; Scarlata, C. J.; Sluiter, A. D.; Templeton, D. W. *J. Agric. Food Chem.* **2010**, *58*, 9043-9053.
- (7) Zaldivar, J.; Nielsen, J.; Olsson, L. *Appl. Microbiol. Biotechnol.* **2001**, *56*, 17-34.
- (8) Wyman, C. E. *Bioresour. Technol.* **1994**, *50*, 3-16.
- (9) Duff, S. J. B.; Murray, W. D. *Bioresour. Technol.* **1996**, *55*, 1-33.
- (10) Katzen, R.; Fowler, D. E. *Appl. Biochem. Biotechnol.* **1994**, *45-6*, 697-707.
- (11) Grethlein, H. E.; Converse, A. O. *Bioresour. Technol.* **1991**, *36*, 77-82.
- (12) Lora, J. H.; Wayman, M. *Tappi* **1978**, *61*, 47-50.
- (13) Dale, B. E.; Henk, L. L.; Shiang, M. *Dev. Ind. Microbiol.* **1985**, *26*, 223-233.
- (14) Esteghlalian, A.; Hashimoto, A. G.; Fenske, J. J.; Penner, M. H. *Bioresour. Technol.* **1997**, *59*, 129-136.
- (15) Chum, H. L.; Johnson, D. K.; Black, S.; Baker, J.; Grohmann, K.; Sarkanen, K. V.; Wallace, K.; Schroeder, H. A. *Biotechnol. Bioeng.* **1988**, *31*, 643-649.
- (16) Mcmillan, J. D. Pretreatment of Lignocellulosic Biomass. In *Enzymatic Conversion of Biomass for Fuels Production*, Himmel, M.E., Baker, J. O., Overend, R.P., Eds.; ACS Symposium Series 566; American Chemical Society: Washington, DC, 1994, pp 292–324.
- (17) Grous, W. R.; Converse, A. O.; Grethlein, H. E. *Enzyme Microb. Technol.* **1986**, *8*, 274-280.

- (18) Lloyd, T. A.; Wyman, C. E. *Bioresour. Technol.* **2005**, *96*, 1967-1977.
- (19) Chundawat, S. P. S.; Donohoe, B. S.; Sousa, L. d. C.; Elder, T.; Agarwal, U. P.; Lu, F.; Ralph, J.; Himmel, M. E.; Balan, V.; Dale, B. E. *Energy Environ. Sci.* **2011**, *4*, 973-984.
- (20) Ding, S.; Xu, Q.; Ali, M. K.; Baker, J. O.; Bayer, E. A.; Barak, Y.; Lamed, R.; Sugiyama, J.; Rumbles, G.; Himmel, M. E. *BioTechniques* **2006**, *41*, 435-443.
- (21) Ishida, N.; Koizumi, M.; Kano, H. *Ann. Bot.* **2000**, *86*, 259-278.
- (22) Bulcke, J. v. d.; Masschaele, B.; Dierick, M.; Acker, J. v.; Stevens, M.; Hoorebeke, L. v. *Int. Biodeterior. Biodegrad.* **2008**, *61*, 278-286.
- (23) Agarwal, U. P. *Planta* **2006**, *224*, 1141-1153.
- (24) Gierlinger, N.; Schwanninger, M. *Plant Physiol.* **2006**, *140*, 1246-1254.
- (25) Yarbrough, J. M.; Himmel, M. E.; Ding, S. Y. *Biotechnology for Biofuels* **2009**, 2-17.
- (26) Zaia, J. *Mass Spectrom. Rev.* **2004**, *23*, 161-227.
- (27) Gross, J. H. *Mass Spectrometry A Textbook*; Springer-Verlag: Berlin, Germany, 2004.
- (28) de Hoffmann, E.; Stroobant, V. *Mass Spectrometry Principles and Applications, Second Edition*; John Wiley & Sons, LTD: West Sussex, England, 2002.
- (29) Fournet, B.; Dhalluin, J. M.; Strecker, G.; Montreuil, J.; Bosso, C.; Defaye, J. *Anal. Biochem.* **1980**, *108*, 35-56.
- (30) Barber, M.; Bordoli, R. S.; Sedgwick, R. D.; Tyler, A. N. *J. Chem. Soc. Chem. Commun.* **1981**, *7*, 325-327.
- (31) Barber, M.; Bordoli, R. S.; Sedgwick, R. D.; Tyler, A. N. *Nature* **1981**, *293*, 270-275.
- (32) Reinhold, V. N.; Reinhold, B. B.; Costello, C. E. *Anal. Chem.* **1995**, *67*, 1772-1784.
- (33) Yamashita, M.; Fenn, J. B. *J. Phys. Chem.* **1984**, *88*, 4451-4459.
- (34) Harvey, D. J. *International Journal of Mass Spectrometry* **2003**, *226*, 1-35.
- (35) Watson, J. T.; Sparkman, D. O. *Introduction to Mass Spectrometry Instrumentation, Applications and Strategies for Data Interpretation*; John Wiley & Sons Ltd.: Chichester, West Sussex, 2007.

- (36) Domon, B.; Costello, C. E. *Glycoconj. J.* **1988**, *5*, 397-409.
- (37) Mueller, D. R.; Domon, B. M.; Blum, W.; Raschdorf, F.; Richter, W. J. *Biomed. and Environ. Mass Spectrom.* **1988**, *15*, 441-446.
- (38) Laine, R. A.; Pamidimukkala, K. M.; Hall, R. W.; French, A. D.; Matta, K. L. *Glycoconj. J.* **1988**, *5*, 292-292.
- (39) Karas, M.; Bachmann, D.; Bahr, U.; Hillenkamp, F. *Int. J. Mass Spectrom. Ion Process.* **1987**, *78*, 53-68.
- (40) Hillenkamp, F.; Karas, M.; Beavis, R. C.; Chait, B. T. *Anal. Chem.* **1991**, *63*, A1193-A1202.
- (41) Stahl, B.; Steup, M.; Karas, M.; Hillenkamp, F. *Anal. Chem.* **1991**, *63*, 1463-1466.
- (42) Wang, B. H.; Dreisewerd, K.; Bahr, U.; Karas, M.; Hillenkamp, F. *J. Am. Soc. Mass Spectrom.* **1993**, *4*, 393-398.
- (43) Dreisewerd, K. *Chem. Rev.* **2003**, *103*, 395-426.
- (44) Hillenkamp, F.; Karas, M. *Int. J. of Mass Spectrom.* **2000**, *200*, 71-77.
- (45) Karas, M.; Kruger, R. *Chem. Rev.* **2003**, *103*, 427-439.
- (46) Knochenmuss, R.; Zenobi, R. *Chem. Rev.* **2003**, *103*, 441-452.
- (47) Knochenmuss, R.; Stortelder, A.; Breuker, K.; Zenobi, R. *J. of Mass Spectrom.* **2000**, *35*, 1237-1245.
- (48) Jaskolla, T. W.; Karas, M. *J. Am. Soc. Mass Spectrom.* **2011**, *22*, 976-988.
- (49) Berkenkamp, S.; Menzel, C.; Karas, M.; Hillenkamp, F. *Rapid Commun. Mass Spectrom.* **1997**, *11*, 1399-1406.
- (50) Burns, M. S. *Ultramicroscopy* **1988**, *24*, 269-281.
- (51) Griffiths, J. *Anal. Chem.* **2008**, *80*, 7194-7197.
- (52) Walker, A. V. *Anal. Chem.* **2008**, *80*, 8865-8870.
- (53) Sodhi, R. N. S. *Analyst* **2004**, *129*, 483-487.
- (54) McDonnell, L. A.; Heeren, R. M. A. *Mass Spectrom. Rev.* **2007**, *26*, 606-643.

- (55) Touboul, D.; Halgand, F.; Brunelle, A.; Kersting, R.; Tallarek, E.; Hagenhoff, B.; Laprevote, O. *Anal. Chem.* **2004**, *76*, 1550-1559.
- (56) Scripps Center for Metabolomics and Mass Spectrometry.
http://masspec.scripps.edu/mshistory/whatisms_details.php (accessed January 10, 2011).
- (57) Scigelova, M.; Makarov, A. *Proteomics* **2006**, *6*, 16-21.
- (58) March, R. E.; Todd, J. F. J., Eds.; *Practical Aspects of Ion Trap Mass Spectrometry*; CRC Press: New York, NY, 1995; Vol. 1.
- (59) Schwartz, J. C.; Senko, M. W.; Syka, J. E. P. *J. Am. Soc. Mass Spectrom.* **2002**, *13*, 659-669.
- (60) March, R. E.; Todd, J. F. J. *Quadrupole Ion Trap Mass Spectrometry*; Wiley & Sons, Inc.: Hoboken, New Jersey, 2005; .
- (61) Douglas, D. J.; Frank, A. J.; Mao, D. M. *Mass Spectrom. Rev.* **2005**, *24*, 1-29.
- (62) Stafford, G. C.; Kelley, P. E.; Syka, J. E. P.; Reynolds, W. E.; Todd, J. F. J. *Int. J. Mass Spectrom. Ion Process.* **1984**, *60*, 85-98.
- (63) Johnson, J. V.; Yost, R. A.; Kelley, P. E.; Bradford, D. C. *Anal. Chem.* **1990**, *62*, 2162-2172.
- (64) Magparangalan, D. P.; Garrett, T. J.; Drexler, D. M.; Yost, R. A. *Anal. Chem.* **2010**, *82*, 930-934.
- (65) Landgraf, R. R.; Conaway, M. C. P.; Garrett, T. J.; Stacpoole, P. W.; Yost, R. A. *Anal. Chem.* **2009**, *81*, 8488-8495.
- (66) Hager, J. W. *Rapid Commun. Mass Spectrom.* **2002**, *16*, 512-526.
- (67) de Hoffmann, E.; Stroobant, V. In *Mass Spectrometry Principles and Applications*; John Wiley & Sons, Ltd.: Chichester, New York, 2002..
- (68) Chandra, S.; Chabot, J. F.; Morrison, G. H.; Leopold, A. C. *Science* **1982**, *216*, 1221-1223.
- (69) Pacholski, M. L.; Winograd, N. *Chem. Rev.* **1999**, *99*, 2977-3006.
- (70) Denoyer, E.; Vangrieken, R.; Adams, F.; Natusch, D. F. S. *Anal. Chem.* **1982**, *54*, 26-41.

- (71) Wechsung, R.; Hillenkamp, F.; Kaufmann, R.; Nitsche, R.; Vogt, H. *Mikroskopie* **1978**, *34*, 47-54.
- (72) Schwartz, S. A.; Reyzer, M. L.; Caprioli, R. M. *J. Mass Spectrom.* **2003**, *38*, 699-708.
- (73) Kruse, R.; Sweedler, J. V. *J. Am. Soc. Mass Spectrom.* **2003**, *14*, 752-759.
- (74) Baluya, D. L.; Garrett, T. J.; Yost, R. A. *Anal. Chem.* **2007**, *79*, 6862-6867.
- (75) Todd, P. J.; Schaaff, T. G.; Chaurand, P.; Caprioli, R. M. *J. Mass Spectrom.* **2001**, *36*, 355-369.
- (76) Schueler, B. W. *Microsc. Microanal. Microstruct.* **1992**, *3*, 119-139.
- (77) Takats, Z.; Wiseman, J. M.; Gologan, B.; Cooks, R. G. *Science* **2004**, *306*, 471-473.
- (78) Ifa, D. R.; Gumaelius, L. M.; Eberlin, L. S.; Manicke, N. E.; Cooks, R. G. *Analyst* **2007**, *132*, 461-467.
- (79) Kertesz, V.; Ford, M. J.; Van Berkel, G. J. *Anal. Chem.* **2005**, *77*, 7183-7189.
- (80) Ellis, S. R.; Wu, C.; Deeley, J. M.; Zhu, X.; Truscott, R. J. W.; Panhuis, M. I. H.; Cooks, R. G.; Mitchell, T. W.; Blanksby, S. J. *J. Am. Soc. Mass Spectrom.* **2010**, *21*, 2095-2104.
- (81) Brown, R. S.; Lennon, J. J. *Anal. Chem.* **1995**, *67*, 1998-2003.
- (82) Garrison, B. J.; Delcorte, A.; Zhigilei, L.; Itina, T. E.; Krantzman, K. D.; Yingling, Y. G.; McQuaw, C. M.; Smiley, E. J.; Winograd, N. *Appl. Surf. Sci.* **2003**, *203*, 69-71.
- (83) Troendle, F. J.; Reddick, C. D.; Yost, R. A. *J. Am. Soc. Mass Spectrom.* **1999**, *10*, 1315-1321.
- (84) Garrett, T. J.; Yost, R. A. *Anal. Chem.* **2006**, *78*, 2465-2469.
- (85) Garrett, T. J.; Prieto-Conaway, M.; Kovtoun, V.; Bui, H.; Izgarian, N.; Stafford, G.; Yost, R. A. *Int. J. of Mass Spectrom.* **2007**, *260*, 166-176.
- (86) O'Connor, P. B.; Mirgorodskaya, E.; Costello, C. E. *J. Am. Soc. Mass Spectrom.* **2002**, *13*, 402-407.
- (87) Makarov, A. *Anal. Chem.* **2000**, *72*, 1156-1162.
- (88) Hardman, M.; Makarov, A. A. *Anal. Chem.* **2003**, *75*, 1699-1705.

- (89) *Surfer*, Surface Mapping System, version 8.05; Golden Software, Inc.: Golden, CO, 2004.
- (90) Ritter, S. K. *Chem. Eng. News* **2008**, *86*, 59-68.
- (91) WKU Bio 113 - Carbohydrates.
<http://bioweb.wku.edu/courses/BIOL115/Wyatt/Biochem/Carbos.htm> (accessed Aug. 11, 2009).
- (92) Mosier, N.; Wyman, C.; Dale, B.; Elander, R.; Lee, Y. Y.; Holtzapple, M.; Ladisch, M. *Bioresour. Technol.* **2005**, *96*, 673-686.
- (93) Reis, A.; Pinto, P.; Evtuguin, D. V.; Neto, C. P.; Domingues, P.; Ferrer-Correia, A. J.; Rosario, M.; Domingues, M. *Rapid Commun. Mass Spectrom.* **2005**, *19*, 3589-3599.
- (94) Yokoyama, T.; Kadla, J. F.; Chang, H. M. *J. Agric. Food Chem.* **2002**, *50*, 1040-1044.
- (95) Ingle, J. D.; Crouch, S. R. *Spectrochemical Analysis*; Prentice-Hall, Inc/: Upper Saddle River, NJ, 1988.
- (96) Guo, Z.; Lin He *Analytical and Bioanalytical Chemistry* **2007**, *387*, 1939-1944.
- (97) US Department of Energy Biomass Program: Feedstock Composition Glossary.
http://www1.eere.energy.gov/biomass/feedstock_glossary.html (accessed December 20, 2010).
- (98) Sykes, R.; Kodrzycki, B.; Tuskan, G.; Foutz, K.; Davis, M. *Wood Sci. Technol.* **2008**, *42*, 649-661.
- (99) Bose, S. K.; Francis, R. C.; Govender, M.; Bush, T.; Spark, A. *Bioresour. Technol.* **2009**, *100*, 1628-1633.
- (100) Ragauskas, A. J.; Williams, C. K.; Davison, B. H.; Britovsek, G.; Cairney, J.; Eckert, C. A.; Frederick, W. J.; Hallett, J. P.; Leak, D. J.; Liotta, C. L.; Mielenz, J. R.; Murphy, R.; Templer, R.; Tschaplinski, T. *Science* **2006**, *311*, 484-489.
- (101) Lynd, L. R.; Wyman, C. E.; Gerngross, T. U. *Biotechnol. Prog.* **1999**, *15*, 777-793.
- (102) Wyman, C. E.; Dale, B. E.; Elander, R. T.; Holtzapple, M.; Ladisch, M. R.; Lee, Y. Y. *Bioresour. Technol.* **2005**, *96*, 1959-1966.
- (103) McCann, M. C.; Carpita, N. C. *Curr. Opin. Plant Biol.* **2008**, *11*, 314-320.
- (104) Karas, M.; Hillenkamp, F. *Anal. Chem.* **1988**, *60*, 2299-2301.

- (105) Belu, A. M.; Graham, D. J.; Castner, D. G. *Biomaterials* **2003**, *24*, 3635-3653.
- (106) Caprioli, R. M.; Farmer, T. B.; Gile, J. *Anal. Chem.* **1997**, *69*, 4751-4760.
- (107) Cha, S. W.; Song, Z. H.; Nikolau, B. J.; Yeung, E. S. *Anal. Chem.* **2009**, *81*, 2991-3000.
- (108) Jung, S.; Chen, Y.; Sullards, M. C.; Ragauskas, A. J. *Rapid Commun. Mass Spectrom.* **2010**, *24*, 3230-3236.
- (109) Jung, S.; Foston, M.; Sullards, M. C.; Ragauskas, A. J. *Energy Fuels* **2010**, *24*, 1347-1357.
- (110) Tokareva, E. N.; Fardim, P.; Pranovich, A. V.; Fagerholm, H. P.; Daniel, G.; Holmbom, B. *Appl. Surf. Sci.* **2007**, *253*, 7569-7577.
- (111) Li, Z.; Chu, L.; Sweedler, J. V.; Bohn, P. W. *Anal. Chem.* **2010**, *82*, 2608-2611.
- (112) Li, Z.; Bohn, P. W.; Sweedler, J. V. *Bioresour. Technol.* **2010**, *101*, 5578-5585.
- (113) Karas, M.; Bahr, U.; Hillenkamp, F. *Int. J. of Mass Spectrom. Ion Processes* **1989**, *92*, 231-242.
- (114) Blancaflor, E. B.; Gilroy, S. *Am. J. Bot.* **2000**, *87*, 1547-1560.
- (115) O'Brien, T. P.; Feder, N.; McCully, M. E. *Protoplasma* **1964**, *59*, 367-373.
- (116) Lacayo, C. I.; Malkin, A. J.; Holman, H. N.; Chen, L.; Ding, S.; Hwang, M. S.; Thelen, M. P. *Plant Physiol.* **2010**, *154*, 121-133.
- (117) Skoog, D. A.; West, D. M.; Holler, F. J.; Crouch, S. R. In *Fundamentals of Analytical Chemistry*; Brooks/Cole—Thomson Learning: Belmont, CA, 2004; , pp 1051.
- (118) Lakowicz, J. R. In *Principles of Fluorescence Spectroscopy*; Springer Science+Business Media, LLC: New York, NY, 2006.
- (119) Wood, P. J. *Carbohydr. Res.* **1980**, *85*, 271-287.
- (120) Ram, A. F. J.; Klis, F. M. *Nat. Protoc.* **2006**, *1*, 2253-2256.
- (121) Li, K. C.; Reeve, D. W. *J. Wood Chem. Technol.* **2004**, *24*, 169-181.
- (122) Slodzian, G.; Daigne, B.; Girard, F.; Boust, F.; Hillion, F. *Biol. Cell.* **1992**, *74*, 43-50.

- (123) Goacher, R. E.; Jeremic, D.; Master, E. R. *Anal. Chem.* **2011**, *83*, 804-812.
- (124) *Genetics and Genomics of Populus*; Jansson, S., Bhalerao, R.P., Groover, A. T., Eds.; Plant Genetics and Genomics Crops and Models: 8; Springer, New York, NY 2010.
- (125) Mauseth, J. D. In *An Introduction to Plant Biology*; Saunders College Publishing, Philadelphia, PA, 1991.
- (126) Meuzelaar, H. L. C.; Isenhour, T. L., Eds.; *Computer-Enhanced Analytical Spectroscopy*; Plenum Press: New York, NY, 1987.
- (127) Windig, W.; Haverkamp, J.; Kistemaker, P. G. *Anal. Chem.* **1983**, *55*, 81-88.
- (128) Windig, W.; Meuzelaar, H. L. C. *Anal. Chem.* **1984**, *56*, 2297-2303.
- (129) Miller, J. N.; Miller, J. C. In *Statistic and Chemometrics for Analytical Chemistry*; Pearson Education Limited: Essex, England, 2010.
- (130) Brereton, R. G. In *Chemometrics: Data Analysis for the Laboratory and Chemical Plant*; John Wiley & Sons, Ltd.: West Sussex, England, 2003.
- (131) Brereton, R. G. *Analyst* **1995**, *120*, 2313-2336.
- (132) Altelaar, A. F. M.; Luxembourg, S. L.; McDonnell, L. A.; Piersma, S. R.; Heeren, R. M. A. *Nat. Protoc.* **2007**, *2*, 1185-1196.
- (133) Wu, L.; Felton, J. S.; Wu, K. J. J. *Mass Spectrometry Imaging: Principles and Protocols* **2010**.
- (134) McCombie, G.; Staab, D.; Stoeckli, M.; Knochenmuss, R. *Anal. Chem.* **2005**, *77*, 6118-6124.
- (135) Deininger, S.; Ebert, M. P.; Fuetterer, A.; Gerhard, M.; Roecken, C. *J. Proteome Res.* **2008**, *7*, 5230-5236.
- (136) Deininger, S.; Becker, M.; Suckau, D. *Mass Spectrometry Imaging: Principles and Protocols* **2010**, , 385-403.
- (137) Vaezian, B.; Anderton, C. R.; Kraft, M. L. *Anal. Chem.* **2010**, *82*, 10006-10014.
- (138) Rakotomalala, R. *Proceedings of EGC2005, RNTI-E-3* **2005**, *2*, 697-702.
- (139) Xia, J.; Psychogios, N.; Young, N.; Wishart, D. S. *Nucleic Acids Res.* **2009**, *37*, W652-W660.

- (140) Pouwels, A. Analytical Pyrolysis Mass Spectrometry of Wood Derived Polymer Fractions, FOM Institute for Atomic and Molecular Physics, Amsterdam, The Netherlands, 1989.
- (141) Qiao, H.; Spicer, V.; Ens, W. *Rapid Commun. Mass Spectrom.* **2008**, *22*, 2779-2790.
- (142) Kroto, H. W.; Heath, J. R.; O'Brien, S. C.; Curl, R. F.; Smalley, R. E. *Nature* **1985**, *318*, 162-163.

BIOGRAPHICAL SKETCH

Kyle Ann Lunsford, the daughter of Bonnie and 'Jeff' Lunsford and younger sister of Quin Lunsford, grew-up in Augusta, Georgia, where she completed elementary, middle and high school. In 2007, Kyle graduated from Elon University, a small liberal arts school in Elon, North Carolina, with a B.S. in chemistry (one of four) and minor in mathematics. While at Elon, Kyle conducted undergraduate research under Dr. Joel Karty using electrical resistivity experiments to elucidate the mechanism of periodic precipitation reactions.

During the summer of 2005 and 2006, Kyle had the unique experience to intern at the Idaho National Laboratory (INL) with Dr. Jeffrey Giglio at the Material Fuels Complex. At INL, Kyle worked on characterizing nuclear fuel rods using inductively coupled plasma mass spectrometry (ICP-MS). In addition to working at the INL, Kyle spent a semester interning at Mother Murphy's Laboratories, Inc, a flavor lab in Greensboro, NC. Kyle assisted in compounding new flavors, as well as integrating flavors into products, such as doughnuts and hard candies. Both of these experiences pushed Kyle to pursue a graduate degree in chemistry, specifically analytical chemistry.

Kyle started graduate school at the University of Florida fall of 2007 and later joined the Yost group. Throughout her four years, she worked on a Department of Energy funded research project in collaboration with Dr. Gary F. Peter in the School of Forest Resources and Conservation. Kyle received her PhD in analytical chemistry in the summer of 2011.